VOLUME 77 NOVEMBER 22, 1973 NUMBER 24

JPCHAx

THE JOURNAL OF PHYSICAL CHEMISTRY

PUBLISHED BIWEEKLY BY THE AMERICAN CHEMICAL SOCIETY

THE JOURNAL OF

PHYSICAL CHEMISTRY

All manuscripts should be sent to *The Journal of Physical Chemistry*, Department of Chemistry, University of Minnesota, Minneapolis, Minn. 55455.

Additions and Corrections are published once yearly in the final issue. See Volume 76, Number 26 for the proper form.

Extensive or unusual alterations in an article after it has been set in type are made at the author's expense, and it is understood that by requesting such alterations the author agrees to defray the cost thereof.

The American Chemical Society and the Editor of *The Journal of Physical Chemistry* assume no responsibility for the statements and opinions advanced by contributors.

Correspondence regarding accepted copy, proofs, and reprints should be directed to Editorial Processing Department, American Chemical Society, 20th and Northampton Sts., Easton, Pa. 18042. Head: CHARLES R. BERTSCH. Assistant Editor: EDWARD A. BORGER. Editorial Assistant: JOSEPH E. YURVATI.

Advertising Office: Centcom, Ltd., 142 East Avenue, Norwalk, Conn. 06851.

Business and Subscription Information

Send all new and renewal subscriptions *with payment* to: Office of the Controller, 1155 16th Street, N.W., Washington, D. C. 20036. Subscriptions should be renewed promptly to avoid a break in your series. All correspondence and telephone calls regarding changes of address, claims for missing issues, subscription service, the status of records, and accounts should be directed to Manager, Membership and Subscription Services, American Chemical Society, P.O. Box 3337, Columbus, Ohio 43210. Telephone (614) 421-7230.

On changes of address, include both old and new addresses with ZIP code numbers, accompanied by mailing label from a recent issue. Allow four weeks for change to become effective.

Claims for missing numbers will not be allowed (1) if loss was due to failure of notice of change in address to be received before the date specified, (2) if received more than sixty days from date of issue plus time normally required for postal delivery of journal and claim, or (3) if the reason for the claim is "issue missing from files."

Subscription rates (1973): members of the American Chemical Society, $20.00 for 1 year; to nonmembers, $60.00 for 1 year. Those interested in becoming members should write to the Admissions Department, American Chemical Society, 1155 Sixteenth St., N.W., Washington, D. C. 20036. Postage to Canada and countries in the Pan-American Union, $5.00; all other countries, $6.00. Single copies for current year: $3.00. Rates for back issues from Volume 56 to date are available from the Special Issues Sales Department, 1155 Sixteenth St., N.W., Washington, D. C. 20036.

Subscriptions to this and the other ACS periodical publications are available on microfilm. Supplementary material not printed in this journal is now available in microfiche form on a current subscription basis. For information on microfilm or microfiche subscriptions, write Special Issues Sales Department at the address above.

Notice to Authors last printed in the issue of June 21, 1973

THE JOURNAL OF

PHYSICAL CHEMISTRY

Volume 77, Number 24 November 22, 1973

JPCHAx 77(24) 2823–2930 (1973)
ISSN 0022-3654

COMMUNICATIONS TO THE EDITOR

■ Supplementary material for this paper is available separately, in photocopy or microfiche form. Ordering information is given in the paper.

* In papers with more than one author, the asterisk indicates the name of the author to whom inquiries about the paper should be addressed.

AUTHOR INDEX

ANNOUNCEMENT

On the last two pages of this issue you will find reproduced the table of contents of the October 1973 issue of the Journal of Chemical and Engineering Data.

THE JOURNAL OF
PHYSICAL CHEMISTRY

VOLUME 77, NUMBER 24 NOVEMBER 22, 1973

Exploratory Shock-Wave Study of Thermal Nitrogen Trifluoride Decomposition and Reactions of Nitrogen Trifluoride and Dinitrogen Tetrafluoride with Hydrogen[1a,b]

Garry L. Schott,* Larry S. Blair, and John D. Morgan, Jr.
Los Alamos Scientific Laboratory, University of California, Los Alamos, New Mexico 87544 *(Received July 9, 1973)*
Publication costs assisted by the U.S. Atomic Energy Commission

Shock waves in gas mixtures containing ≥94% Ar are combined with time-resolved spectrometry of NF_2 absorption at 260 nm and HF emission at 2.7 μm, plus secondary diagnostics, in a survey of rapid thermal reactions of NF_3 and mixtures of H_2 with NF_3 or N_2F_4. NF_3 decomposition between 1100 and 1500 K produces maximum NF_2 concentrations accountable by the equilibrium $NF_3 \rightleftharpoons NF_2 + F$, followed by slower, irreversible NF_2 removal. NF_3–H_2 mixtures were inert for ≳2 msec below ~1000 K, and reacted in ≲50 μsec above ~1500 K, exhibiting (i) complete HF yield, preceded by supraequilibrium infrared emission, (ii) no resolvable [NF_2] transient, and (iii) copious NH ($A^3\Pi \rightarrow X^3\Sigma^-$) chemiluminescence at 336 nm during the reaction. Delayed and gas dynamically unstable reactions occurred over the $1000 \lesssim T < 1500$ K range. Near 700–900 K, N_2F_4–H_2 mixtures, containing butene to suppress room-temperature reaction, quantitatively form NF_2 which, like NF_3, is inert for ~2 msec. At higher temperatures, the NF_2 yield from these mixtures is transient, and HF vibrational emission, NH chemiluminescence, and gas dynamic instabilities occur very similarly to the NF_3–H_2 reaction. The roles of pyrolytic dissociation and subsequent bimolecular reactions of the intermediates in the mechanism of stoichiometric formation of HF and N_2 are discussed.

Introduction

Recent use of NF_3 and N_2F_4 as reagents in premixed HF chemical lasers[2] has prompted us to investigate the occurrence of rapid thermal reactions of these substances with H_2. Although flames of NF_3 and H_2 have been reported,[3a] these gases may be mixed up to 100° without reaction.[3b] Thermal decomposition kinetics of NF_3 have only been reported since the present work was completed.[3c] In contrast, N_2F_4–H_2 mixtures without an inhibitor are spontaneously explosive near room temperature,[3b] and several kinetics studies have been made[4] of the forward[4a-c] and reverse[4d] dissociation of N_2F_4, as well as of subsequent decomposition[5,6] of the resulting NF_2.

Ultraviolet absorption by NF_2 near 260 nm is an established method[3c,4,5b,7] of determining NF_2 concentration *in situ*. It is the central diagnostic used here, in conjunction with incident shock waves in gas mixtures with ≥94% Ar, to explore NF_3 thermal decomposition and the partial reaction behavior of N_2F_4–H_2–C_4H_8 mixtures. Infrared and ultraviolet emission spectrometry are used as complementary means of detecting the formation of HF and the presence of nonequilibrium intermediates in the reaction between H_2 and either NF_3 or N_2F_4.

The salient findings are the following.

(i) Measurable NF_2 is formed during NF_3 decomposition above about 1100 K, in amounts accountable by equilibrium dissociation according to

$$NF_3 + M \rightarrow NF_2 + F + M \quad (1)$$

followed by slower, irreversible formation of the permanent products, N_2 and F atoms.

(ii) Below about 900 K, neither NF_3 nor NF_2 reacts detectably with H_2 for up to 0.002 sec, at partial pressures in the neighborhood of 1–5 Torr.

(iii) The lowest temperature experiments (~1000–1400 K) with detectable HF formation in these mixtures exhibit pronounced, large-scale shock wave instabilities driven by the exothermic overall reactions

$$\tfrac{1}{2}H_2 + \tfrac{1}{3}NF_3 \rightarrow HF + \tfrac{1}{6}N_2 \qquad \Delta H^\circ_{298} = -54.8 \text{ kcal/mol of HF} \quad (2)$$

$$\tfrac{1}{2}H_2 + \tfrac{1}{4}N_2F_4 \rightarrow HF + \tfrac{1}{4}N_2 \qquad \Delta H^\circ_{298} = -64.4 \text{ kcal/mol of HF} \quad (3)$$

(iv) With H_2 and either NF_3 or N_2F_4, prompt HF formation occurs above ~1500 K. The reaction is accompanied by intense chemiluminescent NH emission at 336

nm, and by 2.7-μm HF emission, which exceeds the subsequent stable, equilibrium thermal intensity. No NF_2 was detected in the $H_2 + NF_3$ case.

Experimental Section

Test mixtures of commercially supplied gases of the following grades, H_2 and Ar, 99.9% purity; NF_3 (Pennsalt) 98% purity, principal impurity air; N_2F_4 (Air Products) and *cis*-2-butene (Phillips), (the only C_4H_8 isomer used in this work) research grade, were prepared using a precision quartz bourdon pressure gauge (Texas Instruments, 0–1000 Torr range) and stored in a stainless steel vessel. Mass spectrometric analysis of the mixture batches and of the nitrogen fluoride supplies determined the absence of major or unexpected impurities.

A liquid N_2-trapped oil diffusion pump served the shock tube and the gas manifold comprising copper, brass, bronze, and aluminum parts, silver-soldered joints, and Viton valve seats and O-rings, lubricated with Halocarbon grease. The brass, 10.2 cm i.d., bursting diaphragm shock tube was internally electroplated with Ni. A pair of 12.7-mm diameter flat synthetic sapphire optical windows were diametrically situated in the test section 3.84 m from the diaphragm plane. Five 2-mm diameter piezoelectric pressure sensors were spaced along the test section at intervals of 10 cm or greater for shock velocity measurement and instrument triggering. The postshock thermodynamic states of gases were computed by established methods[8] using the initial state data, the measured shock velocity, and standard thermochemical data.[9]

Ultraviolet spectrometric measurements used a 0.5-m grating monochromator (JACO Model 82-000), an RCA 1P28 photomultiplier, and a dc Hg–Xe arc lamp, in a setup similar to Figure 1 of ref 10. Slit settings provided approximately 4-mm axial resolution in the shock tube, and the spectral band defined by the monochromator in the absorption measurements on NF_2 was triangular, centered at 260 nm with 6.4 nm half-width.

Infrared emission measurements were made with about 5-mm axial space resolution, using an InAs detector (Philco) operated at room temperature in reverse-voltage biased mode in a straightforward setup with collimating slits, a condensing mirror, and a multilayer filter with 0.7-μm half-width centered at 2.72 μm, which selected the vibrational fundamental of HF.

Auxiliary, time-integrated photographic spectra of NF_3–H_2 and N_2F_4–H_2–C_4H_8 reactions in reflected shock waves were also taken, through a sapphire window in the end of the shock tube, using a Hilger medium quartz spectrograph.

Results

Uv Absorption Measurements of $[NF_2]$. NF_2 formation during NF_3 pyrolysis was examined by absorption spectrophotometry at $254 \leq \lambda \leq 266$ nm in eight incident shock wave experiments in a 5% NF_3, 95% Ar mixture. These experiments had a preshock pressure of 30 Torr and covered a range of postshock, no reaction temperatures of 1100–1850 K. F_2, should it be formed, absorbs too weakly[11] at this wavelength to have been detected, and NF_3 and the other expected products of its decomposition, NF, N_2, N, and F are thoroughly transparent.

Oscillograms from two of the NF_3 pyrolysis experiments are shown in Figure 1. In the upper record, at the highest temperature examined, transmission drops within $\leq$20 μsec after shock front arrival to a minimum of 33%, and

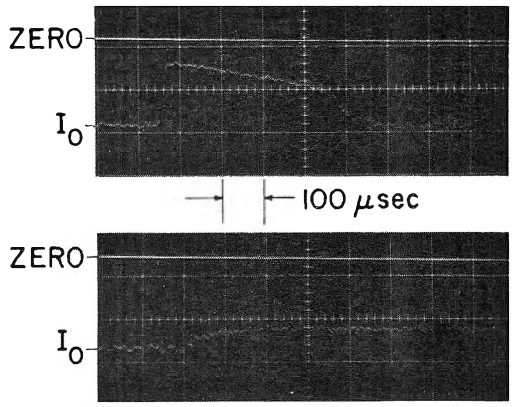

Figure 1. The 260-nm absorption profiles of shock waves in 5% NF_3, 95% Ar, showing presence of NF_2, time advancing to right: upper record, 1.37 km/sec shock speed, $T_{\text{no reaction}}$ = 1846 K, T_{NF_2} = 1481 K; lower record, 1.07 km/sec shock speed, $T_{\text{no reaction}}$ = 1246 K, T_{NF_2} = 1177 K.

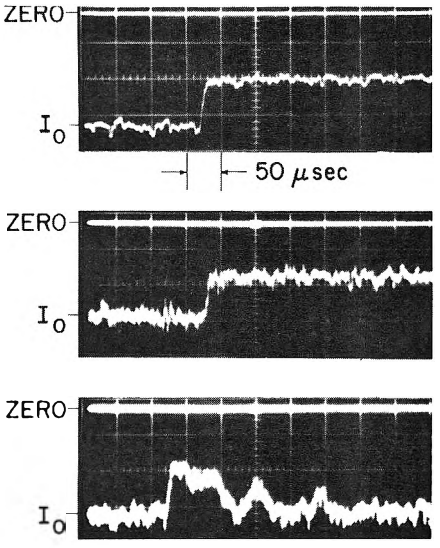

Figure 2. The 260-nm absorption profiles of shock waves in gas mixtures containing N_2F_4, time advancing to right: upper record, 1% N_2F_4, 99% Ar, 0.79 km/sec shock speed, T_{NF_2} = 775 K; middle and lower records; 1% N_2F_4, 0.2% C_4H_8, 98.8% Ar, 0.79 and 1.1 km/sec shock speeds, and T_{NF_2} = 760 and 1300 K, respectively.

then rises steadily over the next ~400 μsec, until the experiment is ended by disappearance of the incident shock flow. This is interpreted qualitatively as rapid formation of NF_2, followed by slower disappearance, in keeping with the known instability of NF_2 near 1500 K.[5] In the lower temperature experiment represented in the lower oscillogram of Figure 1, the appearance of NF_2 continues for about 200 μsec after shock wave arrival, the transmission reaching a minimum level of 77%. No subsequent disappearance of NF_2 is evident over the remaining ~550 μsec of incident shock flow.

Quantitative interpretation of the absorption levels in the above experiments was based on calibration experiments in which known NF_2 concentrations were produced by the prompt, complete dissociation of N_2F_4

$$N_2F_4 + M \longrightarrow 2NF_2 + M \qquad (4)$$

Specimen oscillograms of these N_2F_4 experiments are shown in Figure 2, and the Beer's law plot of NF_2 absorbance for a 10.2-cm path over the range $0.5 \times 10^{-4} \leq [NF_2]$

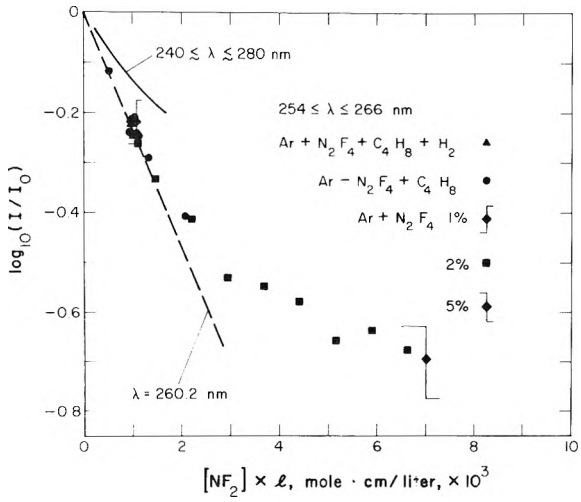

Figure 3. The 260-nm absorbance *vs.* NF_2 optical density, determined in shock waves with quantitative dissociation of N_2F_4: points present results for gas mixtures specified in Table I; dashed curve, 260-nm monochromatic extinction coefficient (Napierian) of 550 M^{-1} cm^{-1} from ref 4a and 7; solid curve, broader spectral band results from Figure 3 of ref 4b.

TABLE I: Summary of 260-nm Absorbance Experiments in N_2F_4 Mixtures

Mixture composition, %				No. of experiments	Preshock pressure(s), Torr	T_{NF_2} range, K
N_2F_4	C_4H_8	H_2	Ar			
5.0	0	0	95.0	9	30	527–1608
2.0	0	0	98.0	9	15–90	920–950
1.0	0	0	99.0	10	30	735–1935
1.0	0.2	0	98.8	8	15–60	760–1305
1.0	0.2	2.0	96.8	3	30	755–915

$\leq 7 \times 10^{-4}$ M is shown in Figure 3. The range of conditions of these experiments is summarized in Table I. Temperatures, denoted T_{NF_2}, and the corresponding gas concentrations, were reckoned for these experiments by the steady shock wave equations, including the thermochemistry of reaction 4 but assuming no other reactions.

The results in Figure 3 from the three N_2F_4–Ar mixtures with no fuel provide the basic calibration used to evaluate the peak NF_2 concentrations achieved in the NF_3 decomposition experiments (refer to Figure 1). Absorbances (decadic) in the range 0.046–0.484 yielded $[NF_2]$ over the range $0.17–2.72 \times 10^{-4}$ M.

These concentrations are compared to the formal NF_3 concentrations and to the equilibrium position of reaction 1 in the following way. Postshock equilibrium conditions of temperature and species concentrations were calculated for the range of shock velocities in the 5% NF_3–95% Ar mixture initially at 30 Torr, assuming reaction 1 as the sole chemical reaction. The calculated equilibrium fraction of NF_3 dissociated is plotted *vs.* final temperature, again called T_{NF_2}, in Figure 4. The measured peak NF_2 concentrations for the same shock velocities are represented by the points in this figure, $[NF_2]$ being normalized by the calculated formal NF_3 concentration and plotted at the calculated T_{NF_2}. The agreement between the points and the curve shows that the peak NF_2 yield during NF_3 decomposition is closely accountable by the reversible occurrence of reaction 1, without appreciable formation of N_2 or other products. The two highest temperature points lie systematically below the equilibrium curve, but uncertainty in the measured $[NF_2]$ leaves it unclear whether this discrepancy represents a true measure of the finite NF_2 decomposition which has occurred.

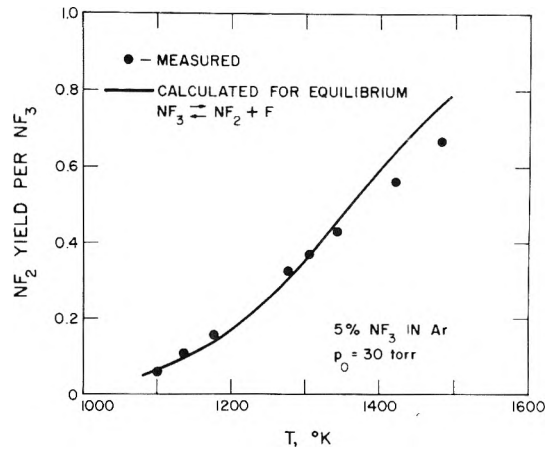

Figure 4. Peak NF_2 yield during pyrolysis of NF_3 in shock waves.

Calculations of poststock conditions in the experiments were also performed including equilibrium occurrence of the side reactions

$$2F \rightleftharpoons F_2 \quad (5)$$

$$NF_2 \rightleftharpoons NF + F \quad (6)$$

$$NF \rightleftharpoons N + F \quad (7)$$

but excluding the formation of N_2. These calculations gave essentially the same values of $[NF_2]$ and temperature as those including only reaction 1, showing that our experiments are insensitive to the equilibrium occurrence of reactions 5–7 over the range of conditions employed. With NF_3 as the starting point, reactions 6 and 7 are suppressed by the sizable F atom concentration accumulated from reaction 1.

An estimate of the rate of reaction 1 was made for one experiment in the middle of the temperature range. At T = 1400 ± 30 K and p = 0.7 atm, the initial differential rate of NF_2 formation from 0 to 10% dissociation of the original NF_3 is described by a first-order rate coefficient of 2.9×10^3 sec^{-1}. Interpreted as a second-order dissociation process, for the 95% Ar collisional environment, this yields $k_1 = 4.75 \times 10^8$ cm^3 mol^{-1} sec^{-1}. Division by the equilibrium constant[9] gives the third-order coefficient $k_{-1} = 1.4 \times 10^{15}$ cm^6 mol^{-2} sec^{-1}, a quite ordinary value for a simple atom attachment.

Table I and Figures 2 and 3 also include results of experiments with mixtures of N_2F_4 and hydrogenous fuels. These experiments yield NF_2 absorbances, based on the stoichiometry of reaction 4, which agree with the calibration determined in the absence of such fuel. This finding shows that under these conditions no reactions between either N_2F_4 or NF_2 and these fuels were rapid enough to compete with the complete occurrence of reaction 4. In fact, the middle oscillogram in Figure 2, and those like it in both the C_4H_8 and C_4H_8 plus H_2 mixtures at temperatures up to about 900 K, show that no discernible reaction of NF_2 with these fuels occurs within ~2 msec, the maximum observed residence time in the shock-heated condition. The bottom oscillogram in Figure 2 illustrates the behavior observed in these same mixtures at somewhat higher temperatures. The formation of NF_2 behind the shock front, although complete, is temporary and is followed by an unstable reaction zone. At temperatures

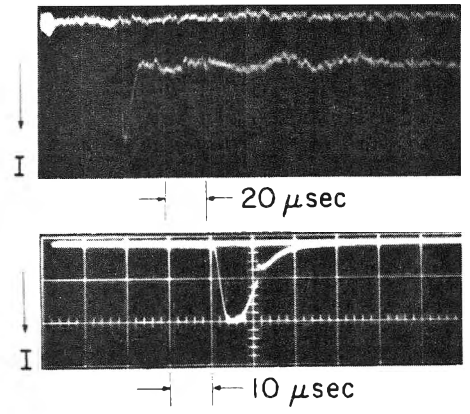

Figure 5. Simultaneous emission spectrometric profiles of reaction zone of 1.36 km/sec shock wave in 2% NF_3, 4% H_2, 94% Ar: $T_{no\ reaction}$ = 1805 K, time advancing to right: upper record, 2.4 $\leq \lambda \leq$ 3.1 μm, vibrational fundamental band of HF; lower record, 334.4 $\leq \lambda \leq$ 337.6 nm, $A^3\Pi \rightarrow X^3\Sigma^-$, $\Delta v = 0$ transition of NH.

above the uppermost values given for these mixtures in Table I, the further reaction was fast enough that the NF_2 transient was progressively truncated and ultimately, near 2000 K, altogether unresolved. Attempts to examine the reaction of NF_3 with H_2 by NF_2 absorption yielded no resolvable NF_2 concentration. We did not examine the rate of NF_2 disappearance quantitatively, either in the NF_3 or N_2F_4 pyrolysis runs or in the N_2F_4 plus fuel experiments, where the reaction leading to HF was gas dynamically unstable and/or inadequately resolved in time.

Emission Spectrometry of Reacting NF_3 + H_2 and N_2F_4 + H_2 + C_4H_8 Mixtures. Formation of HF in the shock-wave reaction zone at elevated temperature is directly detectable by monitoring the intensity of its strong, fundamental vibrational emission bands near 2.5 μm. Shock-wave profiles of this infrared emission were observed in several dilute mixtures of H_2 with NF_3 or N_2F_4, the latter stabilized against reaction at room temperature by inclusion of small amounts of butene.[3b] Table II gives the ranges of conditions of these experiments.

The upper oscillogram in Figure 5 is typical of the infrared emission profiles of these mixtures in shock waves sufficiently strong that the exothermic reaction occurs promptly and no coarse-scaled instabilities are noticed. The infrared emission exhibits a single, narrow spike at the shock front which is followed by long-term, level emission continuing until the end of the incident shock flow. The amplitude of this level emission was found to increase with computed, fully reacted postshock temperature and with reagent concentrations in a manner accountable as the thermally excited radiation from the final, equilibrium HF under conditions of small but noticeable self absorption. Progressive inclusion of butene in the N_2F_4 mixtures did not alter the infrared emission profile.

Since the final HF concentration is believed to be the stoichiometric maximum, we interpret the spike at the shock front as arising from suprathermally excited HF vibrational states present while nonequilibrium conditions prevail. This interpretation is consistent with the known occurrence of laser action from these reactions under other circumstances,[2] and our setup did not permit determination of the HF vibrational condition during the spike. Other transient emitters or fine-scaled transverse shock waves cannot be dismissed as contributory mechanisms in the 2.7-μm emission spikes.

TABLE II: Summary of Nitrogen Fluoride–Hydrogen Ignition Experiments at 30 Torr Preshock Pressure

Mixture composition, %					T_{2msec}, K	$T_{unstable}$, K
H_2	NF_3	C_4H_8	N_2F_4	Ar		
0.33	0.33	0	0	99.3	Not investigated	1550
4.0	2.0	0	0	94.0	990	1450
2.0	4.0	0	0	94.0	Not investigated	1340
2.0	0	0.05	1.0	96.95	780	1700
2.0	0	0.15	1.0	96.85	900	1800
2.0	0	0.50	1.0	96.50	1010	2070

Early attempts to observe 260-nm absorption during the NF_3 + H_2 reaction revealed instead the presence of strong ultraviolet chemiluminescent emission. The main component of this chemiluminescence was identified by photographic spectroscopy as the $A^3\Pi \rightarrow X^3\Sigma^-$ transition of NH. The Q-branch of the 0,0 component of this transition, at 336 nm, is the strongest feature, followed by the 1,1 Q branch at 337 nm. The P and R branches of these transitions are also evident.

The NH 336-nm chemiluminescence was also found in the N_2F_4–H_2–C_4H_8 reaction system, although progressive addition of butene diminished the 336-nm intensity and introduced other spectral components, particularly in the 500–600-nm region, which are tentatively attributed to NH_2 and C_2. CN and C_2 electronic spectra were found to dominate over NH chemiluminescence in pulsed-laser initiated N_2F_4–H_2–C_4H_8 explosions,[21] particularly with excess N_2F_4.

The lower oscilloscope trace in Figure 5 is typical of the 336-nm chemiluminescence profile of the gas mixtures in Table II under conditions of prompt reaction, above about 1500 K. This chemiluminescence is confined to a narrow zone immediately behind the shock front, and the rise in intensity is distinctly more abrupt than the decay. The duration of this 336-nm pulse above scattered light background is generally greater than that of the supraequilibrium infrared spike, by a factor between 1 and 2. At a given shock strength and mixture composition, the duration of the 336-nm emission varied inversely with the gas density, and the peak amplitude varied in direct proportion to the density. From these observations we hypothesize that emission at 336 nm coincides with the occurrence of exothermic, HF-forming reaction between H_2 and these nitrogen fluorides, and that cessation of the NH emission corresponds to substantial completion of the reaction.

Using the 336-nm emission oscillograms of the NF_3–H_2 reaction, the transient NH excited state population within the reaction zone and the electronic radiation yield were estimated. The known radiative lifetime,[12] approximate photomultiplier sensitivity, monochromator transmission characteristics, and the shocked gas viewing geometry were combined with the peak oscilloscope amplitude in a typical NF_3–H_2 experiment to deduce that the peak density of NH in the $A^3\Pi$ state was about 1×10^{11} molecules/cm^3 under conditions where the formal NF_3 concentration was 3×10^{16} molecules/cm^3. Integration of the chemiluminescence profile indicated that only about 4000 NF_3 molecules are consumed per 336-nm photon emitted, from which one deduces that about 0.01% of the energy available from reaction 2 is released as 3.7-eV photons.

As this chemiluminescence is remarkably strong and NH is not a permanent reaction product, a test was made

of the enticing possibility that a population inversion might exist between the $A^3\Pi$ and $X^3\Sigma^-$ states of NH. A capillary flashlamp filled with 10 Torr each of N_2 and H_2 was aligned in place of the Hg-Xe lamp used for NF_2 absorption. This lamp was energized by a damped 10-kV capacitor discharge and emitted the NH $A \rightarrow X$ spectrum in addition to copious N_2 second positive radiation.[13] About 1.5 msec after triggering, the lamp output reaching the monochromator exit was suitably stable over the time of passage of the shock wave and strong enough to be measured in superposition with the radiation originating in the shock tube. Tests were made with the monochromator set to transmit a 0.8-nm full-width triangular band centered at either 336 or 337 nm, in the NF_3-H_2-Ar mixtures (see Table II) with either excess NF_3 or excess H_2. All these experiments yielded peak signals no larger than the sum of the independent lamp and reaction zone signals, and the 336-nm shots indicated between 10 and 25% attenuation of the lamp radiation amplitude. The lamp signal returned to 100% transmission after the chemiluminescent reaction was over. Thus, there is no evidence of amplification, and an indication of absorption by NH within the reaction.

Nitrogen Fluoride-Hydrogen Ignition Characteristics in Shock Waves. The infrared and ultraviolet emission profiles accompanying the formation of HF in shock-heated NF_3-H_2 and N_2F_4-H_2-C_4H_8 mixtures provide a semiquantitative means of examining the effect of shock wave strength, and hence, of gas temperature, upon the time scale of the reaction This study has taken an unconventional form, dictated by the facts that under the high-temperature conditions that produce oscillograms such as Figure 5, the reaction is too rapid for its duration to be resolved faithfully by the slit widths employed, whereas, under conditions of slower reaction, a steady, one-dimensional reaction zone was unobtainable. With these constraints, the most definite quantities we were able to determine were the maximum and minimum shock wave velocities at which macroscopically unstable reaction zones were observed. Above this maximum velocity, where oscillograms such as Figure 5 were obtained, shock front arrival times along the tube indicated shock velocities unperturbed by more than ~1% over successive intervals of 10 cm or longer. Likewise, below the minimum, where no evidence of reaction was found for the ~2 msec lifetime of the heated gas, unperturbed shock trajectories were measured. In the unstable regime between these velocities, multiple maxima and minima were present in the emission oscillograms, similar in appearance to the irregularities in the NF_2 absorption record at the bottom of Figure 2, and shock velocity data were often erratic by more than 1%. At velocities just above the minimum for unstable reactions, the shock fronts propagated stably through the test section, and reaction was found from 100 to 400 mm or more behind the front. Such delayed reaction phenomena, detached from the shock front, were nonstationary, and pressure gauge oscillograms revealed secondary shock waves.

The minimum shock velocity observed to give unstable shock waves defines an ignition temperature, which we denote $T_{2\,\mathrm{msec}}$, associated with the shocked gas conditions under which observable reaction just fails to develop in the maximum observation time set by the experimental arrangement, ~2 msec. The maximum shock velocity giving observably unstable shock waves provides a less direct measure of reaction speed. Although the correspondence with reaction kinetics is not formulated quantitatively, the extensive study of gas detonation front structure[14] has taught that the scale of shock wave instabilities is associated with reaction zone length. The transition of such instabilities in our particular apparatus from a resolvably large size to a condition of apparent (or actual?) disappearance is a uniform measure of reaction speed among experiments involving the same chemicals. To characterize this measure of prompt ignition, associated with completion of exothermic reaction in a few tens of microseconds, we calculate the temperature T_{unstable} from the corresponding shock velocity and the arbitrary condition of no postshock reaction.

Table II includes the values of $T_{2\mathrm{msec}}$ and T_{unstable}, corresponding respectively to the lower and upper limits of the range of unstable shock waves, determined for the several gas mixtures at preshock pressures of 30 Torr. The main results of these measurements are that (i) temperatures of ~1000 K or higher are needed for HF formation in less than $\sim 10^{-3}$ sec in either the NF_3-H_2 system or the N_2F_4 (NF_2)-H_2-C_4H_8 system at partial pressures of a few Torr; (ii) these two systems exhibit quite similar values of both $T_{2\mathrm{msec}}$ and T_{unstable}, the N_2F_4 mixtures being prone to shock-wave instability over a somewhat wider span of temperatures; and (iii) variation of the C_4H_8 content of the N_2F_4-H_2 system exerts a small but consistent effect upon both $T_{2\mathrm{msec}}$ and T_{unstable}, in the sense of C_4H_8 acting to diminish the reaction speed. The implication from the trend of $T_{2\mathrm{msec}}$ with C_4H_8 content is that thermal ignition of N_2F_4 and H_2, although achievable at temperatures below 100°, does not become rapid enough to support HF laser action or gas detonation phenomena until much higher temperatures are reached.

The occurrence of easily observable reaction zone instability in the NF_3-H_2 mixture with 99.3% Ar, and at preshock pressures down to 15 Torr, is a remarkably extreme case in the annals of gas detonation instability phenomena,[15] where high dilution of the exothermically reacting components and low working pressures have generally been found to suppress transverse shock wave development. A proper study of the instability structure and detonation limit behavior of the nitrogen fluoride-hydrogen system was beyond the scope of the present work.

Discussion

NF_2 Formation and Stability. The very recently published experiments in ref 3c are operationally very like those represented in Figure 1, but at several times greater dilution in Ar. Time-of-flight mass spectrometric runs on reflected shock wave decomposition of NF_3 in Ne near 1500 K, as blank experiments ancillary to a study of NF_3 formation from NF_2, have also been reported.[5c] These runs evidently did not lead to quantitative interpretation, and may have revealed stoichiometric complexity not seen in the present work or ref 3c. Nevertheless, the correspondence exhibited in Figure 4 between the NF_2 yields and the equilibrium condition of reaction 1 directly indicates the existence of conditions where this reaction is well enough isolated from other processes for meaningful measurement of its unimolecular kinetics from initial NF_2 appearance rates, especially at high dilution.

Direct comparison is possible between our estimate of the rate of reaction 1 at 1400 K and $[M] = 6 \times 10^{-3}$ M, in 95% Ar, and the Arrhenius expression determined in ref 3c, whose high-temperature end is determined by data at 99% Ar and 3.1×10^{-2} M. The present result is higher by

the factor 1.9. As both measurements are subject to the same, presumably minor influence of irreversible NF_2 decomposition, this discrepancy may arise from such causes as (i) ref 3c's measurements being farther into the pressure region of departure from second-order kinetics than ours, notwithstanding the evidence for first-order dependence on [Ar] presented in ref 3c's Figure 3, (ii) NF_3 being a markedly more effective collision partner for reaction 1 near 1400 K than is Ar, (iii) secondary reactions such as ref 3c's sequence (3), (7) or (4), (−6) contributing more to accelerated NF_2 formation in our more concentrated mixture, or (iv) a real discrepancy of primary shock wave data or their analysis between ourselves and ref 3c. Possibility ii seems unlikely, in that ref 3c detected no systematic difference between results with 1 and 2% NF_3, and such a difference in efficiencies, quite familiar in diatomic dissociation, is contrary to previous experience with tetratomic and larger molecules, *e.g.*, N_2F_4.[4c,d]

The prompt and quantitative occurrence of reaction 4 over the range of conditions of Table I has been established in previous studies,[4] and is consistent with the thermochemical data.[9] The stability of NF_2 to further decomposition on the time scale of the experiments in Figures 2 and 3 is also in accord with previous studies of both bimolecular disproportionation[6]

$$NF_2 + NF_2 \longrightarrow NF_3 + NF \qquad (8)$$

and unimolecular dissociation,[5] reaction 6 followed by subsequent steps. Kinetic parameters of some direct reactions of NF_2 with hydrocarbons are also known from measurements in the 350–550 K range, both for addition of NF_2 to certain olefins[16a]

$$NF_2 + \gt C{=}C\lt \longrightarrow -\overset{|}{\underset{\cdot}{C}}-\overset{|}{\underset{|}{C}}-NF_2 \qquad (9)$$

including *cis*-2-butene, and for abstraction[16b] of H atoms from certain alkanes

$$NF_2 + RH \longrightarrow HNF_2 + R\cdot \qquad (10)$$

Reaction 10 with H_2 has not been observed directly, but a correlation[16b] based on the alkane results would give an activation energy some 6 kcal/mol greater than the endothermicity, or 36 kcal/mol. The coexistence of NF_2 with C_4H_8 and H_2 found here for up to 2 msec near 900 K is consistent with the reported[16] and inferred Arrhenius parameters for reactions 9 and 10.

The effective extinction coefficient of NF_2 for $254 \le \lambda \le 266$ nm at low absorbance is indicated by the slope of data in Figure 3 near the origin. This slope and the departure from Beer's law at high absorbance are seen to be intermediate between the reported monochromatic absorption coefficient at λ 260.2 nm[4a,c,7] and the experience of Modica and Hornig[4b] in the 350–750 K range, recently corroborated[4d] at 293 K, using an interference filter with ~25 nm bandwidth. Most of the data in Figure 3 were measured between 750 and 1000 K, and the spans of data from the enlarged temperature ranges of the 5 and 1% N_2F_4 mixtures are indicated. Within these spans, we do not detect a systematic shift of the calibration curve with temperature as reported by Modica and Hornig,[5b] although we recognize the possibility of a small systematic error in applying the mean results of Figure 3 over the 1100–1500 K range of Figure 4.

Circumstances and Mechanism of HF Production. The qualitative conclusion from the present results is that under conditions where NF_2 reacts rapidly enough with H_2 to support chemical laser or gas detonation phenomena, NF_3 does also. In fact, we observe that the temperatures of rapid HF formation from H_2 and either NF_3 or NF_2 coincide with those at which these nitrogen fluorides independently undergo rapid pyrolysis, liberating F atoms and ultimately N_2.

The decomposition kinetics of NF_3 and NF_2 are complex and incompletely determined, but it is clear enough that the processes have a multistep, free-radical nature, initiated by reactions 1 and 6, respectively, and have many steps in common. The interaction between these dissociatively decomposing nitrogen fluorides and H_2 is likewise a sequence of free radical steps linked to the pyrolysis mechanism by the well-established, rapid elementary reaction

$$F + H_2 \longrightarrow HF + H \qquad (11)$$

Reaction 11 is recognized as the major contributor to HF vibrational laser pumping under circumstances where electric discharge or flash photochemical events have led to F atom liberation.[2] Further reaction which consumes the H atoms arising from (11) and transforms them to additional HF is logically necessary in the high-temperature thermal mechanism to account for the observed prompt generation of the full HF yield and for the failure of NF_2 to accumulate from NF_3.

The behavior of F and H atoms as reactive intermediates is suggestive of the possible importance of reaction chains in the rapid achievement of the stoichiometric reactions 2 and 3, with reaction 1 serving as initiating step in the NF_3 case and reactions 4 followed by (6) and perhaps (8) or (10) in the N_2F_4 case. Indeed, the known[3b] phenomenological behavior of N_2F_4–H_2 explosions near room temperature is that of a free-radical chain process, and Kuhn and Wellman[3b] have pointed out the viability of reaction 10 as a low-temperature initiation step not accessible in mixtures of H_2 with NF_3, HNF_2, or N_2F_2.

In considering reaction chains in these systems, we call primary attention to the heart of chain mechanisms, namely, propagation by a closed sequence of elementary reactions of the intermediates which combine to produce the stoichiometric transformation of reactants to unreactive products while simultaneously regenerating no fewer of the intermediates than are consumed in the propagation. Here, we observe that an essential aspect of reaction 2 is that it entails a significant net increase in number of molecules, which means that it cannot be accomplished solely by atom transfer steps, but must include a definite measure of dissociation events in which a greater number of thermochemically significant linkages between atoms are destroyed than are formed. Specifically, reaction 2 requires one dissociation event per NF_3 molecule reduced.

By comparison, reaction 3 entails net breakage of two bonds per N_2F_4 molecule reduced. The energetically inexpensive dissociation of N_2F_4 by reaction 4 provides half of this requisite dissociation, and by our observation at high temperature precedes the burning with H_2. Thus, the stoichiometry to be achieved by a chain sequence becomes

$$\tfrac{1}{2}H_2 + \tfrac{1}{2}NF_2 \longrightarrow HF + \tfrac{1}{4}N_2 \qquad (3a)$$

which still entails the net participation of one dissociation event per two NF_2 fragments reduced. We observe, incidentally, that the mole number increases in reactions 2 and 3, by factors of 7/5 and 5/3, respectively, make the explosion pressures generable in these systems larger than

in familiar fuel-oxygen systems of comparable specific exothermicity, but where the final-to-initial mole number ratio is smaller.

The simplest chain mechanisms formulable for the NF_3–H_2 or N_2F_4–H_2 systems at high temperature suffice to illustrate the role of dissociation steps. Consider the mechanisms comprising reactions 1, 11 or 4, 6, 11, plus the generic steps

$$H + NF_{x+1} \longrightarrow HF + NF_x \qquad (12\text{-}x)$$

$$H + NF_{y+2} \longrightarrow HF + NF_y + F \qquad (13\text{-}y)$$

to consume H atoms and

$$NF_x + NF_z \longrightarrow N_2 + (x + z)F \qquad (14\text{-}x,z)$$

to form N_2. The indices x, y, and z may have those several integer values appropriate for the species NF_3, NF_2, NF, N, N_2, HF, H, and F. We observe the absence of dissociation in reactions 11 and 12, so that the capacity to supply the dissociation component of chain propagation rests in reactions 13 and 14. Simple chains of reactions 11, 12, and 14 producing N_2 and HF are possible in the NF_3–H_2 system provided reaction 14 occurs with an average value, $\langle x + z \rangle$, of no less than 3. Alternatively, a fraction, α, of the H atom traffic occurring by reaction 13 would reduce the necessary $\langle x + z \rangle_{min}$ to $(3 - 2\alpha)$. For chain accomplishment of reaction 3a, the corresponding minimum, $\langle x + z \rangle_{min}$, is $(2\text{–}2\alpha)$. Values of $\langle x + z \rangle$ greater than these minima can produce chain branching by returning more F atoms than are invested in reaction 11. Lesser values result in net consumption of chain centers, so that reaction 1 or 6 supplies an essential portion of the overall dissociation, and the subsequent reactions of the intermediates constitute a self-limited sequence of secondary steps.

The actual mechanisms occurring in our shock-wave ignition experiments are doubtless more complex than represented above. In particular, pyrolysis kinetics experiments on NF_2 have shown formation of NF_3 which is permanent near 800 K[6] and transitory at 1400–2000 K,[5a] and N_2F_2 is also formed[2e,17] in the photochemical decomposition of N_2F_4 at room temperature, and believed[5] to be an intermediate in the pyrolytic decomposition of NF_2 at 1400–2000 K as well as in HF-forming reactions studied at lower temperatures.[3b,6,18] Suffice it to observe that reactions of the family

$$NF_{(t+1)} + NF_{(u+1)} \longrightarrow N_2F_2 + (t + u)F \qquad (15\text{-}t,u)$$

forming N_2F_2 which subsequently dissociates unimolecularly are equivalent to reaction 14, while N_2F_2 removal by

$$H + N_2F_2 \longrightarrow HF + N_2 + F \qquad (16)$$

alters the net dissociation derived from the liberation of N_2. Simple F atom transfer reactions between nitrogen centers, such as reaction 8, entail no dissociation, and likewise attachment of H to N by transfer processes makes no contribution, and it is not profitable to pursue the whole spectrum of reactions involving exchange of H for F in the several nitrogen–fluorine species, as these are surely minor side reactions beside (2) and (3).

The present observations do not firmly preclude the propagation of indefinitely long chains in NF_3–H_2 ignition. Neither do they provide positive evidence for chain propagation, the circumstances being such that reaction 1 proceeds significantly, and there is not time for independent termination mechanisms to be recognized.

There are several observations of the NF_3–H_2 reaction under other circumstances which show the absence of significant chain propagation. First, electric discharge laser experiments[2c,d,g] not only show no identifiable pumping contribution from reactions subsequent to (11), but at low pressures and a particular discharge intensity,[2g] there was not even a propagating chemical ignition subsequent to the laser event. In contrast, thermally ignited laser pulses[2a] did show stimulated HF emission from the fourth vibrational level, indicating a contribution from one or more of reactions 12, but not distinguishing which.

More explicit information is provided by a recent low-temperature investigation[18] of partially dissociated hydrogen flow-mixed with NF_3, which showed that neither reaction 12 nor 13 occurred on a short time scale at room temperature. Between 476 and 599 K, a reaction occurred which produced HF and N_2 while simultaneously consuming both the H atoms and H_2. There was no evidence of a propagating chain, and the rate of H atom removal was evidently that of reaction 12-3, whose rate coefficient was determined to be $6 \times 10^{14} \exp(-13.2 \text{ kcal}/RT)$ cm^3 mol^{-1} sec^{-1}. Evaluation of this expression at 1000–1500 K shows that reaction 12-3 is capable of removing H atoms rapidly in our experiments, but by the reasoning of the preceding paragraphs, this atom transfer step is not sufficient to sustain a chain.

The contribution of chain propagation to the NF_2–H_2 ignitions generated above 1000 K is also unclear, owing somewhat to the complicating role of the C_4H_8. As with the electric discharge NF_3–H_2 experiments, there are no reported contributions to pumping of N_2F_4–H_2 lasers[2b,d] by processes subsequent to reaction 11. In undiluted N_2F_4–H_2–C_4H_8 mixtures initiated by pulsed 10.6-μm[2i] laser radiolysis, the observations indicated a slow, photolytically initiated chain reaction occurring near 1100 K during an induction period, finally leading to thermally augmented explosion. This description is supported by the present findings.

Chain processes surely occur in the ignition of N_2F_4–H_2 systems at lower temperatures, but the need for inclusion of dissociation events beyond reaction 4 may be removed under such conditions by coproduction of NF_3 or perhaps other amines so that (3a) might be replaced by[3b]

$$\tfrac{1}{2}H_2 + 2NF_2 \longrightarrow HF + NF_3 + \tfrac{1}{2}N_2 \qquad (3b)$$

which conserves the number of moles. The documented viability of reactions 14-0,2[19] and 14-1,1,[5a] which provide sufficient dissociation for reaction 3a, makes direct chain propagation a firm possibility. Still it is clear from our results that the chain processes responsible for explosion of N_2F_4–H_2 mixtures near room temperature are not accelerated markedly by raising the temperature to ~1000 K, so that still higher temperatures, where massive pyrolytic initiation occurs, are needed for submillisecond burning at least of mixtures containing more than trace quantities of inhibitor. Failure of chain processes to dominate NF_2–H_2 burning above ~1000 K is a strong indication that the mechanism of NF_3–H_2 burning contains at least as great a measure of essential pyrolytic dissociation.

NH Chemiluminescence. Chemiluminescent emission of the NH $A^3\Pi \rightarrow X^3\Sigma^-$ spectrum near 336 nm has been observed previously in the NF_3–H_2 flame,[3a] and it is also a known spectral feature of other flames[20] which contain compounds of nitrogen, including particularly the NH_3 flame with F_2 as the oxidizer.[20b] The yield of ultraviolet photons measured here in the shock-wave reaction is an order of magnitude larger than that deduced[21] for the already remarkably strong vacuum uv chemiluminescence

in the CO fourth positive system from the C_2H_2-O_2 reaction, also occuring in low-density shock waves.

The thermochemistry of attachment of H atoms in H_2, HF, and to N in the presence or absence of additional H or F is such that there are no thermoneutral or exothermic bimolecular atom transfer reaction paths of ground-state reactants for generating NH in its $A^3\Pi$ state. Electronic energy transfer from a nonradiating excited electronic state of another molecule, such as the $A^3\Sigma_u^+$ state of N_2, is logically possible, but it is difficult to believe that the supply of this molecule and of ground-state NH is large enough to support the observed strong chemiluminescence. We are thus left to believe that $NH(A^3\Pi)$ arises in the NF_3-H_2 and NF_2-H_2 reaction course primarily by association of bare N and H atoms. That H atoms are formed in reaction 11 and are intermediates in the total HF formation mechanism is entirely credible, and the strong NH chemiluminescence thus provides evidence for the presence of N and hence, the significant occurrence of such reaction paths as reaction 12 with $x = 0$ and/or reaction 13 with $y = 0$, producing N and reaction 14 with $x = 0$, $z = 1$ or 2, consuming it.

The relation between these results and conclusions and the recently reported[22] observations and interpretations of visible NF ($b^1\Sigma^+ \rightarrow X^3\Sigma^-$) and N_2 first positive chemiluminescence in flowing NF_2 plus H atom mixtures at room temperature remains to be understood. These emissions were not identified in the present experiments.

Acknowledgments. The authors wish to acknowledge the technical assistance of Jerome Damitz and James Young in performing the experiments. We also wish to thank Dr. E. D. Loughran for mass spectrographic analyses of the gas mixtures used in this study.

References and Notes

(1) (a) Work performed under the auspices of the U. S. Atomic Energy Commission. (b) Material reported here was presented at the 27th Southwest Regional Meeting of the American Chemical Society, San Antonio, Tex., Dec 1–3, 1971, Paper No. 349.

(2) (a) R. J. Jensen and W. W. Rice, *Chem. Phys. Lett.*, **8**, 214 (1971); (b) D. W. Gregg, *et al.*, *ibid.*, 8, 609 (1971); (c) M. C. Lin, *J. Phys. Chem.*, **75**, 284 (1971); (d) W. H. Green and M. C. Lin, *IEEE J. Quantum Electron.*, **QE-7**, 98 (1971); (e) L. E. Brus and M. C. Lin, *J. Phys. Chem.*, **75**, 2546 (1971); (f) T. D. Padrick and G. C. Pimentel, *J. Chem. Phys.*, 54, 720 (1971); (g) R. K. Pearson, J. O. Cowles, G. L. Hermann, K. J. Pettipiece, and D. W. Gregg, *IEEE J. Quantum Electron.*, **QE-9**, 723 (1973); (h) R. K. Pearson, J. O. Cowles, G. L. Hermann, D. W. Gregg, and J. R. Creighton, *ibid.*, **QE-9**, 879 (1973); (i) J. L. Lyman and R. J. Jensen, *J. Phys. Chem.*, **77**, 883 (1973).

(3) (a) P. L. Goodfriend and H. P. Woods, *Combust. Flame*, **9**, 421 (1965); (b) L. P. Kuhn and C. Wellman, *Inorg. Chem.*, **9**, 602 (1970); (c) K. O. MacFadden and E. Tschuikow-Roux, *J. Phys. Chem.*, **77**, 1475 (1973).

(4) (a) L. M. Brown and B. deB. Darwent, *J. Chem. Phys.*, **42**, 2158 (1965); (b) A. P. Modica and D. F. Hornig, *ibid.*, **49**, 629 (1968); (c) E. Tschuikow-Roux, K. O. MacFadden, K. H. Jung, and D. A. Armstrong, *J. Phys. Chem.*, **77**, 734 (1973); (d) M. A. A. Clyne and J. Connor, *J. Chem. Soc., Faraday Trans. 2*, **68**, 1220 (1972).

(5) (a) R. W. Diesen, *J. Chem. Phys.*, **41**, 3256 (1964); **45**, 759 (1966); (b) A. P. Modica and D. F. Hornig, *ibid.*, **43**, 2739 (1965); **45**, 760 (1966); (c) R. W. Diesen, *J. Phys. Chem.*, **72**, 108 (1968).

(6) J. B. Levy and W. N. Corbin, *U.S. Govt. Res. Develop. Rep.*, 70(16), **76** (1970); CFSTI AD-707784; *Chem. Abstr.*, **74**, 27661f (1971).

(7) F. A. Johnson and C. B. Colburn, *J. Amer. Chem. Soc.*, **83**, 3034 (1961).

(8) P. F. Bird, G. L. Schott, and R. E. Duff, Los Alamos Scientific Laboratory Report No. LA-2980 (1964).

(9) D. R. Stull and H. Prophet, *Nat. Stand. Ref. Data. Ser., Nat. Bur. Stand.*, **No. 37** (1971).

(10) G. L. Schott and R. W. Getzinger in "Physical Chemistry of Fast Reactions," B. P. Levitt, Ed., Plenum Press, New York, N. Y., 1973, Chapter 2.

(11) R. K. Steunenberg and R. C. Vogel, *J. Amer. Chem. Soc.*, **78**, 901 (1956).

(12) W. H. Smith, *J. Chem. Phys.*, **51**, 520 (1969).

(13) J. N. Bradley, R. N. Butlin, and D. Lewis, *Trans. Faraday Soc.*, **63**, 2962 (1967).

(14) (a) K. I. Shchelkin and Ya. K. Troshin, "Gasdynamics of Combustion," Izd-vo AN SSSR, Moscow, 1963; English Translation, Mono Book Corp., Baltimore, Md., 1965; (b) R. A. Strehlow and C. D. Engel, *AIAA J.*, **7**, 492 (1969); R. A. Strehlow, R. E. Maurer, and S. Rajan, *ibid.*, **7**, 323 (1969).

(15) (a) R. I. Soloukhin and C. Brochet, *Combust. Flame*, **18**, 59 (1972); R. I. Soloukhin, *Fiz. Goreniya Vzryva*, **2**(3), 12 (1966); (English translation) *Combust. Explos. Shock Waves (USSR)*, **2**(3), 6 (1966); (b) G. L. Schott, *Amer. Chem. Soc., Div. Fuel Chem., Prepr.*, **11**, (4), 29 (1967).

(16) (a) A. J. Dijkstra, J. A. Kerr, and A. F. Trotman-Dickenson, *J. Chem. Soc. A*, 582 (1966); (b) J. Grzechowiak, J. A. Kerr, and A. F. Trotman-Dickenson, *Chem. Commun.*, **6**, 109 (1965).

(17) C. L. Bumgardner and M. Lustig, *Inorg. Chem.*, **2**, 662 (1963).

(18) S. W. Rabideau, *J. Magn. Resonance*, **11**, 163 (1973).

(19) K. H. Homann, W. C. Solomon, J. Warnatz, H. Gg. Wagner, and C. Zetsch, *Ber. Bunsenges. Phys. Chem.*, **74**, 585 (1970).

(20) (a) A. G. Gaydon and H. G. Wolfhard, "Flames—Their Structure, Radiation and Temperature," 3rd ed, Chapman and Hall, Ltd., London, 1970, Chapter XIV; (b) R. A. Durie, *Proc Roy. Soc., Ser. A*, **211**, 110 (1952).

(21) G. B. Kistiakowsky and L. W. Richards, *J. Chem. Phys.*, **36**, 1707 (1962).

(22) (a) M. A. A. Clyne and I. F. White, *Chem. Phys. Lett.*, 6, 465 (1970); (b) J. M. Herbelin and N. Cohen, *ibid.*, **20**, 685 (1973).

Intersystem Crossing Paths in Excited Charge-Transfer Systems

N. Orbach, J. Novros, and M. Ottolenghi*

Department of Physical Chemistry, The Hebrew University, Jerusalem, Israel *(Received May 8, 1973)*

Publication costs assisted by the U.S. National Bureau of Standards

Pulsed laser photolysis experiments are carried out in aromatic exciplex systems, investigating the generation of triplet states under varying conditions of dissolved oxygen and solvent polarity. Four different intersystem-crossing (ISC) paths, leading to the triplet states of the donor (D) or the acceptor (A), are identified: (I) intersystem crossing within the thermalized exciplex, $^1(A^-D^+)^*$, formed in nonpolar solvents. This is a "slow" ISC mechanism, competing with fluorescence emission from $^1(A^-D^+)^*$. (II) Triplet states are generated in polar solvents *via* the homogeneous recombination of solvated radical ions: $A_s^- + D_s^+ \rightarrow {}^3A^* + D$ (or $^3D^* + A$). (III) Intersystem crossing may occur in both polar and nonpolar solutions from nonrelaxed donor–acceptor pairs. This "fast" process circumvents the thermalized exciplex in hydrocarbon solvents and the separated ions in methanol or acetonitrile. (IV) Triplet states may also be formed as a result of quenching of the exciplex fluorescence by molecular oxygen: $^1(A^-D^+)^* + O_2 \rightarrow {}^3A^* + D + O_2$ (or $^3D^* + A + O_2$).

Introduction

The technique of pulsed laser photolysis has been recently applied to the study of charge-transfer complexes in the excited state, leading to new information concerning exciplexes and excited electron donor–acceptor (EDA) complexes.[1] A particular aspect of significant photochemical relevancy is the mechanism by which triplets are generated in excited, intermolecular, charge-transfer states.

In previous publications[2,3] we have suggested that in the cases of the exciplexes formed between *N,N*-diethylaniline (DEA) and pyrene or anthracene, intersystem crossing occurs from nonrelaxed excited complex states. Namely, crossing to the triplet manifold precedes the population of the thermalized fluorescent exciplex, $^1(A^-D^+)^*$, in nonpolar solvents as well as the formation of separated radical ions in polar solutions. This suggestion was based on the observation that the absorbance, at the characteristic maxima of the anthracene and pyrene triplets, appears immediately after a ~10-nsec laser pulse, prior to any substantial decay of the fluorescent exciplex.[2] This prefluorescence ISC mechanism, later found to be consistent with temperature effects on triplet and fluorescence yields,[3] was also postulated by Mataga and coworkers in the case of the tetracyanobenzene–toluene EDA complex, excited within its charge-transfer absorption band.[4]

Recently, the above mechanism was questioned by Land, Richards, and Thomas,[5] who observed in the case of the exciplex formed between anthracene and *N,N*-dimethylaniline (DMA) a distinct growing-in of the anthracene triplet state, matching the decay of the exciplex fluorescence. It will be shown below that similar growing-in processes are also observed in the case of exciplexes involving TMPD (*N,N,N′,N′*-tetramethyl-*p*-phenylenediamine), indicating that ISC occurs within the thermalized exciplex in competition with the emission of fluorescence. The failure to observe a triplet growing-in in other systems is attributed by Land, *et al.*,[5] to a coincidence of the corresponding triplet and exciplex absorptions, so that transitions such as $^1(A^-D^+)^* \rightarrow {}^3A^* + D$ are not associated with a net change in absorbance.

With the purpose of clarifying the apparent controversy concerning the mode of triplet-state generation, we have submitted nine exciplex systems to a nanosecond laser photolysis study in both polar and nonpolar solvents. Detailed light-induced spectral changes were recorded starting ~15 nsec after triggering the laser, aiming to provide unambiguous evidence showing that the initial spectrum, recorded prior to any significant decay of the exciplex (nonpolar solvents) or the ions (polar solvents), does include a triplet-state contribution. We have also studied the process of the exciplex fluorescence quenching by molecular oxygen investigating its possible association with intersystem crossing. The results bear on the general picture of triplet state generation during charge-transfer interactions in the excited state.

Experimental Section

The nanosecond nitrogen laser (337.1 nm) photolysis technique[6] as well as the steady-state fluorimeter[3] have been described previously.

N,N-Dimethylaniline (DMA) and *N,N*-diethylaniline (DEA) obtained from BDH were redistilled under nitrogen. Spectroscopic grade acetonitrile (AcN), methanol (both Fluka), and toluene (Matheson), as well as methylcyclohexane (MCH) (Fluka, puriss.), were used without further purification. Pyrene, anthracene (Anth), *N,N,N′,N′*-tetramethyl-*p*-phenylenediamine (TMPD), naphthalene (Naph), and biphenyl (Biph) were all zone refined. Solutions were deaerated by bubbling nitrogen or by a freeze and thaw technique. All experiments were carried out at room temperature.

Results

I. Deaerated Nonpolar Solutions. Pulsed laser experiments were carried out in deaerated nonpolar solvents such as methylcyclohexane or toluene, where the quenching of an excited donor, $^1A^*$ (or acceptor, $^1D^*$), by a ground-state D (or, correspondingly, A) molecule is associated with the formation of a fluorescent exciplex. In all the presently investigated systems this quenching process was also found to be associated with intersystem crossing,

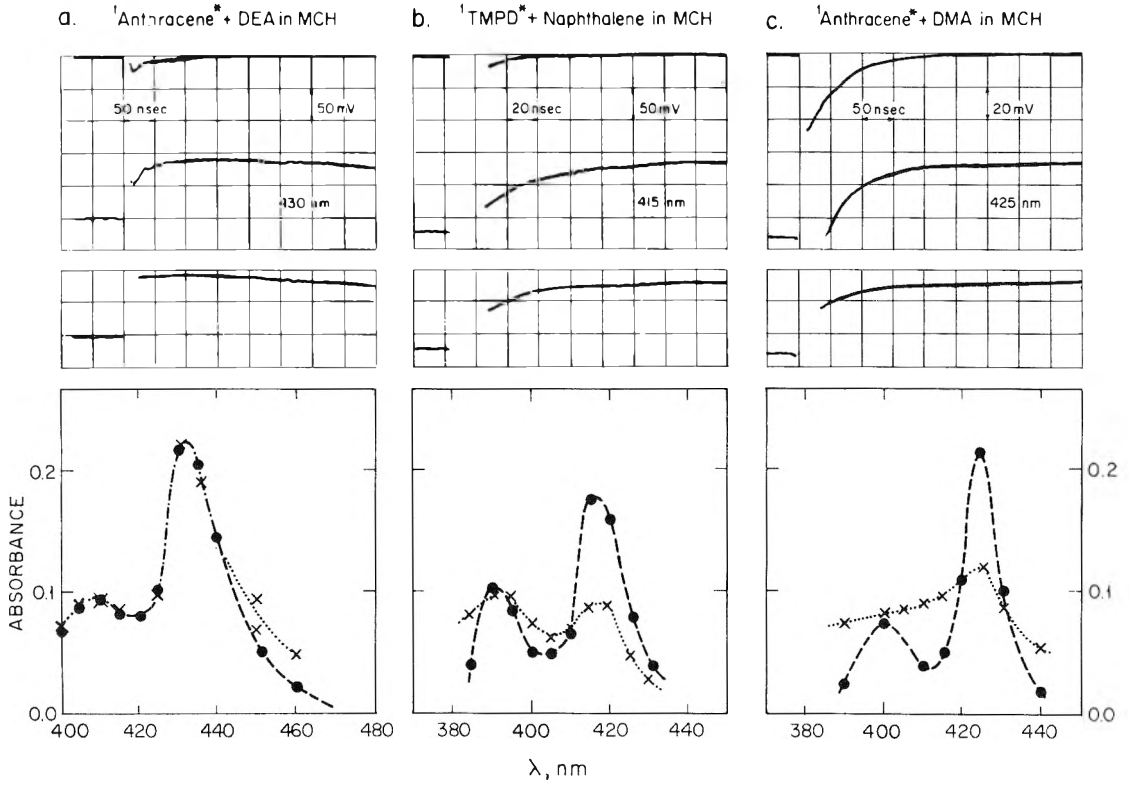

Figure 1. Characteristic oscillograms and transient spectra in exciplex systems prepared in deaerated nonpolar solvents by pulsed laser excitation. In each case three oscilloscope traces are reported. The upper one represents the separate contribution of fluorescence (monitoring light shutter closed) to the lower trace (absorbance + fluorescence) recorded in the presence of the monitoring pulse. The lowest trace is the separate contribution of the absorption obtained by substracting the fluorescence. a, [Anth] = 10^{-2} *M*, [DEA] = 0.5 *M*. . . . × . . . , (ΔD_0) values recorded at the end of the laser pulse (15 nsec after triggering); --●--, (ΔD_∞) values recorded 200 nsec after triggering. (Since the triplet decay is substantial even during the first 200 nsec, we have normalized the maximum of the ΔD_{∞} curve to fit that of ΔD_0, thus rendering easier the comparison of the two spectra); b, [TMPD] = 2 × 10^{-3} *M*, [Naph] = 0.1 *M*; . . . × . . . , (ΔD_0) 15 nsec; --●--, (ΔD_∞) 350 nsec; c, [Anth] = 8 × 10^{-4} *M*, [DMA] = 0.75 *M*; . . . × . . . , (ΔD_0) 15 nsec (by graphical extrapolation); --●--, (ΔD_∞) 350 nsec.

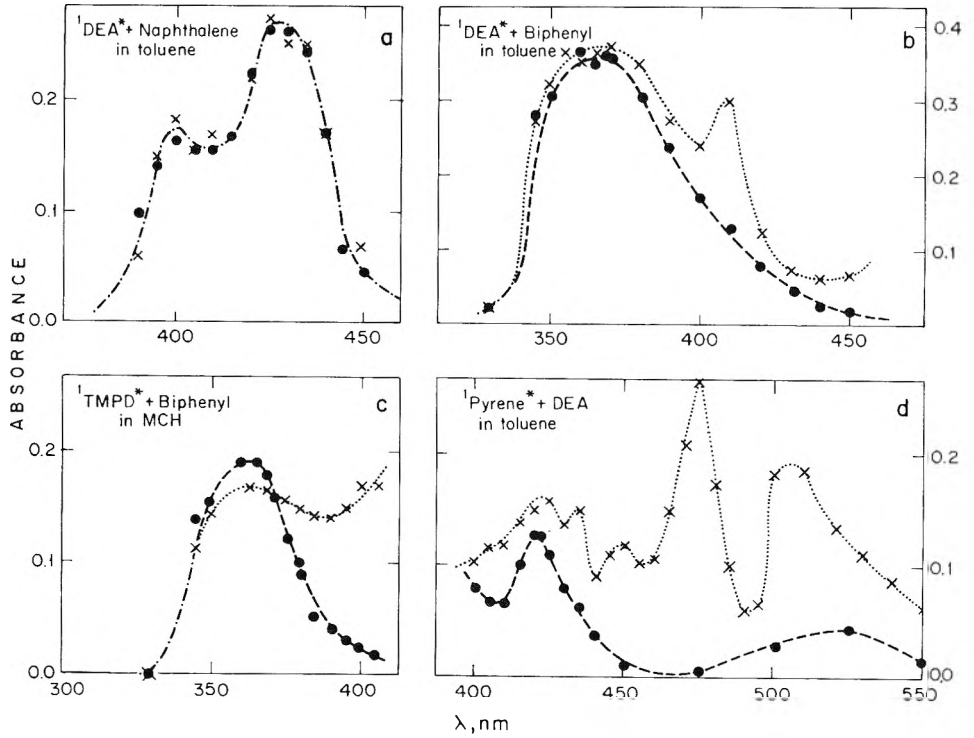

Figure 2. Transient absorbance changes in the laser photolysis of exciplex systems in deaerated nonpolar solvents: – – ● – –, (ΔD_∞), points recorded 200 nsec after triggering; . . . × . . . , (ΔD_0), points recorded 50 nsec (a,b) or 10 nsec (c, by graphical extrapolation, and d); a, [DEA] = 0.25 *M*. [Naph] = 0.2 *M*; b, [DEA] = 0.25 *M*, [Biph] = 0.2 *M*; c, [TMPD] = 2 × 10^{-3} *M*, [Biph] = 0.1 *M*; d, [Pyrene] = 10^{-3} *M*, [DEA] = 0.5 *M*.

leading to the triplet state of either donor ($^3D^*$) or acceptor ($^3A^*$). This is shown in Figures 1 and 2 where some characteristic oscillograms and flash difference spectra are presented for various donor-acceptor pairs. It can be seen that the transient absorbance recorded a few hundred nanoseconds after the laser pulse (OD_∞), when most of the exciplex has decayed, consists of the characteristic triplet-triplet absorbtion bands of either A or D. When considering OD_0, the "initial" change in absorbance recorded at the end of the laser pulse (~15 nsec after triggering), one should bear in mind that at this time most of the exciplex, whose lifetime is of the order of 80 nsec, is still present. Thus, OD_0 will possibly include the contributions of: (a) the exciplex,[7] (b) the relatively small amount of triplets which might have been populated *via* intersystem crossing from the thermalized exciplex within the first 15 nsec, and (c) triplets populated *via* fast mechanisms circumventing the thermalized exciplex.

For example, we examined the ^{1}TMPD + Naph pair (Figure 1b), where around the 415-nm peak of ^{3}Naph* $OD_0 < OD_\infty$, indicating a growing-in process for the naphthalene triplet. Outside the above spectral range $OD_0 > OD_\infty$, reflecting the decay of the exciplex absorbance.[7] Within the limits of experimental accuracy the triplet growing-in rate matches the decay of the exciplex absorption or fluorescence, in agreement with the competition scheme

$$^1(A^-D^+)^* \longrightarrow A + D + h\nu \quad \text{(fluorescence)} \quad (1)$$

$$^1(A^-D^+)^* \longrightarrow {}^3A^* + D \quad \text{(intersystem crossing)} \quad (2)$$

in which $^1(A^-D^+)^*$ represents the thermalized fluorescent state of the complex. Distinct growing-in stages within the range of the triplet band were also observed (see Figures 1 and 2) for ^{1}Anth* + DMA and TMPD* + Biph. No substantial growing-in was observed for ^{1}Anth* + DEA, ^{1}DEA* + Naph, ^{1}DEA* + Biph, and ^{1}Pyrene* + DEA around the absorption maxima of the corresponding triplets. In the cases of ^{1}perylene* + DMA and ^{1}pyrene* + DMA an exact growing-in analysis was prevented by the intense interfering fluorescence in the range of the triplet absorption.

II. Aeareated Nonpolar Solutions. Laser photolysis experiments were also carried out in aerated solutions under conditions in which O_2 could not efficiently compete with the excited donor-acceptor interaction leading to the exciplex. Thus (see Table I) the concentrations of A or D were set so as to assume that $k(D^* + A)[A] \gg k(D^* + O_2)[O_2]$ or $k(A^* + D)[D] \gg k(A^* + O_2)O_2]$ correspondingly. In all cases we found the exciplex fluorescence to be efficiently quenched by oxygen, the results in Table I being consistent with quenching rate constants of $\sim 10^{10}\ M^{-1}\ \text{sec}^{-1}$.

Although quenched by O_2, the relatively low value of their reaction rate constants ($\sim 10^9\ M^{-1}\ \text{sec}^{-1}$) allowed the detection of triplet states even in aerated solutions (Figure 3). By carrying out appropriate extrapolations, the relative intersystem crossing yields were estimated as presented in Table I. Figure 3 shows two different characteristic oxygen effects. In the ^{1}TMPD* + Naph system, the oxygen quenching process is associated with a drop in the triplet yields. Since $F/F^0 = D_T/D_T^0$ (where F and D_T are correspondingly the fluorescence intensity and the triplet absorbancy in the presence of O_2, while F^0 and D_T^0 are the corresponding values in deaerated systems) and since we have previously shown that for ^{1}TMPD*-Naph ISC occurs primarily *via* process 2, we may conclude that the O_2-quenching reaction competes with (2) leading to deactivation according to

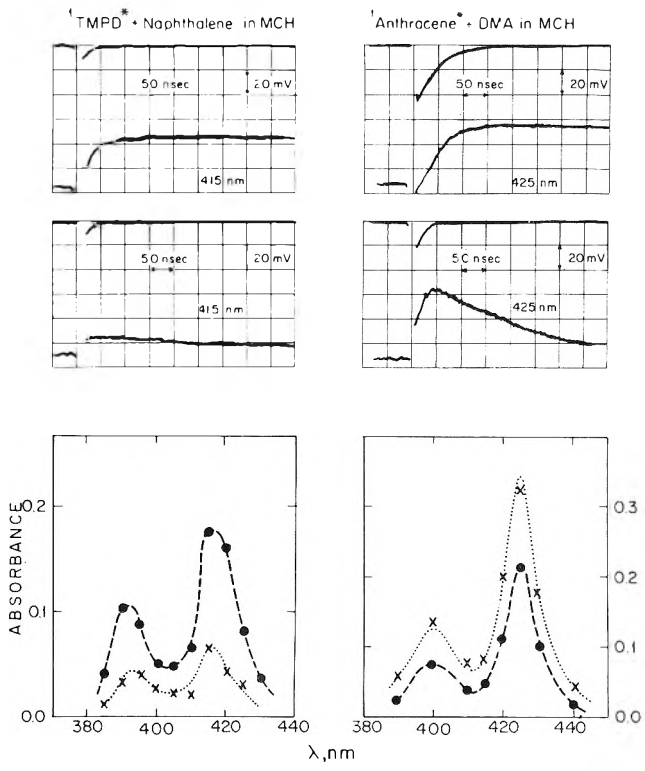

Figure 3. Oscillograms and transient spectra showing oxygen effects on triplet yields in exciplex systems. In both cases the upper oscillograms were recorded in deaeratec solutions and the lower ones in air-saturated systems. Upper and lower traces are correspondingly in the absence and presence of monitoring pulse: --●--, hydrocarbon triplet absorption recorded in deaerated solutions (~300 nsec after triggering); ...×..., hydrocarbon triplet in air saturated solutions (~20 nsec after triggering). Concentrations: [TMPD] = 2×10^{-3} *M*, [Naph] = 0.2 *M*; [Anth] = 8×10^{-4} *M*, [DMA] = 0.75 *M*.

$$^1(D^+A^-)^* + O_2 \longrightarrow D + A + O_2 \quad (3)$$

By contrast, the O_2-quenching effect in the ^{1}Anth* + DMA system leads to an enhancement of the triplet absorbance, establishing the alternative process

$$^1(D^+A^-)^* + O_2 \longrightarrow {}^3A^* + D + O_2 \quad (4)$$

Table I shows that process 3 also occurs in the case of ^{1}TMPD* + Biph while process 4 predominates for ^{1}pyrene* + DMA, ^{1}Anth* + DMA and ^{1}Anth* + DEA.

III. Polar Solutions. Upon carrying out the CT quenching experiments in a polar solvent such as acetonitrile or methanol, no exciplex fluorescence or absorption can be detected. Instead, the quenching process is associated with ionization, leading to the solvated radical ions A_s^- and D_s^+.[8] This is confirmed for the present systems in Figures 4 and 5, showing the transient absorbance changes induced by laser excitation in polar solvents. The same figures show that, with the exception of the ^{1}TMPD* [or ^{1}(DEA)*] + Biph systems, the decay of the characteristic absorbtion bands of A_s^- and D_s^+ is associated with a matching growing-in within the range of the corresponding triplet bands, establishing the process

$$A_s^- + D_s^+ \longrightarrow {}^3A^* + D \text{ (or } {}^3D^* + A) \quad (5)$$

Such reactions have been recently investigated in chemiluminescence studies.[9]

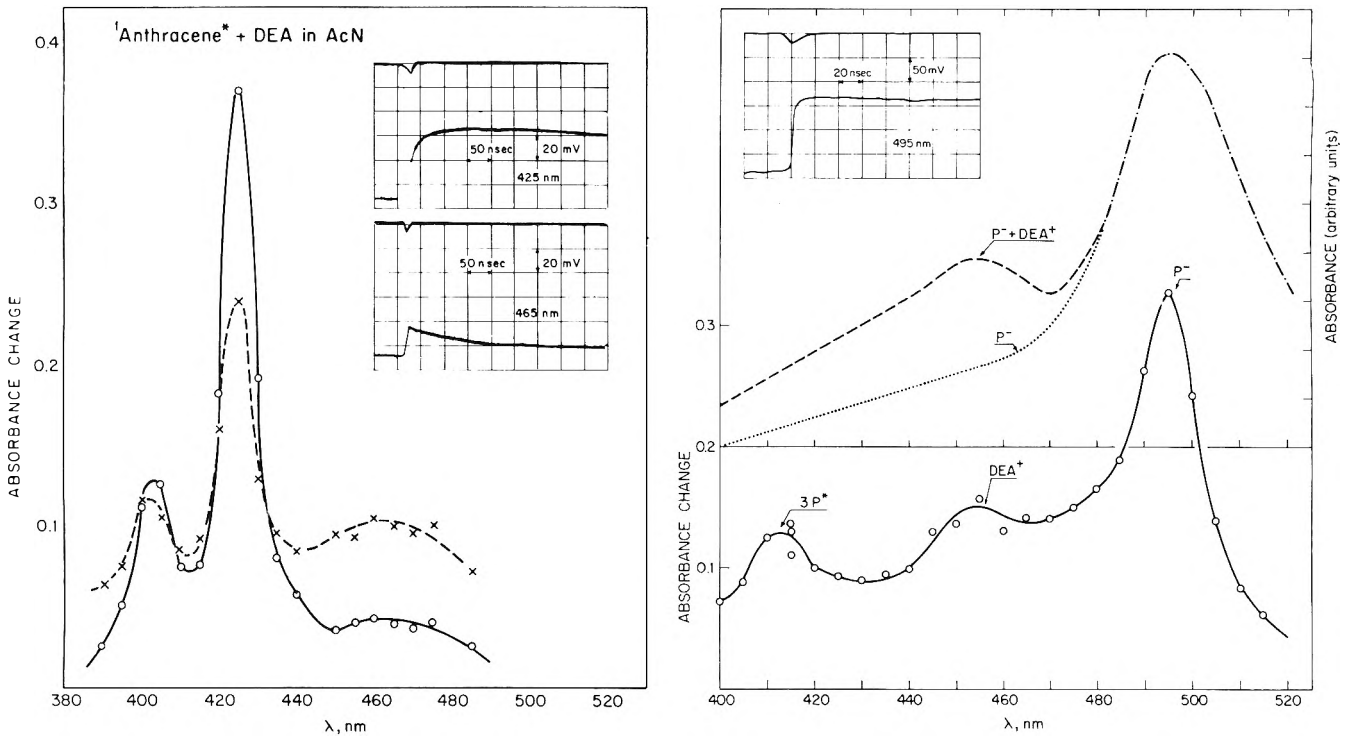

Figure 4. Transient spectra and characteristic oscillograms in the laser photolysis of anthracene and pyrene quenched by DEA in polar solvents. Left: 10^{-3} *M* anthracene and 0.2 *M* DEA in acetonitrile; 15 nsec (– – × – –) and 300 nsec (. . . O . . .) after triggering. The oscillograms represent the anthracene triplet evolution (425 nm) and the decay of the DEA^+ ion (465 nm). A quantitative comparison between the triplet growing-in and the ions decay is complicated by the superimposed triplet decay which causes its growing-in to look faster than the decay of the ions. Right: solid line: the transient change in absorbance recorded 25 nsec after firing the nitrogen laser in a methanol solution of 10^{-4} *M* pyrene quenched by 5×10^{-2} *M* DEA. Dashed line: the superimposed spectra of pyrene$^-$ and DEA^+ reproduced from available data in the literature (details in ref 3). The 415-nm band which is absent in the superimposed spectra of D^+ and A^- is due to the triplet state of pyrene. Insert: oscillogram taken at the maximum of the pyrene negative ion absorption band.

TABLE I: Oxygen and Solvent Effects on Complex Fluorescence and Triplet Yields in Exciplex Systems

		Nonpolar solutions							Polar solutions		
System	Triplet state obsd	Solvent	Quencher concn [Q], *M*	$\frac{k_{M^*+Q}[Q]}{k_{M^*+O_2}[O_2]}$[a]	Relative fluorescence yields, F/F^0 [b]	τ^0, nsec (deaerated)[c]	τ, nsec (aerated)	Relative triplet yields $D_T/D_T{}^0$ [d]	Solvent	OD_0-(t)[e]	D_T[e]
^{1}Anth* + DEA	^{3}Anth*	Toluene	0.5	13	0.05	55	<10	1.5	AcN	0.21	0.18
									MeOH	0.22	0.20
^{1}Pyrene* + DEA	^{3}Pyrene*	Toluene	0.5	20	0.10	57	<10	1.0	AcN	0.14	0.06
									MeOH	0.21	0.11
^{1}Anth* + DMA	^{3}Anth*	MCH	0.75	100	0.20	47	12	2.5	...	...	...
^{1}Pyrene* + DMA	^{3}Pyrene*	MCH	0.5	20	0.20	40	9	1.7	...	...	...
^{1}TMPD* + Naph	^{3}Naph*	MCH	0.2	100	0.20	46	9	0.3	AcN	0.04	0.04
^{1}TMPD* + Biph	^{3}Biph*	MCH	0.2	100	0.16	50	9	0.2	AcN	0.08	0.05
^{1}DEA* + Naph	^{3}Naph*	Toluene	0.2	20	0.25	30	10	0.7	AcN	0.18	0.13
^{1}DEA* + Biph	^{3}Biph*	Toluene	0.2	20	0.25	20	6	0.9	AcN	0.52	0.43

[a] k_{M^*+Q} denotes the quenching rate constant, of M*≡A* or D*, by Q≡D or A (values obtained from H. Knibbe, Ph.D. Thesis, University of Amsterdam, 1969). The oxygen quenching rate constants, $k_{M^*+O_2}$ are taken from L. K. Patterson, G. Porter, and M. R. Topp, *Chem. Phys. Lett.*, **7**, 612 (1970). All solutions were air saturated except for the ^{1}Anth* + DEA system which was saturated with oxygen. [b] F^0 and F are the exciplex fluorescence intensities measured correspondingly by steady-state fluorimetry in deaerated and aerated solutions. [c] τ^0 and τ are the exciplex fluorescence lifetimes measured on the laser apparatus. [d] $D_T{}^0$ is the total triplet absorbance measured after the exciplex decay (~200 nsec after triggering) in deaerated systems. D_T is triplet absorbance in aerated solutions. [e] $OD_0(t)$ is the initial absorbance change at the peak of the triplet absorption. D_T is the net triplet contribution to $OD_0(t)$ estimated by subtracting the contribution of the ions (*e.g.*, see Figure 4, in the case of ^{1}pyrene* + DEA).

As in the previously discussed low-polarity systems the question arises as to the possible presence of a triplet absorbance at the end of the laser pulse, prior to any substantial ion recombination according to reaction 2. A detailed example of the information relevant to this problem is shown in Figure 4 for ^{1}pyrene* + DEA in methanol. As demonstrated by the oscillogram in the insert, recorded at the 495-nm maximum of pyrene$^-$, no substantial ion decay takes place within the first 100 nsec. Yet, the initial transient spectrum, recorded ~20 nsec after triggering, clearly exhibits the characteristic 415-nm band of ^{3}pyrene superimposed on the tails of the 495-nm band of pyrene$^-$ and the 460-nm band of DEA^+. Initial triplet bands which cannot be attributed to reaction 5 were also observed

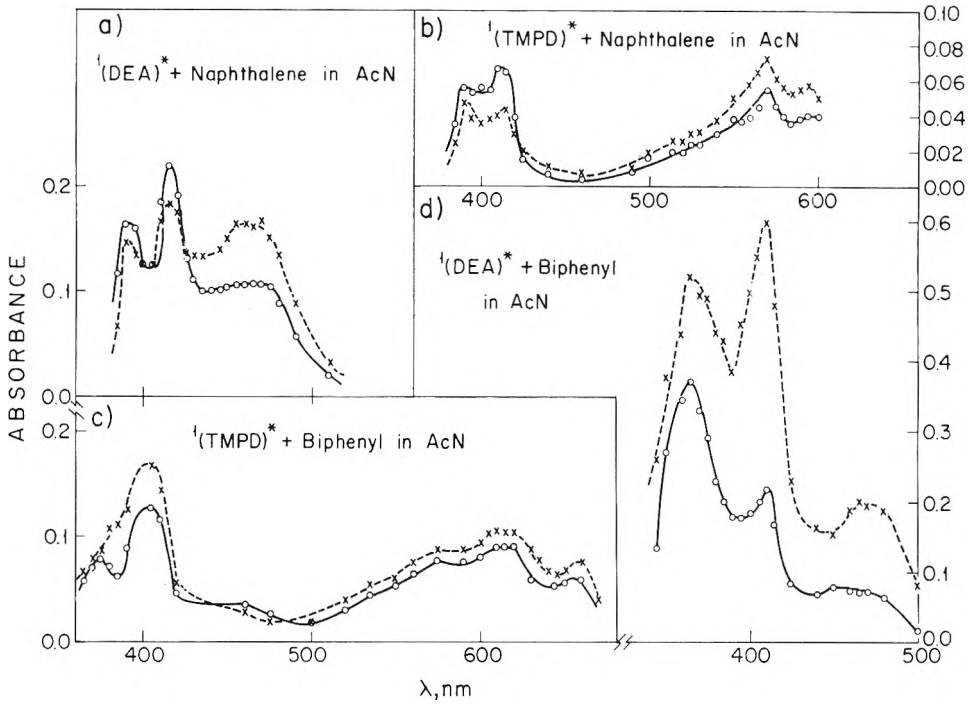

Figure 5. Transient absorbance changes induced in deaerated acetonitrile solutions. Absorbance values are recorded 20 nsec (– – – × – – –) and 100–300 nsec (–O–) after triggering the laser. The time dependence of the spectrum is due to different rates of decay for the triplets and for the ions as well as to contribution from reaction 5. Note that the triplets involved are those of biphenyl (375 nm) and naphthalene (415 nm). The absorption bands between 500 and 650 nm are due to $TMPD^+$. That around 460 nm is due to DEA^+. Concentrations: (a) 0.25 *M* DEA and 0.2 *M* Naph; (b) 2×10^{-3} *M* TMPD and 0.1 *M* Naph; (c) 2×10^{-3} *M* TMPD and 0.1 *M* Biph; (d) 0.25 *M* DEA and 0.2 *M* Biph.

(Figures 4 and 5) in the cases of ^{1}DEA* + Naph (or Biph) and ^{1}anthracene* + DEA. The separate triplet contributions to the initial absorbance change, obtained after correcting for the absorbancy of the ions, are presented in Table I. No data are available for the systems involving DMA since in polar solvents the spectrum of DMA is red-shifted, leading to a substantial extinction coefficient at the 337.1-nm laser line, thus preventing the selective excitation of anthracene, pyrene, or perylene in the presence of DMA as quencher.

Discussion

Considering first the data obtained for OD_0 in deaerated nonpolar solutions, the question arises as to the nature of the absorption bands, characteristic of triplet state, present ~15 nsec after pulsing. As mentioned above such bands may include a contribution from triplets populated *via* ISC within the thermalized exciplex during the first 15 nsec. This can of course be the case only for those systems exhibiting a considerable growing-in effect according to reaction 2. Thus (see, for example, the cases of ^{1}TMPD* + Naph and ^{1}Anth* + DMA, Figure 1b and c), it may be difficult to establish to what extent ΔD_0 contains a contribution to the absorbance, at the characteristic triplet maximum, which is not due to reaction 2. However, in the case of ^{1}TMPD* + Biph (Figure 2c), where the growing-in effect is relatively small, reaction 2 cannot contribute considerably to the intense initial (15 nsec) absorption around 370 nm. Land, *et al.*,[5] have reached a similar conclusion in the case of ^{1}pyrene* + DMA. Thus, with the possible exception of ^{1}TMPD* + Naph and ^{1}anth* + DMA, the initial "triplet bands" contributing to ΔD_0 cannot be rationalized in terms of reaction 2.

Land, *et al.*,[5] attributed these bands to the fluorescent exciplexes, exhibiting absorption transitions identical with those of the corresponding triplet states. In this respect it should be pointed out that a previous analysis of exciplex absorption spectra does not predict such a spectral identity.[7] Moreover, such a coincidence becomes extremely fortuitous in view of the facts that the same observations have been carried out for several different donor–acceptor systems and that in some cases the interpretation of Land, *et al.*, essentially implies a complete identity between the exciplex and triplet absorption bands. Thus in the case of ^{1}Anth* + DEA (Figure 1a) the initial spectral change within the 400–450-nm range of the anthracene triplet absorption is exactly identical with that of ^{3}Anth*; *i.e.*, $OD_0 = OD_\infty$. Especially, the spectrum exhibits the same value (2.2 ± 0.2) for the absorbance ratio between the main peak at 425 nm and the secondary band at 410 nm. We thus infer that, in the above range, the exciplex contribution to the initial absorption is negligible, the absorbance change being exclusively attributable to the anthracene triplet state. A similar situation is also encountered in the case of ^{1}DEA* + Naph (Figure 2a). It is therefore clear, from both examples, that triplet states are present prior to the decay of $^1(D^+A^-)^*$. Though not completely free from an exciplex contribution, all other systems are also characterized by initial absorption spectra exhibiting bands which are exactly identical with those of the corresponding triplets. We therefore conclude that the accumulated experimental evidence in deaerated nonpolar solutions supports two intersystem-crossing mechanisms: (a) the "slow" path within the thermalized exciplex according to reaction 2 and (b) the previously suggested[2,3] "fast" mechanism, involving nonrelaxed excited states of the complexes.[10] As previously discussed, it appears that both mechanisms are not mutually exclusive and that they may operate simultaneously in the same donor–acceptor pair (*e.g.*, ^{1}TMPD* + Biph and ^{1}pyrene* + DMA).

An alternative approach for proving the above arguments involves the use of a selective quencher for the exciplex fluorescence. If the quenching reaction leads directly to the system's ground state, process 2, *i.e.*, mechanism a, can be suppressed, allowing the observation of triplets formed according to (b) without the interfering exciplex absorption bands. Unfortunately, we have not been able to find such a selective quencher. Molecular oxygen does not serve this purpose since, as previously discussed and shown in Table I, the O_2 quenching process may induce intersystem crossing similar to the corresponding reaction of O_2 with excited aromatics.[11] Thus, in systems such as TMPD–Naph and TMPD–Biph, where reaction 3 predominates (F and D_T are reduced by O_2 to the same extent), the oxygen effect confirms the intersystem-crossing mechanism a. However, due to reaction 4, the O_2 quenching effect cannot be used as an independent tool in studying mechanism b. We should finally add that the mechanism of exciplex fluorescence quenching by molecular oxygen is still unclear. Though no experimental evidence from the pulsed laser experiments is available, it is possible that the process proceeds *via* triple exciplexes[12] such as $^1[ADO_2]^*$ undergoing subsequent intersystem crossing.

The "fast" mechanism b is also supported by comparing the initial triplet yields in polar solutions with those observed in nonpolar solvents. We have previously suggested that the efficiency of "fast" intersystem crossing occurring from nonthermalized states, prior to solvent relaxation, should not be markedly affected by the solvent polarity. Unfortunately, a quantitative comparison between the initial triplet yields in polar and nonpolar solvents, confirming this hypothesis, cannot be generally carried out since the exact exciplex contribution to OD_0 in nonpolar systems is unknown. However, one exception is the ^{1}Anth* + DEA pair for which we have previously claimed that $OD_0(t)$ is free from any substantial exciplex contribution. In this case the value $OD_0(t) = 0.22$ (Figure 1a) in toluene is close to the values $D_T = 0.18$ and 0.20 (Table I) obtained correspondingly for the initial triplet yield in acetonitrile and methanol. The values of OD(t) in a nonpolar solvent and those of D_T in polar solutions are of the same order of magnitude also in the cases of ^{1}DEA* + Biph and ^{1}DEA* + Naph (Table I and Figure 2). The small D_T values ~0.05 observed for ^{1}TMPD* + Naph (or Biph) are consistent with the small triplet contributions to $OD_0(t)$ in the corresponding nonpolar systems.

We should finally mention some very recent results, relevant to the above issues, concerning the quenching of biphenyl fluorescence in polar solutions by a series of inorganic salts (A^-).[12] An analysis of the quenching process which involves charge-transfer interactions shows that it is associated with substantial intersystem crossing, leading to the triplet state of biphenyl. However, the reaction is not accompanied by the formation of the $Biph^-$ and A· radicals, ruling out a reverse charge-transfer process leading to triplet population according to $A + Biph^- \rightarrow A^- + {}^3$Biph*. The situation is thus completely analogous to the "fast" intersystem crossing of the present exciplex systems. In both cases a nonrelaxed charge-transfer collision complex has to be postulated,[1-3,13] undergoing a very fast singlet → triplet transition. One should finally recall that, although being now well established experimentally, the details of the very efficient ISC in nonrelaxed states and especially the nature of the corresponding spin-orbital coupling schemes[1] are still unresolved questions open to further experimental and theoretical investigation.

Acknowledgment. This work was carried out under the sponsorship of the U. S. National Bureau of Standards.

References and Notes

(1) M. Ottolenghi, *Accounts Chem. Res.*, **6**, 153 (1973).
(2) C. R. Goldschmidt, R. Potashnik, and M. Ottolenghi, *J. Phys. Chem.*, **75**, 1025 (1971).
(3) N. Orbach, R. Potashnik, and M. Ottolenghi, *J. Phys. Chem.*, **76**, 1133 (1972).
(4) H. Masuhara, N. Tsujino, and N. Mataga, *Chem. Phys. Lett.*, **12**, 481 (1972).
(5) E. J. Land, J. T. Richards, and J. K. Thomas, *J. Phys. Chem.*, **76**, 3805 (1972).
(6) C. R. Goldschmidt, M. Ottolenghi, and G. Stein, *Israel J. Chem.*, **8**, 29 (1970).
(7) R. Potashnik, C. R. Goldschmidt, M. Ottolenghi, and A. Weller, *J. Chem. Phys.*, **55**, 5344 (1971); A. Alchalal, M. Tamir, and M. Ottolenghi, *J. Phys. Chem.*, **76**, 2229 (1972).
(8) H. Leonhardt and A. Weller, *Ber Bunsenges. Phys., Chem.*, **67**, 791 (1963); H. Knibbe, D. Rehm, and A. Weller, *ibid.*, **72**, 257 (1968); M. Koizumi and Y. Yamashita, *Z. Phys. Chem.* **57**, 103 (1968); K. Kawai, N. Yamamoto, and H. Tsubomura, *Bull. Chem. Soc. Jap.*, **42**, 369 (1969).
(9) A. Weller and K. Zachariasse, *J. Chem. Phys.*, **46**, 4984 (1967); K. Zachariasse, Ph.D. Thesis, Free University of Amsterdam, 1972.
(10) We would like to point out that, considering the data of Table I, it can be formally argued that the immediate appearance of triplets in some of the laser flash experiments can be explained on the basis of triplet–triplet energy transfer from the primarily excited molecule to the quencher molecule. Taking, for example, ^{1}DEA* (fluorescence lifetime = 3 nsec, ISC yield = 0.95) which is quenched by 0.2 *M* biphenyl (Figure 5d) with only 85% efficiency, it is plausible that the remaining 15% form ^{3}DEA* which then leads to the rapid appearance of ^{3}Biph* by triplet–triplet energy transfer. Similarly, in the ^{1}Anth* + DEA system, ^{3}Anth* can originate from ^{3}DEA* formed *via* the small light fraction (~10%) absorbed directly by DEA. These alternative explanations, involving triplet–triplet energy transfer rather than the CT quenching postulated in the text, were ruled out by carrying out a set of experiments in, *e.g.*, polar and nonpolar ^{1}DEA* + Biph systems, where the per cent quenching of ^{1}DEA* was varied (in the 73–92% range) by varying the biphenyl concentration. In all cases the amount of triplet observed was exactly proportional to the percent of ^{1}DEA* quenched rather than to the unquenched fraction which directly reflects the amount of ^{3}DEA* formed *via* ISC from ^{1}DEA*. Similarly, in the DEA + ^{1}Anth* system, the light fraction absorbed by DEA was varied (in the 10–2% range) by varying the concentrations of both components. Here too the observed variations in the triplet yields were found to be exactly consistent with mechanism b rather than with triplet energy transfer from unquenched molecules. We should finally point out that the above determinations of relative triplet yields were carried out by measuring the initial (~15 nsec after pulsing) absorbance changes at the corresponding triplet maxima, neglecting (see arguments in the text) the contribution of the exciplex. Obviously, such an analysis cannot be quantitatively performed in systems where the exciplex contributes substantially to the absorption in the range of the triplet band, since it is impossible to separate the relative exciplex and triplet contribution to the initial spectrum.
(11) R. Potashnik, C. R. Goldschmidt, and M. Ottolenghi, *Chem. Phys. Lett.*, **9**, 424 (1971).
(12) H. Beens and A. Weller, *Chem. Phys. Lett.*, **2**, 82 (1968); G. Briegleb, H. Schuster, and W. Herre, *ibid.*, **4**, 53 (1969); Z. Teitelbaum, R. Potashnik, and M. Ottolenghi, *Mol. Photochem.*, **3**, 107 (1971).
(13) A. R. Watkins, *J. Phys. Chem.*, **77**, 1207 (1973).

Photolysis of Surface Methoxides on Several Metal Oxides as Studied by Electron Spin Resonance

Shozo Kubota,* Masamoto Iwaizumi, and Taro Isobe

Chemical Research Institute of Non-Aqueous Solutions, Tohoku University, Katahira-2-chome, Sendai, Japan
(Received April 2, 1973)

Publication costs assisted by Chemical Research Institute of Non-Aqueous Solutions, Tohoku University

Surface methoxides on silica gel, beryllium oxide, aluminum oxide, magnesium oxide, and zinc oxide were irradiated by a low-pressure mercury lamp. The radical species, $SiO\dot{C}H_2$, $\dot{C}H_3$, $H\dot{C}O$, and H from $SiOCH_3$, and $AlO\dot{C}H_2$, $\dot{C}H_3$, and H from $AlOCH_3$, were observed by the photolysis. In photolysis of $BeOCH_3$ and $MgOCH_3$, only $BeO\dot{C}H_2$ and $MgO\dot{C}H_2$ radicals were detected, while no esr signal attributable to the photodecomposition of $ZnOCH_3$ was observed. It has been found that the α proton hyperfine splitting constants of $MO\dot{C}H_2$ radicals change markedly with metal (M) in the metal oxides and they are well correlated with the electronegativities of the metals. These changes are explained by spin delocalization onto the metal oxides. The esr line shapes of the $MO\dot{C}H_2$ radicals also appreciably depend on the metal oxides. From the analysis of the line shapes it is shown that there are two processes for averaging the anisotropic part of g and hyperfine tensors, one process is the rotation of the $-CH_2$ group about the C–O bond, and the other is the fluctuational rotation of the $-OCH_2$ group about the M–O bond.

Recently, there has been considerable interest in the studies of the esr of radicals trapped on solid surfaces.[1] In their studies, esr has proven to be a powerful technique for the observation of microscopic feature of the radicals in the adsorbed state. This paper concerns the esr studies of photolysis of the surface methoxides on several metal oxides, such as silica gel, beryllium oxide, aluminum oxide, and zinc oxide. In a previous paper, Shimizu, *et al.*,[2] have reported that when methanol adsorbed on porous high-silica glasses was irradiated by a uv lamp, $\dot{C}H_3$, $H\dot{C}O$, $\dot{C}H_2OH$, and H were produced. They pointed out that their esr spectra resemble the results of the uv-photolysis of X-irradiated methanol. It was also found in their work that surface hydroxyl groups play an important role in producing these species and no esr signal was obtained in the case of totally fluorinated glass. On the other hand, Ono and Keii[3] investigated the photolysis of alcohols adsorbed on aluminum oxide by esr. They observed $AlO\dot{C}H_2$ radical as a decomposition product of the surface complex $AlOCH_3$, and from an analysis of the line shape they showed that the rotation of the radical around the C–O axis becomes free above $-140°$.

In this paper, it is shown that uv irradiation of methanol chemisorbed on the metal oxides gives different radical species with different metal oxides. It is also shown that the hyperfine splitting constants and the line shapes of the esr spectra of $MO\dot{C}H_2$ radicals (M is short for metals in metal oxides) change appreciably with the metal oxides. These changes in hyperfine splitting constants and line shapes are discussed.

Experimental Section

Silica gel obtained from Kanto Chemical Co. was heated in oxygen at 300° to exclude adsorbed organic materials prior to use. Magnesium oxide was prepared by heating magnesium carbonate (Koso Chemical Co.) at 500° in a nitrogen atmosphere. Aluminum oxide and zinc oxide were obtained from M. Wolem Eschwege Co. and from Koso Chemical Co., respectively. Beryllium oxide was prepared from beryllium carbonate (Mitsuwa Chemical Co.) in the same manner as magnesium oxide. Methanol was obtained from E. Merck Co. and after degassing it was stored in a vacuum line. Purification of methyl iodide and sample preparation for uv irradiation of methyl iodide adsorbed on metal oxides were made in the same manner as that described previously.[4]

Surface methoxides were prepared by the adsorption of methanol on metal oxides. Before the adsorption of methanol, the metal oxides were heated *in vacuo* at 500° for 5 hr. After a large amount of methanol was introduced on the metal oxides through a vacuum line, the sample was heated *in vacuo* at 200° for 2 hr. This process for adsorption of methanol was repeated twice. In the cases of beryllium and aluminum oxides, the contact between the metal oxides and methanol was maintained for 1 day, as the adsorbed amount of methanol was small in these cases. After this treatment, only chemisorbed methanol can be retained on the surfaces.

For photolysis a Toshiba 20-W low-pressure mercury lamp, with wavelengths shorter than 200 nm cut off, was used as a light source. The measurements of esr spectra were carried out with a Hitachi 771 X-band spectrometer.

Results and Discussion

Photolysis of Surface Methoxides on Metal Oxides. The esr spectra obtained from uv irradiation of surface methoxides depend on the adsorbent and irradiation time. Table I shows the radical species produced by photolysis. Interestingly, the products from methoxide on the silica gel surface were the same as those from uv irradiation of methanol adsorbed on a porous high-silica glass.[2] For the case of zinc oxide, no esr signal attributable to decomposition of surface methoxide was obtained after uv irradiation, but signals due to surface center of zinc oxide were observed.[5] Except for zinc oxide, the first esr signal to appear was triplet lines, which were assigned to the $MO\dot{C}H_2$ radical (see Figure 1). In both cases of silica gel and magnesium oxide, the signals attributable to the defect of the oxides were produced together with the signals due to the photolysis products of the methoxides, but these defect

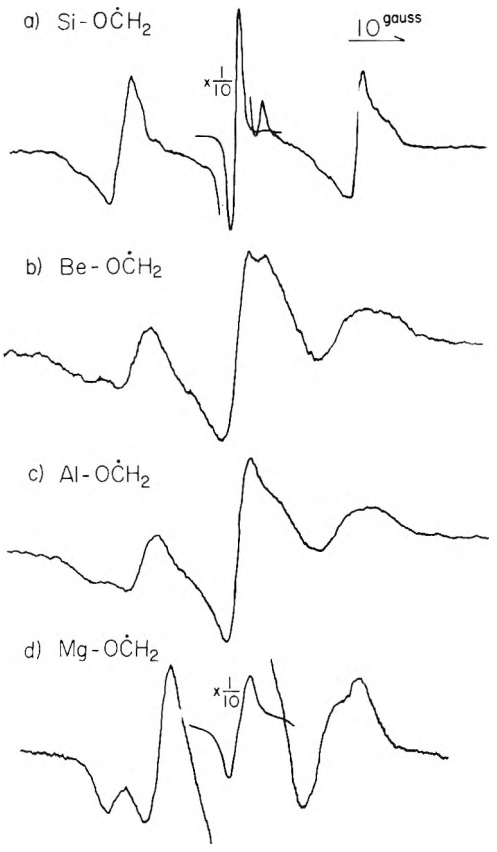

Figure 1. Esr spectra of $MO\dot{C}H_2$ radicals at 77°K.

TABLE I: Free Radicals Detected by Esr in the Photolysis of Surface Methoxides by a Low-Pressure Mercury Lamp at 77°K[a]

Adsorbents	$MO\dot{C}H_2$	$\dot{C}H_3$	$H\dot{C}O$	H
Silica gel	s	m	w	m
Aluminum oxide	s	m		m
Beryllium oxide	s			
Magnesium oxide	s			
Zinc oxide				

[a] S = strong; m = medium; w = weak.

signals could be excluded by annealing the samples at room temperature for 1 day after the photolysis.

The signal intensities of $MO\dot{C}H_2$ change with irradiation time as shown in Figure 2. The intensity of $SiO\dot{C}H_2$ shows a maximum at irradiation time of 2 min, but the signal intensities of the methyl and the formyl radicals increase as the irradiation progresses. On the other hand, in the photolysis of $AlOCH_3$, the $AlO\dot{C}H_2$ and methyl radicals were first produced by decomposition of $AlOCH_3$, and the signal intensities of the radicals increase with irradiation time, but the formation of formyl radical was not observed. These results imply the following process for the decomposition of $SiOCH_3$ and $AlOCH_3$.

$$SiOCH_3 + h\nu \longrightarrow SiO\dot{C}H_2 + H$$
$$\searrow SiO\dot{} + \dot{C}H_3$$
$$SiO\dot{C}H_2 + h\nu \longrightarrow Si\dot{} + H\dot{C}O + H$$
$$AlOCH_3 + h\nu \longrightarrow AlO\dot{C}H_2 + H$$
$$\searrow AlO\dot{} + \dot{C}H_3$$
$$AlO\dot{C}H_2 + h\nu \not\longrightarrow Al\dot{} + H\dot{C}O + H$$

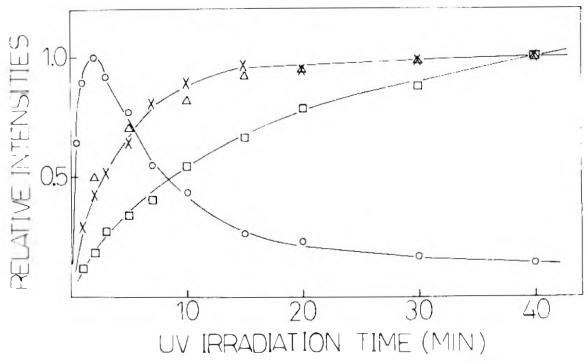

Figure 2. Change of signal intensities of the $MO\dot{C}H_2$ radicals as a function of irradiation time: O, $SiO\dot{C}H_2$; △, $BeO\dot{C}H_2$; ×, $MgO\dot{C}H_2$; □, $AlO\dot{C}H_2$.

The methyl radicals produced from $SiOCH_3$ and $AlOCH_3$ have proton hyperfine splitting constants of 21.1 and 21.4 G, respectively. These methyl radicals show well-resolved hyperfine structure but unusual intensity distribution, *i.e.*, the low-field lines are extensively broader than the high-field lines as in the previously reported cases,[4,6] suggesting that the methyl radicals interact with the surfaces by the $2p_z$ unpaired orbital and they are rotating about the $2p_z$ axis.

On the other hand, in the photolysis of $BeOCH_3$ and $MgOCH_3$, the formation of the methyl radical was not observed and the observed species was only the $MO\dot{C}H_2$ radical. We tried the photolysis of methyl iodide adsorbed on beryllium oxide and found that the methyl radical is formed and well trapped on the beryllium oxide. In view of this observation, it may be considered that in the photolysis of $BeOCH_3$ the cleavage of the C–O bond does not occur with the wavelength of the mercury lamp used. Also for the case of magnesium oxide, the methyl radical formation was not observed in the photolysis of methyl iodide. It is considered likely, however, that the C–O bond rupture would also not occur in the case of $MgOCH_3$, since the formation curve of the $MgO\dot{C}H_2$ radical is similar to that of $BeO\dot{C}H_2$. It is interesting to note that the methyl radical was produced and well trapped in the photolysis of $AlOCH_3$ as mentioned above, whereas it was not observed in the photolysis of methyl iodide adsorbed on aluminum oxide. Thus it may be presumed that only the following cleavage reactions occur in the photolysis of $BeOCH_3$ and $MgOCH_3$.

$$BeOCH_3 + h\nu \longrightarrow BeO\dot{C}H_2 + H$$
$$\not\searrow BeO\dot{} + \dot{C}H_3$$
$$MgOCH_3 + h\nu \longrightarrow MgO\dot{C}H_2 + H$$
$$\not\searrow MgO\dot{} + \dot{C}H_3$$

The stabilities of the $MO\dot{C}H_2$ radicals depend on the metal oxides. The $SiO\dot{C}H_2$ and $MgO\dot{C}H_2$ radicals remained stable even at room temperature, but the $BeO\dot{C}H_2$ and $AlO\dot{C}H_2$ radicals decay at temperatures above −40°.

Hyperfine Splitting Constant of $MO\dot{C}H_2$ Radicals. In most cases of free radicals trapped on solid surfaces, the anisotropic part of the g and hyperfine tensors are partially averaged by the restricted motion of the radical molecules. In such an intermediate case for averaging the anisotropic part of g and hyperfine tensors, it is difficult to determine accurately the hyperfine splitting constants from the observed esr spectra. In the present work, we took the separation between the absorption maxima of the

$M_I = +1$ and $M_I = -1$ lines as a measure of hyperfine splitting constant of CH_2 protons for convenience. Interestingly, this line separation changes appreciably with the metal oxides, and, as Figure 3 shows, it is closely related to the electronegativity of the bonded metal. Previously Takezawa and Kobayashi[7] reported that the wave number of asymmetric CH stretching vibration of methoxides formed on metal oxide surfaces is strongly influenced by the electronegativity of the metal. Their result has been explained by assuming that the C-H bond length of the methoxide decreases or ionic character of the C-H bond increases with the increase of electronegativity of the bonded metal. On the other hand, in studies of AY_3 type radicals,[8,9] it has been shown that if Y is more electronegative than A the radicals will have a nonplanar structure. Symons, *et al.*,[9d,10] have also shown that in the AO_3 type radicals the spin density on A changes with electronegativity of A, *i.e.*, it decreases as the difference between the electronegativities of A and oxygen ($X_O - X_A$) increases.

As their results suggest, the change in the electronegativity of the bonded metals may affect the proton hyperfine splittings in various ways. That is, (1) change of the electronegativity of the metal may cause a change of the C-H bond length, through which the spin polarization effect and finally the proton hyperfine splittings will be affected. (2) The ionic character of C-H bond may be changed with the electronegativity of the bonded metal. This change in the ionic character will also affect the spin polarization effect and proton hyperfine splitting constant. (3) The structure of the radical site, $MOCH_2$, may change with the electronegativity of the bonded metal; this structural change will affect the proton hyperfine splittings since the direct overlap of the odd electron with hydrogen is a sensitive function of the structure. (4) Spin delocalization from the CH_2 site to the metal oxide will be affected by changing the metal, the influence of which will be transmitted to the CH proton hyperfine splittings. In the following we consider these effects in more detail on the present system.

In Figure 4, the spin density on the α proton is shown as a function of C-H bond length, which was calculated by INDO method,[11] using the methyl radical as a model molecule. The calculated result in Figure 4 shows that the proton hyperfine splitting constant becomes larger for a longer C-H bond. In the MO approximation,[12] the spin density on the α proton of the C-H fragment is expressed as

$$\rho_H = (J_{\pi s} - J_{\pi h})/\sqrt{3}(E_{\Psi_e} - E_{\Psi_0})$$

where

$$\Psi_0 = \|\sigma_b\sigma_b\pi\|\alpha\beta\alpha$$

$$\Psi_e = \|\sigma_b\sigma_a\pi\|\frac{1}{\sqrt{6}}(2\alpha\alpha\beta - \alpha\beta\alpha - \beta\alpha\alpha)$$

$$J_{\pi s} = \int \pi(1)s(2)\frac{1}{r_{12}}s(1)\pi(2)\,d\tau$$

$$J_{\pi h} = \int \pi(1)h(2)\frac{1}{r_{12}}h(1)\pi(2)\,d\tau$$

and where σ_b and σ_a are bonding and antibonding MO's constructed with a carbon sp^2 hybrid orbital (h) and a hydrogen 1s orbital (s). The unpaired electron orbital, the $2p_z$ orbital of the carbon, is represented as π. Although the INDO method neglects multicenter exchange integrals, such as $J_{\pi s}$, calculation by the INDO method will

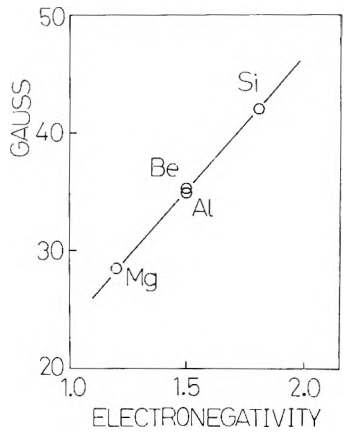

Figure 3. Splitting values between $M_I = -1$ and $M_I = +1$ lines of $MOCH_2$ radicals as a function of the electronegativities (Pauling's scale) of metals in the oxides.

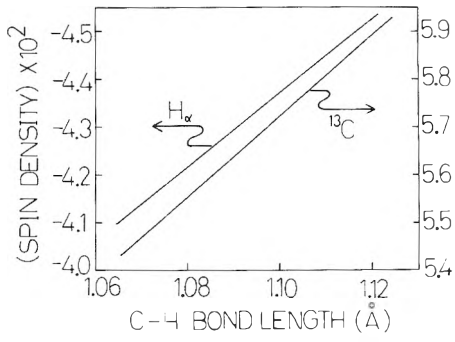

Figure 4. Change in the spin density of the methyl radical as a function of C-H bond length.

apparently still give correct predictions for the effect of change in the C-H bond length, since the value of integral $J_{\pi s}$ decreases with increase of the C-H bond length. From Takezawa and other's observation on the CH vibration of the surface methoxide and the result in Figure 4, the decrease of the C-H bond length and thus decrease of the proton hyperfine splittings are expected for increase of the electronegativity of the bonded metal. This expectation is apparently the reverse of our observation, which presents appreciable increase of the hyperfine splittings with increase of electronegativity of the bonded metal. Therefore, it may be said that the change of the C-H bond length may not be a main cause for observed change of the proton hyperfine splittings. It may also be said that the decrease of the C-H bond length of the surface bound methoxides does not necessarily indicate conclusively that the C-H bond length of the photolysis product also decreases.

Next, we consider the effect of the ionic character of the C-H bond on the spin polarization effect. As mentioned above, Takezawa and others predict that the C-H bond may become more polar, as an alternative for the decrease of the C-H bond length, by the increase of electronegativity of the metal. On the other hand, Higuchi[13] has shown by a theoretical calculation of isotropic hyperfine splittings for a C-H fragment that the proton hyperfine splitting will decrease as the polarity of the C-H bond increases. According to these results, decrease of the proton hyperfine splitting should be expected by the increase of electronegativity of the bonded metal. However, the observed relation is the reverse of this expectation. This means that the change in the spin polarization effect due to polarity of the C-H bond also may not be the main

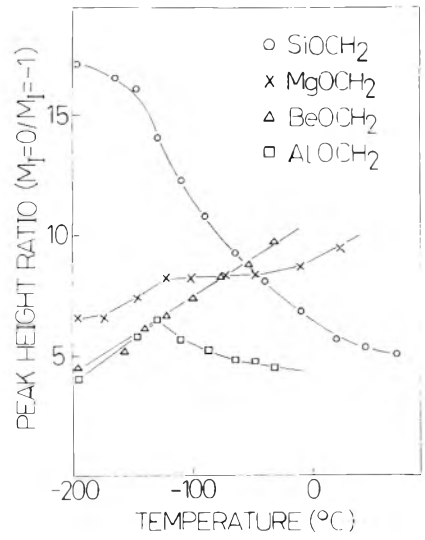

Figure 5. Change of the peak-height ratio between $M_I = 0$ and $M_I = -1$ line, $h(M_I = 0)/h(M_I = -1)$, as a function of temperature.

contribution to the observed change in the hyperfine splitting constants with the electronegativities of the metals.

It is shown also that a structural change of the $MOCH_2$ radical site is not the main cause of the observed change of the proton hyperfine splitting constants. According to the general conclusion for the structure of AY_3 type radicals,[8,9] it is expected that the radical site, $MOCH_2$, will deviate more from the planar structure as the electronegativity of the metal increases. Provided that the proton hyperfine splitting constant of the $MOCH_2$ radical is negative,[14] the deviation from planar structure should result in a decrease of the hyperfine splitting constant, since the direct overlap of the odd electron with the proton is increased by the deformation from the planar structure and gives positive spin densities on the proton.

Last, we consider the effect of the spin delocalization from the $-CH_2$ group to the metal oxide site. In view of the result obtained by Symons, *et al.*,[9d,10] it may be considered that the electron spin on the radical site delocalizes more onto the metal oxide with the decrease of electronegativity of the metal, and thus the proton hyperfine splittings decreases. This expectation coincides well with our observation, which shows the decrease of proton hyperfine splittings with the decrease of electronegativity of the metal. It may be concluded, therefore, that the spin delocalization effect from the radical site to the metal oxide system seems to be the most important mechanism for the observed marked change of the proton hyperfine splittings.

Esr Line Shapes and Molecular Motion of $MOCH_2$ Radicals. The line shape of esr spectrum of a free radical strongly depends on molecular motion. If the molecule can rotate freely in any direction, the anisotropic part of g and the hyperfine tensors are averaged to zero and the spectrum shows hyperfine splittings due only to the isotropic hyperfine interaction. However, in the usual case of free radicals trapped on solid surfaces, the molecular motion is restricted, and esr shows line width broadening due to imperfect averaging of the anisotropic g and hyperfine interaction. Interestingly, the hyperfine patterns observed in the present work are markedly different from one another (Figure 1). These differences may be mainly attributed to variation in the molecular motion of the $MOCH_2$ radicals. One refers to Lefebvre and Maruani's calculations[15] for esr line shapes to understand the observed change in the hyperfine pattern. They calculated the esr line shapes for the CH_2COOH radical in the two special cases: (1) the line shape when there is no molecular rotation, and (2) the line shape when the $-CH_2$ group undergoes fast rotation around the C–C bond. According to their calculations, the line shape when the $-CH_2$ group undergoes fast rotation consists of triplet lines, with a sharp intense central line, while the two outer lines are considerably broad and have some structure; the central line has considerably higher intensity than the outer lines (Figure 13b in ref 15). However, when the molecular motion is perfectly frozen (case 1), the central line also broadens and the spectrum shows a broad triplet pattern, each of which has some structure (Figure 13a in ref 15). In this case the intensity of the central part of the spectrum is rather smaller than the outer parts. On the other hand, it is well known that, when the molecular rotation is fast in all directions, the hyperfine pattern should be sharp triplet lines due to only isotropic hyperfine interaction with an intensity ratio of 1:2:1.

By comparing the observed hyperfine pattern with the calculated line shape, some information about the molecular motion of the $MOCH_2$ radicals may be obtained. For convenience, we take a ratio of the peak height of the $M_I = 0$ and -1 lines, $h(M_I = 0)/h(M_I = -1)$, as a measure of the molecular motion of the radical. Based on the hyperfine patterns calculated by Lefebvre and Maruani, it may be said that if the rotation of the $-CH_2$ group about the C–O bond becomes faster, the intensity ratio will increase, whereas if the molecular tumbling motion in any other direction is allowed, as well as the rotation of the $-CH_2$ group about the C–O bond, the intensity ratio will decrease and approach 2.

In Figure 5, the change of the intensity ratio, $h(M_I = 0)/h(M_I = -1)$, is shown as a function of temperature observed for each metal oxide system. Interestingly, the ratio increases with temperature in the $BeOCH_2$ and $MgOCH_2$ radicals, whereas the ratio for $SiOCH_2$ decreases as the temperature increases. Such changes in the ratio, $h(M_I = 0)/h(M_I = -1)$, with temperature suggest that there are two processes contributing to averaging the anisotropic part of the spectra; that is, one is the rotation of the $-CH_2$ group about the C–O axis, and the other is the fluctuational rotation of the $-OCH_2$ group around the M–O bond. Based on the consideration mentioned above, it is estimated that in the case of the $BeOCH_2$ and $MgOCH_2$ radicals, the rotation of $-CH_2$ group about the C–O bond approaches the free rotational state as the temperature increases, but the fluctuational rotation of $-OCH_2$ about the M–O bond is still restricted. On the other hand, in the case of the $SiOCH_2$ radical, it may be estimated that rotation of the $-CH_2$ group about the C–O axis is almost free even at 77°K, from the high intensity ratio of the line with $M_I = 0$ to the line with $M_I = -1$, and, as the temperature increases, the fluctuational rotation of $-OCH_2$ around the M–O bond will occur as well. The fact that the $AlOCH_2$ radical shows a maximum at about $-130°$ suggests that the following two processes are overlapping. That is, at low temperatures, the molecular motion of the radical sites is restricted, but as the temperature increases the rotation of $-CH_2$ about the C–O bond becomes fast, and thus the intensity ratio, $h(M_I = 0)/h(M_I = -1)$, increases. However, at high temperatures, the fluctuational motion of $-OCH_2$ is allowed as

well as the rotation of $-CH_2$, and, therefore, the intensity ratio, $h(M_I = 0)/h(M_I = -1)$, again becomes small and approaches 2.

Acknowledgments. We are indebted to Professor Yoshida Ogino and Mr. Akira Igarashi for helpful discussions and for supplying the adsorbents.

This work was supported by a grant from the Japanese Ministry of Education. This financial support is gratefully acknowledged.

References and Notes

(1) J. H. Lunsford, *Advan. Catal.*, **22**, 265 (1972).
(2) M. Shimizu, H. D. Gesser, and M. Fujimoto, *Can. J. Chem.*, **47**, 1375 (1969).
(3) Y. Ono and T. Keii, *J. Phys. Chem.*, **72**, 2851 (1968).
(4) S. Kubota, M. Iwaizumi, and T. Isobe, *Bull. Chem. Soc. Jap.*, **44**, 2684 (1971).
(5) R. J. Kokes, *J. Phys. Chem.*, **66**, 99 (1962).
(6) (a) V. B. Kasanskii, G. B. Pariiskii, I. V. Aleksandrov, and G. M. Zhidomirov, *Solid State Phys. (USSR)*, **5**, 649 (1963); (b) J. Turkevich and Y. Fujita, *Science*, **152**, 1619 (1966); (c) G. B. Gurbutt, H. D. Gesser, and M. Fujimoto, *J. Chem. Phys.*, **48**, 4605 (1968).
(7) N. Takezawa and H. Kobayashi, *J. Catal.*, **25**, 179 (1972).
(8) L. Pauling, *J. Chem. Phys.*, **51**, 2767 (1969).
(9) (a) R. W. Fessenden and R. H. Shuler, *J. Chem. Phys.*, **43**, 2704 (1965); (b) J. Cooper, A. Hudson, and R. A. Jackson, *Mol. Phys.*, **23**, 209 (1972); (c) A. Begum, J. H. Sharp, and M. C. R. Symons, *J. Chem. Phys.*, **53**, 3756 (1970); (d) A. Begum, S. Subramanian, and M. C. R. Symons, *J. Chem. Soc. A*, 918 (1970).
(10) R. S. Eachus and M. C. R. Symons, *J. Chem. Soc. A*, 790 (1968).
(11) J. A. Pople and D. L. Beveridge, "Approximate Molecular Orbital Theory," McGraw-Hill, New York, N.Y., 1970.
(12) H. M. McConnell, *J. Chem. Phys.*, **24**, 764 (1956).
(13) J. Higuchi, *J. Chem. Phys.*, **39**, 3455 (1963).
(14) The value 54.7 G was observed as the ^{13}C hyperfine splitting constant of $SiOCH_2$ at room temperature by the use of ^{13}C enriched methanol. This value is larger than that of the hydroxymethyl radical (R. W. Fessenden, *J. Phys. Chem.*, **71**, 74 (1967)) and it is nearly the same as that of CH_2F.[12a] For the CH_2F radical, it has been shown that the proton hyperfine splitting constant s negative (D. L. Beveridge, P. A. Dobosh, and J. A. Pople, *J. Chem. Phys.*, **48**, 4802 (1968)). The ^{13}C hyperfine splitting of the $MgOCH_2$ radical could not be observed because of large line broadening caused by the molecular motion more hindered than the $SiOCH_2$ radical.
(15) R. Lefebvre and J. Maruani, *J. Chem. Phys.*, **42**, 1480 (1965).

Positive-Ion Reactions in Monosilane–Water Mixtures[1]

T. M. H. Cheng and F. W. Lampe*

Davey Laboratory, Department of Chemistry, The Pennsylvania State University, University Park, Pennsylvania 16802
(Received July 23, 1973)

Publication costs assisted by the U.S. Atomic Energy Commission

Tandem mass spectrometry has been used to investigate the ion–molecule reactions occurring in gaseous mixtures of monosilane and water. Reaction rate constants were obtained by direct comparison with the known rate constant for hydride ion transfer from SiH_4 to SiH_2^+. As in other ion–molecule studies of monosilane the principal reaction is one of hydride ion transfer from monosilane to ions derived from water. SiH_4D^+ is observed to be formed in an endothermic process from collision of ground-state D_3O^+ with SiH_4 and in an exothermic process involving an excited state(s) of D_3O^+. Some implications of the results to the aqueous acid hydrolysis of monosilane are discussed.

Introduction

Subsequent to the discovery[2,3] and characterization[4-20] of ion–molecule reactions in methane and to the acceptance of their fundamental role in the radiation chemistry of methane,[21-28] Olah and his coworkers[29,30] demonstrated the importance of similar reactions and ionic products in strong acid solutions of methane. Thus in the case of methane a direct correspondence between the chemistry of ionized gases and that of liquid solution has been established.

One should expect a similar situation to obtain in the case of monosilane. Since the pioneering researches of Stock and his coworkers,[31-33] it has been known that monosilane reacts with water under alkaline or acidic conditions to yield, ultimately, hydrogen in amounts essentially equal to twice that contained in the monosilane. The overall reaction is thought to proceed *via* silanol and disiloxane intermediates[31-34] but the necessity of having alkaline or acidic conditions indicates that ionic reactions are of importance. By analogy with the case of methane, one may expect some of the ionic processes involved in the liquid-phase hydrolysis of monosilane to be of significance in the radiation chemistry of gaseous monosilane–water mixtures. As a part of a general program of study of the radiolytic behavior of silanes, an investigation of the radiolysis of monosilane–water mixtures is in progress in our laboratory. As an aid to the interpretation of the radiolysis experiments, we have carried out a tandem mass spectrometric investigation of the positive-ion chemistry of monosilane–water mixtures. This paper constitutes a report of our findings.

Experimental Section

The tandem mass spectrometer used in these studies permits the injection of mass-selected reactant ions, having kinetic energies variable down to about 1 eV, into a collision chamber containing the neutral reactant molecule. The apparatus, which has been described previously,[35] consists of two quadrupole mass filters separated by the collision chamber and ion lenses. In all experiments

the mass filters were mounted in the "in-line" configuration. Retarding field measurements indicate that the energy spread of the reactant ion beam entering the collision chamber is about 1 eV. Satisfactory operation of the apparatus was checked by examination of the energy dependence of the cross section for the reaction

$$O^+ + N_2 \longrightarrow NO^+ + N \qquad (1)$$

over the range 1–27 eV (laboratory energy). The dependence of the cross section on kinetic energy of O^+ was found to be identical, within experimental error, to that found by Giese.[36]

In addition to identification of the product ions formed in collisions of electron-impact-produced ions of water with monosilane and vice versa, the various relative reaction cross sections were studied as a function of kinetic energy in the range of 2–15 eV. As described previously,[37,38] the shapes of the cross section *vs.* energy curves were used to differentiate between exothermic and endothermic reactions; the cross sections of endothermic reactions generally rise from zero at the energy threshold to a broad maximum several eV above threshold, while cross sections for exothermic processes decrease for all values of ion kinetic energy.

Phenomenological rate constants of exothermic reactions were determined by direct comparison of relative reaction cross sections at 2.5 eV ion energy (lab) with the cross section for reaction 2, *viz.*

$$SiH_2^+ + SiH_4 \longrightarrow SiH_3^+ + SiH_3 \qquad (2)$$

The rate constant of (2) has been previously determined[35] as $2.5 \pm 0.3 \times 10^{-10}$ cm^3/sec. Collision chamber pressures were of the order of 10^{-3} Torr, a pressure sufficiently low to preclude the observation of third-order processes. Ionization chamber pressures of the order of $1–5 \times 10^{-3}$ Torr were employed.

Monosilane was purchased from the J. T. Baker Chemical Co. It was subjected to several freeze–pump–thaw cycles and checked mass spectrometrically for satisfactory purity before use. Deuterium oxide was obtained from Merck of Canada and used as received.

Results and Discussion

1. Nature of the Elementary Reactions. The ion–molecule reactions found to be exothermic on the basis of the dependence of reaction cross section on energy are tabulated in Table I. Also shown in Table I are the standard enthalpy changes calculated for the various reactions from available thermochemical data,[39,40] and phenomenological rate constants at 2.5-eV (lab) ion kinetic energy. In all cases except two the neutral products are written arbitrarily as those that give maximum exothermicity. In the two exceptions, the exothermicity is reduced from the maximum possible by the O–H and H–H bond dissociation energies, respectively. Ony may note immediately that the most rapid reaction of all ions with monosilane is hydride abstraction leading to the SiH_3^+ ion, an observation consistent with other studies[35,38] of the reactions of ions with SiH_4.

The reactions observed to be endothermic, on the basis of the cross-section dependence on energy, are depicted in Table II. Also shown in Table II are the threshold energies observed for the reactions, the energies at which the maximum in the cross section occurs, and the values of the cross sections at the maximum relative to that for reaction 2 at an ion kinetic energy of 2.5 eV.

In the remainder of this section we discuss the characteristics of the reactions that occur when the various reactant pairs are brought together.

(*a*) *$OD^+ + SiH_4$.* When OD^+ ions are injected in SiH_4, reactions 3–8 (Table I) are observed as exothermic processes, in that the cross sections decrease with increasing kinetic energy over the entire range studied, namely, 1.3–10.2 eV in the center-of-mass system. Reaction 9 (Table II) is observed as an endothermic process at relative kinetic energies above 1.9 eV; however, the intensities of the product $HSiOD^+$ (m/e 47) were so small and the energy dependence such in the range of detection that no threshold, other than an upper limit, could be obtained.

In the case of reactions 7–9, the mass of the product ion does not determine the formula since one does not know whether the hydrogen and/or deuterium is bound to silicon or oxygen. By comparison with the reaction of OH^+ with SiH_4, we have established the numbers of hydrogen atoms and deuterium atoms in the product ions of 7–9 and we have written the formulas with the arbitrary assumption that no intramolecular exchange occurs between hydrogen and deuterium originally bound to silicon and oxygen.

As shown in Table I, the enthalpy changes calculated from available thermochemical data[39,40] for 3–7 are in agreement with our observations from the cross-section–kinetic energy dependence that these reactions are exothermic. As will be discussed later, the observed thresholds of (24) and (26), shown in Table II, permit an evaluation of the standard enthalpy of formation of $SiOD^+$ and the value obtained leads to the exothermic enthalpy change for (7) shown in Table I. The standard enthalpy of formation of H_2SiOD^+ is unknown and cannot be evaluated from our data. We can therefore say only that the enthalpy change of (8) is at most zero. Reactions 6 and 7 are exothermic by 140 and 142 kcal, respectively, if the neutral products are written as HDO and $2H_2$, respectively. While this much energy could be shared between the ionic and neutral products, dissociation of the neutrals is energetically possible and we have arbitrarily written these reactions assuming such dissociation occurs.

Hydrogen atom abstraction from SiH_4 by OD^+ with formation of HDO^+ and SiH_3 is an exothermic process and is analogous to reaction 10, shown in Table I. Although a search for HDO^+ formation in the energy range of 2–5 eV (lab) was made, we were unable to detect it.

(*b*) *$D_2O^+ + SiH_4$.* The exothermic reactions 10–17, shown in Table I, and the endothermic reactions 18 and 19, shown in Table II, are observed to occur when D_2O^+ ions are injected into SiH_4. The structures of the ionic products of 13–17 were arrived at by comparison of mass shifts when H_2O^+ was substituted for D_2O^+ and with the arbitrary assumption that silicon and oxygen do not undergo intramolecular exchange of hydrogen and deuterium atoms. The D_2O^+ and H_2O^+ comparison was not able to differentiate between the products $HSiOD_2^+$ and H_3SiOD^+, and we are not really able to choose between them. However, we have a slight preference for $HSiOD_2^+$ because the alternative product H_3SiOD^+ corresponds to the molecular ion of H_3SiOD, an unstable molecule which has never been isolated.[41]

The kinetic energy dependence of the cross section of (10), namely, hydrogen atom abstraction from SiH_4, is interesting. As shown in Figure 1, the reaction is exothermic at low kinetic energies and can only be as written in Table I. However, the cross section goes through a minimum

TABLE I: Exothermic Ion–Molecule Reactions in SiH_4–D_2O Mixtures

Reaction no.	Reaction	ΔH°, kcal	$10^{10} \times k$,[a] cm^3/sec
3	$OD^+ + SiH_4 \rightarrow Si^+ + HDO + H_2 + H$	−29	0.21 ± 0.03
4	$OD^+ + SiH_4 \rightarrow SiH^+ + HDO + H_2$	−72	0.62 ± 0.08
5	$OD^+ + SiH_4 \rightarrow SiH_2^+ + HDO + H$	−44	1.4 ± 0.2
6	$OD^+ + SiH_4 \rightarrow SiH_3^+ + OD + H$[b]	−20	1.8 ± 0.3
7	$OD^+ + SiH_4 \rightarrow SiOD^+ + H_2 + H + H$[b]	−26	1.7 ± 0.3
8	$OD^+ + SiH_4 \rightarrow H_2SiOD^+ + H_2$	≤0	0.86 ± 0.2
10	$D_2O^+ + SiH_4 \rightarrow HD_2O^+ + SiH_3$	−47	0.79 ± 0.1
11	$D_2O^+ + SiH_4 \rightarrow SiH_2^+ + D_2O + H_2$	−17	1.9 ± 0.3
12	$D_2O^+ + SiH_4 \rightarrow SiH_3^+ + D_2O + H$	−9	2.1 ± 0.3
13	$D_2O^+ + SiH_4 \rightarrow SiOD^- + HD + H_2 + H$	+2[c]	0.12 ± 0.02
14	$D_2O^+ + SiH_4 \rightarrow HSiOD^+ + H_2 + HD$	≤0	0.033 ± 0.003
15	$D_2O^+ + SiH_4 \rightarrow H_2SiOD^+ + HD + H$	≤0	0.32 ± 0.04
16	$D_2O^+ + SiH_4 \rightarrow HSiOD_2^+ + H_2 + H$ (or $H_3SiOD^+ + HD$)	−5	0.019 ± 0.005
17	$D_2O^+ + SiH_4 \rightarrow H_2SiOD_2^+ + H_2$	<0	0.039 ± 0.01
20[d]	$D_3O^{+*} + SiH_4 \rightarrow SiH_3^+ + D_2O + HD$	+31[b,c]	>1.1 ± 0.2[b]
21[d]	$D_3O^{+*} + SiH_4 \rightarrow SiH_4D^* + D_2O$	+10[b,c]	>0.19 ± 0.03[b]
22	$SiH_3^+ + H_2O$[b] $\rightarrow H_2SiOH^+ + H_2$	≤0	0.058 ± 0.08
23	$SiH_2^+ + D_2O \rightarrow SiOD_2^+ + H_2$	≤0	0.053 ± 0.08
26	$SiH^+ + D_2O \rightarrow SiOD_2^+ + H$	≤0	0.12 ± 0.02

[a] Ion kinetic energy is 2.5 eV (lab). [b] See text. [c] Refers to ground-state reactants. [d] An asterisk denotes internal excitation.

TABLE II: Endothermic Ion–Molecule Reactions in SiH_4–D_2O Mixtures

Reaction no.	Reaction	Threshold energy (CM), eV	Energy (lab) for σ_{max}, eV	$\sigma_{max}\ \sigma_2$(2.5 eV)
24	$SiH_2^+ + D_2O \rightarrow SiOD^+ + HD + H$	0.40 ± 0.15	3.0 ± 0.2	0.014
25	$SiH_2^+ + D_2O \rightarrow HSiOD_2^+ + H$	0.56 ± 0.15	2.7 ± 0.3	0.018
27	$Si^+ + D_2O \rightarrow SiOD^+ + D$	0.68 ± 0.15	3.3 ± 0.3	0.093
20	$D_3O^+ + SiH_4 \rightarrow SiH_3^+ + D_2O + HD$	1.4[a]	5.3 ± 1	0.30
21	$D_3O^+ + SiH_4 \rightarrow SiH_4D^+ + D_2O$	0.43[a]		
18	$D_2O^+ + SiH_4 \rightarrow SiH^+ + D_2O + H_2 + H$	3.1[a]		
19	$D_2O^+ + SiH_4 \rightarrow Si^+ + D_2O + 2H_2$	−0.06[a]		
9	$OD^+ + SiH_4 \rightarrow HSiOD^+ + H_2 + H$	<1.9	3.5 ± 0.5	0.021

[a] Calculated from thermochemical data.[37,39,40]

about 3 eV (lab) and then reaches a maximum at about 6 eV (lab). It is thus indicated that above the threshold energy an endothermic process contributes also to the formation of HD_2O^+ (or to D_3O^+ in the case of the $D_2O^+ + SiD_4$ reaction also shown in Figure 1). The endothermicity of this process, estimated from the thresholds obtained by linear extrapolation of the straight line portion of the region of positive slope, is 15 ± 5 kcal/mol.

The experimental uncertainties in the linearly extrapolated thresholds in Figure 1 very probably exceed any differences between the reactions of D_2O^+ with SiD_4 and SiH_4.

We believe that the most likely endothermic channels that correspond to the above threshold are as shown by (28) and (29) in which the asterisk denotes an excited

$$D_2O^+ + SiH_4 \longrightarrow HD_2O^+ + SiH_2 + H \quad (28)$$

$$D_2O^+ + SiH_4 \longrightarrow HD_2O^{+*} + SiH_3 \quad (29)$$

state(s). The occurrence of (28) with an endothermicity of 15 kcal implies that the dissociation energy of the H_2Si–H bond is 63 kcal/mol. This is a reasonable number considering that the average of the dissociation energies of the H_2Si–H and HSi–H bonds are known from thermochemical data[39,40,42] to be 70 kcal/mol. On the other hand, a 15-kcal endothermic process for the formation of an excited state of HD_2O^+ from ground-state D_2O^+, as in (29), requires that the energy of the excited state of HD_2O^+ be 63 kcal/mol above the ground state. The recent results of Lindemann, Rozett, and Koski[43] suggest that our D_2O^+ beam in these experiments contains about 20% of D_2O^+ in the first excited state ($^2A_1$). The excess energy of this state,[44] above the ground state of D_2O^+, is 25 kcal/mol. If D_2O^+ in (28) were in the ($^2A_1$) state the observed endothermicity of 15 kcal requires the bond dissociation energy of the H_2Si–H bond to be 88 kcal/mol, a value that would seem to be very high as compared with what would then be required for HSi–H, namely, 52 kcal/mol. Similarly, if D_2O^+ in (29) were in the ($^2A_1$), the 15-kcal endothermicity requires that the excited state of HD_2O^+ be 88 kcal/mol above the ground state of the ion.

For the following reasons, admittedly not compelling, we favor the occurrence of (29) rather than (28) as the explanation of the endothermic channel that is seen in Figure 1.

(1) Reactions 10, 28, and 29 are H-atom pick-up reactions, many of which occur by a direct mechanism as contrasted to complex formation.[45] To the extent that this reaction approaches ideal spectator stripping[46] or modified spectator stripping,[47] the SiH_3 radical does not receive sufficient energy from the collision to dissociate.

(2) As will be seen later a state (or states) of D_3O^+ with internal energy above 31 kcal/mol is required to explain

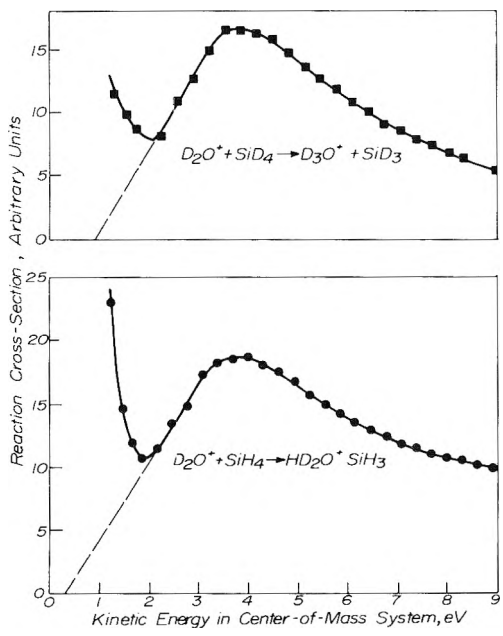

Figure 1. Dependence on energy of reaction cross sections for H atom and D atom abstraction from SiH_4 and SiD_4 by D_2O^+.

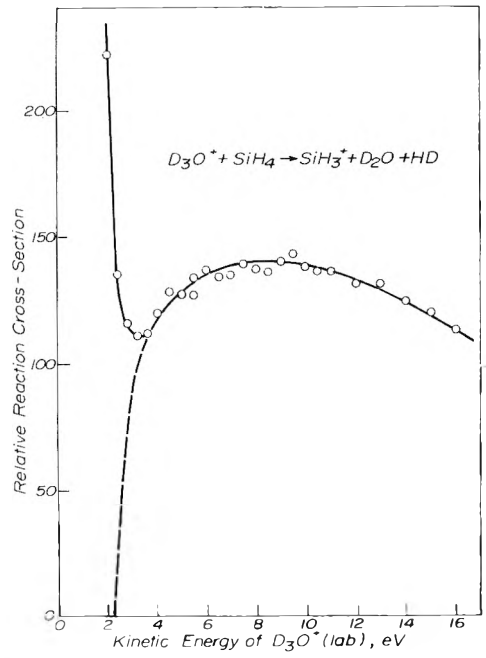

Figure 2. Dependence on energy of reaction cross section for hydride ion transfer from SiH_4 to D_3O^+.

the formation of SiH_3^+ in collisions of D_3O^+ with SiH_4. Thus the existence of an excited state (or states) formed by a similar reaction ($D_2O^+ + D_2O \rightarrow D_3O^+ + OD$ in the ion source) is established in this work. This confirms earlier studies of DePaz, Leventhal, and Friedman.[48]

(3) In other reactions of D_2O^+ and OD^+ that probably involve direct mechanisms, such as (3)–(5), (11), and (12), the variation of cross sections with energy does not indicate the opening of endothermic channels which would correspond to dissociation of the neutral products.

The dependence of the cross sections of (13)–(15) (*cf.* Table I) on kinetic energy indicate the onset of endothermic channels to produce the respective ions. It was not possible to obtain reliable thresholds for these endothermic channels but they appear to lie in the range of 3–4.5 eV (center-of-mass). Since complex formation is a probable mechanism[45] for (13)–(15), it seems likely that these endothermic channels correspond to dissociation of the neutral molecular hydrogen product of these reactions. In the case of (13), the reaction as written (*cf.* Table I) is about thermoneutral and, therefore, the threshold for the endothermic channel (30) would be D(H–H) or 4.4 eV (center-of-mass).

$$D_2O^+ + SiH_4 \longrightarrow SiOD^+ + HD + 3H \qquad (30)$$

The exothermicities of (14) and (15) are not known and so the thresholds corresponding to dissociation of the molecular hydrogen cannot be computed. However, the range of values observed is not inconsistent with such endothermic channels for these reactions.

While it is likely that (16) and (17) also proceed by complex formation, no evidence for the onset of endothermic channels producing $HSiOD_2^+$ and $H_2SiOD_2^+$ was obtained.

Reactions 18 and 19 (*cf.* Table II) appeared to be endothermic processes over the range of energy investigated. Thermochemical calculations[39,40,44] confirm (18) to be endothermic for D_2O^+ in both the ground and first excited state. However, (19) would seem to be slightly exothermic even for ground-state D_2O^+, on the basis of established thermochemistry. The intensity of Si^+ from this reactant pair was very small and we could not study the process to as low an energy as was possible with the more intense ions. It is possible, at the energies we could study Si^+, that we were observing an endothermic channel corresponding to dissociation of one of the H_2 product molecules and that at lower energies the exothermic process corresponding to (19) would be detectable.

(*c*) $D_3O^+ + SiH_4$. When D_3O^+ ions are injected into SiH_4, only two product ions are observed, namely, SiH_3^+ and SiH_4D^+, as shown by (20) and (21) in Tables I and II. At low kinetic energies both (20) and (21) appear to be exothermic on the basis of the kinetic energy dependence of their respective cross sections; at higher kinetic energies, when using 100-eV electrons in the ion source, the suggestion of an endothermic process was noted. For ground-state reactants, (20) and (21) are known[37,39,40,49] to be endothermic by 31 and 10 kcal, respectively. The most plausible explanation for the observation of (20) and (21) as exothermic at low kinetic energies is that a significant proportion of the D_3O^+ beam contains internal energy of at least 31 kcal/mol. It has been reported[48] that a significant fraction of the D_3O^+ prepared in an electron-impact ionization chamber by collision of D_2O^+ with D_2O contains considerable internal excitation energy and that the extent of this excitation depends on the energy of the ionizing electron beam.

As a check on this explanation of our observation that (20) and (21) were exothermic, we examined (20) at an ionizing electron energy of 25 eV and the dependence of the cross section on kinetic energy is shown in Figure 2. It is clear from Figure 2, that superimposed on an exothermic channel producing SiH_3^+ is an endothermic one with a broad maximum centered at about 9 eV (lab). The calculated[39,40,49] threshold for formation of SiH_3^+ is 2.3 eV in the laboratory frame of reference and it may be seen from Figure 2 that the data are consistent with this value. We therefore conclude that the exothermic channels forming SiH_3^+ and SiH_4D^+ are the result of internally excited D_3O^+, while ground-state D_3O^+ produces the same ionic products *via* endothermic channels.

The mechanism of (21) (*cf.* Tables I and II) is most probably a direct one of simple proton transfer, since no other isotopic analogs such as $SiH_3D_2^+$, etc., were observed. The fact that only insignificant amounts (if indeed any) of SiH_2D^+ were found with SiH_3^+ strongly indicates that (20) does *not* occur by the sequence of (21) followed by (31), *viz.*

$$SiH_4D^+ \xrightarrow{a} SiH_3^+ + HD \qquad (31)$$
$$\xrightarrow{b} SiH_2D^+ + H_2$$

Statistical break-down of SiH_4D^+ would yield 40% SiH_3^+ and 60% SiH_2D^+ while the amount of SiH_2D^+ observed is at most ~2.5%. Therefore, the mechanism of (20) would appear to be best described as a direct hydride ion abstraction from SiH_4, with formation of HD and D_2O as neutral products. A similar mechanism has been observed[50] in the reaction of CD_5^+ with SiH_4.

The rate constants of (20) and (21) reported in Table I for 2.5 eV (lab) ions are only lower limits, since at this energy the reaction is brought about mostly by excited states of D_3O^+ and we do not know the fraction of the beam that is excited.

(*d*) *$SiH_3^+ + H_2O$.* When SiH_3^+ ions are injected into D_2O^+, three small peaks at *m/e* 47, 48, and 49 are observed. Substitution of H_2O for D_2O resulted in a single peak at *m/e* 47, whose intensity was considerably greater than the sum of those found for the case of D_2O. We do not understand this behavior, but we have arbitrarily written the product of the reaction with H_2O as H_2SiOH^+ because in our experience the most intense products are those containing one hydrogen atom from the water or water ion. Studies of the cross section of (22) (Table I) as a function of energy indicate the process to be exothermic over the range investigated. No other reactions of SiH_3^+ with H_2O (or D_2O) were detected.

(*e*) *$SiH_2^+ + D_2O$.* The reaction of SiH_2^+ ions with D_2O produces $SiOD_2^+$, $SiOD^+$, and $HSiOD_2^+$ by reactions 23–25, respectively, shown in Tables I and II. The dependence of cross sections on kinetic energy indicates (23) to be an exothermic process while (24) and (25) are both endothermic with thresholds of 0.40 and 0.56 eV (center-of-mass), respectively.

At kinetic energies above 4 eV (lab) an endothermic channel producing *m/e* 48 ($SiOD_2^+$) is observed. This is possibly the result of dissociation of the molecular hydrogen product of (23); however, comparison with experiments in which H_2O was substituted for D_2O suggests that the most likely explanation is the occurrence of (32) as an endothermic process, *viz.*

$$SiH_2^+ + D_2O \longrightarrow H_2SiOD^+ + D \qquad \Delta H > 0 \qquad (32)$$

(*f*) *$SiH^+ + D_2O$.* The only product ion observed when SiH^+ ions were injected into D_2O was $SiOD_2^+$. This product is formed in an exothermic reaction, as shown by reaction 26 in Table I.

(*g*) *$Si^+ + D_2O$.* Only one product ion is observed when Si^+ ions react with D_2O, namely, $SiOD^+$, as shown by (27) in Table II. The dependence of cross section on kinetic energy indicates the reaction to be endothermic with a threshold of 0.68 eV, and a maximum cross section at 3.3 eV, both in the center-of-mass.

2. Thermochemistry of Gaseous Oxysilicon Ions. Determination of the thresholds of endothermic reactions permits calculation of standard enthalpies of formation of the ionic products, since the standard enthalpies of formation of the other components of these reactions are known.[39,40] By linear extrapolation of cross-section-kinetic energy data we are able to determine admittedly approximate thresholds for reactions 24–27 in Table II and thereby obtain approximate enthalpies of formation of the $SiOD^+$ and $HSiOD_2^+$ ions. The pertinent curves and extrapolations for reactions 24 and 27 are depicted in Figure 3.

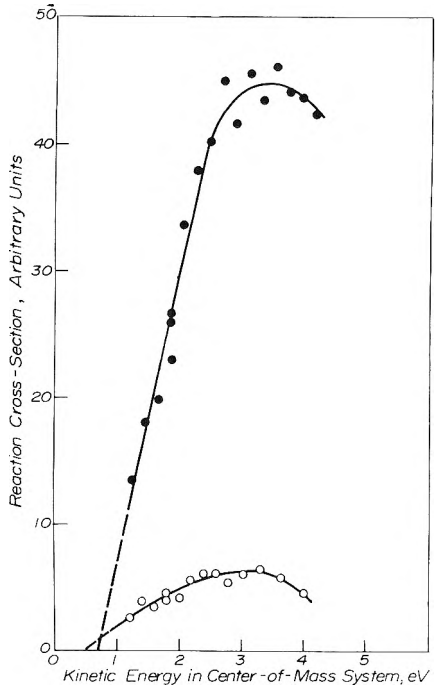

Figure 3. Dependence on energy of reaction cross sections for the formation of $SiOD^+$ in collisions of Si^+ and SiH_2^+ with D_2O: O, reaction 27; ●, reaction 24 (*cf.* Table II).

The measured thresholds of (24) and (27), when combined with established thermochemical data,[39,40] lead to values of 180 and 200 kcal/mol, respectively for $\Delta H_f°(SiOD^+)$. In view of the large uncertainties in the determination of the thresholds (*cf.* Table II and Figure 3) these may be considered to be in agreement and we therefore conclude that $\Delta H_f°(SiOD^+) = 190 \pm 10$ kcal/mol. As may be seen in Table I, this value is consistent within experimental error with the observations of (7) and (13) as exothermic processes. Since $\Delta H_f°(SiO^+)$ and $\Delta H_f°(SiO)$ are known[40] to be +219 and −24 kcal/mol, respectively, our result for $\Delta H_f°(SiOH^+)$ at once leads to the following values: proton affinity (SiO) = 151 kcal/mol; dissociation energy (SiO^+–H) = 81 kcal/mol.

The threshold of (25) leads by a similar procedure to $\Delta H_f°(HSiOD_2^+) = 183 \pm 9$ kcal/mol. This value is consistent with the observation of (16) as an exothermic process as shown in Table I.

3. Implications to Acid Solutions of Monosilane. Olah and coworkers[29,30] have studied the chemistry of strong acid solutions of methane and have based much of the interpretation of their observations on the ion–molecule reaction chemistry established in the gas phase. Thus in the very strong acid, FSO_3H–SbF_5, they propose the following mechanism

$$CH_4 \underset{SbF_5}{\overset{FSO_3H}{\rightleftharpoons}} [CH_5^+] \qquad (33)$$

$$[CH_5^+] \longrightarrow CH_3^+ + H_2 \qquad (34)$$

$$CH_3^+ + CH_4 \longrightarrow [C_2H_7^+] \underset{+H^+}{\overset{-H^+}{\rightleftharpoons}} C_2H_6 \qquad (35)$$

$$[C_2H_7^+] \xrightarrow{-H_2} C_2H_5^+ \underset{+H^+}{\overset{-H^+}{\rightleftharpoons}} CH_2{=}CH_2 \quad (36)$$

$$C_2H_5^+ + CH_4 \longrightarrow [C_3H_9^+] \underset{+H^+}{\overset{-H^+}{\rightleftharpoons}} C_3H_8 \quad (37)$$

In contrast to methane, monosilane is decomposed by weaker aqueous acids[31-34] and, in this regard, it is of interest to point out that the gas-phase proton affinity of monosilane is about 30 kcal/mol larger than that of methane.[37,49] Thus monosilane is a stronger Brönsted base than methane. In addition, monosilane is also a stronger Lewis base than methane in the gas phase, since hydride ion transfer from SiH_4 to any given ion is 47 kcal/mol more favorable energetically than is hydride transfer from CH_4 to the same ion.[39,40]

We suggest that a carry-over to the solution phase of this relative base strength of monosilane and methane is the basic reason that monosilane undergoes chemical decomposition even in aqueous acids, while much stronger acids (termed superacids by Olah, *et al.*[29,30]) are required to induce reaction of methane. Then by analogy with the Olah mechanism describing the "superacid" chemistry of methane, but based on the establishment of reactions 20 and 21, we propose the long-known aqueous acid hydrolysis[31-33] of monosilane to occur by the following mechanism

$$SiH_4 \underset{}{\overset{H_3O^+}{\rightleftharpoons}} [SiH_5^+] \quad (38)$$

$$SiH_4 \xrightarrow{H_3O^+} SiH_3^+ + H_2 \quad (39)$$

$$SiH_3^+ + H_2O \rightleftharpoons [SiH_3OH_2^+] \underset{-H^+}{\overset{-H^+}{\rightleftharpoons}} SiH_3OH \quad (40)$$

In the present study we have observed an energetically favorable reaction of SiH_3^+ with H_2O, namely, (22) (*cf.* Table I), that forms H_2SiOH^+ and H_2. However, this observation was made at sufficiently low pressures in the collision chamber that third-order stabilization of an energetic association product, such as $SiH_3OH_2^+$, was precluded. On the other hand, in ionized SiH_4-H_2O mixtures examined in a single-source mass spectrometer at ~0.25 Torr, the ion $SiH_3OH_2^+$ is a major product.[51] Thus reaction 40 would seem to be established.

Following formation of the silanol in (40), further decomposition proceeds *via* unknown mechanisms according to (41) and (42), to produce disiloxane, silicic acid, and

$$SiH_3OH + SiH_3OH \longrightarrow SiH_3OSiH_3 + H_2O \quad (41)$$

$$SiH_3OSiH_3 + 5H_2O \longrightarrow 2H_2SiO_3 + 6H_2 \quad (42)$$

hydrogen, as proposed long ago by Stock, *et al.*[31-34] The overall reaction describing the acid hydrolysis of monosilane is then from (38)-(42), that described by (43) which,

$$SiH_4 + 3H_2O \longrightarrow H_2SiO_3 + 4H_2 \quad (43)$$

at constant pressure, yields the fourfold volume increase above the solution observed by Stock and coworkers.[31-33]

Acknowledgment. This work was supported by the U. S. Atomic Energy Commission under Contract No. At(11-1)-3416.

References and Notes

(1) U. S. Atomic Energy Commission Document No. COO-3416-9.
(2) V. L. Tal'roze and A. K. Lyubimova, *Dokl. Akad. Nauk SSSR*, **86**, 909 (1952).
(3) D. O. Schissler and D. P. Stevenson, *J. Chem. Phys.*, **24**, 926 (1956).
(4) F. H. Field, J. L. Franklin, and F. W. Lampe, *J. Amer. Chem. Soc.*, **78**, 5697 (1956).
(5) D. P. Stevenson and D. O. Schissler, *J. Chem. Phys.*, **23**, 1353 (1955).
(6) F. H. Field, J. L. Franklin, and F. W. Lampe, *J. Amer. Chem. Soc.*, **79**, 2419 (1957).
(7) V. L. Tal'roze and E. L. Frankevich, *Zh. Fiz. Khim.*, **34**, 2709 (1960).
(8) R. Fuchs, *Z. Naturforsch. A*, **16**, 1026 (1961).
(9) S. Wexler and N. Jesse, *J. Amer. Chem. Soc.*, **84**, 3425 (1962).
(10) D. A. Kubose and W. H. Hamill, *J. Amer. Chem. Soc.*, **85**, 125 (1963).
(11) F. H. Field, J. L. Franklin, and M. S. B. Munson, *J. Amer. Chem. Soc.*, **85**, 3575 (1963).
(12) G. A. W. Derwish, A. Galli, A. Giardini-Guidoni, and G. G. Volpi, *J. Chem. Phys.*, **40**, 5 (1964).
(13) C. E. Melton and W. H. Hamill, *J. Chem. Phys.*, **41**, 1469 (1964).
(14) C. W. Hand and H. von Weyssenhoff, *Can. J. Chem.*, **42**, 195 (1964).
(15) K. R. Ryan and J. H. Futrell, *J. Chem. Phys.*, **42**, 824 (1965).
(16) F. H. Field and M. S. B. Munson, *J. Amer. Chem. Soc.*, **87**, 3289 (1965).
(17) S. O. Colgate and T. W. Schmidt, *J. Chem. Phys.*, **45**, 367 (1966).
(18) F. P. Abramson and J. H. Futrell, *J. Chem. Phys.*, **45**, 367 (1966).
(19) A. G. Harrison, A. Ivko, and T. W. Shannon, *Can. J. Chem.*, **44**, 1351 (1966).
(20) S. K. Gupta, E. G. Jones, A. G. Harrison, and J. J. Myher, *Can. J. Chem.*, **45**, 3107 (1967).
(21) F. W. Lampe, *J. Amer. Chem. Soc.*, **79**, 1055 (1957).
(22) (a) D. P. Stevenson, *J. Phys. Chem.*, **61**, 1453 (1957); (b) G. G. Meisels, W. H. Hamill, and R. R. Williams, Jr., *ibid.*, **61**, 1456 (1957); (c) K. Yang and P. J. Manno, *J. Amer. Chem. Soc.*, **81**, 3507 (1959).
(23) P. Ausloos and S. G. Lias, *J. Chem. Phys.*, **38**, 2207 (1963).
(24) R. W. Hummel, *Discuss. Faraday Soc.*, **36**, 75 (1963).
(25) L. W. Sieck and R. H. Johnsen, *J. Phys. Chem.*, **67**, 2281 (1963).
(26) P. Ausloos, S. G. Lias, and R. Gordon, Jr., *J. Chem. Phys.*, **39**, 3341 (1963).
(27) P. Ausloos, R. Gordon, Jr., and S. G. Lias, *J. Chem. Phys.*, **40**, 1854 (1964).
(28) R. Gordon, Jr., and P. Ausloos, *J. Chem. Phys.*, **46**, 4823 (1967).
(29) G. A. Olah and R. H. Schlosberg, *J. Amer. Chem. Soc.*, **90**, 2726 (1968).
(30) G. A. Olah, G. Klopman, and R. H. Schlosberg, *J. Amer. Chem. Soc.*, **91**, 3261 (1969).
(31) A. Stock and C. Somieski, *Berichte*, **49**, 111 (1916).
(32) A. Stock, C. Somieski, and R. Wintgen, *Berichte*, **50**, 1754 (1917).
(33) A. Stock and C. Somieski, *Berichte*, **51**, 989 (1918).
(34) A. G. MacDiarmid, *Advan. Inorg. Radiochem.*, 3, 207 (1961).
(35) T-Y. Yu, T. M. H. Cheng, V. Kempter, and F. W. Lampe, *J. Phys. Chem.*, **76**, 3321 (1972).
(36) C. F. Giese, *Advan. Chem. Ser.*, **No. 58**, 20 (1966).
(37) T. M. H. Cheng and F. W. Lampe, *Chem. Phys. Letts.*, **19**, 532 (1973).
(38) T. M. H. Cheng, T-Y. Yu, and F. W. Lampe, *J. Phys. Chem.*, **77**, 2587 (1973).
(39) P. Potzinger and F. W. Lampe, *J. Phys. Chem.*, **73**, 3912 (1969).
(40) J. L. Franklin, J. G. Dillard, H. M. Rosenstock, J. T. Herron, K. Drexl, and F. H. Field, *Nat. Stand. Ref. Data Ser., Nat. Bur. Stand.*, **No. 26** (June 1969).
(41) E. A. V. Ebsworth, "Volatile Silicon Compounds," Pergamon Press, New York, N. Y., 1963, p 123.
(42) A. E. Douglas, *Can. J. Phys.*, **35**, 76 (1957).
(43) E. Lindemann, R. W. Rozett, and W. S. Koski, *J. Chem. Phys.*, **56**, 5490 (1972).
(44) C. R. Brundle and D. W. Turner, *Proc. Roy. Soc., Ser. A*, **307**, 27 (1968).
(45) Z. Herman and R. Wolfgang, "Ion-Molecule Reactions," J. L. Franklin, Ed., Plenum Press, New York, N. Y., 1972, p 571.
(46) A. Henglein, K. Lacmann, and G. Jacobs, *Ber. Bunsenges. Phys. Chem.*, **69**, 279 (1965).
(47) Z. Herman, J. Kerstetter, T. L. Rose, and R. Wolfgang, *Discuss. Faraday Soc.*, **44**, 123 (1967).
(48) M. DePaz, J. J. Leventhal, and L. Friedman, *J. Chem. Phys.*, 51, 3748 (1969).
(49) M. A. Haney and J. L. Franklin, *J. Phys. Chem.*, **73**, 4328 (1969).
(50) G. W. Stewart, J. M. S. Henis, and P. P. Gaspar, *J. Chem. Phys.*, **57**, 2247 (1972).
(51) T. M. Mayer and F. W. Lampe, unpublished results.

The Methanol–Silica Gel System. V. Pulse Deuteron Magnetic Resonance Measurements in the Adsorbed Phase[1]

S. J. Seymour, M. I. Cruz, and J. J. Fripiat*

Department of Chemistry, School of Chemical Sciences, and Department of Geology, University of Illinois, Urbana, Illinois 61801
(Received May 29, 1973)

Deuteron longitudinal (T_1) and transversal (T_2) relaxation times have been measured for CD_3OH adsorbed on the hydroxylic surface of a Xerogel silica gel (the CD_3OH–XOH system) and for the related CH_3OD–XOD system. These data complement those obtained and discussed earlier for the proton resonance. In the CD_3OH–XOH system, T_1 is associated with a coverage independent correlation time $\langle\tau_{Dt}\rangle = 2.9 \times 10^{-16} \exp(5.4 \text{ kcal mol}^{-1}/RT)$ sec which has been associated with a molecule tumbling on an adsorption site. T_2 seems to be mostly influenced by reorientational effects even though no doublet splitting is apparent in the decay of the magnetization following a 90° pulse. In the CD_3OD–XOD system, T_1 has contributions from a molecular diffusion and an exchange term, the latter becoming increasingly important at lower degrees of coverage. At $\theta = 1.7$, the correlation time associated with T_1 and T_2 is indeed in the range of those obtained primarily for molecular diffusion: $\langle\tau_{Dd}\rangle = 3.15 \times 10^{-14} \exp(5.5 \text{ kcal mol}^{-1}/RT)$ sec. For smaller θ, T_2 is influenced by another process and with analogy to what was found for the proton resonance, it appears that this may be a deuteron exchange such as $CH_3OD_2^+ + CH_3OD$. If this is the case, then the quadrupole coupling constant is significantly lower (perhaps 50%) than that used for molecular diffusion. For the two systems studied here, approximately the same distribution of correlation times considered in the proton resonance study is used to account for the experimental data.

Introduction

The study of nuclear magnetic relaxation times of molecules adsorbed on a surface provices valuable information about the interactions at the interface and the dynamics of the system. The relative contributions of the different relaxation mechanisms to the relaxation times are often difficult to separate, even in the liquid state, unless a particular mechanism such as the nuclear quadrupolar interaction is known to predominate. In the latter case, it is then possible to investigate the reorientational diffusional and exchange properties of adsorbed molecules, which is of particular interest in the kinetics of heterogeneous catalysis and molecular dynamics.

In a preceding contribution[2] to this series, the molecular diffusion of methanol adsorbed on the surface of a Xerogel (X), silica gel, and the proton exchange between the surface and the adsorbed species have been studied by pulse proton magnetic resonance. In the CH_3OD–XOD system, only one T_1 or T_2, spin-lattice and spin-spin relaxation time, respectively, was observed and the experimental data could be well accounted for by a translational motion of the CH_3OD, with the methyl group rotating rapidly about the triad axis. In the CD_3OH–SiOH system, one T_1 and two T_2 were observed, where the T_1 resulted from the superimposition of two functions corresponding to two populations of adsorbed species. The rate of exchange between the two populations is fast relative to T_1^{-1} but is slow with respect to T_2^{-1}. The long T_2 corresponded to the diffusional motion observed for the CH_3OD–XOD system, while the short T_2 was assumed to represent a proton exchange process between the hydroxylic proton of CD_3OH molecules. The frequency ratio of the proton exchange to molecular diffusion increases as the degree of coverage decreases, suggesting that the "turn over" of the surface proton on the adsorbed species is higher at lower degrees of coverage. At 25° the surface diffusion coefficient of adsorbed methanol was found to be reduced by two orders of magnitude at a degree of coverage, $\theta \simeq 0.6$, as compared to the liquid state. θ might be as high as 3 to obtain diffusion coefficients comparable to the bulk liquid at the same temperature.

The deuteron relaxation rate is determined by a dominant intramolecular, quadrupolar interaction relaxation mechanism, involving the coupling of the nuclear quadrupole with the electrostatic field gradient at the nucleus. Measurement of the deuteron T_1^{-1} and T_2^{-1} would thus shed further light on the molecular or exchange motions in CD_3OH–XOH or CH_3OD–XOD systems. These relaxation rates for deuterium are given by the following relationships[3]

$$T_1^{-1} = \left(\frac{3}{80}\right)\left(1 + \frac{1}{3}\eta^2\right)(e^2qQ/\hbar)^2[J(\omega_0) + 4J(2\omega_0)] \quad (1)$$

$$T_2^{-1} = \left(\frac{1}{160}\right)\left(1 + \frac{1}{3}\eta^2\right)(e^2qQ/\hbar)^2[9J(0) + 15J(\omega_0) + 6J(2\omega_0)] \quad (2)$$

where $(e^2qQ/\hbar)$ is 2π times the quadrupole coupling constant (QCC) in hertz, η is a parameter associated with the asymmetry of the electric field gradient, and $J(\omega_0)$ is the power density spectrum which is the Fourier transform of the correlation function describing the time dependence of the motion. Neglecting the asymmetry parameter and assuming in conformance with the proton resonance study[2] a Gaussian distribution of correlation times,[4] these equations may be rewritten

$$T_1^{-1} = \frac{2\kappa}{\omega_0}[F_1 + 2F_2] \quad (3)$$

$$T_2^{-1} = \frac{\kappa}{\omega_0}[3F_0 + 5F_1 + F_2] \quad (4)$$

where $\kappa = (3/80)(e^2qQ\hbar)^2 = 1.48(\mathrm{QCC})^2$ and also

$$F_1 = \int_0^\infty P(\tau)\frac{\omega_0\tau}{1 + \omega_0^2\tau^2}\,d\tau \quad (5)$$

$$F_2 = \int_0^\infty P(\tau)\frac{2\omega_0\tau}{1 + 4\omega_0^2\tau^2}\,d\tau \quad (6)$$

$$F_0 = \int_0^\infty P(\tau)\omega_0\tau\,d\tau = \omega_0\tau_m \exp(\beta^2/4) \quad (7)$$

The normalized Gaussian distribution function is defined as

$$P(\tau)\,d\tau = \beta^{-1}\pi^{-1/2} \exp[-(Z/\beta)^2]\,dZ \quad (8)$$

where

$$Z = \ln(\tau/\tau_m)$$

$$\tau_m = \exp\langle\ln\tau\rangle = \tau_0 \exp(\bar{H}/RT) \quad (9)$$

τ_m is the average correlation time, hereafter referred to as τ for simplicity. The parameters in the above equations, β and $\bar{H}$, as well as the functions F_1 and F_2, were calculated according to the procedure described earlier.[2]

The deuteron QCC of liquid CH_3OD is given as 192 ± 15 kHz by O'Reilly, *et al.*,[5] while the corresponding value for liquid CD_3OH is 170 kHz according to Hertz, *et al.*[6] *A priori*, it is not expected that the QCC in the adsorbed state would be significantly different since it has been shown that large changes in liquid density (see, for instance, Lee and Jonas[7] and references therein) are required to affect the quadrupole interaction constant noticeably. However, in the adsorbed state the hydrogen bond network may be quite modified with respect to that in the bulk liquid, and the additional fact that possible deuteron transfer from a surface site to a cluster of adsorbed species produces $CH_3OD_2^+$ species that play a significant role in the deuteron relaxation process necessitates one to keep in mind a possible modification of the QCC.

For obvious experimental reasons such as the weakness of the deuteron resonance signal and the very short decay times of the magnetization, very few papers have been published on deuteron magnetic resonance measurements in the adsorbed phase. From a recent and very complete review by Pfeifer,[8] it appears that only 3% of the papers devoted to magnetic resonance studies in the adsorbed state were concerned with deuterium measurements. In fact, they deal almost exclusively with D_2O present in large excess (*i.e.*, much more than 3 layers). For the D_2O studies mentioned, either the deuteron QCC of the ice[9] or of the liquid[10] was utilized in discussing the results in the adsorbed state.

As a significant advancement of studies in the adsorbed phase, the pulse deuteron relaxation times for CH_3OD–XOD and CD_3OH–XOH systems for coverages less than 3 monolayers and a temperature range of −60 to 40° are reported. The results are discussed in terms of molecular reorientation and exchange phenomena.

Experimental Section

The materials and the samples used in this study were exactly the same as those used for the proton pulse magnetic resonance study published earlier.[2] The adsorption characteristics and physical properties of the Xerogel have been described elsewhere.[11,12]

The deuteron relaxation data were obtained at 9.2 MHz using pulse nuclear magnetic resonance techniques. A Varian Model V-4013A 12-in. high-resolution electromagnet equipped with superstabilizer was used. The nmr pulsed spectrometer was constructed in the School of Chemical Sciences Laboratory and is similar in design to one described previously.[13] Signal averaging was accomplished using a Biomation transient recorder Model 610 and a 10-bit, 256-word memory device. The signals were displayed on a Tektronic storage oscilloscope.

The single-coil nmr probe was especially designed for low temperatures and high stability.[14] The temperature was regulated to within ±0.2° and a range of ±1° was maintained for any given measurement.

Spin–lattice relaxation times, T_1, were measured using a 180°–τ–90° pulse sequence, with the logarithm of the magnetization being plotted as a function of τ to obtain T_1. The transversal relaxation times, T_2, were derived from the free induction decay signal following a 90° pulse. The errors in T_1 and T_2 are estimated generally to be ±5–10%.

Experimental Results

1. The CD_3OH–XOH System. In Figure 1 the proton relaxation rates are compared to the deuteron relaxation rates for two "symmetrical" systems, *i.e.*, CH_3OD–XOD and CD_3OH–XOH, respectively, at the same degree of coverage, namely $\theta = 1.7$. In spite of the fact that in the investigated temperature domain the situation for deuteron is such that $\omega_0\tau < 1$, there is a large gap between the deuteron T_1 and T_2 that cannot be accounted for by a wide distribution of correlation times. The proton T_2 data diverge increasingly from the theoretical values shown by the solid line as the temperature increases while the T_1 data fit well the upper dashed line, for which some correction with paramagnetic impurities has been introduced. The solid lines in Figure 1 were obtained for the proton resonance assuming a broad Gaussian distribution of correlation times ($\beta = 3.5$, $\bar{H} = 4$ kcal mol^{-1}) and a second moment which is one-fourth the rigid CH_3 second moment. The curvature of the theoretical proton T_2 at low temperature arises from the truncation of the distribution because at low temperature an increasing number of resonating nuclei have correlation times higher than the cut-off period. Figure 2 shows other interesting features of the deuteron T_1 and T_2 measured at three degrees of coverage. T_1 is within the experimental error independent of the surface coverage while T_2 is obviously a function of θ. In Figure 2, a theoretical T_1 has been obtained by assuming the following parameters: $\beta = 3$, $\bar{H} = 5.4$ kcal mol^{-1}, $\tau_0 = 2.9 \times 10^{-16}$ sec, and QCC = 170 kHz. The inverse of the temperature at which the minimum of T_1 should occur, namely $10^3/T$ °K, is 6.43. The average activation energy is nearly that observed for the molecular diffusion motion in the proton system but the correlation time τ_{Dt}, as it will be illustrated later in Figure 6, is approximately two orders of magnitude lower than that derived from the proton resonance study and assigned to a diffusional translation. It does not correspond to the rotation of the CD_3 group around the triad axis because the activation energy for this rotation is below 3 kcal mol^{-1}.[5,12]

It seems appropriate to suggest that τ_{Dt}, ruling the deuteron T_1, is that of a molecule tumbling in a potential well on top of an adsorption site because this motion implies the same average activation energy as diffusion, *i.e.*, that of breaking hydrogen bonds and of course the same distribution law for the activation enthalpy. Also

this motion should be coverage independent since it does not imply any cooperative effect in opposition to diffusion.[15]

In order to explain the gap between the predicted and measured proton T_2 in the "high" temperature range, as shown in Figure 1, it had been suggested that it could originate from those molecules facing a very high energy barrier for diffusion.[4] A similar explanation appears less convincing for the deuteron measurements if the suggestion that the longitudinal relaxation rate is demonstrated by a tumbling motion is accepted. There is, however, another explanation that could be proposed to explain why T_2 is appreciably lower than expected while in a region where $\omega_0\tau \ll 0.63$. It has been shown[16] that a broadening by preferred orientation can occur even though doublet splitting is not observed and for molecules adsorbed by a powdered solid. However, in the absence of such a splitting, the application of the following development has to be considered as a limiting case. Following a 90° pulse, the magnetization decays as described in the following manner, where Φ is the time independent angle between the symmetry axis of the intramolecular field gradient and the direction of the stationary magnetic field

$$M_\perp(t) = M_0 \exp(-t/T_2) \cos(\omega' t) \quad (10)$$

$$\omega' = -\left(\frac{3}{8}\right)\mathrm{QCC}(3\cos^2\Phi - 1) \quad (11)$$

If Φ is made time dependent due to molecular motion, then

$$\omega' = B(3\cos^2\Phi' - 1) \quad (12)$$

where Φ' is the angle between the static magnetic field and the normal to the surface, and where

$$B = -\left(\frac{3}{16}\right)\mathrm{QCC}(3\cos^2\Phi'' - 1) \quad (13)$$

where Φ'' is the angle between the symmetry axis of the intramolecular electrostatic field and the normal to the surface. These equations are valid if the distribution of the preferred orientations is axially symmetric about this normal.

In a powder, where Φ' has to be averaged over all possible directions

$$\langle\cos\omega' t\rangle_{AV} = \frac{1}{2}\int_0^\pi \cos[Bt(3\cos^2\Phi' - 1)]\,\mathrm{d}\cos\Phi' \quad (14)$$

Woessner, *et al.*,[16] have calculated the variation of $\langle\cos\omega' t\rangle_{AV}$ with respect to Bt. From their data, d ln $\langle\cos\omega' t\rangle_{AV}$/d Bt has been obtained for $Bt < 2.2$ (above this limit $\langle\cos\omega' t\rangle_{AV}$ changes sign) and the results are shown in Figure 3.

Now suppose that eq 10 can be approximated by

$$\ln M_\perp(t) = \ln M_0 - t/T_{2app} = \ln M_0 - t/T_{2real} + \ln\langle\cos\omega' t\rangle_{AV} \quad (15)$$

then

$$T_{2app}^{-1} = T_{2real}^{-1} - B[\mathrm{d}\ \ln\langle\cos\omega' t\rangle_{AV}/\mathrm{d}Bt] \quad (16)$$

For $Bt < 2.2$, the derivative is always negative, that is, $T_2^{-1}{}_{app}$ is therefore higher than $T_2^{-1}{}_{real}$. For D_2O adsorbed in powdered clay, Woessner observed B to be of the order of 10^3 radian-sec. Therefore in the region where [d ln $\langle\cos\omega' t\rangle_{AV}$/d Bt] $\simeq -1$, $T_2^{-1}{}_{app}$ should be much higher than $T_2^{-1}{}_{real}$.

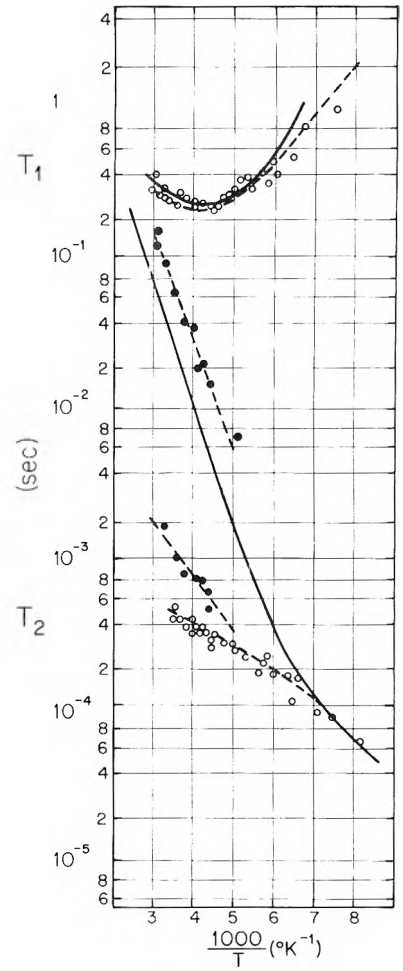

Figure 1. A comparison of proton T_1 and T_2 data in the CH_3OD–XOD system (open circles) for ref 2 to the deuteron T_1 and T_2 results (solid circles) from the symmetrical CD_3OH–XOH system at $\theta = 1.7$. The solid and dashed theoretical lines fitting the proton data are from ref 2.

For $10^3/T°K = 3.5$ (12.7°C), and assuming the derivative to be the order of −1 for adsorbed CD_3OH, B would be 749 at $\theta = 1.7$, 2480 at $\theta = 1.3$, and 4328 at $\theta = 0.8$ if T_{2real} is given by the solid line in Figure 2. For the reason already invoked, these values are rough indications, but it is interesting to observe that they decrease linearly with increasing θ (see Figure 3).

For D_2O adsorbed on clay it has been observed that B times the D_2O content was approximately constant with large concentrations of adsorbate. Both observations are compatible if B takes the form $B = a/a + b\theta$; then for low coverage of adsorbed molecules, $B \simeq 1 - (b/a)$, as in this study, while for higher adsorbed content $B \simeq a/b\theta$. Thus, the orientational effect does offer an alternative explanation for the observed T_2 in the region where $\omega\tau > 0.63$.

2. *The CH_3OD–XOD System* The temperature-dependent experimental data obtained at two degrees of coverage, $\theta = 1.7$ and 1.3, are shown in Figure 4. Measurements were also attempted for a sample $\theta = 0.8$ where T_2 was found temperature independent and equal to approximately 4.5×10^{-5} sec. However, the reliability of this latter result, and the inability to obtain corresponding T_1 values due to the shortness and weakness of the signal, limits our discussion of this system to two coverages. In general, as could be expected, the scatter of experimental

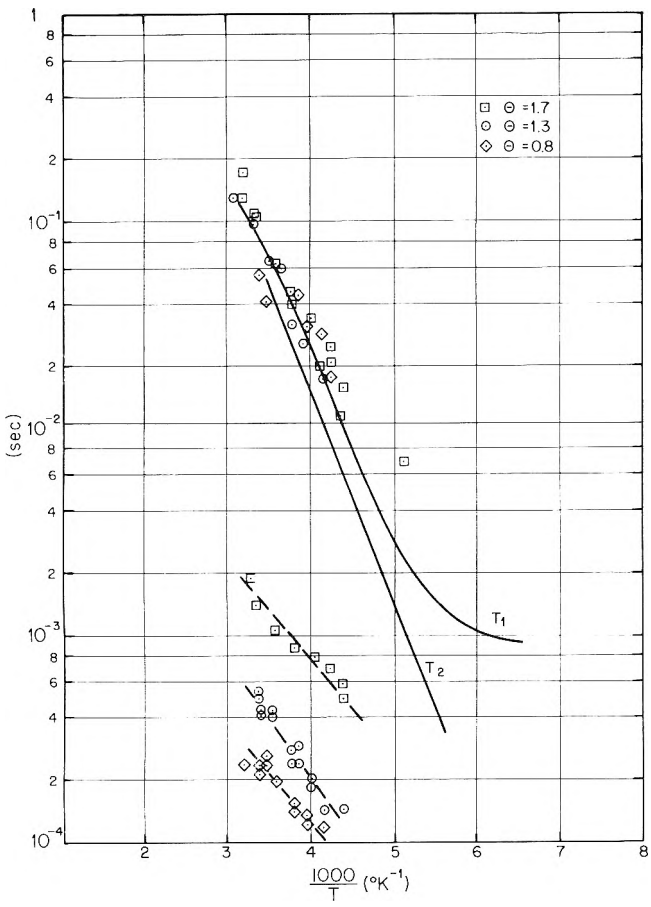

Figure 2. CD_3OH–XOH system. The deuteron T_1 and T_2 at three degrees of coverage. The solid lines are obtained through the application of eq 3 and 4 and using the average correlation time τ_{Dt} as shown in Figure 5.

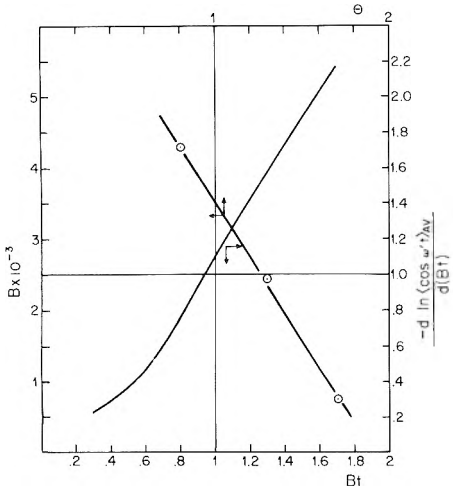

Figure 3. The variation of $d[-\ln \langle \cos \omega' t \rangle_{AV}]/d[Bt]$ as calculated from values in ref 16 and the linear decrease of B at 12.7° for low values of coverage (see text).

data for the CH_3OD–XOD system was more significant than in the CD_3OH–XOH system.

At the highest degree of coverage investigated, good agreement with the experimental T_1 and T_2 was obtained using the following parameters in eq 3 and 4: $\beta = 3.5$, $\bar{H} = 5.5$ kcal/mol, $10^3/T°K = 4.6$ at T_1 minimum, $\tau_0 = 3.15 \times 10^{-14}$ sec, and QCC = 200 kHz. This value of the quadrupole coupling constant is near that reported[5] for liquid CH_3OD, 192 ± 15 kHz. However, the transversal relaxation

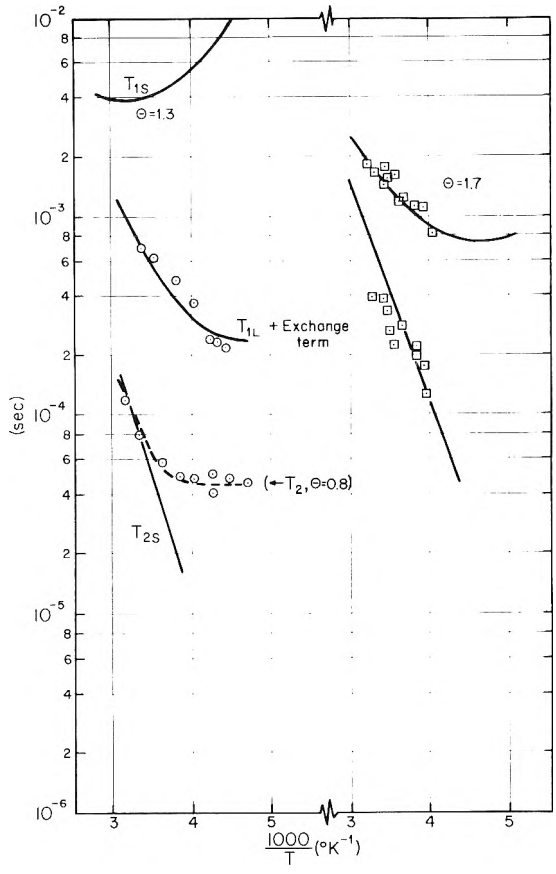

Figure 4. CH_3OD–XOD system. The deuteron T_1 and T_2 for two degrees of coverage. The solid lines for $\theta = 1.7$ are obtained using eq 3 and 4 and the average correlation time τ_{Dd} shown in Figure 5. For $\theta = 1.3$, T_{1S} and T_{2S} are obtained using τ_{De} shown also in Figure 5 (see text).

times at this degree of coverage are possibly influenced by some other competing mechanisms as suggested by the slight deviation between the observed and theoretical values. This hypothesis is supported by examination of the experimental data at a lower degree of coverage.

In the CH_3OD–XOD system at $\theta = 1.3$, the T_1 values are appreciably lower than those at $\theta = 1.7$, such that it could be assumed either that a higher QCC has to be taken into account or that the observed relaxation rate is enhanced by an exchange term corresponding to a nuclear transfer between two populations. Since it will be shown below that the QCC should decrease, the introduction of an exchange term appears more probable. The model proposed earlier[2] to explain the relaxation behavior of the proton in the symmetrical CD_3OH–XOH system will therefore be considered again.

It was assumed that the adsorbed species were distributed among two populations relaxing independently with intrinsic relaxation times T_{1S} and T_{2S}, T_{1L} and T_{2L}, S and L standing for short and long transverse relaxation times. Each population is also characterized by its fractional abundance P_S or $P_L = 1 - P_S$ and the lifetimes C_S^{-1} or C_L^{-1}. For a slow exchange between the populations ($C_i T_i \ll 1$) $i = 1, 2$, the observed variation in the magnetization with time is the sum of the exponential functions for each population taken separately

$$\frac{M_\perp}{M_0} = P_S \exp(-t/T_{iS}) + P_L \exp(-t/T_{iL}) \quad (17)$$

For the fast exchange, the observed relaxation is the

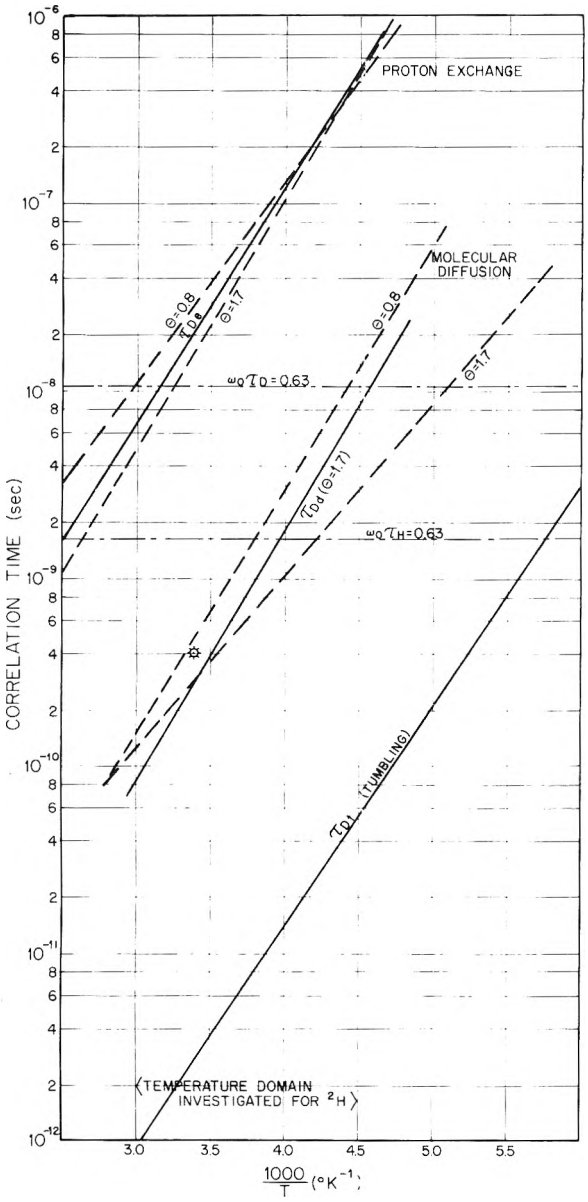

Figure 5. Correlation times obtained from the ceuteron relaxation times in the CD_3OH–XOH and CH_3OD–XOD systems as compared to those obtained for the proton resonance (ref 2). The star indicates the correlation time for the proton exchange from $CH_3OH_2^+$ to CH_3OH observed by Luz, *et al.*,[20] at 22° in the liquid state.

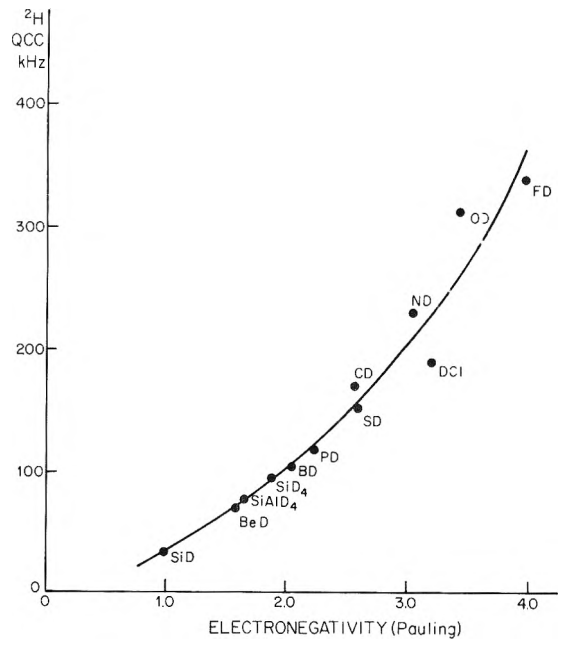

Figure 6. Deuteron quadrupole coupling constant dependence on Pauling electronegativity of elements X in X–D compounds from ref 17.

weighted average of the relaxation rates for each population

$$T_i^{-1} = P_S T_{iS}^{-1} + P_L T_{iL}^{-1} \qquad (18)$$

For intermediate exchange between the two populations, the relationships between the observed relaxation rates and the intrinsic relaxation rates are more complicated. In the proton study it was proposed that population S was composed of those methanol molecules involved in the transfer of a surface proton to neighboring absorbed species, while population L had contributions from those methanol molecules diffusing on the surface. The lifetime in these populations had been evaluated as $\sim 10^{-3}$ sec. The proton T_1 was then in the limiting case of the fast exchange (eq 18) while the proton T_2 was ruled by eq 17.

The observed deuteron T_1 and T_2 for the CH_3OD–XOD system are such as T_1^{-1} is of the order of the exchange rate between the two populations while T_2^{-1} is appreciably higher, especially at $\theta = 1.3$. At this degree of coverage, the single component behavior observed for T_2 and the values obtained for T_1 and T_2 could be explained as follows.

Suppose that in eq 17, the observed transversal relaxation rate is controlled by the intrinsic transversal relaxation rate of population S, *e.g.*, that $T_{2L}^{-1} < T_{2S}^{-1}$. The signal intensity does not permit the detection and thus the measurement of T_{2L}. To obtain an estimate for the deuteron T_{2S} and T_{1S}, it is assumed that the average correlation time is in the range of that obtained earlier for the proton exchange and that the distribution parameter β and the activation enthalpy are identical. This is the correlation time represented as τ_{De} in Figure 5. Here a deuteron is captured from the acidic surface of the deuterated silica gel by the adsorbed CH_3OD forming $CH_3OD_2^+$ and it is then exchanged with neighboring CH_3OD. Using eq 3 and 4, $\beta = 3.5$, $\bar{H} = 5.75$ kcal, $10^3/T°K = 3.15$ at T_1 min and $\tau_0 = 1.1 \times 10^{-12}$ sec, the T_{2S} and T_{1S} shown by solid lines in Figure 4 are obtained. The surprizing result is that to fit the experimental T_2 data, the QCC in population S has to be about 90 kHz. This will be commented upon further.

In order to account for the observed longitudinal relaxation time at $\theta = 1.3$ it is suggested that the rate of exchange of nuclei between populations S and L, which should not be confused with the frequency of the deuteron jumps within population S, contributes for approximately 60% to T_1. Under this condition, the remaining contribution may be accounted for by a function such as that described by eq 3 with a correlation time almost identical with that used at $\theta = 1.7$ and represented as τ_{Dd} in Figure 5. The QCC for this contribution is also 200 kHz.

The model suggested here above presents the main advantage to be coherent with the results of the proton resonance study. Yet the reason why a diffusional correlation time is obtained from deuteron T_1 and T_2 at $\theta = 1.7$ for the CH_3OD–XOD system should be explained.

If in population S, the active species for relaxation is $CH_3OD_2^+$, the lowering of the QCC could be expected since it is known that the higher the electronegativity of the atom attached to the deuteron, the higher the QCC.[17-19] Figure 6, which shows this fact graphically, allows one to evaluate the decrease of the QCC from 200 to 90 kHz as corresponding to a lowering of the electronegativity of the oxygen atom by approximately 1.0 unit. This is not unreasonable for the $CH_3OD_2^+$ structure.

It was unfortunately impossible to measure the relaxation times of the bare XOD surface because of the sensitivity. If they were known, the leveling observed in T_2 at low temperature for $\theta = 1.3$ and the unreliable values of T_2 observed for $\theta = 0.8$ might perhaps be explained.

Discussion

In the CD_3OH-XOH system, the spin-lattice relaxation rate is associated with a correlation time τ_{Dt}, whose variation is shown in Figure 5 as a function of temperature. This correlation time is appreciably different from those obtained in the proton resonance study, the latter which was considered due to molecular diffusion and a function of the degree of coverage. The correlation time τ_{Dt} is not coverage dependent within the limits of experimental error. However, the average activation enthalpy and the width of the Gaussian distribution associated with τ_{Dt} are similar to those obtained for the translational motion on the surface in the proton resonance study. For these reasons, it is suggested that τ_{Dt} is the average correlation time for a molecule tumbling on the top of an adsorption site, which provides a reasonable intramolecular relaxation mechanism.

The spin-spin relaxation rate in the CD_3OH-XOH system obtained from the decay after a 90° pulse results from the combined contributions of the correlation function associated with τ_{Dt} and of a modulation due to an additional reorientational effect that is coverage and temperature dependent. The T_2 observed in the CD_3OH-XOH system is a function of θ and the relaxation time activation energy is different from that from T_1 values. However, due to the weak signals obtained from these systems at low degrees of coverage, it is difficult to be more specific at this time about the parameters involved in discussing this important reorientation contribution. As a consequence of this, the origin of the deviation of the observed proton T_2, in the symmetrical CH_3OD-XOD system, with respect to the calculated function (see an example in Figure 1) should be reconsidered. This deviation was assigned to the existence of CH_3OD adsorbed on high energy sites and thus relaxing differently. It is possible this hypothesis is incorrect and orientational effects are more probably responsible for the observed curvature. This is a very interesting consideration indeed since it suggests that a preferred orientation exists even on the surface of an amorphous porous materials. Probably this preferred orientation is a result of some regular arrangements of surface hydroxyls and of the hydrogen bond formation between these hydroxyls and clusters of partially ordered adsorbed species.

In the CH_3OD-XOD system, the results obtained at a high degree of coverage will be considered first. There is a very good fitting between the correlation time τ_{Dd} observed at $\theta = 1.7$ and that observed for molecular diffusion in the proton resonance study. Probably the contribution of the orientational effects to the relaxation becomes much less important than in the CD_3OH-XOH system because the transversal relaxation rate is much higher. Though surprizing, the fact that a "translational" correlation time is derived from the deuteron T_1 and T_2 in this case is in agreement with similar observations by O'Reilly, *et al.*,[5] who compared the translational correlation time derived from the self-diffusion coefficient (D) obtained by the field gradient technique in CH_3OD with the rotational correlation time of OD using eq 1. If the former is expressed as $\tau = \langle l^2 \rangle / 12D$, then for $l \simeq 5$ Å, $\tau = 0.8 \times 10^{-11}$ sec while from eq 1, $\tau = 0.5 \times 10^{-11}$ sec. Moreover, the activation energies are the same within 0.1 kcal.

The reason for this agreement is probably that a molecule does not reorient appreciably in a manner to modulate the QCC unless during diffusional jumps. It might then be objected that, as shown in Figure 5, τ_{Dt}^{-1} is about 100 times higher than τ_{Dd}^{-1} and therefore that tumbling does not imply diffusional steps. The answer is then that the rotational motion accompanying diffusion and modulating the CH_3OD QCC is different, for instance, from the methyl group (as a unit) rotation about the OD axis.

At lower degree of coverage ($\theta = 1.3$) the deuteron T_1 data cannot be fitted unless an important contribution from an exchange mechanism between two populations is assumed, in agreement with the model used for the proton resonance in the symmetrical CD_3OH-XOH system. In the S population the main contribution to relaxation mechanism is the deuteron exchange between surface deuteron and CH_3OD, the "active" intermediate being $CH_3OD_2^+$. In the L population the main contribution is that of a molecular rotational diffusion. In this respect at $\theta = 1.7$, the observed relaxation effect would be almost entirely due to that of population L.

Finally, there is an exchange of nuclei between the two populations at a frequency that was suggested to be of the order of 10^3 sec^{-1} from the proton resonance study. With consideration of this model, it is possible to account for the experimental T_1 at $\theta = 1.3$ (Figure 4) by assuming that the exchange between populations contributes for approximately 60% to the relaxation rate. Also, the transversal relaxation time which, for the reason already discussed, is not influenced markedly by a orientational effect would be associated by the correlation time τ_{De} shown in Figure 5. This correlation time is in the region where the correlation times for proton exchange (in population S) were obtained previously. These correlation times at room temperature are approximately two orders of magnitude lower than that observed by Luz, *et al.*,[20] in protonated liquid methanol (see the star in Figure 5). This was discussed before,[2] but a rather unexpected consequence of the above model is that the QCC that has to be considered to account for the relaxation times in case of a deuteron exchange mechanism is markedly lower than that used for the neutral molecule. At $\theta = 1.3$ in the CH_3OD-XOD system, the QCC used to calculate the linear variation of T_2 in Figure 3 is approximately 90 kHz while a value of 200 kHz was used for the neutral adsorbed species. It seems appropriate to suggest that this strong decrease of the quadrupole coupling constant is associated with the presence in the "S" population of $CH_3OD_2^+$ intermediates. Figure 6, which points out that the deuteron quadrupole coupling constant increases markedly with Pauling's electronegativity of the atom to which the deuteron is attached, suggests that the electronegativity of the

oxygen decreases by approximately one unit in our system. That this is reasonable is seen from results in comparable examples[17] where the deuteron QCC changes considerably with the presence of ionic species, *e.g.*, in liquid ND_3 QCC is 282 kHz,[21] while the QCC of ND_4^+ is of the order of 180 kHz.[22] If the above interpretation of T_2 is correct, a measurement of the QCC of adsorbed species would be of considerable interest in acid catalysis.

Acknowledgments. The authors wish to thank Professor J. Jonas for the use of the pulse spectrometer and his cooperation in the use of various facilities. M. I. C. wishes to acknowledge the continuous support of Glaverbel (Belgium) and the suggestion of Professor Plumat to undertake the study of the interaction of methanol and silica surfaces.

References and Notes

(1) This work was supported in part by the National Science Foundation under Grant GP 28268X.
(2) M. I. Cruz, W. E. E. Stone, and J. J. Fripiat, *J. Phys. Chem.*, **76**, 3078 (1972).
(3) A. Abragam, "Principles of Nuclear Magnetism," Clarendon Press, Oxford, 1961.
(4) H. A. Resing, *Advan. Mol. Relaxation Processes*, **1**, 109 (1967).
(5) D. E. O'Reilly and E. M. Peterson, *J. Chem. Phys.*, **55**, 2155 (1971).
(6) E. Goldammer and H. G. Hertz, *J. Phys. Chem.*, **74**, 3734 (1970).
(7) Y. Lee and J. Jonas, *J. Chem. Phys.*, **57**, 4233 (1972).
(8) H. Pfeifer, "NMR Basic Principles and Progress," Vol. I, Springer-Verlag, New York, N. Y., 1972, p 55.
(9) D. E. Woessner and B. S. Snowden, Jr., *J. Colloid Interface Sci.*, **34**, 290 (1970).
(10) M. J. Tait, S. Ablett, and F. W. Wood, *J. Colloid Interface Sci.*, **41**, 594 (1972).
(11) M. I. Cruz, K. Verdinne, J. Andre, and J. J. Fripiat, *An. Quim.*, **69**, 895 (1973).
(12) M. I. Cruz, L. Van Cargh, and J. J. Fripiat, *Bull. Cl. Sci. Acad. Roy. Belg.*, **58**, 439 (1972).
(13) J. Jonas, T. E. Bull, and C. A. Eckert, *Rev. Sci. Instrum.*, **41**, 1240 (1970).
(14) M. A. Vannice, M. Boudart, and J. J. Fripiat, *J. Catal.*, **17**, 359 (1970).
(15) J. J. Fripiat and H. Van Damme, submitted for publication.
(16) D. E. Woessner and B. S. Snowden, Jr., *J. Chem. Phys.*, **50**, 1516 (1968).
(17) B. M. Fung and Y. Wei, *J. Amer. Chem. Soc.*, **92**, 1497 (1970).
(18) S. Z. Merchant and B. M. Fung, *J. Chem. Phys.*, **50**, 2265 (1969).
(19) P. L. Olympia, I. Y. Wei, and B. M. Fung, *J. Chem. Phys.*, **51**, 1610 (1969).
(20) Z. Luz, D. Gill, and S. Meiboom, *J. Chem. Phys.*, **30**, 1540 (1959).
(21) P. Thaddeus, L. C. Krisher, and P. Cahill, *J. Chem. Phys.*, **41**, 1542 (1964).
(22) R. R. Knispel, H. E. Petch, and M. M. Pintar, *J. Chem. Phys.*, **56**, 676 (1972).

Secondary Effects Due to the Presence of Sulfur Hexafluoride in Hydrocarbon Radiolysis

J. Niedzielski* and J. Gawlowski

Laboratory of Radiochemistry and Radiation Chemistry, Warsaw University, 02-089 Warsaw, Poland *(Received June 25, 1973)*

SF_6, used as an electron scavenger in the radiolysis of gaseous ethylene and propane, is found to decompose with a yield close to the yield of electrons. The products of SF_6 decomposition do not compete with parent molecules for electrons. The radiolysis of gaseous ethylene–*cis*-2-butene–1,3-butadiene–SF_6 mixtures reveals that secondary products, derived from SF_6, react with butadiene and act as chain carriers of cis–trans isomerization. Both processes involve the same radical species. A free-radical mechanism is established on the basis of photoelectron and vacuum-uv photolysis experiments.

Introduction

We have recently reported some preliminary results on the secondary reactions, due to the presence of SF_6, used as an electron scavenger in the radiolysis of gaseous ethylene.[1] These reactions led to the decrease in the yields of higher unsaturated hydrocarbons, in particular of 1,3-butadiene. A similar observation has been reported in the radiolysis of liquid ethane.[2] It was suggested in both papers that the products, resulting from the decomposition of SF_6^- ions undergoing neutralization, are responsible for the effect.

On the other hand, there are many data in the literature on the radiation-induced cis–trans isomerization of olefins in the gas[3-5] and liquid phases.[6,7] Negative SF_6^- ions and SF_5 radicals have been suggested as the chain carriers. We present here evidence that both the decrease in the yields of olefins and cis–trans isomerization are due to processes involving the same intermediary radical species derived from SF_6, most probably SF_5 radicals.

Experimental Section

Materials. All hydrocarbons, ethylene, propane, *cis*-2-butene, and 1,3-butadiene, were Fluka puriss. grade. They were rigorously purified by gas chromatography before use. Matheson sulfur hexafluoride was used after trap-to-trap vacuum distillations.

Vacuum-Ultraviolet Photolyses. Resonance lamps, operated with a high-frequency discharge from a 22.7-MHz high-frequency power supply, were used. The lamp filled with 10% H_2 in argon at a total pressure of 1 Torr emits Lyman emission (1216 Å, 10.2 eV).[8] The lamp was fitted with a lithium fluoride window and a ballast volume of about 250 ml to freeze out the impurities during operation of the lamp.[9] Lamp intensities, measured by NO acti-

nometry, using a 200-ml cell equipped with a pair of rectangular 4 × 10 cm nickel electrodes positioned 3 cm apart and used in conjunction with a Unipan nanoammeter, were in the range 5×10^{11}–5×10^{12} quanta sec^{-1}.

The Xe lamp was fitted with a sapphire window which eliminates the 1295-Å resonance line and transmits only the 1470-Å line. The lamp was provided with a titanium getter assembly similar to those described in the literature.[10] Ethylene was used as a chemical actinometer, based on the quantum yield of acetylene formation 0.9.[11] Lamp intensities were of about 10^{12} quanta sec^{-1}.

The vacuum system and 200-ml photolysis cell were mercury free. All experiments were performed at ambient temperature.

Photoelectrons. A photocell constructed from a Pyrex tube, fitted with a titanium wire anode of 1-mm diameter in the center and an aluminum photocathode made from 3 × 10-cm foil, positioned 2 cm apart, was used. Photoelectrons were generated at the cathode by the action of ultraviolet light from a medium-pressure mercury lamp. A 0.5 cm thick filter of 2 *M* aqueous solution of CH_3COONa was used to eliminate light below *ca.* 2400 Å; 10 V voltage was applied to the cell electrodes during experiments.

Radiolysis. Dosimetry, irradiation, and gas chromatographic procedures have been previously described.[12] All experiments were conducted at room temperature to about 0.1% conversion.

Results

Radiolysis. The yields of radiation-induced cis–trans isomerization of 3.3% *cis*-2-C_4H_8 + 0.5% SF_6 in ethylene are shown in Table I, along with the yields obtained in the presence of different scavengers. The dependence of the yield of isomerization on the presence of 1,3-butadiene, added to ethylene–*cis*-2-butene–SF_6 mixtures, is presented in Figure 1.

The dependence of SF_6 concentration upon dose is shown in Figure 2. From the slope of the straight line, seen in this figure, $-G(SF_6) = 3.65 \pm 0.2$ may be inferred. The effects of O_2 and NH_3 on the decomposition of SF_6 in irradiated ethylene and propane are shown in Table II. Neither of the scavengers used has any appreciable effect.

Photoelectrons. The yield of cis–trans isomerization of pure *cis*-2-butene subjected to the action of photoelectrons at 2.4 Torr was found to be 1.5 molecules per electron. The total charge collected was 3.8×10^{-5} C. A nearly twofold increase was observed upon addition of 8% SF_6 to *cis*-2-C_4H_8 at the same total pressure, the yield being then equal to 2.75 molecules per electron. The total charge collected in this experiment was 2.5×10^{-5} C.

Vacuum-Uv Photolysis. (*a*) *10.2-eV Photons.* The yield of cis–trans isomerization of pure *cis*-2-C_4H_8 photolyzed at a pressure of 0.9 Torr was $M/N^+ < 3$ molecules per ion pair (the limit of detection under the experimental conditions). Photolysis times were about 40 min in duration, equivalent to about 0.05% conversion.

In the presence of 8% SF_6 in *cis*-2-C_4H_8 (other experimental conditions being unchanged) the yield of isomerization was greatly enhanced, $M/N^+ = 540$ molecules per ion pair.

(*b*) *8.4-eV Photons.* In a mixture of 0.5% *cis*-2-C_4H_8 in SF_6 irradiated at a pressure of 20 Torr for 20 min about 20% of the *cis*-2-butene underwent isomerization. When argon was used instead of SF_6 the yield of isomerization was greatly reduced, the conversion of cis isomer being less than 0.05%.

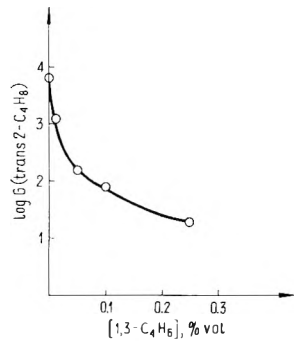

Figure 1. Radiolysis of 3.2% *cis*-2-butene + 0.5% SF_6 in ethylene in the presence of 1,3-butadiene; total pressure 200 Torr, dose absorbed 0.11 Mrad. Dependence of *G*(*trans*-2-butene) on the concentration of butadiene.

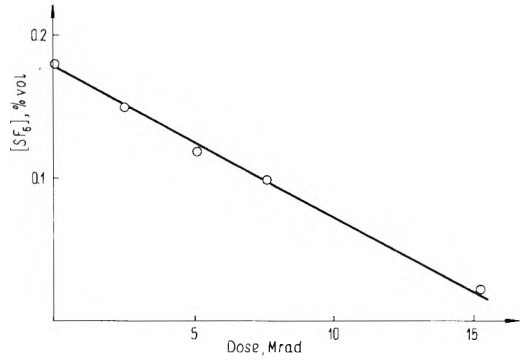

Figure 2. Radiolysis of ethylene at 300 Torr in the presence of SF_6. Dose dependence of SF_6 concentration.

TABLE I: γ Radiolysis of Ethylene + 3.3% *cis*-2-Butene + 0.5% SF_6. Dependence of *G* (isom) on the Presence of Additives[a]

	Additive concn, mol %							
NH_3	...	0.5	2	...	...	...	1.9	...
O_2	...	...	...	0.9	...	...	...	0.7
NO	...	...	...	...	2.2	...	...	...
1,3-C_4H_6	...	...	...	...	...	0.1	0.1	0.1
G (isom)	6700	6650	6480	30	<3	77	63	8

[a] Total pressure 200 Torr, dose absorbed 0.11 Mrad, dose rate 0.44 Mrad hr^{-1}.

Discussion

Effect of Butadiene on Butene Isomerization. We have previously established that 1,3-butadiene, formed as a product of ethylene radiolysis as well as that purposely added to ethylene (3×10^{-3}%) before irradiation, is consumed entirely in the presence of SF_6.[1] The present results shown in Table I and Figure 1 indicate that the presence of butadiene greatly reduces the yield of cis–trans isomerization. This effect is apparently due to the capture by butadiene of isomerization catalysts—intermediary species formed in the presence of SF_6. This may be taken as evidence that both secondary effects due to the presence of SF_6, *i.e.*, the catalysis of isomerization and the reduction in the yields of some unsaturated hydrocarbons, involve the same reactive species derived from SF_6.

Therefore from now on we will be concerned mainly with the elucidation of the mechanism of isomerization, this process being easier to observe.

In the presence of radical scavengers such as O_2 and NO the yield of cis–trans isomerization is markedly reduced. Thus, a radical mechanism of isomerization may be assumed, involving the reversible addition of radical species to *cis*-2-butene. Such a mechanism was originally proposed by van Ingen and Cramer in their study of liquid pentenes.[7] The neutralization of negative SF_6^- ions was assumed to involve dissociation, yielding SF_5 radicals, subsequently adding to the double bond of an olefin. Relating this mechanism to butenes rather than to pentenes, the following sequence of reactions is proposed.

$$RH^+ + SF_6^- = R + HF + SF_5 \quad (1)$$

$$SF_5 + cis\text{-}2\text{-}C_4H_8 = SF_5C_4H_8 \quad (2)$$

$$SF_5C_4H_8 = SF_5 + trans\text{-}2\text{-}C_4H_8 \quad (3)$$

Our results may well be accounted for by this mechanism except for the effect of ammonia which was found to inhibit the yield of isomerization of liquid 2-pentene, whereas it has no effect on this yield in our experiments, as may be seen in Table I.

SF_5 radicals are known to react with ethylene.[13]

$$SF_5 + C_2H_4 = SF_5C_2H_4 \quad (4)$$

In the system C_2H_4–3.2% *cis*-2-C_4H_8–SF_6, reaction 4 probably competes with reaction 2 for SF_5. The high value for G(isom) clearly indicates that reaction 2 is a few orders of magnitude faster than reaction 4.

The inhibiting effect of 1,3-butadiene on the isomerization as well as the elimination of butadiene from the radiolysis products seems also to be due to the scavenging of SF_5 radicals.

$$SF_5 + 1,3\text{-}C_4H_6 = SF_5C_4H_6 \quad (5)$$

On the assumption of this mechanism the rough kinetic treatment (neglecting the changes in butadiene concentration as the radiolysis proceeds) leads to the relationship shown in Figure 2. The values of k_5 and k_2 are approximately of the same order and can be shown to be at least 10^4 times greater than k_4, *i.e.*, equal to about 10^8 M^{-1} sec^{-1}, based on the value $k_4 = 1.6 \times 10^4$ M^{-1} sec^{-1}.[13]

A free-radical mechanism has also been advanced in two studies which have been reported on the isomerization of gaseous 2-butene. Radical catalysts were CH_3S[14] and SH,[15] respectively. In both cases the inhibiting effect of butadiene has been observed. The value for the rate constant of CH_3S addition to butadiene determined by Graham and Soltys is 6.9×10^7 M^{-1} sec^{-1} which is very close to our estimate for k_5.

The radical mechanism disagrees, however, with Hummel's suggestions that the cis–trans isomerization is due to the interaction of negative SF_6^- ions with the double bond of an olefin.[3] From now on the major effort in this paper will be directed at establishing the correctness of a free-radical mechanism. To this end the photoelectron and vacuum-uv photolysis experiments have been carried out.

Radical Mechanism of Isomerization. Photoelectrons ejected from an aluminum cathode are expected to attach to SF_6 molecules, forming negative SF_6^- ions, drifting to the anode upon the application of an electrostatic field. Applying the electric field at X/P of about 0.7 V cm^{-1} $Torr^{-1}$ at the cathode, and assuming a mean electron energy of 0.072 eV,[16] an average electron drift velocity of 4×10^6 cm sec^{-1},[16] and a rate coefficient of electron attachment to SF_6 of 2.2×10^{-7} cm^3 $molecule^{-1}$ sec^{-1},[17] we obtain the mean path of free electrons of approximately 0.005 cm. Thus, electrons drift practically the whole distance between the cathode and anode as SF_6^- ions under our experimental conditions. The mean lifetime of a negative ion (*i.e.*, drift time between cathode and anode) is given by $\tau_D = d^2/\mu V$, where d is the cathode–anode separation distance, μ is the negative ion mobility, and V is the voltage applied. Taking a mobility of approximately 200 cm^2 V^{-1} sec^{-1} for negative ions at 2.4 Torr (based on $\mu_0 = 0.57$ cm^2 V^{-1} sec^{-1} for SF_6^- at 760 Torr, 273°K[18]) gives $\tau_D = 2 \times 10^{-3}$ sec. This has to be compared with the mean negative ion lifetime in the radiolysis experiments equal, at the dose rate reported in Table I, to $\tau_r = 4 \times 10^{-3}$ sec (the ion recombination rate constant for SF_6^- taken as equal to *ca.* 10^{-6} cm^3 ion^{-1} sec^{-1}[19]). It follows that taking into account the differences in butene concentration in both experiments the number of collisions which SF_6^- undergoes with butene molecules is about six times less in the photoelectron experiment than in radiolysis. If the initiator of isomerization were a negative ion, the presence of SF_6 should lead to the increase in the yield of trans isomer in the photoelectron experiment up to a value of *ca.* 250 molecules per electron. In fact, the increase observed is inappreciable—less than twofold (from 1.5 to 2.75 molecules per electron) as compared with more than two orders of magnitude greater increase caused by irradiation with 10.2-eV photons.

This observation is inconsistent with Hummel's mechanism, assuming that SF_6^- is directly responsible for the catalytic effect. The electrons formed in the photoionization of *cis*-2-C_4H_8 would be scavenged by SF_6, and the SF_6^- ions would ultimately undergo neutralization with the less reactive breed of positive ions, derived from $C_4H_8^+$. This would be a process analogous to reaction 1. In photoelectron experiments neutralization of negative SF_6^- ions on the electrode rather than in the body of the gas may change the nature of the neutralization process, thus suppressing the formation of SF_5 radical.

A slight increase in the yield of geometric isomer upon addition of SF_6 to *cis*-2-butene in photoelectron experiments may be due to the inhomogeneity of electrostatic field applied in our reaction cell. Some contribution may also be due to the dissociative attachment of higher energy electrons to SF_6[20]

$$SF_6 + e = SF_5^- + F \quad (6)$$

Radical ions SF_5^- neutralized on the anode may yield species catalyzing the isomerization.

Finally, the ionic mechanism is inconsistent with the observation that photolysis of *ca.* 0.5% *cis*-2-C_4H_8 in SF_6 with 8.4-eV photons leads to very efficient isomerization. At this photon energy no ionization is possible in the system, I.P.(*cis*-2-C_4H_8) = 9.13 eV, I.P.(SF_6) = 19.3 eV.[21] This may well be conclusive evidence for a radical mechanism.

Decomposition of SF_6. The secondary radical intermediates, catalyzing the isomerization, are expected to be formed in neutralization of SF_6^-. It is commonly assumed that the mechanism of such neutralization involves dissociation as in reaction 1.[19] According to some authors, however, an alternate reaction 7 is also possible.[22]

TABLE II: Dependence of $-G(SF_6)$ on the Presence of Additives[a]

Ethylene		Propane	
Additive	$-G(SF_6)$	Additive	$-G(SF_6)$
...	3.65 ± 0.2	...	4.4 ± 0.4
0.5% O_2	3.4 ± 0.4	2% NH_3	4.4 ± 0.4
2% NH_3	4.1 ± 0.4		
2% NH_3 + 0.5% O_2	3.9 ± 0.4		

[a] Hydrocarbon pressure 300 Torr; initial concentration of SF_6 0.2%. Dose absorbed 6 Mrads, equivalent to about 50% conversion of SF_6.

$$RH^+ + SF_6^- = RH + SF_6 \quad (7)$$

To assess the contribution of these two reactions the yields of radiolytic decomposition of SF_6 in ethylene were determined. The yield depends linearly upon dose as demonstrated in Figure 2. It indicates that the products of SF_6 decomposition do not compete with SF_6 for electrons. The value $-G(SF_6) = 3.65 \pm 0.2$ corresponds well with $G_{electron} = 3.92$, based on $W(C_2H_4) = 25.5$ eV.[23] It is noted in Table II that $-G(SF_6)$ is unaffected by the presence or absence of the additives O_2 and NH_3. The determination of $-G(SF_6)$ in irradiated propane gives also the value very close to that of the yield of electrons: $-G(SF_6) = 4.4 \pm 0.4$, $G_e = 4.22$, based on $W(C_3H_8) = 23.7$ eV.[24]

Thus, it may be concluded that independent of the nature of the hydrocarbon, and the presence of scavengers, ion-ion neutralization of SF_6^- leads to the dissociation of excited neutral molecules of SF_6, most probably according to reaction 1.

Reactions of SF_5 Radicals. The identity of the radical intermediate acting as the chain carrier of isomerization and scavenging unsaturated hydrocarbons is not certain. Even though the choice of SF_5 species seems to be obvious, it should be pointed out that we lack definite proof. We could not unambiguously establish the occurrence of radiolysis products of the type RSF_5 or S_2F_{10}. Moreover, the occurrence of either reaction 8 or 9 in the radiolysis of ethylene may be rejected on the ground that the decrease in the yields of products resulting from the reactions of primary radicals CH_3 and C_2H_5 when SF_6 is added is much less than that expected on the basis of SF_6 decomposition.[25] Thus, the fate of the products derived from SF_6 remains unknown.

$$R + SF_5 = RSF_5 \quad (8)$$

$$R + SF_5C_2H_4 = SF_5C_2H_4R \quad (9)$$

Conclusions

(1) SF_6 used as an electron scavenger in the radiolysis of hydrocarbons undergoes decomposition upon neutralization of SF_6^- ions with a yield close to that of electrons.

(2) The products of SF_6 decomposition do not compete with the parent molecule for electrons.

(3) Radicals derived from SF_6, most probably SF_5, act as catalysts for cis-trans isomerization.

(4) The same radicals reduce the yields of some unsaturated hydrocarbons (in particular of 1,3-butadiene) in the radiolysis of ethylene. This is probably true in the case of other hydrocarbons. Thus, care should be taken not to overestimate the contribution of ion neutralization processes on the basis of the observed effect of SF_6 on radiation yields.

Acknowledgments. We should like to thank Professor J. Kroh of Lódź Institute of Radiation Chemistry for permission to use the cobalt source. The assistance of Miss D. Brzegowska in some of the experiments is deeply appreciated.

References and Notes

(1) J. Niedzielski and J. Gawlowski, *Int. J. Radiat. Phys. Chem.*, **5**, 239 (1973).
(2) P. T. Holland and J. A. Stone, *Can. J. Chem.*, **48**, 3277 (1970).
(3) R. W. Hummel, *Nature (London)*, **218**, 1050 (1968).
(4) J. Gawlowski, J. Niedzielski, J. Sobkowski, and A. Zechowska, *Radiat. Effects*, **11**, 85 (1971).
(5) L. W. Sieck, S. G. Lias, L. Hellner, and P. Ausloos, *J. Res. Nat. Bur. Stand.*, **76A**, 115 (1972).
(6) R. B. Cundall and W. Tippett, *Advan. Chem. Ser.*, **No. 82**, 387 (1968).
(7) J. W. F. van Ingen and W. A. Cramer, *J. Phys. Chem.*, **74**, 1134 (1970).
(8) H. Okabe, *J. Opt. Soc. Amer.*, **54**, 478 (1964).
(9) J. R. McNesby and H. Okabe, *Advan. Photochem.*, **3**, 157 (1964).
(10) R. Gorden, Jr., R. E. Rebbert, and P. Ausloos, *Nat. Bur. Stand., Tech. Note*, 496 (1969).
(11) G. G. Meisels and T. J. Sworski, *J. Phys. Chem.*, **69**, 2867 (1965).
(12) J. Niedzielski and J. Gawlowski, *Nukleonika*, **15**, 531 (1970).
(13) H. W. Sidebottom, J. M. Tedder, and J. C. Walton, *Trans. Faraday Soc.*, **65**, 2103 (1969).
(14) D. M. Graham and J. F. Soltys, *Can. J. Chem.*, **47**, 2719 (1969).
(15) G. J. Collin and P. M. Perrin, *Can. J. Chem.*, **50**, 2400 (1972).
(16) L. G. Christophorou, "Atomic and Molecular Radiation Physics," Wiley-Interscience, New York, N. Y., 1971; the values cited refer to ethylene, no data for butenes being available.
(17) K. G. Mothes and R. N. Schindler, *Ber. Bunsenges. Phys. Chem.*, **75**, 938 (1971).
(18) E. W. McDaniel and M. R. C. McDowell, *Phys. Rev.*, **114**, 1028 (1959).
(19) G. R. Freeman, *Radiat. Res. Rev.*, **1**, 1 (1968).
(20) W. M. Hickam and R. E. Fox, *J. Chem. Phys.*, **25**, 642 (1956).
(21) V. I. Vedeneyev, L. V. Gurvich, V. N. Kondrat'yev, V. A. Medvedev, and J. L. Frankevich in "Bond Energies, Ionisation Potentials and Electron Affinities," Edward Arnold, London, 1966.
(22) K. Shinsaka and S. Shida, *Bull. Chem. Soc. Jap.*, **43**, 3728 (1970).
(23) R. M. Leblanc and J. A. Herman, *J. Chim. Phys.*, **63**, 1055 (1966).
(24) T. A. Stoneham, D. P. Ethridge, and G. G. Meisels, *J. Chem. Phys.*, **54**, 4054 (1971).
(25) J. Gawlowski and J. Niedzielski, *Int. J. Radiat. Phys. Chem.*, in press.

Spur Recombination and Diffusion Processes in Pulse Irradiated Inorganic Glasses

Aaron Barkatt,* Michael Ottolenghi, and Joseph Rabani

Department of Physical Chemistry, The Hebrew University, Jerusalem, Israel *(Received February 20, 1973; Revised Manuscript Received August 30, 1973)*

Pulse radiolysis studies are carried out in pure and doped metaphosphate, borate, and silicate glasses in the range between 80 and 315°. The observed decay patterns are shown to be due to the recombination of ions, holes, and electron centers, within spurs. The time dependence of the fraction of surviving radicals is in good agreement with the empirical expression $F(t) = \exp(k_s/\alpha)\ \mathrm{erfc}(k_s t/\alpha)^{1/2}$ (where α is a constant and k_s is the diffusion-controlled recombination rate constant) predicted by Rzad, *et al.*, for systems undergoing spur recombination processes. Differences of several orders of magnitude among the diffusion coefficients of the various ions and centers explain the large variations in the rates of the corresponding diffusion-controlled electron-transfer reactions in glasses. The possibility of calculating relative diffusion coefficients in glasses from the annihilation data is discussed. Our results indicate that the diffusion coefficient of Mn^{3+} is $(3 \pm 1) \times 10^3$ higher than that of Cd^+ in the temperature range 80–240°.

Introduction

The effects due to the nonhomogeneous initial distribution of the primary irradiation products in photochemistry and radiation chemistry have been the subject of considerable experimental and theoretical work. The terms "cage" and "spur" are correspondingly used in photo- and radiation chemistry to denote the isolated volume elements in which the primary irradiation products are generated in sets. Phenomenologically both effects are indirectly reflected through the dependence of the final irradiation yields on the presence of high concentrations of an external scavenger, capable of competing efficiently with radical recombinations within the cage or the spur. A more powerful tool in the experimental investigation of such recombinations involves pulse irradiation techniques, leading to the direct observation of the initial, nonhomogeneous, radical decay processes. Very short pulses, combined with nanosecond and subnanosecond detection systems, are necessary in order to follow the initial decays in ordinary liquids at room temperature. In highly viscous liquids or glasses radical diffusion rates are slowed by several orders of magnitude so that spur and cage reactions may occur within the more accessible microsecond, millisecond, and even second ranges. Unfortunately, time-dependence data attributable to such nonhomogeneous processes are still limited. However, while no direct observation of a photochemical cage recombination has been reported yet, a few cases of transient decay processes in radiation chemistry have been ascribed to radical recombination within spurs. Some of these studies concern trapped or solvated electrons (e_s^-). Thus, Thomas and Bensasson[1] and Buxton[2] attribute the initial decay of e_{aq}^- observed in the nanoseconds range, after firing a 5-nsec electron pulse in liquid water, to spur recombination processes. Various investigators,[3-5] working in low-temperature aqueous glasses, observed nonhomogeneous electron decay reactions which, being slowed by the high viscosities of the system, occur in time ranges between $\simeq 10^{-5}$ and $\simeq 10$ sec. A similar observation was also reported by Taub and Gillis in the case of the initial decay of e_s^- in squalane at $-140°$.[6] Nonhomogeneous decays of irradiation products other than solvated electrons were also reported. These involve CH_3 or C_2H_5 in 3-methylpentane,[7] TPA^+ and TPA^- in TPA (triphenylamine),[8] biphenyl and anthracene radical ions in hydrocarbons,[9] as well as the intermediates in the pulse radiolysis of polystyrene.[10]

In the present work we have submitted various inorganic glasses to pulse irradiation, carrying out a quantitative analysis of radical recombination kinetics. We have previously[11] pulse-irradiated sodium metaphosphate glasses observing a series of consecutive decays in the microsecond range, due to transients attributed to electron excess and electron deficiency (hole) centers. It was concluded however that such decays represent unimolecular reactions of the corresponding centers with the phosphate matrix rather than intercenter recombination processes. Thus, the observed decay patterns did not seem to be relevant to the problem of the primary radical distribution. In the present work we have doped metaphosphate, silicate, and borate glasses with metal-ionic electron and hole scavengers (M) capable of preventing the formation of all centers by reacting with their mobile ("dry") precursors.[11] Due to the very high efficiency of the scavenging process, it was reasonable to assume that the primary (mobile) electron and hole species react with M close to their initial location, yielding a nonhomogeneous distribution of the corresponding reduced [M(red)] and oxidized [M(ox)] species. We therefore expected that the annihilation reactions of the scavenging products (such as M(ox) + M(red) → 2M) should reflect the initial distribution of their precursors. In addition to the interest associated with the direct observation of spur processes in radiation chemistry, the results of the present work bear also upon the mechanism of electron transfer reactions in inorganic glasses.

Experimental Section

The accelerator (operated at 5 MeV, 200 mA) and the optical analyzing system, as well as the preparation of the metaphosphate glass rods, have been previously described.[11] Borate and silicate samples were cast in the same way after melting $Na_2B_4O_7 \cdot 10H_2O$ and $Na_2SiO_3 \cdot 9H_2O$ at 1150°. The glass rods were heated and pulse irradiated in an oven illustrated in Figure 1. Temperature variations in the sample did not exceed ±1°. Before irra-

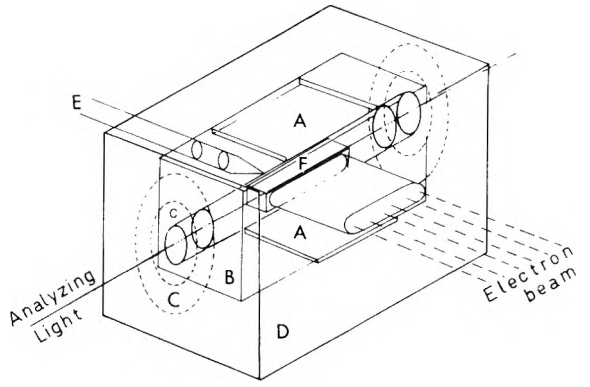

Figure 1. Oven: A, heating elements; B, copper block; C, suprasil windows and round copper slits; D, asbestos insulation; E, thermometer; F, glass sample.

diation, samples were kept for at least 1 hr at the desired temperature obtained by regulation of the voltage across the heating elements. Most experiments were carried out in the 80–315° range since at higher temperatures phosphate glasses undergo fast devitrification.

Results

(*I*) *Scavenging Efficiencies of Primary Hole and Electron Centers.* In our previous pulse radiolytic study[11] dealing with pure metaphosphate glasses at room temperature, transient absorbance changes in the 500–700-nm range were observed which could be described by the consecutive exponential decays of three spectrally distinguishable fractions (I, II, and III). After all decays, a residual permanent absorption at 500 nm (fraction IV) was left. The effects of doping the glass with characteristic electron and hole scavengers, reacting with the precursors of the various decaying species, led to the conclusion that fraction I ($\tau_{1/2}$ = 3.2 μsec) is a (solvated) electron center. Fractions II ($\tau_{1/2}$ = 0.29 msec), III ($\tau_{1/2}$ = 6.3 msec), and IV were assigned to various electron deficiency (hole) centers. Denoting the mobile precursors of the various species by X_I, X_{II}, X_{III}, and X_{IV}, simple competition schemes such as

$$\left\{\begin{array}{l} X_I \xrightarrow{k_I'} (\text{fraction I}) \\ X_I + M \xrightarrow{k_I} M(\text{red}) \end{array}\right\}$$

and

$$\left\{\begin{array}{l} X_{II} \xrightarrow{k_{II}'} (\text{fraction II}) \\ X_{II} + M \xrightarrow{k_{II}} M(\text{ox}) \end{array}\right\}$$

etc., were found to describe quantitatively the effects of [M] in decreasing the yields of each fraction and, correspondingly, in increasing the yields of the scavenging products, M(red) or M(ox). The analysis of the M concentration effects led to the scavenging-efficiency parameters $K_I = k_I'/k_I$ and $K_{II} = k_{II}'/k_{II}$ for each of the scavengers employed.[11]

In the present work, pulse irradiation experiments were carried out in a pure sodium metaphosphate (MP) glass as well as in MP doped with Cd^{2+}, Ni^{2+}, Co^{2+}, Ag^+, Pb^{2+}, and (Mn^{2+} + Cd^{2+}). (Except for Pb^{2+}, added as carbonate, the sulfates of all other cations were employed. In the case of Ag^+ identical results were obtained following the addition of Ag_2SO_4 and $AgNO_3$.) The relative scavenging efficiency parameters of the above scavengers are presented in Table I along with the concentrations

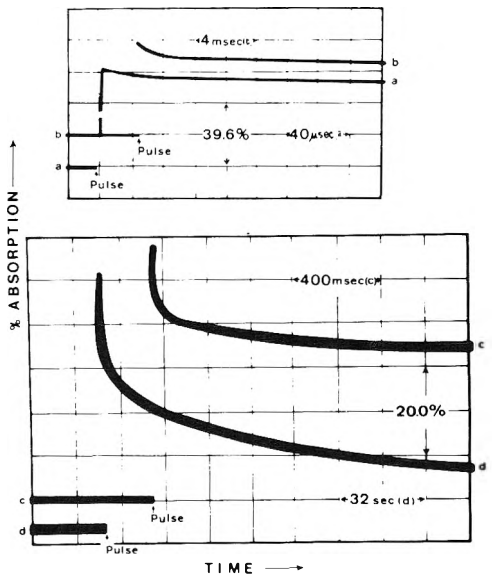

Figure 2. Oscilloscope traces at 390 nm obtained in 0.4 *m* Co^{2+} in MP at 240° with the same 1.5-μsec pulse.

TABLE I: Relative Rate Constants for Mobile Electrons (K_I, K_I*) and Holes (K_{II}*) in the Pulse Radiolysis of MP

Cation	Temp, °C	Rel rate constants,[a] *m* K_I	K_I*	K_{II}*	Scavenger concn, *m*
Ag^+	27	0.019	0.018	0.11	0.5
Ag^+	315	0.006			
Ni^{2+}	27	0.069	0.073	0.03	0.3
Co^{2+}	27	0.045	0.045	0.06	0.4
Cd^{2+}	27	0.028	0.024	>0.5	0.4
Cd^{2+}	225	0.013			
Mn^{2+}	27		0.23	0.06	0.4 (+0.2 *m* Cd^{2+})
Pb^{2+}	27	0.025	0.026	0.15	0.6
Pb^{2+}	225	0.017			

[a] K_I* and K_{II}* denote the relative rate constants values (k_I'/k_I and k_{II}'/k_{II}) obtained, correspondingly, from the analysis of the scavenger concentration effects on the yields of fractions I and II (see ref 11 for details). K_I is identical with K_I* but denotes the ratio k_I'/k_I obtained from the scavengers concentration effects on the yields of the M(red) product.

used in the present measurements. It can be seen that raising the temperature causes an increase in the scavenging efficiency. In any case, with the only exception of Cd^{2+}, which is unreactive to holes, more than 90% of the mobile electron and hole precursors are always scavenged at the ion concentrations employed. Borate and silicate glasses were doped only with Pb^{2+} (0.6 *m*). Detailed competition kinetic experiments aiming at determining *K* values in Pb^{2+} doped borates and silicates were not carried out. In analogy with the corresponding phosphate systems, it was assumed that all hole and electron precursors are totally scavenged at 0.6 *m* Pb^{2+}.

(*II*) *General Pulse Radiolysis Patterns.* Upon exposure to the electron pulse at relatively high temperatures, all glasses exhibited transient absorbance changes, extending over a time scale of several orders of magnitude (in the present work only the range between $\simeq 10^{-6}$ and 10^2 sec was scanned). Figure 2 presents a characteristic oscillogram showing the transient phenomena (attributed to the process $Co^+ + Co^{3+} \rightarrow 2Co^{2+}$) in a metaphosphate glass doped with Co^{2+}. In a pure metaphosphate glass the transient absorbance change observed at elevated temperature

(above 140°) corresponds uniquely to the decay of the 500-nm species (fraction IV). At such temperatures the decays of fractions I, II, and III are beyond the time resolution (≃2 μsec) of our pulse radiolysis system, as confirmed by the fact that the transient spectrum is maintained unchanged throughout the decay process (Figure 3a). A similar time independency of the transient spectrum (corresponding to M(ox) or M(red)) was also observed in all doped metaphosphate glasses (Figure 3b–f). (Figures 3c–f are available as supplementary material.) Special attention should be paid to the 0.4 *m* Cd^{2+}–MP system (Figure 3b) where the 290-nm decay of Cd^{+} and that of the positive holes at 500 nm show the same time dependence. Below 140°, in pure MP and in Ag^{+} doped MP, the fast reactions associated with spectral changes preceding the final annihilation process are still observable in the microsecond range (Figures 4a–b).

In the case of a pure silicate glass, the thermal annihilation of the irradiation products was followed at 313, 440, and 620 nm. These wavelengths correspond to electron and hole centers which are stable at room temperature.[12] As in the case of metaphosphate glasses, pulse irradiation at 30° is associated with transient spectral changes in the 300–650-nm range which are probably due to interconversions between various electron and hole centers (see Figure 5). We have not carried out a detailed study of such effects, but extended the pulse irradiation experiments to higher temperatures where the transient phenomena are due to the decay of the 313 electron, 440 and 620 nm (hole) bands, without being accompanied by a change in the spectrum. Under such conditions, one is uniquely following the final thermal annihilation of the irradiation centers, the initial relaxation phenomena being beyond the time resolution of the apparatus. In the case of pure borate glasses the thermal annihilation was followed in the range 500–600 nm of the single (positive hole) absorption band reported in the literature.[13] A peak around 550 nm is observed. Again the transient spectrum was maintained unchanged during the decay. It should be noted that in borate glasses we did not observe even at room temperature any initial decay process attributable to interconversions between irradiation centers. Figures 4a–l (Figures 4f–l are available as supplementary material) present the complete decay patterns for all investigated systems. A logarithmic time scale is employed to cover the entire range of the decay. In Figure 4e the measurements have been extended to the latest stages of the decay process. Such data, involving time intervals after irradiation which are too long to be observed using the pulse radiolysis detection system, were obtained by placing an irradiated glass disk in a thermostated Beckmann DB-G spectrophotometer and measuring its absorbance *vs.* time using an unirradiated sample as reference.

(III) Principal Characteristics of the Decay Patterns. The examination of the decay patterns in the various glasses showed that a general feature, characterizing all systems, is the complete insensitivity of the decay kinetics to the following operations. (1) Variations of up to a factor of 8 in the pulse intensity. Such intensity changes were accompanied only by proportional changes in the absorbance at any determinate time during the decay, *e.g.*, Figure 4e, g. (2) The accumulation of up to 100 pulses (1.5 μsec and 2500 rads each). (3) Changes in the energy of the electron beam within the 2–7 -MeV range.

In some systems the relaxation kinetics were measured at different scavenger concentrations. $[Co^{2+}]$ in MP was

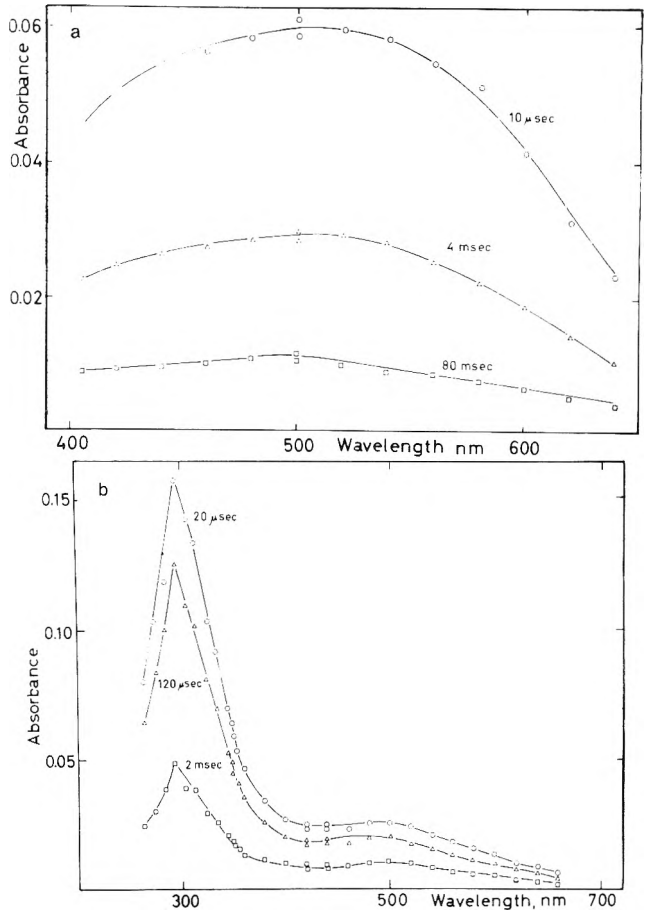

Figure 3. Absorption spectra of various glasses at high temperatures as a function of time: (a) pure MP, 315°; (b) 0.4 *m* Cd^{2+} in MP, 275°.

varied from 0.4 to 1 *m* and $[Ag^{+}]$ from 0.5 to 1.5 *m*. The concentrations of the pair Mn^{2+} + Cd^{2+} in the same glass were varied correspondingly from 0.4 and 0.2 *m* to 0.8 and 0.4 *m*. In all three sets of experiments the decay kinetics were found to be independent of the scavenger concentration.

Roughly, the main kinetic features can be summarized as follows: $\tau_{0.9}$ (the time required for a 10% drop in the absorbance) exhibits a nearly exponential time dependence, so that the decay fits neither a simple first-order nor a second-order process. Although a composite first-order characterization is formally possible, it requires not less than five arbitrarily defined first-order stages. It is also important to note (Figure 4) that the time scale over which the decay extends at a determinate temperature is substantially sensitive to the nature of the glass as well as to the presence and to the nature of the added cationic scavengers. However, the general shape of the plot is essentially identical in all cases: an initial plateau curving to a nearly linear section which finally flattens at low absorbance. The slope of the linear section relative to the initial absorbance ($s = \Delta D/(D_0 \Delta \log t)$ is for all samples in the 0.1–0.3 range.

As the temperature in a determinate glass is increased, a small increase in the initial absorbance is observed (~10–20% in MP glasses). The value of s is however essentially independent of temperature, the only temperature effect being that of shifting, almost parallelly, the whole S-shaped decay curve. In order to examine the temperature dependence of the decay rates we measured the

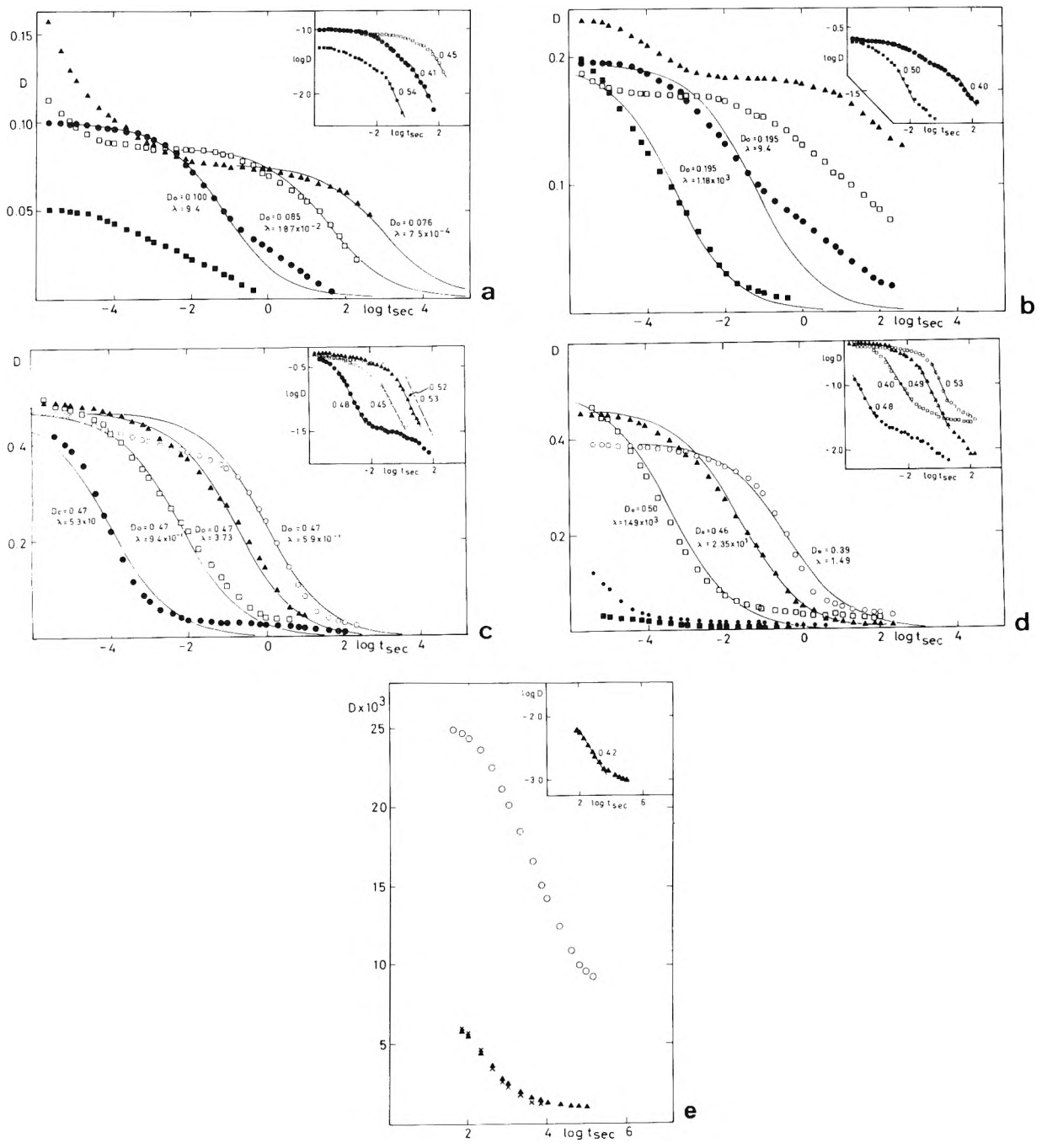

Figure 4. Optical density (D) vs. log time plots for annihilation processes at various temperatures: O, 30°; Δ, 80°; □, 140°; ●, 240°; ▲, 275°; ■, 315°. The lines were calculated according to the model of Rzad, *et al.*[18] The appropriate values for D_0 and for λ (sec^{-1}) represent the initial optical density, and the parameter λ,[18] respectively, chosen for the calculations. I, J, K, and L denote pulse intensities of the same order of magnitude (corresponding to 1.5-μsec pulses used on different days and not normalized): (a) pure MP, 580 nm, I; (b) 0.5 *m* Ag^+ in MP, 365 nm, 0.075 I; (c) pure $Na_2B_4O_7$, 550 nm, 0.5 J; (d) pure Na_2SiO_3, 440 nm, 0.2 J; (e) 0.4 *m* Mn^{2+} + 0.2 *m* Cd^{2+} in MP, 380 nm, long time scales. (D calculated for one pulse of intensity K: O, 30°, 20 pulses; Δ, 80°, 100 pulses; ×, 80°, 20 pulses).

parameter $k_{0.9} = [\ln (10/9)]/\tau_{0.9}$ for several phosphate glasses around the absorbances corresponding to 35 and 65% decay (Figure 6). Table II shows the apparent activation energies obtained from the slopes of the ln $k_{0.9}$ *vs.* $1/T$ plots. It is apparent that such slopes, increasing with temperature, can be divided into two essentially linear sections with a sharp break around t_T = 240° for all MP systems. Table II shows that the same apparent activation energies (E_a) are obtained for 35 and 65% decay. E_a is in all cases around 5 kcal/mol below the transition temperature (t_T), while it is around 40 kcal/mol above t_T. With the only exception of Pb^{2+} doped silicates, borate and silicate glasses are characterized by E_a = 5–10 kcal/mol. Up to the highest temperature of the present investigation (around 315°) we did not observe any sharp change in E_a indicative of a transition temperature for such glasses.

Discussion

(I) Annihilation Reactions and Their Assignment to Recombinations within Spurs. The annihilation processes observed in the glasses of the present work are associated with the following reactions. (1) In a pure, undoped, metaphosphate glass

TABLE II: Apparent Activation Energies for Annihilation Processes in MP Glasses

System	35% decay			65% decay		
		E_a, kcal/mol			E_a, kcal/mol	
	t_T, °C	$t < t_T$	$t > t_T$	t_T, °C	$t < t_T$	$t > t_T$
Pure MP	245	4 ± 1	30 ± 10	227	<9	30 ± 10
0.3 *m* Ni^{2+} in MP	248	5 ± 1	40 ± 10	242	5 ± 1	40 ± 10
0.4 *m* Co^{2+} in MP	234	4 ± 1	40 ± 10	232	4 ± 1	50 ± 10
0.2 *m* Mn^{2+} in MP		5 ± 1			6 ± 1	
0.4 *m* Mn^{2+} + 0.2 *m* Cd^{2+} in MP		4 ± 1			5 ± 1	

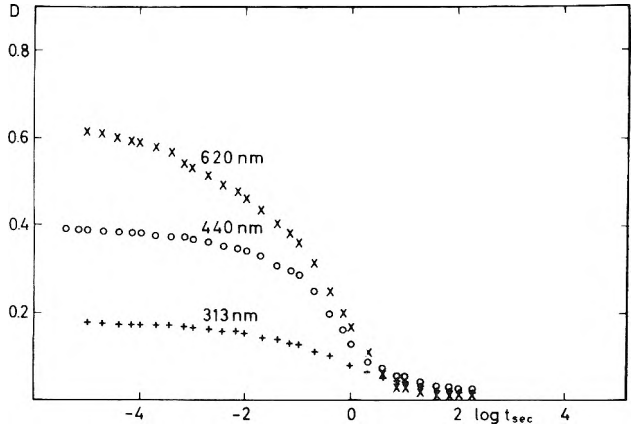

Figure 5. Decay kinetics in pure Na_2SiO_3 at 30° and pulse intensity 0.2 J at various wavelengths.

$$MP^+ + MP^- \longrightarrow 2MP$$

where MP^+ and MP^- represent correspondingly a positive hole and an electron excess center.[11] As previously discussed the process was followed at the 500-nm band of MP^+. Due to experimental difficulties we have not followed the decay of the <250 nm electron center.[14]

The corresponding processes in silicate (SI) and borate (BO) glasses ($SI^+ + SI^- \rightarrow 2SI$ and $BO^+ + BO^- \rightarrow 2BO$) were followed at the 440-nm hole absorption in the case of silicates and at the 550-nm hole band in the case of borates. (2) In doped glasses the observed decays are attributed to the following.[14] (a) $Ag_2^+ + Ag^{2+} \rightarrow 3Ag^+$, in Ag^+ doped MP glasses. (The decay was followed at the 365 nm absorption of Ag_2^+.)[11] (b) $Ni^+ + Ni^{3+} \rightarrow 2Ni^{2+}$, in Ni^{2+} doped MP glasses. (The decay was followed at the 350 nm absorption of Ni^+.) (c) $Cd^+ + Mp^+ \rightarrow Cd^{2+} + Mp$, in Cd^{2+} doped MP glasses. (The decay was followed at the 313-nm band of Cd^+ as well as at the 500-nm absorption of MP^+.) (d) $Co^+ + Co^{3+} \rightarrow 2Co^{2+}$, in Co^{2+} doped MP glasses. (The decay was followed at the 390-nm absorption of Co^+.) (e) $Cd^+ + Mn^{3+} \rightarrow Cd^{2+} + Mn^{2+}$, in MP glasses doped with both Cd^{2+} and Mn^{2+}. (The decay was followed at the 380-nm tail of the Cd^+ absorption band.) In the absence of Cd^{2+}, the annihilation reaction is due to $Mn^+ + Mn^{3+} \rightarrow 2Mn^{2+}$. The rate of this reaction was measured at 380 nm. Due to the relatively low absorbances the results are not very accurate. Values of $\tau_{0.9}$ are presented in Figure 6. The results are very similar to those in Mn^{2+}-Cd^{2+} doped glasses. (f) $Pb^+ + Pb^{3+} \rightarrow 2Pb^{2+}$, in MP, SI and BO glasses doped with Pb^{2+}. (The decay was followed within the 290-nm Pb^+ band.)

All the decays represent radical recombinations within spurs, taking place between geminate partners which are

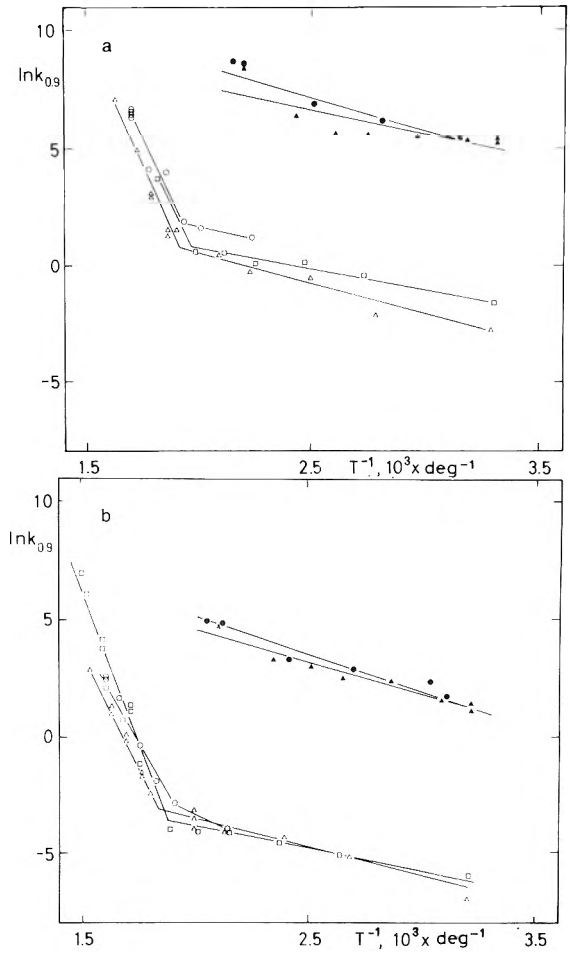

Figure 6. Arrhenius plots for the temperature dependence of the annihilation: ○, MP; △, 0.3 *m* Ni^{2+} in MP; □, 0.4 *m* Co^{2+} in MP; ●, 0.2 *m* Mn^{2+} in MP; ▲, 0.4 *m* Mn^{2+} + 0.2 *m* Cd^{2+} in MP: (a) at 35% decay; (b) at 65% decay.

inhomogeneously distributed in the medium. This conclusion is based on the following experimental observations. (1) The annihilation patterns do not obey second-order kinetics as implied for recombinations occurring between homogeneously spaced species. It is our estimate that the contribution of homogeneous (second order) recombination never exceeds 10% of the total change. In one case (Figure 4e), where careful kinetic measurements were carried out following the decay for a period of ≃30 hr, no contribution from homogeneous kinetics could be observed even after the system reached the 99% decay stage. (2) The decays are completely insensitive to variations in the pulse intensity. Contributions from homogeneous recombination processes would have easily been detected by the

present intensity variations. (3) The possibilities that one is actually observing a set of unimolecular interconversions between various centers or a multistaged decay of a single species may be correspondingly ruled out by (a) the time independency of the transient spectra throughout the decay process, and (b) the fact that the general form of the S-shaped decay curve is the same for all investigated systems, being completely independent of the specific glass, the temperature, and the nature of the decaying species.

An elementary condition for the occurrence of an efficient geminate (spur or cage) reaction is a recombination rate constant which is diffusion controlled or very close to diffusion controlled. Our observation that the apparent activation energies of the decays are only function of the medium (and in some ranges also of the temperature), without being affected by the nature of the reacting species, is entirely consistent with this requirement. DTA measurements in pure and Co^{2+}-doped metaphosphate glass show the existence of a glass transition point at 230°. This corresponds to a phosphate chain length of 35–50 monomer units.[15] It can be seen that the break in activation energies in metaphosphate at (235 ± 10)° (Figure 6) coincides with this transition temperature. Since similar breaks at the transition point are generally observed for ionic diffusion rates in glasses[16,17] this provides a further confirmation of our analysis attributing the pulse radiolysis phenomena to diffusion-controlled processes.

We should finally note that the time scale within which geminate recombinations occur is inversely proportional to the diffusion coefficients of the reacting species. Data concerning the diffusion of ions in glasses are only available for silicates.[17] At 200° ionic diffusion coefficients in such glasses are around 10^{-9} cm^2 sec^{-1} as compared with $\simeq 10^{-5}$ cm^2 sec^{-1} for ordinary liquids at room temperature. Spur processes are therefore predicted to shift from a time scale of 10^{-10}–10^{-9} sec in ordinary liquids to 10^{-6}–10^{-5} sec in silicate glasses at 200°. Roughly, this agrees with the results of the present work. We shall later return to the discussion as to why large variations in the geminate recombination rates are still observable for different pairs of reactants in the same glass and at the same temperature.

(II) Analysis of the Spur Processes. In an attempt to analyze the time dependence patterns observed in the present glass systems we first consider the data of Rzad, *et al.*, concerning the scavenging of electrons in the radiolysis of liquid hydrocarbons[18] and of aqueous solutions.[19] The effects of high scavenger concentrations, interpreted in terms of the competition between scavenging and geminate radical recombinations, were found to be described by the empirical expression

$$F(c) = A + (1 - A\sqrt{\alpha C}/[1 + \sqrt{\alpha C}]) \qquad \text{(I)}$$

$F(c)$ denotes the fraction of radicals scavenged at a scavenger concentration c, and α is an empirical parameter. A, the value of $F(c)$ measured in very dilute solutions, when no spur scavenging occurs, represents the residual yield of radicals escaping geminate recombination. In hydrocarbons, $A \simeq 0$, while in water $A \simeq 0.5$. Hummel[20] has pointed out that $F(c)$ is related to the time dependence for the rate of ion recombination (in the absence of scavenger), $f(t)$, *via* the expression

$$1 - F(c) = \int_0^\infty f(t) \exp(-k_s c t)\, dt \qquad \text{(II)}$$

Thus, since $1 - F(c)$ is the Laplace transform of $f(t)$, the latter function can be specified for a given form of $F(c)$. Rzad, *et al.*, obtained an expression for $f(t)$ using empirical expression I for $F(c)$. The fraction of radicals in a spur surviving at time t, (given by $F(t) = \int_t^\infty f(t)\, dt$ assumes in such a case (for $A = 0$) the form

$$F(t) = \exp\left(\frac{k_s}{\alpha}t\right) \operatorname{erfc}\left(\frac{k_s}{\alpha}t\right)^{1/2} \qquad \text{(III)}$$

Such a dependence was found[18] to represent quite satisfactorily the electron decay in low-temperature squalene[6] and that of the biphenylide negative ion in pulse-irradiated cyclohexane solutions of biphenyl.[9] Both I and III (with the appropriate A values) are correspondingly in fair agreement with the concentration dependence and the time dependence of the aquated electron yields as predicted by Schwarz[21] by applying the spur diffusion model to water.

In the present glass systems it is essentially impossible to verify eq I. This is due to the difficulties associated with finding a scavenger for M(ox), M(red), MP^+, MP^-, etc., which will compete with their recombination in the spurs without inhibiting their formation by reacting with the corresponding hole and electron precursors.[11] We have therefore proceeded to checking the applicability of eq III to the time-dependence observations of the present work. As pointed out previously the assumption $A \simeq 0$ is valid in the systems of the present work where, in analogy with the hydrocarbon systems of Rzad, *et al.*,[18] the observed residual yields are essentially zero. The analysis is carried out in Figures 4a–l for a few representative cases in which complete decay curves are available. (At high and low temperatures the initial and final stages of the decay are correspondingly out of our observation ranges.) The log D *vs.* log t plots, presented as inserts in the various cases, show the fulfillment of the long-time approximation of eq III[16]: $F(t) \simeq [\alpha/\pi k_s t]^{1/2}$, predicting a limiting $t^{-1/2}$ dependence of $F(t)$.

An important conclusion which can be derived from the above analysis is that spur recombination kinetic patterns are essentially the same in liquid hydrocarbons, in liquid water, and in the present inorganic glasses. Such systems widely differ in the nature of the recombining radicals, in their initial separation, in the polarity and in the viscosity of the medium, in the number of radicals in each spur, and in the number of possible spur reactions. This point has already been commented on by Balkas, *et al.*,[19] in reference to their hydrocarbon and aqueous systems, by pointing out that the solutions of the Smoluchowski equations show essentially little dependence on whether the recombination is between oppositely charged ions or between neutral radicals. Our present data are entirely consistent with such a conclusion extending it to reactions in solids between ions with varying charges of the same sign. The deviations from eq III in several systems may be due to differences in encounter-pair lifetimes among those pairs of various reactants which are initially separated by small distances.[22]

We tested the following theoretical treatments on our results: (a) the treatment by Noyes[23] based on the considerations of Chandrasekhar,[24] for a single pair of neutrals; (b) the diffusion model of Kuppermann,[25] (c) the analysis according to Mozumder[26,27] for two or ten radicals per spur.

In all cases, the theoretical calculations of concentrations *vs.* log t gave much steeper decays as compared with

the experiments. However, we are unable to rule out the possibility that the model of Mozumder might agree with our results when an appropriate distribution of radicals in the spurs is taken into account.

The large variations in the rates of annihilation unaccompanied by similar differences in activation energies among various reacting species in the same medium may seem surprising. The annihilation reactions must be diffusion controlled, otherwise the initial nonhomogeneous distribution of species would not have influenced the results, and no agreement would have been obtained with any kind of spur kinetics. Differences in rates of diffusion-controlled reactions in the same medium may arise from: (a) differences in the reaction radii and (b) differences in the diffusion rates.

(a) Differences in reaction radii are not expected to be very large among the reactants investigated here, unless we invoke tunnelling effects.[28] However, even so, the large differences which it is necessary to assume are in contradiction with the spur model. Suppose a smallest radius of reaction ~0.3 nm. In order to account for the rate of annihilation observed in the Mn^{2+} doped glasses which is 10^5-fold faster than the slowest rate observed (in Co^{2+} doped glasses), one must assume a reaction radius of >300 nm for the reaction of Mn^{3+} with Mn^{+} or with Cd^{+}. Such a reaction radius is much larger than the sizes of the spurs.

(b) The main reason for the large differences in the lifetime of the transients must be due to differences in their diffusion rates. In ordinary liquids, diffusion rates are inversely proportional to the radius of the diffusing entity, and no large differences in rates between similar ions such as Mn^{3+} and Co^{3+} are expected. This is contrary to our observations in metaphosphate glasses which imply that Mn^{3+} diffuses about 10^5-fold faster than, *e.g.*, Co^{3+}. The possibility that different ions may have very different diffusion rates in glasses with identical activation energies for the diffusion has been demonstrated by Doremus[29] who measured electrical conductivities and tracer diffusion in silica glasses. He found that the relative diffusion coefficients of Na^{+}, Li^{+}, K^{+}, and Ag^{+} ions were 1, 0.15, >0.002, and 0.08, respectively. This supports the hypothesis that the different annihilation rates in our systems are due to differences in diffusion rates. Note that the reactions $Mn^{3+} + Cd^{+} \rightarrow Mn^{2+} + Cd^{2+}$ and $Mn^{3+} + Mn^{+} \rightarrow 2Mn^{2+}$ have the same exceptionally fast rates at all temperatures. This is in agreement with the suggestion that Mn^{3+} has a relatively high rate of diffusion, as compared with all other species in the phosphate system.

The large variation in diffusion coefficients among different ions may be in part due to different degrees of association with the medium. The formation of phosphate complexes in metaphosphate glasses has been reported previously.[30] The greater the degree of association, the smaller the apparent diffusion coefficient expected. Other factors, such as the size of the diffusing species and the relation with the geometry of the matrix, are also important.

As the rate of a diffusion-controlled reaction depends on the diffusion constants of both reacting species it is not possible to obtain from our data the separate diffusion coefficients directly. In a few cases, where an ion was investigated in two separate reactions ($Mn^{3+} + Mn^{+}$ and $Mn^{3+} + Cd^{+}$, $MP^{+} + Cd^{+}$ and $MP^{+} + MP^{-}$), the relative diffusion coefficients can be calculated. From Figure 4 we find that the diffusion coefficient of Cd^{+} is smaller by a factor of $(3 \pm 1) \times 10^3$ than the diffusion coefficient of Mn^{3+} in the temperature range 80–240°. For the other ions, only upper limits can be calculated from the relative decay rates. All other diffusion coefficients are lower than that of Cd^{+}.

By the use of additional combinations of various metal ions, our method can be used for measurement of relative diffusion coefficients.

Acknowledgments. The authors are indebted to Mr. Y. Ogdan for careful operation of the linac, and to Dr. M. S. Matheson for helpful suggestions and discussions.

This research has been supported by the Central Research Fund of the Hebrew University.

Supplementary Material Available. Most of the time-independent spectra observed in our systems (Figures 3c–f) as well as most of the annihilation curves (Figures 4f–l) will appear following these pages in the microfilm edition of this volume of the journal. Photocopies of the supplementary material from this paper only or microfiche (105 × 148 mm, 20× reduction, negatives) containing all of the supplementary material for the papers in this issue may be obtained from the Journals Department, American Chemical Society, 1155 16th St., N.W., Washington, D. C. 20036. Remit check or money order for $3.00 for photocopy or $2.00 for microfiche, referring to code number JPC-73-2857.

References and Notes

(1) J. K. Thomas and R. V. Bensasson, *J. Chem. Phys.*, **46**, 4147 (1967).
(2) G. B. Buxton, *Proc. Roy. Soc., Ser. A*, **328**, 9 (1972).
(3) F. S. Dainton and C. Gopinathan, *Trans. Faraday Soc.*, **65**, 151 (1969).
(4) G. V. Buxton, F. C. R. Cattell, and F. S. Dainton, *Chem. Commun.*, 27 (1971); *Trans. Faraday Soc.*, **67**, 687 (1971).
(5) J. Kroh, Cz. Stradowski, and J. Mayer, *Radiochem. Radioanal. Lett.*, **2**, 209 (1969).
(6) I. A. Taub and H. A. Gillis, *J. Amer. Chem. Soc.*, **91**, 6507 (1969).
(7) J. E. Willard and M. Shirom, *J. Phys. Chem.*, **72**, 1702 (1968).
(8) J. A. Leone and W. H. Hamill, *J. Chem. Phys.*, **49**, 5294 (1968).
(9) J. K. Thomas, K. Johnson, T. Klippert, and R. Lowers, *J. Chem. Phys.*, **48**, 1608 (1968).
(10) S. K. Ho, S. Siegel, and H. A. Schwarz, *J. Phys. Chem.*, **71**, 4527 (1967); S. K. Ho and S. Siegel, *J. Chem. Phys.*, **50**, 1142 (1969).
(11) A. Barkatt, M. Ottolenghi, and J. Rabani, *J. Phys. Chem.*, **76**, 203 (1972).
(12) J. S. Stroud, *J. Chem. Phys.*, **35**, 844 (1961); **37**, 836 (1962); *Phys. Chem. Glasses*, **5**, 71 (1964).
(13) A. M. Bishay, *J. Amer. Ceramic Soc.*, **45**, 389 (1962).
(14) For the identification of the absorptions due to the various oxidized and reduced forms in the present work see A. Treinin, in "Radical Ions," E. T. Kaiser and L. Kevan, Ed., Interscience, New York, N. Y., 1968, p 525.
(15) A. Eisenberg and T. Sasada, *Proc. Int. Conf. Delft Amsterdam*, 99 (1964).
(16) W. C. Hagel and J. D. Mackeezie, *Phys. Chem. Glasses*, **5**, 113 (1964).
(17) R. Terai, *Phys. Chem. Glasses*, **10**, 146 (1969).
(18) (a) S. J. Rzad, P. P. Infolta, J. M. Warman, and R. H. Schuler, *J. Chem. Phys.*, **50**, 5034 (1969); (b) *ibid.*, **52**, 3971 (1970).
(19) T. I. Balkas, J. H. Fendler, and R. H. Schuler, *J. Phys. Chem.*, **74**, 4497 (1970).
(20) A. Hummel, *J. Chem. Phys.*, **49**, 4840 (1968).
(21) H. A. Schwarz, *J. Phys. Chem.*, **73**, 1928 (1969).
(22) E. Peled and G. Czapski, *J. Phys. Chem.*, submitted for publication.
(23) (a) R. M. Noyes, *J. Amer. Chem. Soc.*, **77**, 2042 (1955); (b) R. M. Noyes, *Progr. React. Kinet.*, **1**, 129 (1961).
(24) S. Chandrasekhar, *Rev. Mod. Phys.*, **15**, 1 (1943).
(25) A. Kuppermann in "Actions Chimiques et Biologiques des Radiations," M. Haissinsky, Ed., Masson, Paris, 1961, 5th Series, p 85.
(26) A. Mozumder, *J. Chem. Phys.*, **55**, 3020 (1971); *ibid.*, **55**, 3026 (1971).
(27) G. C. Abell and A. Mozumder, *J. Chem. Phys.*, **56**, 4079 (1972).
(28) Y. Maruyama and K. Funabashi, *J. Chem. Phys.*, **56**, 2342 (1972).
(29) (a) R. H. Doremus, *J. Phys. Chem.*, **68**, 2212 (1964); (b) *Phys. Chem. Glasses*, **10**, 28 (1969).
(30) J. A. Duffy, *Phys. Chem. Glasses*, **13**, 65 (1972).

Stable Product Yields from the γ-Irradiation of 3-Methylpentane-h_{14} Glass, Liquid, and Gas and 3-Methylpentane-d_{14} Glass[1,2]

D. D. Mainwaring[2] and J. E. Willard*
Department of Chemistry, University of Wisconsin, Madison, Wisconsin 53706 *(Received August 24, 1973)*

Publication costs assisted by the U. S. Atomic Energy Commission

Yields from the γ-irradiation of 3-methylpentane-h_{14} (3MP-h_{14}) as a gas (300°K), liquid (273°K), and glass (77°K), and from the γ-irradiation of 3MP-d_{14} glass, have been determined for 40 products in the mass range from H_2 to C_{12} hydrocarbons. The G values (molecules per 100 eV absorbed) for total products from the gas, liquid, and glass are 16.6, 12.7, and 9.0, respectively. The yields of C_6 compounds (isomers of 3MP and olefins) are all lower in the liquid than the glass and in the gas than the liquid, whereas the yields of most other products are higher in the liquid than the glass, and in the gas than the liquid, but with major differences in the magnitude of these phase effects. The yield of each hydrocarbon product from 3MP-d_{14} is essentially the same as that from 3MP-h_{14}.

Introduction

The purposes of this work have been to determine the effect of phase (gas at 298°K, liquid at 273°K, and glass at 77°K) on the yields of stable products formed by the γ-radiolysis of 3-methylpentane (3MP), and to compare the yields from radiolysis of 3MP-h_{14} and 3MP-d_{14} in the glassy phase. 3MP glass has been extensively used as a matrix for trapping and examining radiolytically and photochemically produced radicals, electrons, and ions,[3] but no systematic study of the stable products which result on melting following irradiation has previously been made.

Earlier studies of the effects of phase on the radiation chemistry of hydrocarbons have included (1) comparisons of the G values of H_2 and C_1–C_5 carbon compounds from crystalline *n*-heptane at 77°K with those from the liquid at 300°K;[4] (2) comparison of the H_2 yields from cyclohexane and isooctane at 77°K with those at 300°K;[4] (3) comparison of other yields from cyclohexane in the gas, liquid, and solid phases;[5] (4) radiolysis of *n*-butane in the gas, liquid, and solid phases;[6] (5) radiolysis of *n*-hexane in the gas, liquid, and solid phases;[7] (6) comparison of the radiolysis of neopentane in the gas and liquid phases;[8a] (7) determination of H_2 yields from 13 saturated hydrocarbons at 77, 201, and 293°K.[8b] Effects of changes in temperature without change in phase have also been noted in liquid *n*-hexane,[4,9,10] cyclohexane,[4] and isooctane.[4] Isotopic hydrogen and hydrocarbon yields from selectively deuterated liquid *n*-hexane have been investigated.[9] The hydrogen and hydrocarbon product yields from the radiolysis of liquid 3MP have been determined.[11]

Experimental Section

3-Methylpentane (Phillips Pure Grade) was purified by passage through freshly activated silica gel, repeated freeze–pump–thaw cycles, pumping on the liquid, and storage over a sodium mirror on the vacuum line. The only detectable impurity by gas chromatographic analysis was 2-methylpentane present at less than 0.2 mol %. 3-Methylpentane-d_{14} (Merck Sharp and Dohme) was purified by preparative gas chromatography and the same degassing and storage used for 3MP-h_{14}. It contained less than 0.1% impurity as tested by gas chromatography.

The irradiation cells for liquid and solid samples consisted of 2.5 mm i.d. Pyrex tubing attached to a greaseless stopcock which had a Teflon plug and Viton O-rings. Introduction of the known amounts of sample to the cell was done by condensation of 3MP vapor from a volume of known PVT. The cells for irradiation of gaseous 3MP consisted of a glass annulus *ca.* 3 cm high, 17 mm i.d., and 22 mm o.d. with an annular gas volume of 10 mm. This was connected by capillary tubing to a capillary stopcock which could be attached to the vacuum line for filling the cell from a metered volume.

γ-Irradiations were performed with a small high specific activity source positioned adjacent to the liquid and solid samples and in the center of the annulus holding the gaseous samples. The solid samples were irradiated with the cell and source under liquid nitrogen (77°K); the liquid samples were irradiated in an ice–water bath at 273°K; and the gaseous samples were irradiated in air at room temperature. A dose of 1.2×10^{21} eV g^{-1} was used for every sample. The dose rates, determined by Fricke dosimetry, and corrected for the relative electron fractions in the dosimeter solution and 3MP, range from 4.1×10^{18} eV g^{-1} min^{-1} to 3.8×10^{18} eV g^{-1} min^{-1}. A value of 2160 M^{-1} cm^{-1} at 305 nm and 22.5° with a temperature coefficient of 0.8% per degree was used as the absorbency of the dosimeter solution, and G(ferric ions) was taken as 15.6. Hydrocarbon analyses were made with a Varian-Aerograph Hy-Fi, Model 600-C, gas chromatograph with flame ionization detector and nitrogen as the carrier gas in a 3 m long 3.8 mm i.d. glass column packed with Chromosorb P coated with 20 wt % of GE SF-96 silicone oil. Temperatures of 27 and 103°, and flow rates of 8 and 75 ml min^{-1}, were used for the low and high boiling products, respectively. The hydrocarbons were eluted in the order of their boiling points.

In analyses of samples where bromine had been added to convert alkenes to dibromides a 6 m long 1.2 mm i.d. stainless steel column packed with 3% Ucon 50HB 2000 on Chromosorb P was used at 100° at a flow rate of 25 ml min^{-1}. This resulted in the retardation of the polar species relative to the alkanes.

The area under each product peak (height times half-width) indicated the number of molecules injected. The proportionality factors were read from a plot of log (retention time) *vs.* (molecules/peak area) for 13 known hydrocarbons.

For determination of the low boiling products from irradiated samples (solid, liquid, or gas), the total sample was

vaporized on the vacuum line and an aliquot was taken and injected into the gas chromatography line with the aid of a Carle microvolume valve. Samples for analysis for the high boiling products were removed from the liquid phase of the irradiated 3MP with a 10-μl syringe and injected into the gc column. For this purpose the gaseous samples were condensed in a small side arm of the irradiation tube.

To separate olefins from the other hydrocarbons, bromine was added on the vacuum line (in the dark) to some of the irradiated samples. Excess bromine was removed by distillation onto mercury.

Analyses for H_2 and D_2 were made on the noncondensible gases from irradiated samples at 77°K, collected by means of a Toepler pump. An AEI MS-10 mass spectrometer calibrated with standard samples of H_2, D_2, HD, CH_4, and air was used.

Results

Table I shows the G value (molecules per 100 eV) obtained in this work. These yields are, in each case, the average of at least three independent experiments. The maximum deviations from the average G values listed, for different G value ranges, are $G > 1$, ±5%; $G = 0.1$–1, ±8%; $G = 0.01$–0.1, ±12%.

The gas chromatographic techniques used did not, in general, resolve compounds with boiling points within 2° of each other in the range above 90°, or within 3° of each other above 189°. Consequently, some of the values in Table I represent two or more products, but individual boiling point estimates are included where partial resolution was achieved. The boiling points in column 2 of Table I were estimated from the retention times of the gc peaks by reference to a plot of retention times of known products *vs.* their boiling points. The major low boiling compounds were identified by comparison to the gc retention times of known compounds. Other products were tentatively identified by comparing their boiling points to those of compounds which might be expected products from the radiolysis of 3MP.

Peaks 20, 23, and 24 were absent in the gc analysis of liquid and solid samples exposed to bromine before analysis. This coupled with boiling point comparisons indicates that they are 3-methylpentenes. No higher molecular weight alkenes were observed, as has also been found to be the case in *n*-hexane.[9] Alkenes of molecular weight lower than 50 would not have been detected in the present work.

Peaks 41–45 are thought to represent dodecane (C_{12}) isomers. Ten such isomers could conceivably be formed by various combinations of 3MP chains. The boiling point of diethyloctane is given in the literature as 203°.[5] Six dodecane isomers which would not be expected to be produced from 3MP have boiling points ranging from 186 to 216°.[6b] In our analyses the glassy 3MP samples seem to yield at least five isomers, no one of which predominates; the liquid samples give at least six; and the gaseous samples at least eight.

The mass spectrometric results for hydrogen yields given in Table I, row 1, are the average, for each phase, of determinations on at least three irradiated samples with a maximum deviation from the average value of 5.6%.

The G values for the products from glassy 3MP-d_{14} (Table I, column 6) appear to be within experimental error of the analogous products from 3MP-h_{14} (Table I, column 3). The values in column 6 are the average from three irradiated samples which showed a maximum deviation from the average of 15% for $G > 0.1$ and 20% for $G < 0.1$.

As an example of a rather satisfactory reproducibility of G values from laboratory to laboratory, the results for groups of compounds from liquid 3MP shown in Table I are compared with earlier work[11] in Table II.

Discussion

Table I shows that the yields of most products of the irradiations are higher in the liquid than in the solid and are higher in the gas than in the liquid. Exceptions are those for the C_6 species and peak 25, which decrease for both phase transitions, and the species of peaks 3, 6, 8, 11, 16, 35, and 36, which decrease from the liquid to the gas. The trends are summarized in Table III. In general they are consistent with the expectation that permanent fragmentation of molecules decreases with increasing density of the medium as a result of increasing probability of energy transfer from excited molecules to the medium and of reduction in fragmentation by caging effects. Examined in more detail, however, there are large differences in the effects of the phase transitions on different products. This would be expected considering the many processes contributing to product formation. These include combination, disproportionation, and abstraction reactions of free radicals; ion–molecule reactions and other charge transfer steps; and excitation and deexcitation encounters. Some of these are surely temperature sensitive as well as phase sensitive. It is impossible to speculate meaningfully on the precise identity of the interrelated reaction steps responsible for the phase effects. The major trends are similar to those observed by others for phase effects in alkanes.[4-7]

A yield of particular interest in relation to studies of trapped electrons and ions in glassy 3MP is the sum of the olefins, since experiments in which olefins have been added prior to irradiation indicate that they are able to trap positive charge, thereby enhancing the yields of trapped electrons.[12] The sum of the yields of peaks 20, 23, and 24 from glassy 3MP, which have been assigned to olefins, is 1.63. This is a minimum value for the olefin yield since analysis for olefins of molecular weight less than 50 was not made and since olefin gc peaks underlying alkane peaks would not have been observed. If this value is correct and independent of dose, then for doses in the range of 10^{19}–10^{20} eV g^{-1}, which are typical of those used in charge trapping studies, the mole fraction of olefins is in the range of 2×10^{-5} to 2×10^{-4}. This is much lower than the concentration of added olefin demonstrated to have a scavenging effect for positive charge.[12] However, the *effective* concentration of olefins for charge scavenging is increased if they are localized in the spurs. On the other hand, most of those olefin molecules which are formed by disproportionation between trapped radicals which must diffuse before encountering each other are not available for charge scavenging at 77°K until minutes or hours[3] after the end of irradiation. At least half of the olefin molecules are formed by processes other than disproportionation, as noted in the next paragraph.

The C_{12} yield of $G = 0.68$ in the glassy state sets an upper limit of $G = 1.4$ for 3-methylpentyl radicals which decay by radical–radical combination, which is about half of the trapped radical yield of 3.1 ± 0.3.[13] This suggests an upper limit of 50% for the probability of combination rather than disproportionation when 3-methylpentyl radicals encounter each other in the glass at 77°K and during

TABLE I: Gc Elution Order, Estimated Boiling Points, *G* Values, and Tentative Identification of Products from γ-Irradiation of 3MP-h_{14} Glass, Liquid, and Gas, and 3MP-d_{14} Glass[a]

Peak no.	Bp, °C	*G*(glass) 3MP-h_{14}	*G*(liquid) 3MP-h_{14}	*G*(gas) 3MP-h_{14}	*G*(glass) 3MP-d_{14}	Probable product
1	−253	3.2	3.4	3.6		Hydrogen
2	−161	0.08	0.20	0.80	0.09	Methane
3	−104	0.20	1.00	0.86	0.20	Ethylene
4	−89	0.45	1.90	1.98	0.45	Ethane
5	−45	0.02	0.09	0.40	0.02	Propane
6	−28	...	0.02	0.01	...	
7	−15	...	0.02	0.14	...	Isobutane
8	−4	0.19	0.37	0.60	0.20	1-Butene
9	−0.5	0.31	0.45	1.45	0.30	*n*-Butane
10	+3.0	0.14	0.22	0.30	0.16	2-Butene
11	+8.0	0.05	0.15	0.06	0.05	
12	+16	...	Trace	...	...	
13	+26	0.01	0.06	0.31	0.01	2-Methylbutane
14	+32	0.03	0.03	Trace	0.03	2-Methyl-1-butene
15	+34	0.04	0.07	0.08	0.04	2-Pentene
16	+37	0.05	0.09	0.03	0.06	*n*-Pentane
17	+38	...	Trace	...	...	
18	+40	0.02	0.05	0.07	0.02	
19	+47	...	Trace	Trace	...	
20	+57	0.40	0.27	0.11	0.41	3-Methyl-1-pentene
21	+60	0.80	0.65	0.10	0.79	2-Methylpentane
22	+63					3-Methylpentane
23	+70	0.80	0.55	...	0.82	3-Methyl-2-pentene
24	+78	0.43	0.26	0.16	0.46	3-Methyl-1,3-pentadiene
25	+84	0.42	0.28	0.19	0.46	Dimethylpentane
26	+92	0.18	0.26	1.50	0.20	3-Methylhexane, 3-ethylpentane
27	+109	...	...	0.06	...	
28	+120	0.21	0.51	1.26	0.23	2-Ethyl-3-methylpentane, 3-methylheptane, 3-ethyl-3-methylpentane
29	+139	...	0.03	0.07	...	3,5-Dimethy - heptane
30	+143	0.02	0.04	0.17	0.02	3-Methyl-4-ethylhexane
31	+148	...	...	0.09	...	
32	+158	...	...	0.05	...	3-Methyl-5-ethylheptane
33	+160	0.04	...	0.08	0.03	3,6-Dimethy - octane; 3,4-diethylhexane
34	+163	0.07	...	...	0.07	3,4,5-Trimethyl-heptane
35	+166	0.08	0.29	0.20	0.08	3,4-Dimethyl-3-ethylhexane
36	+171	0.05	0.17	0.17	0.04	
37	+181	0.02	0.03	0.06	0.02	An undecane
38	+185	0.02	0.05	0.09	0.02	3,4-Dimethyl-5-ethylheptane
39	+187	...	...	0.07	...	
40	+189	...	0.03	...	...	3-Methyl-3,4-diethylhexane
41	+193	...	...	0.16	...	Dodecane isomers
42	+198/201	0.36	0.63	0.78	0.32	
43	+202, 204 207	0.32	0.35	0.43	0.29	Dodecane isomers
44	+211	...	0.02	Trace	...	
45	+217	...	0.11	0.14	...	
Total		9.02	12.65	16.63	5.90[b]	

[a] Dashes in the G value columns indicate that no gc peak could be detected. The blank in column 6 of row 1 indicates that $G(D_2)$ was not determined. In every case the results are for samples which had received a dose of 4×10^{21} eV g^{-1}. [b] The value for *G*(total) from glassy 3MP-d_{14} is for the products other than D_2.

TABLE II: Comparision of Product Yields from Liquid 3MP as Obtained in this Work and that of Dewhurst[11]

	This work	Ref 11[a]
H_2	3.4	3.4
CH_4	0.2	0.2
C_4	1.5	2.4
C_5	0.3	0.3
C_7	0.5	0.5
C_8	0.6	1.1
C_{10}	0.5	0.7
C_{12}	1.1	1.0

[a] Using 800-keV electrons, a dose rate of 8×10^{20} eV g^{-1} min^{-1} and a dose of 2.9×10^{21} eV g^{-1}. The dose rate from ^{60}Co radiation for the determinations of the present work, reported in the second column, was 4×10^{18} eV g^{-1} min^{-1} and the dose was 1.2×10^{21} eV g^{-1}.

TABLE III: *G* Values for Groups of Products Produced by γ-Radiolysis of 3MP

	G values		
	Solid	Liquid	Gas
H_2	3.20	3.40	3.60
C_1–C_5	1.59	4.72	7.09
C_6 + peak 25	2.85	2.01	0.56
C_7–C_{11}	0.70	1.41	3.87
C_{12}	0.68	1.11	1.51
Total	9.02	12.65	16.63

warm-up for analysis. If combination of radicals is responsible for all of the C_{12} yield, only half of the observed olefin yield of 1.6 can be accounted for by disproportionation of the observed radicals [(3.1 − 1.4)/2 = 0.8] since two radicals are used in forming one olefin molecule.

The similarity of the yields of each of the hydrocarbons from C_6D_{14} as compared to those from C_6H_{14} is striking and argues against those types of intermediate reactions which would be expected to show isotope effects.

Of related interest to the phase effects reported here is evidence that (1) the radiolytic yield of trapped free radicals in glassy 3MP at 77°K as determined by esr (G = 3.1)[13] is less than half the radical yield found in the liquid at 298°K by scavenger methods (G = 7);[16] (2) the trapped free radicals formed by γ-irradiation of glassy 3MP are predominantly *sec*-3-methylpentyl radicals,[17] whereas in the liquid and gas phase substantial fractional yields of several radicals are normally produced from alkanes;[18] (3) thermal H atoms are produced in liquid hydrocarbons[19] but not in glassy hydrocarbons.[20]

References and Notes

(1) This work has been supported in part by the U. S. Atomic Energy Commission under Contract No. AT(11-1)-1715 and by the W. F. Vilas Trust of the University of Wisconsin.
(2) Further details are given in the M.S. thesis of D. D. Mainwaring, University of Wisconsin, 1971.
(3) For examples and references see J. E. Willard, *Science*, **180**, 553 (1973).
(4) A. V. Topchiev in "Radiolysis of Hydrocarbons," R. A. Holroyd, Ed., Elsevier, Amsterdam, 1964, p 58.
(5) (a) W. A. Cramer in "Aspects of Hydrocarbon Radiolysis," T. Gäumann and J. Hoigne, Ed., Academic Press, New York, N. Y., 1968, Chapter 4; (b) M. J. Bouillot, *Int. J. Radiat. Phys. Chem.*, **2**, 117 (1970).
(6) T. Miyazaki, S. Arai, S. Shida, and S. Sunohara, *Bull. Chem. Soc. Jap.*, **37**, 1352 (1964).
(7) (a) H. A. Dewhurst, *J. Amer. Chem. Soc.*, **83**, 1050 (1961); (b) L. Kevan and W. F. Libby, *J. Phys. Chem.*, **39**, 1288 (1963); (c) H. A. Dewhurst, *ibid.*, **62**, 15 (1958).
(8) (a) M. Hamashima, M. P. Reddy, and M. Burton, *J. Phys. Chem.*, **62**, 246 (1958); (b) T. Kimura, K. Fueki, and Z. Kuri, *Bull. Chem. Soc. Jap.*, **43** 1657 (1970).
(9) T. Gaumann, ref 5a, Chapter 5.
(10) W. P. Bishop and R. F. Firestone, *J. Phys. Chem.*, **74**, 2274 (1970).
(11) H. A. Dewhurst, *J. Amer. Chem. Soc.*, **80**, 5609 (1953).
(12) J. P. Guarino and W. H. Hamill, *J. Amer. Chem. Soc.*, **86**, 777 (1964).
(13) Results of M. Neiss in our laboratory now indicate that the G value of 1.6 for trapped 3MP radicals in γ-irradiated 3MP at 77°K reported earlier[14] using an esr power of 7 mW is low because of power saturation and that the correct value is 3.1 ± 0.3. A similar value (2.8) has been reported in the literature.[15]
(14) M. Shirom and J. E. Willard, *J. Phys. Chem.*, **72**, 1702 (1968).
(15) D. P. Lin and L. Kevan, *J. Chem. Phys.*, **55**, 2629 (1971).
(16) E. N. Weber, P. F. Forsyth, and R. H. Schuler, *Radiat. Res.*, **3**, 68 (1955).
(17) D. Henderson and J. E. Willard, *J. Amer. Chem. Soc.*, **91**, 3014 (1969).
(18) R. A. Holroyd, ref 5a, Chapter 1.
(19) For examples and references see M. C. Sauer, Jr., and J. Mani, *J. Phys. Chem.*, **72**, 3856 (1968); K. M. Bansal and S. J. Rzad, *J. Phys. Chem.*, **74**, 3486 (1970).
(20) D. Timm and J. E. Willard, *J. Phys. Chem.*, **73**, 2403 (1969).

Pulse Radiolysis of Mercuric Ion in Aqueous Solutions

Shin'ichi Fujita,* Hideo Horii, and Setsuo Taniguchi

Radiation Center of Osaka Prefecture, Shinke-cho, Sakai, Osaka, Japan *(Received January 24, 1973; Revised Manuscript Received May 23, 1973)*

The pulse radiolysis method was used to study deaerated aqueous solutions of the mercuric ion in the wavelength range 220–300 nm. The transient mercurous ion gave two absorption maxima at 225 and 250 nm with $\epsilon^{255} = (1.4 \pm 0.1) \times 10^4\ M^{-1}\ \text{sec}^{-1}$. Stable mercurous ion, Hg_2^{2+}, was formed *via* an additional step after the disproportionation reaction of the initial species: $Hg^+ + Hg^+ \rightarrow Hg^0 + Hg(II)$; $Hg^0 + Hg(II) \rightarrow Hg_2^{2+}$. The formation rate of Hg_2^{2+} depended on the concentration of mercuric ion and the pH of the solution. The result was ascribed to the reaction of Hg^0 with three partially hydrolyzed species of mercuric ion. Rate constants for the reactions were determined.

Introduction

The radiolysis of aqueous solutions of some metal ions gives various species in unstable valence states by the action of the transient primary products from water, such as OH radical, H radical, and hydrated electron. The technique of pulse radiolysis, as well known, is used to investigate the reaction processes of such short-lived species. By this method cadmium and zinc of group IIb metals have been investigated in detail; their monovalent states are strong reducers[1] and show transient absorptions, due to charge transfer spectra, at about 310 nm.[2,3]

The chemistry of mercury differs from that of zinc and cadmium not only because of inherent peculiarities of the element but also because of the existence of the stable mercurous ion, Hg_2^{2+}, which is readily obtained by reduction of mercuric salts. According to Higginson,[4] Hg_2^{2+} dissociates to Hg^+ at low concentrations and the absorption spectrum of the monomeric ion is entirely different from the charge transfer spectra for other group IIb metals. On the radiolysis of an aqueous solution of mercuric ion, the hydrated electron or H radical reduces the ion to form the mercurous ion. Recently, Faraggi and Amozig[5] have reported that the transient Hg^+ shows an absorption maximum at 272 nm by the pulse technique.

The present report sheds light on the chemical processes between stable and unstable mercurous ions by studies in the range 220–300 nm. The obtained spectrum of the transient species was fairly different from the result by Faraggi and Amozig. Another interesting result obtained is that the stable mercurous ion is produced by the bimolecular reaction of the zero-valent mercury with mercuric ion after disproportionation of the transient monovalent mercury.

Experimental Section

The electron beam was produced in a linear accelerator (High Voltage Engineering Co.) giving 10-Mev electrons with a variable pulse width up to 5 μsec; its peak current being about 0.4 A. The electron beam, spread by an aluminum plate 4 mm thick, entered the cell through a brass slit and fell on a brass collector. The current was monitored as voltage on a condenser with a digital voltmeter having a holding mechanism.

The irradiation cell was 1.5 cm long, made of quartz having *thermal* end windows. The sample solution was refreshed from a Pyrex stock bottle of 0.5–1 l. by combination of argon and a magnetic valve.

The analytical system consisted of a 150-W D_2 lamp, three lenses, a mirror, a Bosch and Lomb grating monochrometer, and a 1P28 photomultiplier tube. This combination gave only a little scattered light of lower wavelength, which was about 5.5% at 220 nm and less at longer wavelength.

The water used throughout this work was triply distilled. The aqueous solutions of mercuric ion were prepared from two sources: mercuric perchlorate and usually mercuric oxide with perchloric acid. The solutions were deaerated by bubbling with argon for longer than 2 hr. All materials were used without further purification from the commercial sources. Only nitrous oxide was specially ordered ($O_2 < 0.1\%$).

The determination of the concentration of mercuric ion was carried out spectrophotometrically as its EDTA complex in acidic solution at 247 nm where the complex has an absorption maximum with $\epsilon = (2.28 \pm 0.05) \times 10^3\ M^{-1}\ \text{cm}^{-1}$.

The dosimetry was carried out by means of 0.1 *M* KCNS solutions saturated with oxygen using the reported value of $\epsilon^{475}(CNS)_2^- = 7600\ M^{-1}\ \text{cm}^{-1}$ and $G = 2.8$.[6]

Results

Pulse radiolysis of deaerated aqueous solutions of mercuric ion yielded a transient species, Hg^+, with two absorption maxima at 225 and 250 nm. Figure 1 shows the spectrum 2 μsec after the pulse and its change with time in a 50 μM HgO solution at pH 4.3. The half-lives of the absorptions at two peaks were identical within experimental errors and were inversely proportional to the initial absorption. Similar results were obtained in the solution of perchlorate salt. After the initial species has decayed, another absorption, which has a peak at 236 nm and can be assigned to a stable mercurous ion, Hg_2^{2+}, appears and reaches constancy within a few milliseconds. The permanent absorption was formed faster in solutions of higher concentration of mercuric ion or of lower pH. Figure 2 shows the typical synchroscopic traces of absorptions at 236 nm. Decay of the initial species and formation of the stable mercurous ion are not simultaneous. Essentially similar results were obtained with the addition of *tert*-butyl alcohol, although the spectrum of its radical over-

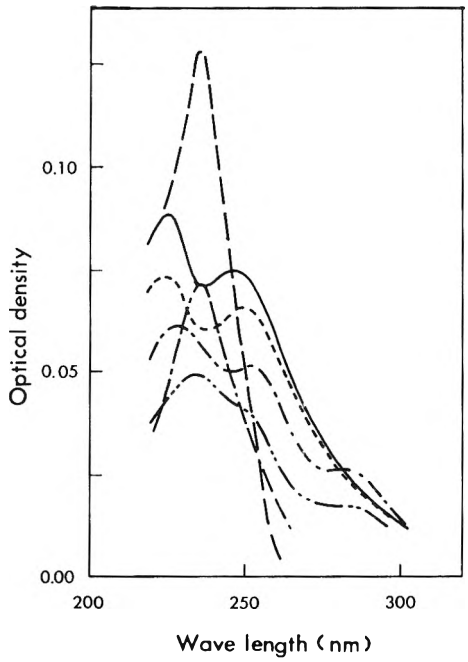

Figure 1. Spectrum and its change with time after a pulse in a deaerated aqueous solution of 50 μM HgO at pH 4.3: average dose, 2700 rads/pulse; (——) 2 μsec, (·····) 15 μsec, (–·–) 50 μsec, (–···–) 1550 μsec, (––·) 500 μsec, (– –) 3 msec.

lapped. However, little absorption appeared in the solution saturated with nitrous oxide. In a solution of 1 mM HgO at pH 2 the spectrum of the transient species was similar to that in Figure 1. However, the absorption yield of the transient at a fixed dose increased markedly compared with that obtained in the solution of 50 μM at pH 4.3. Also in the presence of *tert*-butyl alcohol, the yield increased with increase in the concentration of Hg^{2+} up to a few millimoles per liter. The dependencies were similar between the absorptions of the transient at 255 nm and of stable mercurous ion at 236 nm. The contribution from *t*-BuOH radical to the observed absorption was negligible at 255 nm.[7] Both yields reach constant values at above 10 mM of mercuric ion. The Hg^{+} yield is reduced at low concentrations of mercuric ion by the competion of H radical recombination. Then, the product G values should be equal to that of H radical at 10 mM mercuric ion. Taking $G(H) = 3.2$, each molar extinction coefficient is calculated to be $\epsilon^{255}(Hg^{+}) = (1.4 \pm 0.1) \times 10^4$, $\epsilon^{236}(Hg_2^{2+}) = (2.4 \pm 0.2) \times M\ 10^4\ M^{-1}\ cm^{-1}$, where the molecular yield of Hg_2^{2+} is half of that of the transient according to the stoichiometrical relation.

Figure 3 shows that the plots of $1/D$ *vs.* time after the end of the pulse fall into a good linear line in a 50 μM HgO solution of pH 4.3. The slope of the lines equals $2k/\epsilon l$ where k is the second-order rate constant, ϵ is the molar extinction coefficient, and l is the light path length in the irradiation cell. In a 1.0 mM HgO solution of pH 2.0, the linearity was not as good due to the fast formation of stable mercurous ions. In this case, the results were improved by plotting $1/D'$, where $D' = D_0(D - D_\infty)/(D_0 - D_\infty)$, on an assumption that Hg^{+} ions recombine simultaneously to form Hg_2^{2+}. D' represents the optical density of the pure transient species. The improved slopes are also shown in Figure 3. Table I lists the results in both pH solutions containing various concentration of sodium perchlorates. The second-order rate of decay of the transient at each pH approximately equals within experimental

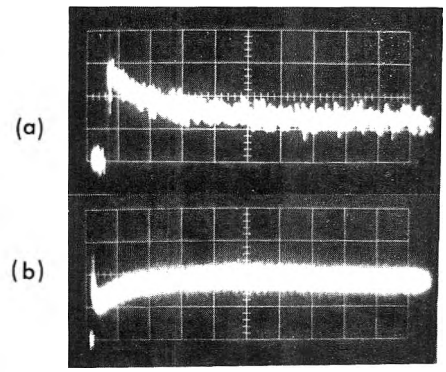

Figure 2. Synchroscopic traces at 236 nm obtained in a deaerated aqueous solution of 50 μM of mercuric ion, pH 4.3: pulse doses, 1420 rads/pulse; ordinates 4.4%/cm for (a) and (b); abscissa, (a) 20 μsec/division, (b) 1 msec/division.

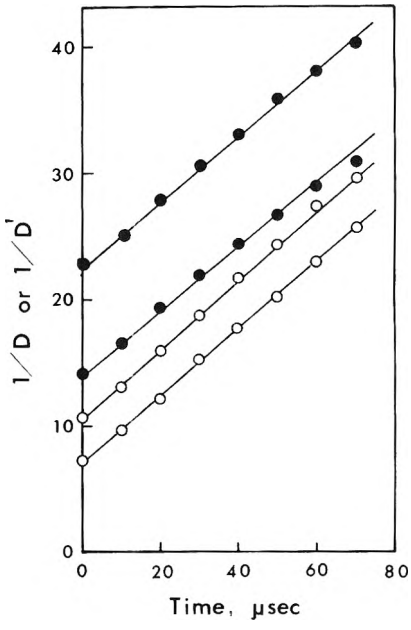

Figure 3. Test of second-order rate law for the decay of transient absorption at 255 nm in the presence of 2 mM *tert*-butyl alcohol: (●) $1/D$, 50 μM HgO at pH 4.3; dose, (upper) 1800 rads/pulse, (lower) 2800 rads/pulse; (○) $1/D'$, 1 mM HgO at pH 2.0; dose, (upper) 1800 rads/pulse, (lower) 2800 rads/pulse, where $D' = D_0\,(D - D_\infty)/(D_0 - D_\infty)$.

TABLE I: Decay Rate Constants of Hg^{+} in Solutions of 50 μM HgO at pH 4.3 and 1 mM HgO at pH 2.0 with Various Concentrations of $NaClO_4$

pH	[HgO]	$[NaClO_4]$, M	$2k/\epsilon \times 10^{-5}$, cm sec^{-1}	$2k_0 \times 10^{-9}$, M^{-1} sec^{-1}
4.3	50 μM	0	3.9 ± 0.2	5.2 ± 0.5
		0.15	5.1 ± 0.2	
2.0	1.0 mM	0	3.9 ± 0.3	4.9 ± 0.5
		0.03	4.2 ± 0.3	
		0.08	4.8 ± 0.3	

error and increases with increase in ionic strength. $2k_0$ in the last column shows the rate constant at zero ionic strength, by plotting log $2k/\epsilon$ as a function of $\mu^{1/2}/(1 + \mu^{1/2})$, multiplied by ϵ.

The formation of the stable mercurous ion obeyed the first-order rate law in the absence of *tert*-butyl alcohol, the radical of which was effective to some extent in absorption at 236 nm. When the formation of Hg_2^{2+} was rel-

TABLE II: Rates of Formation of Hg_2^{2+} at 236 nm, Abundance Ratios of the Mercuric Ion in the Three Hydrolyzed Forms, and the Resulting Rate Constants of the Respective Components

pH	[HgO],[a] μM	Rates of formation × 10^{-3} sec^{-1}	$k_f^{pH} \times 10^{-8}$ M^{-1} sec^{-1}	α	β	γ
4.0	59	3.6 ± 0.3				
	36	2.5 ± 0.2	0.67 ± 0.07	0.019	0.038	0.943
	16	1.2 ± 0.1				
3.5	36	5.9 ± 0.5	1.6_6 ± 0.1	0.150	0.095	0.755
	15	2.5 ± 0.2				
3.0	16	6.8 ± 0.7	4.2 ± 0.4	0.588	0.118	0.298

$k_\alpha = 5.9 \times 10^8$, $k_\beta = 5.0 \times 10^8$, $k_\gamma \leq 5 \times 10^7$ M^{-1} sec^{-1}

[a] Corrected values with consumption by e_{aq}^- and H radical.

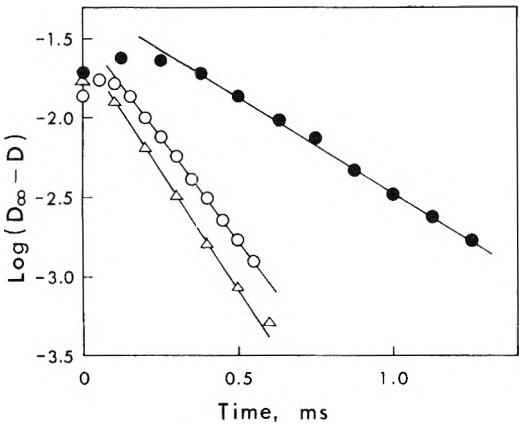

Figure 4. First-order formation of Hg_2^{2+} at 236 nm in the absence of *tert*-butyl alcohol, average dose, 1250 rads/pulse: (●) 36 μM HgO at pH 4.0; (○) 36 μM HgO at pH 3.5; (△) 16 μM HgO at pH 3.0.

atively slow, the linearity of the plots of log $(D_\infty - D)$ *vs.* t was satisfactory in a considerable range of time except in an earlier stage (Figure 4). The apparent rate of formation calculated from the slope appeared to vary along an S-type curve against pH ($pK \sim 3.5$) in the 50 μM HgO solution. Even at this concentration, however, the linearities of the plots were poor at low pH's due to the fast formation of Hg_2^{2+}. Therefore, the rates at low pH's were determined in the more diluted solutions of HgO. The results at three pH's were listed in Table II.

Discussion

In order to explain the appearance of the transient mercurous ion, the following reactions were taken into consideration, based on the scavenger effects.

$$H_2O \longrightarrow e_{aq}^-, H, OH, \text{other stable products} \quad (1)$$

$$e_{aq}^- + Hg(II) \longrightarrow Hg^+ \quad (2)$$

$$H + Hg(II) \longrightarrow Hg^+ \quad (3)$$

$$e_{aq}^- + N_2O \longrightarrow N_2 + OH + OH^- \quad (4)$$

$$OH + t\text{-BuOH} \longrightarrow t\text{-BuOH radical} + H_2O \quad (5)$$

In pH 2 solutions reaction 3 plays the important part, since e_{aq}^- reacts with H^+ to form the H radical.

$$e_{aq}^- + H^+ \longrightarrow H \quad (6)$$

The reaction of the H radical with *t*-BuOH can be neglected. [8] In the absence of *t*-BuOH most of the OH radicals must be consumed by their recombination reaction; some would oxidize the transient.

The unstable monovalent cations of some other metals have been reported to have charge transfer spectra at about 300 nm.[2,3] The transient mercurous ion seems to be unique in the spectrum and its large absorption coefficients at the maxima. Our result of the absorption maximum is not consistent with Faraggi and Amozig.[5] They have reported that the maximum is situated at 272 nm. We have also obtained the same result in 1 mM mercuric perchlorate solution using a xenon lamp as the light source.[9] The difference might arise from the presence of much scattered light when the xenon lamp is used at short wavelength settings of the monochromator. According to Higginson,[4] Hg^+ has an absorption spectrum rising monotonously from 250 nm to the shorter wavelength and its absorption coefficient is at most 3×10^3 M^{-1} cm^{-1} even at 225 nm. The transient species observed here might be alternatively assigned to HgH^{2+}, which has been proposed in matrix experiments by esr,[10] though the matrix is extremely acidic. However, the slope of the plots, log $2k$ *vs.* $\mu^{1/2}(1 + \mu^{1/2})$, is calculated to be rather smaller than +1, even in the solution of pH 2.0. This result suggests that the transient carries a single charge with it, based on the Debye-Brönsted theory. Thus, the transient may be assigned most likely to Hg^+.

The analysis of the second-order rate of decay is expected to be complicated because the absorption of Hg_2^{2+} intervenes at the rates according to the concentration of HgO and the pH of the solution. Thus, two simple conditions were chosen to determine the rate: (1) a solution of 50 μM HgO at pH 4.3, where the formation rate of Hg_2^{2+} is slow (The pH (4.3) was chosen since the solution of mercuric perchlorate shows that the pH in that concentration would be due to hydrolysis.); (2) a solution of 1 mM HgO at pH 2.0, where it would be assumed that Hg_2^{2+} forms instantaneously after the transient has decayed. In this case, D' was used instead of D (the apparent optical density), where $D' = D_0(D - D_\infty)/(D_0 - D_\infty)$. Good agreement with the rates of decay between the two solutions suggests that the transient absorptions in both solutions originate from the same species, Hg^+.

In high pH solutions of HgO the stable mercurous ion does not appear immediately after the decay of the transient as seen in Figure 1 and 2. However, it was concluded that the transient finally becomes Hg_2^{2+} after one or more steps, because both yields (transient Hg^+ and Hg_2^{2+}) depended similarly on the concentration of mercuric ion. The dependencies can be interpreted by the competition of the reaction 3[11] with the recombination reaction of H radicals.[12] Thus, the following reaction mechanism is assumed for the formation process of Hg_2^{2+}. The transient may disproportionate to form zero valent mercury, Hg^0,

and mercuric ion. Later, Hg^0 may react with Hg(II) to form the stable mercurous ion.

$$2Hg^+ \longrightarrow Hg^0 + Hg(II) \quad (7)$$

$$Hg^0 + Hg(II) \longleftrightarrow Hg_2^{2+} \quad (8)$$

Equation 8 is a well-known equilibrium reaction (log K_8 = 1.92 at 25°)[13] when an aqueous solution of mercuric ion contacts with liquid mercury. Further support of the mechanism is presented by two facts of the formation rate of Hg_2^{2+}: the pH dependency and the linear proportionality to the concentration of mercuric ion (Table II). It should be noted that the formation rate is not shown correctly at the low pH region since it becomes fast and the apparent rate is affected by the decay of the transient. Therefore, the values obtained in more diluted solutions are listed in Table II.

The pH dependency of the formation rate may come from the fact that Hg(II) has three conjugate forms, according to the pH.[14]

$$Hg^{2+} \underset{H^+}{\overset{K_a}{\longleftrightarrow}} HgOH^+ \underset{H^+}{\overset{K_b}{\longleftrightarrow}} Hg(OH)_2 \quad (9)$$

where $K_a = 10^{-3.7}$, $K_b = 10^{-2.6}$. From equilibrium 9, the total concentration, $[Hg(II)]_T$, is the sum of the three components

$$[Hg(II)]_T = [Hg^{2+}] + [HgOH^+] + [Hg(OH)_2] = (\alpha + \beta + \gamma)[Hg(II)]_T$$

then, $d[Hg_2^{2+}]/dt = (k_\alpha\alpha + k_\beta\beta + k_\gamma\gamma)[Hg(II)]_T[Hg^0]$. The apparent rate constant of formation of Hg_2^{2+} at a given pH value, k_f^{pH}, is expressed as

$$k_f^{pH} = k_\alpha\alpha + k_\beta\beta + k_\gamma\gamma$$

The respective rate constants for the three forms of Hg(II) were resolved from the ternary simultaneous equations which are obtained from the values in Table II. The abundance ratios (α, β, and γ) were calculated from K_a and K_b at the respective pH. All values used and the resulting rate constants are listed in Table II. These results suggest that the rate is determined by the exchange process between a ligand and a mercury nucleus, considering that Hg^{2+} is also complexed with water molecules. The larger value of k_α than that of k_γ is compatible with the general concept that a metal ion makes a more stable complex with a ligand having opposite charge.

It is interesting that even $Hg(OH)_2$ reacts with Hg^0 at such a rate, while dissolved mercuric oxide does not react with metallic mercury in a neutral solution. We are also studying neutral solutions by the pulse technique and find that Hg_2^{2+} is not observed but a species having another spectrum is found just after the decay of a transient species. More detailed information will be expected from the successive investigation.

Figure 1 also reveals that an absorption appears at 285 nm that reaches maximum in a few tens of μsec after the pulse, and then decays. It may correspond to Hg_2^+ proposed by Faraggi, *et al.*[5]

$$H + Hg_2^{2+} \longrightarrow Hg_2^+ + H^+ \quad (10)$$

A small part of the H radicals or hydrated electrons might be able to react with the product, Hg_2^{2+}.

References and Notes

(1) D. Meyerstein and W. A. Mulac, *J. Phys. Chem.*, **72**, 784 (1968).
(2) G. E. Adams, J. H. Baxendale, and J. W. Boag, *Proc. Chem. Soc.*, 241 (1963).
(3) J. H. Baxendale, E. M. Fielden, and J. P. Keene, *Proc. Roy. Soc., Ser. A*, **286**, 320 (1965).
(4) W. C. Higginson, *J. Chem. Soc.*, 1438 (1951).
(5) M. Faraggi and A. Amozig, *Int. J. Radiat. Phys. Chem.*, **4**, 353 (1972).
(6) J. H. Baxendale, P. L. T. Bevan, and D. A. Scott, *Trans. Faraday Soc.*, **64**, 2389 (1968).
(7) (a) A. Appleby, G. Scholes, and M. Simic, *J. Amer. Chem. Soc.*, **85**, 3891 (1963); (b) J. Rabani, *J. Phys. Chem.*, **66**, 361 (1962); *J. Chem. Phys.*, **37**, 1865 (1962); (c) A. Appleby, *J. Amer. Chem. Soc.*, **67**, 1610 (1963).
(8) M. Simic, P. Neta, and E. Hayon, *J. Phys. Chem.*, **73**, 3794 (1969).
(9) S. Fujita, H. Horii, and S. Taniguchi, *Proc. Congr. Radiat. Chem., 14th*, 56 (1971).
(10) R. J. Booth, H. C. Starkie, and M. C. R. Symons, *J. Chem. Soc. A*, 3198 (1971).
(11) (a) E. Hayon and M. Moreau, *J. Chim. Phys.*, **62**, 391 (1965); (b) M. Faraggi and J. Désalos, *Int. J. Radiat. Phys. Chem.*, **1**, 335 (1969).
(12) M. S. Matheson, *Radiat. Res. Suppl.*, **4**, 1 (1964).
(13) H. L. Roberts, *Advan. Inorg. Chem. Radiochem.*, **11**, 337 (1968).
(14) S. Hietanen and L. G. Sillen, *Acta Chem. Scand.*, **6**, 747 (1952).

Resolution of the Optical Spectra of Sodium Solutions in Liquid Ammonia into Two Experimentally Unresolvable Bands

Gabriel Rubinstein, T. R. Tuttle, Jr.,* and Sidney Golden

Department of Chemistry, Brandeis University, Waltham, Massachusetts 02154 *(Received November 20, 1972; Revised Manuscript Received May 24, 1973)*

Spectra of the solvated electron were determined at −55, −65, and −75° for solutions in NH_3 and in NH_3 0.08 *M* in NaI by extrapolations to infinite dilution. Spectra obtained for $Na-NH_3$ solutions and for $Na-NH_3$–NaI solutions were shown to fulfill the expectations of a two absorber model. The data rule out the possibility that the second absorber incorporates only a single solvated electron. The data support the assumption that the second absorber involves a binary combination of solvated electrons. Spectra of the second absorber are obtained at all three temperatures and for solutions in both NH_3 and in NH_3 0.08 *M* in NaI. Spectra due to Gold and Jolly appear to be characteristic of the second absorber and not the solvated electron.

Introduction

There have been a number of experimental studies of the optical spectra of dilute metal solutions in liquid ammonia. The conclusion that has been drawn in connection with most recent studies is that the broad structureless band in the near infrared, observed in all metal solutions, arises from the solvated electron.[1-6] The observed shift of the band which correlates with solution composition has been attributed to ion pair formation.[7] However, the optical studies have covered a range of metal concentrations over which magnetic properties change appreciably.[8-10] As a result there has arisen an apparent paradox.[11] It appears that the optical spectrum obeys Beer's law under conditions where the species in solution change their relative concentrations drastically. This state of affairs has been rationalized through an ionic cluster model of these solutions[3] in which all the species are constructed from solvated electrons and metal cations such that the solvated electron retains essentially the same light absorbing properties in all the aggregates which contain it. It has been pointed out that available data do not support this view entirely, and suggested that a two absorber model be applied to account for the dependence of spectra on metal concentration.[12]

In this work, the idea that different ionic associates of the same species have similar light absorbing properties (an idea originally incorporated in the ionic cluster model) is applied in conjunction with a two absorber model for the optical spectra of $Na-NH_3$ solutions. The two absorber model is tested and its validity established. Spectra of the solvated electron are obtained. These spectra differ in important details from some spectra previously purported to be due to the solvated electron. Spectra of a second species formed by the coalesence of two solvated electrons are also obtained by resolution of experimental spectra by a method described previously.[13]

Experimental Section

Samples were prepared using standard high-vacuum techniques. Details of sample preparation and apparatus construction are reported elsewhere.[14] Optical spectra were obtained with the aid of a Cary Model 14R spectrophotometer equipped with a dual range absorbance slidewire. Details on the maintenance and operation of the spectrophotometer during these experiments are given elsewhere.[15] One problem encountered which can lead to serious errors in absorbance readings deserves special mention. The lead sulfide detector used at longer wavelengths than 600 mμ had a sufficiently large time constant in its response to incident light at room temperature and below so that the chopped light signal persisted into the dark period. As a result readings greater than about 1.4 absorbance units were too high. At about 2.0 absorbance units the error amounted to 3%. This difficulty was minimized by thermostatting the lead sulfide cell at about 30°. Under this condition absorbance readings of around 2.0 were accurate to about 1%. At higher temperatures the signal-to-noise ratio for the cell deteriorated perceptibly. The temperatures of sample and reference optical cells were thermostatted to within ±0.1°. The apparatus and procedure for maintaining a constant temperature have been described previously.[14]

Optical spectra of 13 different sodium solutions in liquid NH_3 and in 0.08 *M* NaI solutions in liquid NH_3, in the approximate concentration range from about 10^{-6} to 10^{-3} *M*, were measured from 2400 to 375 mμ. Cells with pathlengths 1.00, 0.107, and 0.0302 cm were employed. Spectra were obtained at −55, −65, and −75°. For the most part three successive spectra were recorded for each set of conditions.

Results

The general characteristics of the spectra observed in this work are in most respects similar to those reported in earlier works. In all cases spectra consisted of a single broad asymmetric band peaked in the near infrared with a long tail extending through the visible. However, the data pertain to solutions more dilute in sodium than have been previously studied. Some of the solutions, in which metal concentration and temperature were varied, contained fixed amounts of NaI so that a clearer picture of the concentration and temperature dependences of the spectrum emerges. In this paper, only those data pertinent to making connections with previous work and to making tests of a two absorber model are presented. A more detailed presentation of the data is given elsewhere.[15]

TABLE I: Band Parameters for Na–NH_3 Solutions

Soln no.	A_m/l[a]			$\bar{\nu}_m$[b]			$\Delta\bar{\nu}_{1/2}$[c]		
	−55°	−65°	−75°	−55°	−65°	−75°	−55°	−65°	−75°
1	0.586	0.570	0.565	6863	7067	7273	3245	3231	3214
2	0.751	0.736	0.733	6863	7067	7252	3277	3261	3246
3	1.355	1.364	1.376	6863	7042	7257	3271	3231	3223
4	6.87	6.93	7.00	6868	7038	7194	3287	3241	3245
5	12.42	12.48	12.92	6854	7027	7133	3293	3246	3218
6	17.62	17.95	18.18	6830	6983	7092	3291	3255	3233
7	56.4	52.4	52.3	6711	6817	6920	3276	3232	3175

[a] A_m/l = absorbance at maximum/cell path length. Actual absorbances were between 4 and 1.9. Cell path lengths were 1.00, 0.107, and 0.0302 cm. [b] $\bar{\nu}$ = wave number of maximum absorbance. [c] $\Delta\bar{\nu}_{1/2}$ = width at half-height in wave numbers.

TABLE II: Band Parameters for Na–NaI–NH_3 Solutions[a]

Soln no.	A_m/l			$\bar{\nu}_m$			$\Delta\bar{\nu}_{1/2}$		
	−55°	−65°	−75°	−55°	−65°	−75°	−55°	−65°	−75°
0S		0.430	0.442		7123	7289		3296	3260
1S	0.860	1.017	1.110	6925	7092	7231	3308	3288	3258
2S	1.226	1.131	1.076	6920	7082	7231	3319	3301	3258
3S	1.716	1.619	1.547	6916	7062	7194	3308	3301	3241
4S	10.80	9.78	8.12	6803	6920	7032	3287	3262	3138
5S	16.03	14.49	14.35	6780	6882	6978	3293	3187	3080
6S	27.65	28.00	28.90	6711	6826	6920	3240	3138	3003

[a] See footnotes to Table I.

Values of A_m/l, $\bar{\nu}_m$, and $\Delta\bar{\nu}_{1/2}$ are given for each solution of Na in pure NH_3 at each temperature in Table I. The variation of $\bar{\nu}_m$ with changing sodium concentration at −65° is presented graphically in Figure 1. The present results combined with results from previous investigations[1,7,14] reveal the trend in $\bar{\nu}_m$, which is emphasized by the dashed curve in the figure.

Different values of the temperature coefficient of $\bar{\nu}$ for Na solutions in liquid NH_3 at −65° have been reported by different investigators.[1,7,14] These values, along with ones obtained in this work are plotted as a function of log (A_m/l) in Figure 2. The magnitude of the temperature coefficient apparently reaches a maximum value at low sodium concentrations and passes through a minimum as sodium concentration is increased. The range of sodium concentrations over which $\Delta\bar{\nu}_m/\Delta T$ changes is about the same as the range in which $\bar{\nu}_m$ changes.

Values of A_m/l, $\bar{\nu}_m$, and $\Delta\bar{\nu}_{1/2}$ are given for each solution of Na in 0.08 M NaI in NH_3 at each temperature in Table II. The principal effect of added salt is to shift the spectrum.[1,2,4-6] The direction of the shift depends on temperature and metal concentration. At low temperature and high metal concentrations a red shift occurs while at high temperatures and low metal concentrations a blue shift occurs. The values of λ_m obtained in this study for solutions with and without added NaI are summarized together in Figure 3. Data obtained in other works[1-3,5,16,17] were not included in the figure because the salt concentrations differed from 0.08 M, the value used here.

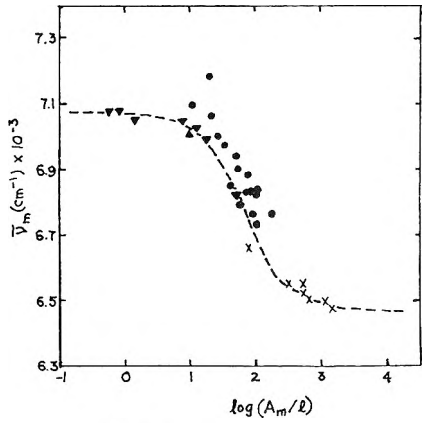

Figure 1. Variation of $\bar{\nu}_m$ with changing optical absorbance for sodium solutions at −65°: ▼, this work; ▲, Hurley;[14] ●, Douthit and Dye;[7] ×, Gold and Jolly.[1]

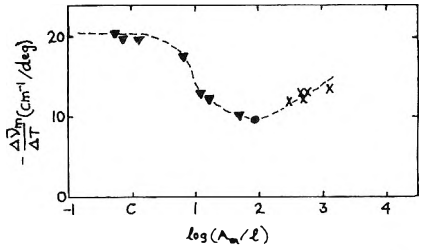

Figure 2. Variation of temperature coefficient of $\bar{\nu}_m$ as solution composition changes at −65°: ▼, this work; ●, Douthit and Dye; ×, Gold and Jolly.

Determination of the Spectra of the Solvated Electron

Spectra of the solvated electron were determined by extrapolating polynomial least-squares fits of the experimental reduced absorbances, $F(\bar{\nu}) = A(\bar{\nu})/A(\bar{\nu}_m)$, *vs.* $A(\bar{\nu}_m)$ to infinite dilution.[14] Details of the extrapolation procedure are given elsewhere.[15] The results of these extrapolations for Na–NH_3 solutions are given in Figure 4. For solutions containing 0.08 M NaI the spectra at infinite dilution were nearly identical with those shown in Figure 4 except for a blue shift of about 50 cm^{-1}. Band parame-

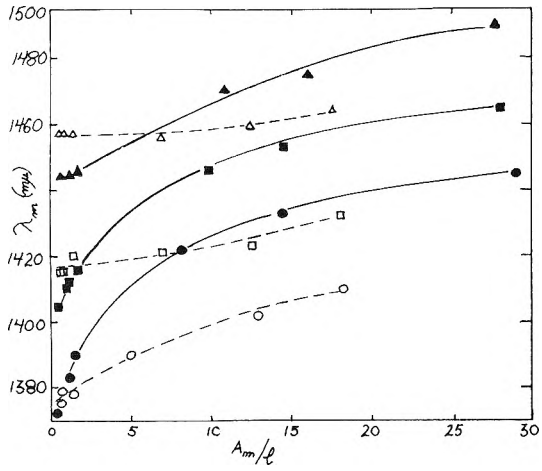

Figure 3. Variation of λ_m with changing optical density for sodium solutions in NH_3 and in NH_3 with added NaI: triangles, −55°; squares, −65°; circles, −75°; open symbols no NaI.

ters for the spectra at infinite dilution are given in Table III. These parameters refer to the absorption band of the solvated electron in pure NH_3 and in NH_3–NaI solutions.

At a given temperature the absorption band of the solvated electron in NH_3 occurs at appreciably higher frequencies than has been previously reported by some investigators. For example, according to Gold and Jolly[1] at −65°, $\bar{\nu}_m$ = 6500 cm^{-1} while Quinn and Lagowski[4,5] report a value of $\bar{\nu}_m$ = 6870 cm^{-1}. Both of these values are lower than the 7067 cm^{-1} obtained in this work. In fact, as we shall see later, the value of $\bar{\nu}_m$ reported by Gold and Jolly actually refers to the absorption band of a species other than the solvated electron. On the other hand, spectra in the most dilute solutions reported by Douthit and Dye[7] resemble the spectra of the solvated electron very closely in both shape and position (see Figure 1).

Application of the Two Absorber Model to the Analysis of the Results

For the most part, the effects reported in this work, *i.e.*, the variation of $\bar{\nu}_m$ with changing temperature, metal, or salt concentration, have been noticed by previous investigators. However, the effect of such concentration changes appears not to have received the attention it deserves, often having been minimized and sometimes even having been overlooked. For example, virtually no mention is made in the recent literature of the variation of $\Delta\bar{\nu}_m/\Delta T$ with changing metal concentration even though values obtained by different investigators differ by as much as a factor of 2. In addition, the reporting of how $\bar{\nu}_m$ depends on metal and on salt concentrations has nearly vanished in recent work in accordance with the view that the spectra of these solutions arise from a single absorbing unit, the solvated electron, independent of metal concentration. Although the concentration dependent shifts are relatively small, as much as 600 cm^{-1} for the band whose breadth at half-height is about 3000 cm^{-1}, these shifts are real and correlate with changes in sodium and sodium iodide concentrations, as well as changes in temperature, as is shown in Figures 1 and 3. Also, $\Delta\bar{\nu}_m/\Delta T$ at −65° varies smoothly as sodium concentration is increased as is shown in Figure 2.

Whether the relatively small changes in spectra associated with changes in metal concentration indicate only minor structural changes in the absorbing species or not is

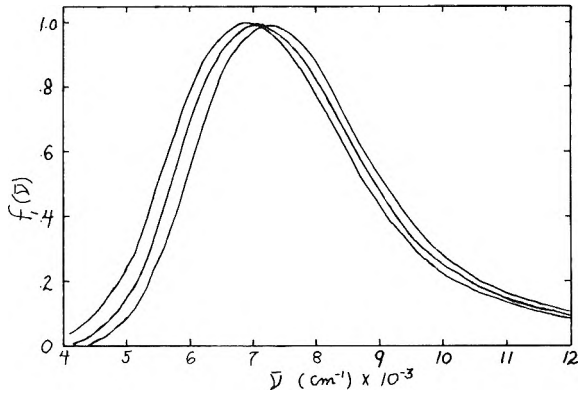

Figure 4. Spectra at infinite dilution (solvated electron spectra): from left to right −55, −65, and −75°.

TABLE III: Band Parameters for $f_1(\bar{\nu})$

	$\bar{\nu}_m$		$\Delta\bar{\nu}_{1/2}$	
t, °C	NS	S[a]	NS	S[a]
−55	6863	6925	3275	3316
−65	7067	7123	3255	3296
−75	7273	7321	3232	3283

[a] [NaI] = 0.08 *M* at −75°.

a moot question which cannot be answered in any definitive fashion with the aid of the present results. However, it is clear that a single absorber model, such as is assumed in conjunction with the ionic cluster model, cannot literally account for the observed compositional dependences of the optical spectra.

On the other hand, a two absorber model can account for spectral shifts that are observed with changing concentrations. For example, both the variation of $\bar{\nu}_m$ and of $\Delta\bar{\nu}_m/\Delta T$ (see Figures 1 and 2) which take place over the same range of metal concentrations can be accounted for by the conversion of one absorber into another. Clearly, the second absorber, *i.e.*, the one which becomes more important at higher metal concentrations, must absorb at relatively longer wavelengths than the solvated electron. Consequently, the red shift of the band produced by addition of NaI to the more concentrated sodium solutions can also be attributed to an increased importance of the second absorber. These observations provide sufficient impetus to subject the data to an analysis which provides a quantitative test of the two absorber model.

An analysis using a two absorber model had been presented previously.[13] For sake of clarity the method of analysis will be reviewed and amplified in the present context. The basic assumption of the two absorber model is that the observed absorbance, $A(\bar{\nu})$, can be expressed as

$$A(\bar{\nu}) = A_1(\bar{\nu}) + A_2(\bar{\nu}) \tag{1}$$

in which the subscripts denote the distinctly absorbing species. In this discussion species 1 is identified as the solvated electron and species 2 is unknown. It is convenient to express the absorbances in terms of normalized line shape functions, *i.e.*

$$\begin{aligned} A(\bar{\nu}) &= F(\bar{\nu})A(\bar{\nu}_m) \\ A_1(\bar{\nu}) &= f_1(\bar{\nu})A_1(\bar{\nu}_{1m}) \\ A_2(\bar{\nu}) &= f_2(\bar{\nu})A_2(\bar{\nu}_{2m}) \end{aligned} \tag{2}$$

in which $\bar{\nu}_m$, $\bar{\nu}_{1m}$, and $\bar{\nu}_{2m}$ are the frequencies of maxi-

mum absorbance for the composite absorption, for the solvated electron, and for the second absorber, respectively. $F(\bar{\nu})$, $f_1(\bar{\nu})$, and $f_2(\bar{\nu})$ are the respective normalized line shapes. Consequently, in terms of these shape functions, we may write

$$F(\bar{\nu}) = xf_1(\bar{\nu}) + yf_2(\bar{\nu}) \quad (3)$$

where $x \equiv A_1(\bar{\nu}_{1m})/A(\bar{\nu}_m)$ and $y \equiv A_2(\bar{\nu}_{2m})/A(\bar{\nu}_m)$. Clearly, both x and y depend on composition, but not on $\bar{\nu}$. In fact $xA(\bar{\nu}_m)$ is proportional to the concentration of the solvated electron and $yA(\bar{\nu}_m)$ is proportional to the concentration of the second species. On the other hand, $f_1(\bar{\nu})$ and $f_2(\bar{\nu})$ depend on frequency alone and are independent of the composition of the solution. It is important to emphasize that the succeeding analysis makes no restrictions of an *ad hoc* character about the f's except that each is normalized to unity at its maximum. In particular, they need not be identical in shape[18] with one another, nor need they have any prescribed functional form such as gaussian or lorentzian.

In order to determine $yf_2(\bar{\nu})$ (and hence $f_2(\bar{\nu})$ since $f_2(\bar{\nu}_{2m}) = 1$) from eq 3 it is necessary to know $F(\bar{\nu})$, x, and $f_1(\bar{\nu})$. Since only the first and last of these quantities are directly determinable from the available experimental data, a less direct procedure must be employed. By rearranging eq 3 we get

$$\frac{F(\bar{\nu})}{f_1(\bar{\nu})} = x + y\frac{f_2(\bar{\nu})}{f_1(\bar{\nu})} \quad (4)$$

In addition, differentiation of this equation with respect to $\bar{\nu}$ yields

$$\partial\left\{\frac{F(\bar{\nu})}{f_1(\bar{\nu})}\right\}\Big/\partial\bar{\nu} = y\,\partial\left\{\frac{f_2(\bar{\nu})}{f_1(\bar{\nu})}\right\}\Big/\partial\nu \quad (5)$$

Clearly, any extremum in $F(\bar{\nu})/f_1(\bar{\nu})$ as a function of $\bar{\nu}$ implies an extremum in $f_2(\bar{\nu})/f_1(\bar{\nu})$ at the same frequency, $\bar{\nu}_0$. But since the ratio $f_2(\bar{\nu})/f_1(\bar{\nu})$ must be independent of the composition of the solution so also must $\bar{\nu}_0$. This requirement of the two absorber model is satisfied by the data since plots of $F(\bar{\nu})/f_1(\bar{\nu})$ *vs.* $\bar{\nu}$, such as those shown in Figure 5, do reveal minimum values all of which occur at the same frequency. As a result we proceed to a more definitive test of the model.

This can be accomplished by first representing the experimental spectra by

$$F(\bar{\nu}) = x_0f_1(\bar{\nu}) + y_0f_2^0(\bar{\nu}) \quad (6)$$

in which f_2^0 is an empirical shape function that is fixed by requiring $f_2^0(\bar{\nu}_0) = 0$ as well as being normalized to unity at its maximum. As a result of this choice

$$x_0 = F(\bar{\nu}_0)/f_1(\nu_0) \quad (7)$$

which ratios are obtained entirely from the experimental data. These values of x_0 determine the amounts of solvated electron spectrum to be subtracted from the $F(\bar{\nu})$ to give the difference spectra, $y_0f_2^0(\bar{\nu})$. Since the empirical shape function is normalized to unity at its maximum, y_0 is simply the value of the difference spectrum at this maximum.

Values of x_0 and y_0 are given in Table IV. The test of the two absorber model is obtained by comparing the empirical shape functions for different amounts of dissolved sodium at a given temperature. A comparison among the empirical shape functions for solutions of Na in NH_3 at $-65°$ is given in Figure 6. These shape functions are independent of Na concentration within experimental error for each set of Na solutions at a given temperature and with and without added NaI. Solutions with y_0 great-

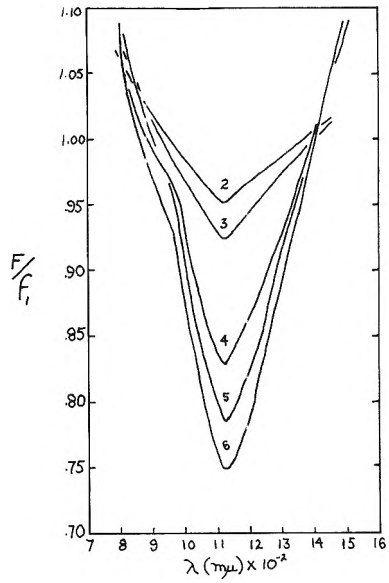

Figure 5. Plots of F/f_1 for Na solutions in NH_3 containing 0.08 *M* NaI at 75° for solutions 2S through 6S.

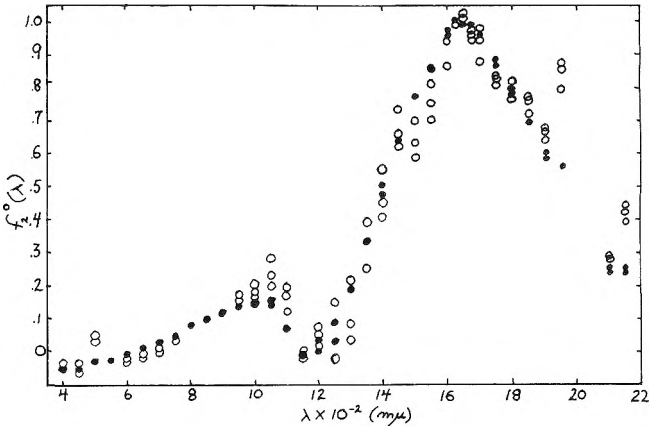

Figure 6. Results of analysis of spectra of solutions 5 and 6 according to eq 2 at −65°: ○, no. 5; ●, no. 6.

TABLE IV: Parameters Resulting from Analysis According to Eq 2

Soln no.	−55°		−65°		−75°	
	x_0	y_0	x_0	y_0	x_0	y_0
1	1.000	0.000	1.000	0.000	0.991	0.014
2	1.000	0.000	1.000	0.000	0.999	0.004
3	1.000	0.000	1.000	0.000	0.986	0.017
4	1.000	0.000	0.990	0.015	0.967	0.047
5	1.000	0.000	0.968	0.050	0.933	0.102
6	0.987	0.022	0.966	0.058	0.920	0.127
7	0.938	0.115	0.891	0.180	0.826	0.266
1S	0.985	0.016	0.979	0.030	0.938	0.087
2S	0.985	0.017	0.975	0.039	0.940	0.085
3S	0.982	0.025	0.970	0.050	0.930	0.106
4S	0.929	0.095	0.887	0.160	0.831	0.230
5S	0.923	0.114	0.865	0.191	0.787	0.290
6S	0.886	0.162	0.823	0.241	0.748	0.334

er than about 0.05 (see Table IV) yielded sufficiently reliable $f_2(\bar{\nu})$'s so that comparisons could be made. Because $f_2^0(\bar{\nu})$ is independent of Na concentration, the data provide further support for the two absorber model for the optical spectra.

The next step leading to a determination of $f_2(\bar{\nu})$ involves relating x_0 and y_0 to the actual concentrations of the two absorbers. Combination of eq 3 and 6 and introduction of $f_2^0(\bar{\nu}) = 0$ leads to

$$x_0 = x + \frac{f_2(\bar{\nu}_0)}{f_1(\bar{\nu}_0)} y \tag{8}$$

so that x_0 depends on the concentrations of both species in a linear way. Furthermore eq 8 may be used with eq 3 and 6 to yield

$$y_0 = \left\{ \frac{f_2(\bar{\nu})}{f_2^0(\bar{\nu})} - \frac{f_2(\bar{\nu}_0)}{f_1(\bar{\nu}_0)} \frac{f_1(\bar{\nu})}{f_2^0(\bar{\nu})} \right\} y \tag{9}$$

Since the quantity in brackets is independent of solution composition y_0 is proportional to y.

We are now in a position to determine values of x by requiring the data to satisfy an appropriate equilibrium relationship. Combination of eq 8 and 9 show that values of x are constrained in their relation to corresponding values of x_0 and y_0 that are obtained from the data by

$$x = x_0 - \beta y_0 \tag{10}$$

in which β is a constant to be determined. Consequently, each choice of β yields a set of x's which may be tested along with the corresponding y_0's in an equilibrium constant expression

$$g(A_m x, A_m y_0) = k \tag{11}$$

in which g is a function of quantities proportional to the concentrations of the two absorbing species and k depends on the equilibrium constant, activity coefficients, concentrations of nonabsorbing species, molar extinction coefficients, and values of spectral shape functions at particular wavelengths. The important point about eq 11 is that k can be assumed to be a constant over a wide range of Na concentration under attainable conditions, *i.e.*, that neither activity coefficients, nor concentrations of nonabsorbing species vary appreciably. We shall assume that these conditions are met for the solutions containing 0.08 *M* NaI. Certainly, the mean ionic activity coefficients and $[Na^+]$ ought to remain virtually constant in such solutions.

The simplest chemical equilibrium which can be assumed is one in which a single solvated electron is converted to a single second absorber. In this particular case eq 11 may be expressed as

$$A_m x / A_m y_0 = k \tag{12}$$

For eq 12 to be satisfied the relative contributions of the two absorbers to spectra at varying Na concentrations must remain fixed. Were this to be the case the value of λ_m would be independent of Na concentration. In fact, as can be seen from the data in Figure 3 and in Table II, λ_m varies appreciably with changing Na concentration. Clearly, the assumed equilibrium cannot account for these variations in λ_m. Consequently, a number of possibilities for the second absorber are ruled out. Important among these are all species with stoichiometry Na or Na_2^+.

A second simple possibility is an equilibrium in which the second absorber is formed through the coalesence of two solvated electrons. In this case, the relationship implied by eq 11 is

$$(A_m x)^2 / A_m y_0 = k \tag{13}$$

Accordingly, the method adopted in testing this pairing equilibrium was to plot $(A_m x)^2$ *vs.* $A_m y_0$ for different values of β until a straight line was obtained. Results of this procedure for −75° are illustrated in Figure 7. Straight line fits were also obtained at −65 and −55° although the scant three data points at −55° made the value of β highly uncertain at this temperature. The straight line fits obtained serve to validate the pairing equilibrium so that the second species is identified as incorporating two solvated electrons. Values of β assigned (see Table V) to the NaI containing solutions were as-

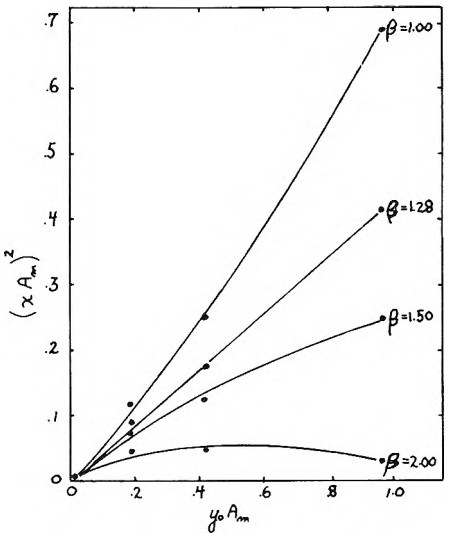

Figure 7. Fitting optical data for NaI containing solutions to pairing equilibrium at −75°.

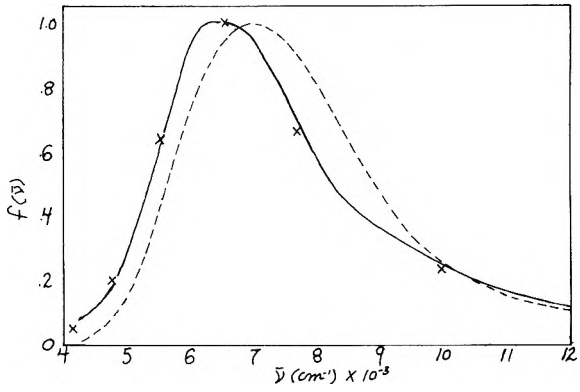

Figure 8. Comparison of spectra at −65°: ---, solvated electron; —, second species; ×, Gold and Jolly.

TABLE V: Band Parameters for $f_2(\nu)$

	ν_m		$\Delta\nu_{1/2}$		
t, °C	NS	S[a]	NS	S[a]	β
−55	6329	6473	3029	2854	1.7[b]
−65	6494	6636	2943	2859	1.47
−75	6653	6780	2830	2768	1.28

[a] [NaI] = 0.08 *M* at −75°. [b] This value of β is a guestimate.

sumed to apply also in calculating values of x for solutions without added NaI.

Finally, with the values of x available, eq 3 in rearranged form is used to determine the spectra of the second absorber. Parameters characterizing $f_2(\bar{\nu})$ at the three temperatures in solutions with and without added NaI are given in Table V. The average temperature coefficient of $f_2(\bar{\nu})$ is between -15 and -20 cm^{-1}/degree, a value similar to that for $f_1(\bar{\nu})$. The shape of $f_2(\bar{\nu})$ is also similar to the shape of $f_1(\bar{\nu})$ as is shown in Figure 8. However, $f_2(\bar{\nu})$ is somewhat narrower than $f_1(\bar{\nu})$ (*cf.* data in Tables III and V), and also has a longer tail into the visible as can be seen in Figure 8. However, the most striking difference is that $f_2(\bar{\nu})$ peaks about 600 cm^{-1} to the red of $f_1(\bar{\nu})$.

Included in Figure 8 for comparison are reduced absorbances calculated from Gold and Jolly's data on their 0.0295 M solution of Na in NH_3. Clearly, Gold and Jolly's spectra resemble $f_2(\bar{\nu})$ very closely and so are characteristic of the second absorber and not the solvated electron.

Acknowledgments. The authors gratefully acknowledge the support of the National Science Foundation. The Cary spectrophotometer was purchased under NSF Grant No. GP-1745.

References and Notes

(1) M. Gold and W. L. Jolly, *J. Inorg. Chem.*, **1**, 818 (1962); C. Hallada and W. L. Jolly, *ibid.*, **2**, 1076 (1963).
(2) D. F. Burow and J. J. Lagowski, *Advan. Chem. Ser.*, **No. 50**, 125 (1965).
(3) M. Gold, W. L. Jolly, and K. S. Pitzer, *J. Amer. Chem. Soc.*, **84**, 2264 (1962).
(4) R. K. Quinn and J. J. Lagowski, *J. Phys. Chem.*, **72**, 1374 (1968).
(5) R. K. Quinn and J. J. Lagowski, *J. Phys. Chem.*, **73**, 2326 (1969).
(6) W. H. Koehler and J. J. Lagowski, *J. Phys. Chem.*, **73**, 2329 (1969).
(7) R. C. Douthit and J. L. Dye, *J. Amer. Chem. Soc.*, **82** 4472 (1960).
(8) E. Huster, *Ann. Phys.*, **33**, 477 (1938).
(9) S. Freed and N. Sugarman, *J. Chem. Phys.*, **11**, 354 (1943).
(10) C. A. Hutchison and R. C. Pastor, *Rev. Mod. Phys.*, **25**, 285 (1953); *J. Chem. Phys.*, **21**, 1959 (1953); *J. Phys. Chem.*, **57**, 546 (1953).
(11) J. L. Dye, "Metal-Ammonia Solutions," Butterworths, London, 1970, p 1.
(12) S. Golden, C. Guttman, and T. R. Tuttle, Jr., *J. Chem. Phys.*, **44**, 3791 (1966).
(13) T. R. Tuttle, Jr., G. Rubinstein, and S. Golden, *J. Phys. Chem.*, **75**, 3635 (1971).
(14) I. Hurley, S. Golden, and T. R. Tuttle, Jr., "Metal-Ammonia Solution," Butterworths, London, 1970, p 503.
(15) G. Rubinstein, Thesis, Brandeis University, 1973.
(16) H. Blades and J. W. Hodgins, *Can. J. Chem.*, **33**, 411 (1955).
(17) H. C. Clark, A. Horsfield, and M. C. R. Symons, *J. Chem. Soc.*, 2478 (1959).
(18) Two normalized functions are considered to be identical in shape if, and only if, they may be superimposed by shifting the frequency scale of the one with respect to the other. If written in terms of the variables $\Delta\bar{\nu}_i = \bar{\nu} - \bar{\nu}_{im}$, in which i denotes the species, two such functions will be identical.

Determination of the Signs of the Fluorine Hyperfine Coupling Constants of Monosubstituted Benzyl Radicals

Joachim Bargon and Karl-Gerhard Seifert*

IBM Research Laboratory, San Jose, California 95193 *(Received June 8, 1973)*

Publication costs assisted by IBM Research

The signs of the fluorine hyperfine coupling constants of monosubstituted benzyl radicals have been determined by CIDNP studies of fluorobenzyl phenyl ketones. The para and ortho couplings are found to be positive whereas the meta coupling is negative.

The signs of isotropic hyperfine coupling constants in free radicals are essential for their theoretical interpretation, but there are only a limited number of methods from which the signs can be deduced in an indirect way: for example, from asymmetric line width variations in electron spin resonance (esr) spectra, from spectra of partially oriented radicals in liquid crystals, or from higher order corrections of the line positions in esr spectra. However, all these methods require some knowledge about other magnetic resonance parameters, such as the g tensor or the dipolar interaction in the radicals, and such data are rarely available. The knowledge is particularly scarce concerning the signs of halogen coupling constants.[1]

Whereas the signs and the magnitudes of proton hyperfine coupling constants a_H can be related to the spin density ρ_c at the adjacent carbon atom according to the McConnell formula[2] $a_H = Q_H\rho_c$ with $Q_H = -29.3$ G, there is some discrepancy in the literature as to how to relate the fluorine hyperfine splitting a_F to the spin density ρ_c.[3,4] At least three different relations have been proposed, but none of them yields satisfactory results. In the simplest approach, a formula similar to McConnell's is assumed $a_F = Q_F\rho_c$,[5] and it has been shown for a number of analogous radicals that $Q_H/Q_F = -2.5$.[1] Accordingly, the fluorine hyperfine coupling constants should always be larger than the corresponding proton hyperfine coupling in the parent fluorine free radicals, and they should have the opposite sign. However, there are difficulties encountered with this simple approach, and in some cases the above relation breaks down. Thus, for example, in phenyl and fluorinated phenyl radicals, the ortho and meta proton and fluorine coupling constants are both positive.[6] On the

other hand, in CH_3 and CF_3, respectively, the proton and fluorine hyperfine coupling constants appear to have opposite signs.[7]

To account for such difficulties, equations with up to three parameters relating a_F with ρ_C, with the spin density at the fluorine atom, and with the spin polarization of the C–F bond have been proposed, but no set of consistent parameters has yet been found.[3] A definite knowledge of the signs of the fluorine hyperfine coupling constants in odd alternate carbon radicals, where the signs of the spin densities at the various carbon atoms are obvious, would be most useful: for example, in allyl, benzyl, or cyclohexadienyl radicals.

We wish to report the determination of the signs of the fluorine hyperfine coupling constants in mono-fluorinated benzyl radicals with the chemically induced dynamic nuclear polarization (CIDNP) method. The rules of this method relate the sign of the observed nuclear spin polarization (enhanced absorption or emission) with four parameters: the spin multiplicity of a radical pair, the g value difference of the radicals forming the radical pair, the pathway to the diamagnetic reaction product (separation or combination product of the pair) in which the nuclear spin polarization is observed, and the signs of the isotropic hyperfine coupling constant of the nucleus under investigation. For detailed description see ref 8 and 9.

If three of these parameters are known, the fourth can be determined from CIDNP studies. We have chosen a system involving the three isomeric mono-fluorinated benzyl radicals,[10] where the chemical details and all other magnetic resonance parameters but the signs of the fluorine hyperfine coupling constants are known from previous CIDNP studies, namely, the photolysis of benzyl phenyl ketone.[11] We have studied the photolysis of fluorobenzyl phenyl ketones with fluorine CIDNP.

Experimental Section

The fluorobenzyl phenyl ketones were prepared according to Fischer, *et al.*,[12] by Friedel-Crafts acylation of benzene with fluorophenylacetyl chlorides. The phenylacetyl chlorides were obtained by refluxing the commercially available fluorophenyl acetic acids (PCR, Inc., Gainesville, Fla.) with thionyl chloride.

Solutions of the fluorobenzyl phenyl ketones in carbon tetrachloride were irradiated inside the modified probe of a Varian HA 60 nmr spectrometer in an all-quartz apparatus at room temperature. The light source was a 5 kW Hanovia 932-B39 high-pressure mercury–xenon lamp. The light was filtered through water to reduce the warming up of the sample.

Results and Discussion

Figure 1 shows the benzylic proton region of the proton nmr spectrum before (A) and during (B) irradiation of the *p*-fluorobenzyl phenyl ketone. The absorption of the CH_2 group in the ketone at σ = 4.4 ppm downfield from TMS turns into emission upon irradiation. Simultaneously, a new enhanced absorption line of the product *p*-fluorophenyl-2,2,2-trichloroethane is observed at σ = 4.1 ppm. In agreement with earlier CIDNP studies of fluorine-free benzyl phenyl ketones[11] we explain the polarization of these products with the following scheme (Figure 2).

Thus benzyl phenyl ketone (BPK) decomposes from a triplet state into a pair of a benzyl and a benzoyl radical with triplet multiplicity of the two unpaired electrons.[11] The g values of the two radicals are known[13] and quite

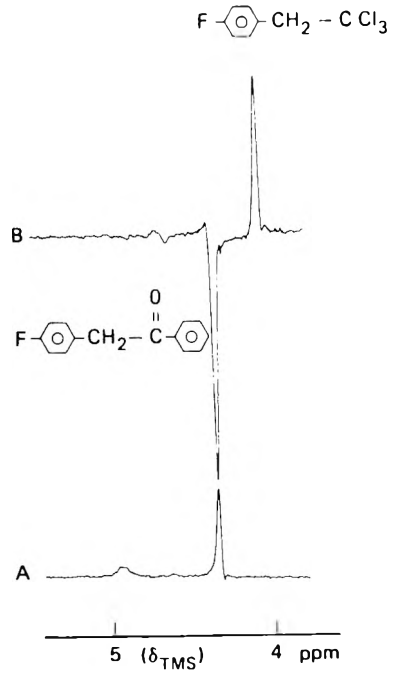

Figure 1. (a) ^{1}H nmr spectrum of the benzylic region of *p*-fluorobenzyl phenyl ketone. (b) CIDNP spectrum during photolysis.

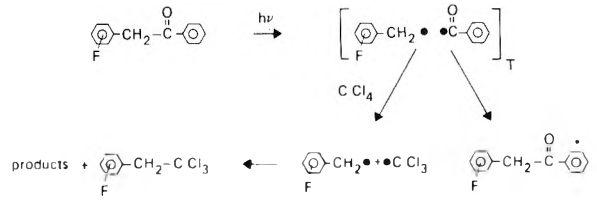

Figure 2.

different. This g value difference gives rise to a net polarization of the nuclear spins in the reaction products; *i.e.*, they appear in enhanced absorption or emission. The quantum yield for product formation is low in this system,[14] probably because of a high degree of recombination of the radical pair in the solvent cage. The radicals diffusing out of the solvent cage attack the solvent and abstract chlorine atoms or they combine with other radicals, for example, with the trichloromethyl radical resulting from the solvent after chlorine abstraction. Because of the intersystem crossing in the triplet radical pairs, which is nuclear spin dependent and which has to occur prior to the cage return, the products and the starting material show CIDNP. Of the products, the recombination product of the benzyl radical with the trichloromethyl radical gives rise to the strongest CIDNP.

From the above and the rules of CIDNP,[8,9] it follows that an emission line resulting from a nucleus in the benzyl group of the starting material indicates a negative hyperfine coupling constant of the corresponding nucleus in the benzyl radical, whereas an enhanced absorption line indicates a positive hyperfine coupling constant. Conversely, in the product *p*-fluorophenyl-2,2,2-trichloroethane (*p*-FPTE) the opposite relation holds; *i.e.*, emission for a positive and absorption for a negative coupling constant.

As the same rules hold for fluorine nuclei, we have studied the *o*-, *m*-, and *p*-monofluorobenzyl phenyl ketones with both proton and fluorine CIDNP and came to the following conclusions: the proton spectra showed

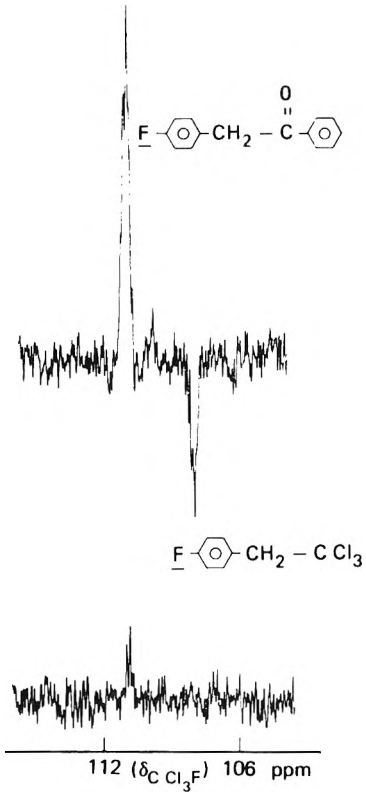

Figure 3. (a) ^{19}F nmr spectrum of *p*-fluorobenzyl phenyl ketone. (b) ^{19}F CIDNP spectrum during photolysis.

emission for the benzylic protons of the starting material and enhanced absorption of those for the isomeric FPTE in all three cases, indicating that the three fluoro ketones decomposed photolytically in the same way as the fluorine-free parent ketone.

Figure 3 shows the ^{19}F nmr spectrum before (A) and during (B) irradiation of the *p*-FBPK. The enhanced absorption of the fluorine nucleus in the starting material at $\delta(CFCl_3)$ = 110 ppm and the emission of the fluorine in the product *p*-FPTE indicate a *positive* sign of the *para* fluoro coupling in the benzyl radical. Analogously, we have found a *positive* sign of the *ortho* fluorine coupling. The relative changes of the intensities are in agreement with the absolute magnitudes of the known values $|a_F(\text{ortho})|$ = 8.17 G and $|a_F(\text{para})|$ = 14.53 G, which have been measured in esr spectra.[15] The meta isomer showed the inverse behavior relative to the ortho and para isomers in the fluorine CIDNP studies, from which we conclude that the *meta* fluorine hyperfine coupling constant in the benzyl radical is *negative*.

To assure these conclusions we have generated the three isomeric FPTE and their precursors, *i.e.*, the pairs of a trichloromethyl and a fluorobenzyl radical, by an independent chemical pathway, namely, by photolysis of di-*tert*-butyl peroxide in a mixture of fluorotoluenes and CCl_4. All these compounds are commercially available. Thus we observed, for example, emission for the *p*-FPTE, which proves the correctness of the above results, *i.e.*, a positive hyperfine coupling constant for the para fluorine in the benzyl radical.[16]

These results agree with earlier assumptions of Hudson, *et al.*,[17] who calculated the signs and the values of the fluoro hyperfine coupling constants in fluorobenzyl radicals with the Pople INDO and with the McLachlan method.

Our observations are also in line with the findings of Sinclair and Kivelson, who derived $a_F > 0$ for *p*-fluorophenyldiphenylmethyl radicals from line width variations in esr spectra.[4]

The exact knowledge of the fluorine hyperfine coupling constants is of great importance for future CIDNP studies involving the fluorobenzyl radicals, and we have already used them successfully in order to determine the photolytic decomposition scheme of phenylacetaldehydes in solution, which cleave into benzyl and formyl radicals.[18]

Acknowledgment. We wish to thank F. R. Rodgers for preparing the fluorobenzyl phenyl ketones.

References and Notes

(1) A. Hudson and K. D. J. Root, *Advan. Magn. Resonance*, 5, 1 (1971).
(2) H. McConnell, *J. Chem. Phys.*, **24**, 764 (1956).
(3) G. Fraenkel, J. Kaplan, and J. Bolton, *J. Chem. Phys.*, **42**, 955 (1965).
(4) J. Sinclair and D. Kivelson, *J. Amer. Chem. Soc.*, **90** 5074 (1968).
(5) A. Maki and D. Geske, *J. Amer. Chem. Soc.*, **83**, 1852 (1961).
(6) J. Bargon, unpublished results.
(7) R. Fessenden and R. Schuler, *J. Chem. Phys.*, **43**, 2704 (1965).
(8) G. L. Closs, *Proc. Int. Congr. Pure Appl. Chem., XXIIIrd Spec. Lect.*, **4**, 19 (1971).
(9) R. Kaptein, *J. Amer. Chem. Soc.*, **94**, 6251 (1972).
(10) CIDNP studies involving fluorobenzyl radicals have been conducted previously, but the signs of the hfs coupling constants have not yet been deduced, *cf.*, J. W. Rakskys, *Chem. Commun.*, 578 (1970).
(11) G. L. Closs and D. R. Paulson, *J. Amer. Chem. Soc.*, **92**, 7229 (1970).
(12) A. Fischer, J. Packer, and J. Vaughan, *J. Amer. Chem. Soc.*, **83**, 4208 (1961).
(13) (a) P. J. Krusic and T. A. Rettig (*J. Amer. Chem. Soc.*, **92**, 722 (1970)) report the *g* value of the benzoyl radical to be 2.0015, while Paul and Fischer claim a lower value (*g* = 2.0008) (H. Fischer in "Free Radicals," Vol. 2, J. Kochi, Ed., Wiley-Interscience, p 271 ff). (b) R. V. Loyds and D. E. Woods (*Mol. Phys.*, **20**, 735 (1971)) determined the *g* value of the benzyl radical by esr (*g* = 2.0025). Closs has measured the same value by CIDNP (ref 8).
(14) H. G. Heine, private communication.
(15) A. Hudson and J. W. E. Lewis, *Mol. Phys.*, **19**, 241 (1970).
(16) Additional evidence for $a_F(\text{para}) > 0$ follows from the phase of the multiple effect in ref 10.
(17) H. G. Benson, A. Hudson, and J. W. E. Lewis, *Mol. Phys.*, **21**, 935 (1971).
(18) J. Bargon and K. G. Seifert, unpublished results.

Location of Cations in Synthetic Zeolites X and Y. III. Potassium–Alkylammonium Y Zeolites

W. J. Mortier,* M. L. Costenoble, and J. B. Uytterhoeven

Centrum voor Oppervlaktescheikunde en Colloidale Scheikunde, De Croylaan 42, B-3030 Heverlee, Belgium

(Received March 7, 1973)

Publication costs assisted by the Instituut voor Wettenschappelijk onderzoek in Nijverheid en Landbouw

The exchange of monoalkylammonium ions into potassium Y zeolite proceeds to certain limits. X-Ray powder diffraction and structure analysis were preformed on KY samples partially exchanged with NH_4^+, $CH_3NH_3^+$, $C_2H_5NH_3^+$, or $C_3H_7NH_3^+$. The samples exhibit a gradual change of physicochemical properties. Variations in the distribution pattern of the K^+ ions are related to the state of hydration of the samples. Although the alkylammonium ions were not located, some speculations can be made on the exchange mechanism.

Introduction

The exchange of alkylammonium ions in Linde Molecular Sieves X and Y has been studied by Theng, *et al.*[1] These authors also review earlier work of other investigations in the same area. They found that each organic ion is characterized by a given maximum exchange limit. This limit decreased linearly with increasing molecular weight of the organic ions and was also influenced by the nature of the outgoing ions. It was postulated by Vansant, *et al.*, that the maximum exchange limit was not exclusively due to space requirements but was dependent on thermodynamic conditions.[2] A satisfactory explanation has not been given thus far.

The present structural study has been undertaken to help the understanding of the exchange phenomena by locating the unexchanged inorganic cations (potassium). It was not our intention to locate the alkylammonium ions, since they hardly fit the symmetry of the faujasite framework.

Experimental Section

A Linde Zeolite Y, containing 54.7 exchangeable cations per unit cell, was saturated with K^+ ions by repeated exchanges with a 0.1 *N* KCl solution followed by washing. Aliquots of this sample (~3 g) were equilibrated at room temperature during three days in 200 ml of 0.5 *N* solutions of ammonium or alkylammonium chlorides. The alkylammonium ions (RNH_3^+) used were methyl-, ethyl- and propylammonium. With NH_4^+ a second exchange was performed to ensure maximum exchange. Only one equilibration was made with the alkylammonium ions. It was the intention to replace only an amount of K^+ ions approximately equal to the "loosely bound" or "unlocated" ions. From previous work[3] we know that there are 20.1 such ions per unit cell in the hydrated KY sample. The propyl- and ethylammonium samples were indeed exchanged to that extent, but the amount of methylammonium ions was significantly higher. The samples were washed free from excess electrolyte, air-dried at room temperature, and stored in an 80% humidity atmosphere until they reached constant weight. The unit cell composition of the samples was inferred from the weight loss upon calcination at 800° and from the alkylammonium content determined by the microkjehldahl method.[1] The unit cell composition of the samples is given in Table I. The symbols quoted in that table contain the initials of the exchangeable cations and are used throughout the text.

The X-ray method was essentially the same as that used in previous work[3,4] on the distribution of the K^+ ions in the KY samples. Therefore we only mention here the most important definitions and specific modifications used for this work.

The spectra were recorded on a Phillips diffractometer at a scanning rate of 0.02°/min. For the estimation of the peak intensities a least-squares program was used which fitted an experimental profile with a set of theoretical Cu $K\alpha_1$–Cu $K\alpha_2$ combined line profiles. The theoretical profile for KPrY was a Gauss function. For the other samples we used an experimental profile obtained by the method described by Gangulee.[5] In this way the intensity ratio of overlapping peaks could be determined accurately. Details of this procedure were published elsewhere.[6]

The least-squares refinement was performed using a block-diagonal approximation as described earlier.[3] This program refined on the basis of structure factors. A modified version of the full-matrix program POWOW,[7] refining on the basis of intensities, was used for the statistical treatment explained further. It must be remembered that the standard deviations obtained in the block-diagonal approach are too small.

To strengthen the validity of our conclusions we made some statistical comparisons. A subset of q parameters ($\hat{\beta}_i$) of one structure is statistically compared to the same set of parameters ($\hat{\beta}_0$) of a reference structure using the expression

$$Q = \frac{(\hat{\beta}_i - \hat{\beta}_0)' S_1 (\hat{\beta}_i - \hat{\beta}_0)}{2qs^2} = F_{q,n-p}(\alpha)$$

S_1 is the $q \times q$ matrix on the coefficients of the normal equations, $s^2 = \Sigma(\sqrt{w_i}\Delta_i)^2/(n - p)$, n is the number of observations ($n = 128$), and p is the total number of parameters. If $Q > F_{q,n-p}(\alpha)$ we may reject the equality of the two-parameter vectors with probability α to take a wrong decision. The test is performed on a conditional basis, *i.e.*, that the remaining $p-q$ parameters are not considered. The same method was applied to the hydrated

and dehydrated K zeolites X and Y and described elsewhere in full detail.[8]

The application of liquid scattering functions to unlocated scattering material has been successful in the study of the hydrated KX and KY zeolites.[3] Therefore we applied a similar technique in this work. RNH_3^+ and water molecules were considered as unlocated material. They were supposed to be randomly located in a sphere with a radius of 2.3 Å inside the cuboctahedra, or in a shell formed by two concentric spheres with radii R_1 and R_2 in the large cages. An additional temperature factor of 15 Å^2 was applied. In fact, the occupancy of the sites I′, II′, and II must be considered as superimposed on a background, since the sphere of statistically distributed scattering material includes these sites. The residuals were defined as

$$R_F = \sum_{hkl}(k|F_o| - |F_c|)/\sum_{hkl} k|F_o|$$

and

$$R_I = \sum_{N}(kI_o - I_c)/\sum_{N} kI_o$$

The interatomic distances and bond angles were calculated using the ORFFE program.[9]

We used the cation site notation proposed by Smith.[10] The sites I (16 per unit cell) are inside the hexagonal prism. The sites I′ (32 per unit cell) are inside the cuboctahedron sharing a six ring of oxygen ions with the sites I. Sites II and II′ (32 per unit cell of each) are inside the supercages and inside the cuboctahedra, respectively, sharing the free six-membered ring of oxygen ions of the cuboctahedra. Sites III are inside the supercages, associated with a four-membered ring of oxygen ions of the cuboctahedra. In former work[3,4] we defined sites III′ as being inside the supercages and composed of four oxygen ions (O_4–O_1–O_1–O_4). Evidence for the location of cations on sites III′ was given by Mikovsky, *et al.*[11]

Results

The unit cell compositions and parameters are given in Table I. The structure parameters are listed in Table II, together with the R_F and R_I values. The interatomic distances, the bond angles, and the distances between the center of the large cage or of the cuboctahedron and the surrounding atoms are collected in Table III.

For the samples KPrY and KEtY an electron density peak was obtained at site III on a difference Fourier map in a plane passing through this site. For the sample KAmY difference Fourier calculations located an electron density peak at the site II′. These peaks seemed to refine by least squares, but the uncertainty is large. They will not be discussed further.

Table IV is a summary of data characterising the samples. It contains the number of water molecules and the number of K^+ and RNH_3^+ ions per unit cell. Assuming that the electron density at the ion exchange sites is due to K^+ or water molecules (at site II) a cation distribution was calculated as given in Table IV. The data obtained earlier for KY hydrated[3] and KY dehydrated[4] are included in that table for comparison. A list of I_o and I_c values is available. (See the paragraph of the end of this article regarding supplementary material.)

The statistical comparisons are presented in Table V. Two different parameter vectors are considered: (i) the 10 positional framework parameters and (ii) the same framework parameters together with the two positional parameters and the two occupancy factors of the potassium ions on the sites I′ and II. The matrix S_1 was obtained from the second cycle of a full matrix refinement with POWOW. The reference vector β_0 is obtained by POWOW. Together with the variance–covariance matrix it defines the confidence region for this vector. The vectors to compare (β_0) are those given in Table II. $n - p$ is close to 100, and $F_{q,n-p}(\alpha)$ is not sensitive to small changes in $n - p$. Therefore we included in Table V a list of $F_{q,100}(\alpha)$ for several values of (α). In Table V we *italicized* the Q values which indicate that there is no significant difference between a given structure and the selected reference structure, with a probability of 0.995. As can be seen in Table V, each particular sample has been taken as a reference structure for the other samples, which resulted in the most complete statistical comparison between the investigated samples.

TABLE I: Composition of the Samples and Unit Cell Parameter a_0

Symbols	Composition	a_0, Å[a]
KPrY	$Pr_{18.8}K_{35.9}Al_{54.7}Si_{137.3}O_{384}\cdot 101H_2O$	24.754 (3)
KEtY	$Et_{23.4}K_{31.3}Al_{54.7}Si_{137.3}O_{384}\cdot 111H_2O$	24.748 (2)
KMeY	$Me_{27.5}K_{27.3}Al_{54.7}Si_{137.3}O_{384}\cdot 124H_2O$	24.742 (3)
KAmY	$Am_{39.5}K_{15.2}Al_{54.7}Si_{137.3}O_{384}\cdot 190H_2O$	24.739 (3)

[a] Obtained by extrapolation against $\cos^2\theta/\sin\theta$.[3]

Discussion

The Framework Parameters. With the exception of KPrY the frameworks of the different samples are not significantly different from each other and from the original hydrated sample KY. The significant difference of KPrY is clearly apparent in Table VA in which the lower row (KPrY compared to all the other samples) and the last vertical column (KPrY taken as a reference) contain high values for $F_{10,100}$ (0,005). The similarity between the other samples is confirmed by all the values in the lower left half of Table VA (italicized). The figures marked with an asterisk in the upper right half of that table do not confirm the corresponding figures of the other half, but such exceptions can be due to the size and shape of the confidence region of the reference structure. Differing residuals (Table II) are an indication of more or less well defined structures and subsequently also of the different size and shape of the confidence region.

These observations become especially meaningful when they are compared to the statistical results obtained with the framework parameters of hydrated and dehydrated synthetic faujasites with widely different Al contents (between 49 and 85 aluminum atoms per unit cell).[8] It was found for these samples that there was no significant difference between the framework of the hydrated samples. A significant difference was found between the framework of the hydrated and dehydrated zeolites. This was taken as proof that dehydration results in a considerable distortion of the framework. The absence of water molecules or the increased cation population of site I after dehydration were considered as possible reasons for these distortions.[8]

The difference in framework between KPrY and all the other samples indicates a distortion in the framework of KPrY. These distortions can be ascribed to the same causes as in the dehydrated synthetic faujasites.[8] Indeed, the data in Table IV reveal a marked decrease of the

TABLE II: Atomic Parameters[a] and Residuals for the Samples K-$C_3H_7NH_3$-Y, K-$C_2H_5NH_3$-Y, K-CH_3NH_3-Y, and K-NH_4-Y

		KPrY	KEtY	KMeY	KAmY
Si	x	0.1245 (2)	0.1241 (2)	0.1245 (2)	0.1253 (2)
	y	0.9445 (2)	0.9452 (2)	0.9446 (2)	0.9450 (2)
(192i)	z	0.0346 (2)	0.0353 (2)	0.0354 (2)	0.0356 (5)
	B	1.29 (14)	1.68 (12)	2.23 (10)	2.15 (10)
O_1	$x = -y$	0.1080 (7)	0.1062 (9)	0.1044 (7)	0.1073 (7)
(96h)	z	0.0	0.0	0.0	0.0
	B	0.22 (30)	0.70 (38)	1.12 (30)	0.57 (31)
O_2	$x = y$	0.2491 (8)	0.2502 (11)	0.2524 (9)	0.2535 (10)
(96g)	z	0.1397 (6)	0.1389 (6)	0.1392 (6)	0.1376 (8)
	B	1.30 (33)	2.20 (50)	2.38 (35)	4.72 (53)
O_3	$x = y$	0.1688 (9)	0.1723 (10)	0.1726 (9)	0.1722 (9)
(96g)	z	0.9684 (7)	0.9645 (8)	0.9646 (6)	0.9664 (6)
	B	3.32 (47)	3.25 (50)	3.27 (37)	2.23 (36)
O_4	$x = y$	0.1795 (10)	0.1776 (13)	0.1785 (11)	0.1792 (10)
(96g)	z	0.3232 (7)	0.3239 (9)	0.3213 (8)	0.3216 (7)
	B	4.67 (50)	6.52 (65)	6.79 (52)	4.71 (50)
K(I)	$x = y = z$	0.0	...	...	...
	Occ.	0.338 (37)	...	...	...
	B	9.28 (2.03)	...	...	...
K(I′)	$x = y = z$	0.0778 (17)	0.0806 (22)	0.0797 (17)	0.0788 (22)
	Occ.	0.515 (22)	0.580 (30)	0.367 (17)	0.260 (16)
(32e)	B	3.48 (55)	6.91 (83)	1.75 (54)	0.12 (84)
K(II)	$x = y = z$	0.2620 (17)	0.2590 (24)	0.2616 (22)	0.2635 (48)
(32e)	Occ.	0.470 (19)	0.457 (23)	0.319 (17)	0.218 (23)
	B	3.53 (59)	2.47 (88)	0.68 (77)	4.10 (2.01)
H_2O(II′)	$x = y = z$	...	...	...	0.1999 (168)
(32e)	Occ.	...	...	...	0.169 (67)
	B	...	...	...	10.38 (8.88)
H_2O(III)	$x = y$	−0.125 (0)	−0.125 (0)	...	...
	z	0.2383 (259)	0.1221 (240)	...	...
(48f)	Occ.	0.121 (36)	0.097 (38)	...	...
	B	0.28 (4.54)	0.0 (5.23)	...	...
H_2O	$x = y = z$	0.125	0.125	0.125	0.125
(8a)	R_1, R_2	2.3; 0.0	2.3; 0.0	2.3; 0.0	2.3; 0.0
	n molec.	28.24	16.0	32	32
	B	15	15.0	15	15
H_2O	$x = y = z$	0.375	0.375	0.375	0.375
(8b)	R_1, R_2	5.75; 2.0	5.7; 2.0	5.7; 0.0	5.7; 0.0
	n molec.	136.6	164	160	240
	B	15	15	15	15
R_I		0.1953	0.1785	0.1742	0.1625
R_F		0.1276	0.1298	0.1265	0.1181

[a] The standard deviations are indicated in parentheses.

water content of the sample KPrY and a K^+ content of site I which is similar to that of the dehydrated KY sample. In all the other samples site I was found to be empty, as was the case in the hydrated KY sample.

The Population of Exchange Sites. The incomplete exchange in this type of material has generally been ascribed to ion sieve effects,[1] but an unambiguous proof for this assumption was never given. Considering the size of the alkylammonium ions it is reasonable to believe that they remain inside the large cavities. The location of the ammonium ions is not unambiguous. NH_4^+ and K^+ have the same radius and it is not clear why NH_4^+ would be excluded from the cuboctahedra while K^+ ions can freely move through the six-membered ring of oxygen ions. On the basis of these assumptions we can translate the electron density into a population of the different sites by K^+ ions or H_2O molecules as presented in Table IV.

Inclusion of the population and positional parameters of the sites I′ and II into the statistical comparison (Table VB) reveals that there is a significant difference between the different samples, except maybe between KAmY and KMeY. KPrY is also significantly different from all the others by the high population of site I which is not included in the parameter vector β.

The interatomic distances (Table III) do not enable us to make a clear distinction between potassium ions and water molecules located on sites II. From a distance of 3.26 Å between site II and O_2 Baur[12] concluded that this site was occupied by water molecules. The distance K-O_2 was found to be 2.8 Å in the hydrated samples.[3] The distance site II-O_2 of 3 Å found in this work indicates that at least an important fraction of this site is occupied by K^+ ions. The distance site I′-O_3 in all the samples is in agreement with an occupancy by K^+ ions.

The KPrY sample has a population of K^+ inside the small cavities which is comparable to that of the dehydrated sample KY. It was stated for the hydrated samples KY and KX as well, that one-fourth of the cations were

TABLE III: Interatomic Distances[a] (Å) and Bond Angles[a] (deg) for the Samples KPrY, KMeY, KEtY, and KAmY

		KPrY	KEtY	KMeY	KAmY
Tetrahedron					
$T-O_1$		1.61 (2)	1.61 (2)	1.58 (2)	1.63 (2)
$T-O_2$		1.67 (2)	1.65 (3)	1.65 (2)	1.63 (2)
$T-O_3$		1.68 (2)	1.63 (3)	1.64 (2)	1.66 (2)
$T-O_4$		1.68 (3)	1.68 (4)	1.65 (3)	1.64 (2)
Mean		1.66	1.64	1.63	1.64
$T-O_1-T$		133.9 (1.2)	137.2 (1.8)	142.6 (1.2)	136.7 (1.1)
$T-O_2-T$		141.8 (1.2)	145.4 (2.5)	148.3 (1.2)	153.5 (1.5)
$T-O_3-T$		138.6 (1.1)	145.6 (2.8)	144.2 (1.0)	142.2 (1.0)
$T-O_4-T$		141.8 (1.3)	141.5 (3.1)	144.6 (1.5)	142.8 (1.4)
Mean		139.0	142.4	144.4	143.8
O_1-T-O_2		117.8 (8)	114.8 (1.3)	111.4 (0.8)	110.6 (1.0)
O_1-T-O_3		119.2 (9)	112.8 (1.6)	111.1 (0.9)	113.6 (0.9)
O_1-T-O_4		106.0 (9)	107.0 (1.9)	111.8 (1.0)	108.1 (0.9)
O_2-T-O_3		101.1 (9)	104.9 (1.9)	106.0 (0.9)	104.9 (1.0)
O_2-T-O_4		107.4 (9)	110.4 (2.2)	108.5 (1.0)	111.0 (1.1)
O_3-T-O_4		104.2 (1.1)	106.7 (1.6)	107.7 (1.2)	108.7 (1.2)
Mean		109.3	109.4	109.4	109.8
O_1-O_2		2.81 (3)	2.74 (4)	2.67 (3)	2.68 (3)
O_1-O_3		2.84 (2)	2.69 (4)	2.65 (2)	2.75 (2)
O_1-O_4		2.63 (3)	2.64 (4)	2.68 (3)	2.65 (3)
O_2-O_3		2.59 (3)	2.74 (4)	2.63 (3)	2.61 (3)
O_2-O_4		2.70 (3)	2.74 (5)	2.68 (3)	2.70 (3)
O_3-O_4		2.66 (3)	2.65 (4)	2.66 (3)	2.68 (3)
Mean		2.71	2.70	2.66	2.68
Cations					
K(I)	$-O_3$	2.95 (2)	2.86 (3)	2.85 (2)	2.85 (2)
	$-K(I')$	3.34 (4)	3.48 (3)	3.42 (4)	3.38 (5)
	$-O_2$	3.46 (2)	3.43 (4)	3.65 (2)	3.41 (2)
	O_1	3.78 (2)	3.72 (2)	3.45 (1)	3.75 (2)
K(I′)	$-O_3$	2.71 (5)	2.89 (5)	2.85 (4)	2.78 (6)
	$-O_2$	3.10 (5)	3.18 (4)	3.23 (5)	3.23 (6)
K(II)	$-O_2$	3.06 (4)	2.99 (6)	3.05 (6)	3.13 (12)
	$-O_4$	3.26 (5)	3.27 (6)	3.26 (6)	3.28 (12)
H_2O(III)	$-O_1$	4.48 (46)	3.15 (7)	...	...
	$-O_4$	4.51 (58)	2.19 (3)	...	...
	$-O_2$	5.04 (31)	4.34 (41)	...	...
	$-O_3$	...	2.71 (47)	...	...
K(II′)	$-O_2$	...	...	...	2.43 (41)
	$-O_4$	...	...	...	3.10 (41)
	$-K(I')$	...	...	...	3.16 (42)
Framework					
Center cuboctahedron					
	$-K(I')$	2.02 (4)	1.88 (3)	1.94 (4)	1.98 (5)
	$-O_3$	4.17 (2)	4.30 (4)	4.30 (2)	4.26 (2)
	$-O_2$	4.35 (2)	4.39 (3)	4.47 (2)	4.51 (2)
	$-T$	5.00 (1)	4.97 (1)	4.98 (1)	4.97 (1)
	$-O_4$	5.25 (2)	5.26 (5)	5.21 (2)	5.22 (2)
	$-K(I)$	5.36 (0)	...	5.36 (0)	5.36 (0)
	$-K(II')$	...	...	...	3.21 (41)
Center large cage					
	$-site(III)$	3.38 (64)	6.26 (60)	...	...
	$-K(II)$	4.84 (4)	4.97 (5)	4.86 (5)	4.78 (12)
	$-O_4$	6.96 (2)	7.02 (3)	7.00 (3)	6.98 (2)
	$-O_2$	7.30 (2)	7.30 (4)	7.24 (2)	7.25 (2)
	$-O_1$	7.31 (2)	7.35 (2)	7.39 (2)	7.32 (2)
	$-T$	7.55 (1)	7.57 (1)	7.56 (1)	7.55 (1)

[a] The standard deviations are indicated in parentheses.

located in the small cavities in order to obtain an equal statistical neutralization of the negative charges supposed to be spread statistically over the different types of oxygen ions.[3] This would amount to 13.7 ions per unit cell for the present samples. This value is reached and even exceeded for the samples KPrY and KEtY, indicating that not only KPrY but also KEtY has a tendency to behave like a dehydrated KY. In the samples KMeY and KAmY the population of site I′ is definitely lower than 13.7. The rule of the statistically uniform neutralization of charges seems

TABLE IV: Summary of Data on the K–Alkylammonium Y Samples, the Hydrated KY Samples, and the Dehydrated KY Sample

	KY Deh	KPrY	KEtY	KMeY	KAmY	KY Hydr
K^+/U.C.	54.7	35.9	31.3	27.2	15.2	54.7
H_2O/U.C.	...	101	111	124	190	240
NH_4^+ or RNH_3^+/U.C.	...	18.8	23.4	27.5	39.5	...
Site I (K)	5.4	5.4	...	...	...	1.3
Site I′ (K)	18.1	16.5	18.6	11.8	8.4	13.3
Sites I + I′ (all K^+)	23.5	21.9	18.6	11.8	8.4	14.6
Site II (K)	26.8	15	14.6	10.2	7.0	20.0
or (H_2O)	...	30	29.2	20.5	14.1	...
Unloc. K^+	4.4	−0.5	−1.9	5.2	−0.2	20.1

TABLE V: Statistical Comparison of Some Framework and Cation Parameters

A. q = 10; Positional Framework Parameters

Reference	KY hydr	KAmY	KMeY	KEtY	KPrY
KY hydr	*0.93*	6.62*	4.03*	5.34*	4.40
KAmY	2.81*	*2.32*	*1.51*	5.15*	4.31
KMeY	*2.27*	*1.66*	*0.39*	2.82*	4.88
KEtY	*1.15*	*2.24*	*1.14*	*1.18*	2.66
KPrY	2.78	6.33	3.65	6.14	2.62

α	$F_{10,100}(\alpha)$
0.10	1.67
0.05	1.94
0.025	2.20
0.01	2.46
0.005	2.77

B. q = 14; Positional Framework Parameters + Positional Parameters and Occupancy Factors of the Cations in Site I′ and II

Reference	KY hydr	KAmY	KMeY	KEtY	KPrY
KY hydr	*0.84*	36.14	13.3	8.20	8.89
KAmY	8.14	*2.49*	*1.10*	13.2	6.03
KMeY	4.16	5.16	*0.49*	4.87	4.23
KEtY	2.25	15.4	3.90	*1.22*	3.83
KPrY	*2.32*	21.1	6.77	4.86	*1.73*

α	$F_{14,100}(\alpha)$
0.10	1.58
0.05	1.81
0.025	2.02
0.01	2.29
0.005	2.52

not to hold for these systems with large cations, although the total amount of K^+ ions in the sample is sufficient to satisfy that rule.

Relevance of These Data for the Understanding of the Ion-Exchange Behavior. Theng, *et al.*,[1] and Vansant[13] have stated that the limited exchange of the alkylammonium ions in zeolites X and Y cannot be understood only on the basis of space requirements of the bulky ions. The present data show that ion sieve effects, *i.e.*, the inaccessibility of the small cavities for large ions, cannot be considered either as the exclusive factor responsible for incomplete exchange. Indeed, the sample KAmY was saturated by NH_4^+ to the maximum possible limit,[1] and there is still an appreciable number of K^+ ions in the large cavities.

The samples KMeY, KEtY, and KPrY were not exchanged to the maximum possible level. The two latter samples already have a population of the sites (I + I′) which is comparable to that in dehydrated KY (see Table IV). Obviously the increase of the number of K^+ ions in the small cavities is due to the decrease in the hydration level. In the hexagonal prisms and inside the cuboctahedra the K^+ ions can still realize optimal coordination with framework oxygen ions and water molecules. In extensively exchanged samples the number of unexchanged K^+ ions was found to be 20.3, 22.7, 24.3, and 28.1 for samples KAmY, KMeY, KEtY, and KPrY, respectively.[1] Even for a maximum occupancy of the sites inside the small cavities (23.1 as in KY dehydrated) there would still be, at least for the sample KPrY, unexchanged potassium ions in the large cavities.

Since the present samples were never heated or outgassed we assume that the sample compositions and water contents given in Table I are close to that of the samples in the ion-exchange suspension. This is in line with the interpretation of the limited exchange behavior given by Vansant.[13] When an RNH_3^+ ion enters the zeolite cage it replaces an inorganic ion but also a number of water molecules sufficient to allow accomodation of the large incoming ion. Vansant considered the possibility that the exchange limit is reached when a further introduction of organic ions would require the removal of the first hydration shell of the remaining inorganic cations. This hypothesis seems to be justified for the larger alkylammonium ions, but it is not applicable to the KMeY sample, which behaves more like the ammonium sample.

Acknowledgment. W. J. M. is grateful to the Belgisch Nationaal Fonds voor Wetenschappelijk Onderzoek for a research grant as "aspirant." M. L. C. thanks the Instituut voor Wetenschappelijk onderzoek in Nijverheid en Landbouw for a research grant. Financial support by the Belgian Government (Wetenschapsbeleid) and the gift of samples by the Linde Division of Union Carbide are gratefully acknowledged. The calculations were performed in the computer center of the Katholieke Universiteit te Leuven.

Supplementary Material Available. A listing of I_o and I_c values will appear following these pages in the microfilm edition of this volume of the journal. Photocopies of the supplementary material from this paper only or microfiche (105 × 148 mm, 20× reduction, negatives) contain-

ing all of the supplementary material for the papers in this issue may be obtained from the Journals Department, American Chemical Society, 1155 16th St., N.W., Washington, D. C. 20036. Remit check or money order for $3.00 for photocopy or $2.00 for microfiche, referring to code number JPC-73-2880.

References and Notes

(1) B. K. G. Theng, E. Vansant, and J. B. Uytterhoeven, *Trans. Faraday Soc.*, **64**, 3370 (1968).
(2) E. Vansant and J. B. Uytterhoeven, *Trans. Faraday Soc.*, **67**, 2961 (1971).
(3) W. J. Mortier and H. J. Bosmans, *J. Phys. Chem.*, **75**, 3327 (1971).
(4) W. J. Mortier, H. J. Bosmans, and J. B. Uytterhoeven, *J. Phys. Chem.*, **76**, 650 (1972).
(5) A. Gangulee, *J. Appl. Cryst.*, **3**, 272 (1970).
(6) W. J. Mortier and M. L. Costenoble, *J. Appl. Cryst.*, in press.
(7) W. C. Hamilton, POWOW, Brookhaven National Laboratory, Brookhaven, N. Y., 1962.
(8) W. J. Mortier, *Acta Cryst.*, **A29**, 473 (1973).
(9) W. R. Busing, K. O. Martin, and H. A. Levy, ORFFE, Oak Ridge National Laboratory, Oak Ridge, Tenn., 1964.
(10) J. V. Smith, *Advan. Chem. Ser.*, **No. 101**, 171 (1971).
(11) R. J. Mikovsky, A. J. Sylvestri, E. Dempsey, and D. H. Olson, *J. Catal.*, **22**, 371 (1971).
(12) W. H. Baur, *Amer. Mineral.*, **49**, 697 (1964).
(13) E. Vansant, Ph.D. Thesis, Katholieke Universiteit te Leuven, 1971.

Potential Energy Curves and Dissociation Energy of Titanium Monoxide

V. S. Kushawaha

Department of Physics, Banaras Hindu University, Varanasi-221005, India

(Received May 24, 1973)

Potential energy curves for Ti–O interactions corresponding to the $X^3\Delta_r$, $A^3\phi$, and $C^3\Delta$ states of the TiO molecule have been calculated using the method of Rydberg–Klein–Rees as modified by Vanderslice, *et al.* The ground-state dissociation energy has been estimated using Lippincott's three-parameter form of the potential function and also using the chemical energy available in a chemiluminescent reaction of $TiCl_4 + O_2$ in the presence of potassium vapor. From the chemiluminescent reaction its value was found to be 167.82 ± 2 kcal/mol.

Introduction

As TiO is observed very strongly in the spectra of M and S type stars, its spectroscopic study has been the subject of interest of many workers,[1-14] and seven electronic band systems are known in the region 3000–1000 Å. High-resolution studies of the TiO bands have confirmed two singlet and three triplet states in the energy region 10000–2000 cm^{-1}. The ground state of TiO is well confirmed[9] to be the $^3\Delta_r$, with a very low lying $^1\Delta$ state at about 581 cm^{-1} and a slightly higher $^1\Sigma$ state at about 2295 cm^{-1}. Uhler's[9] study of the electronic spectrum of TiO has revised the previous designation of the molecular states from $X^3\pi_r$, $B^3\Sigma$ and $C^3\pi_r$ to $X^3\Delta_r$, $A^3\phi$ and $C^3\Delta_r$ and has given a new set of molecular constants for these states only. The molecular constants of the two singlet states are still uncertain. The present communication deals with the experimental potential energy curves of these electronic states using the molecular constants reported by Uhler.[9]

The ground-state dissociation energy of TiO has been determined by a number of workers using different methods, but the values are different from each other. D_0(TiO) is 156.9 ± 2.2 kcal/mol by Hampson, *et al.*,[15] 167.38 ± 2.30 kcal/mol by Wahlbeck, *et al.*,[16] 159.9 kcal/mol by Groves, *et al.*,[17] 157 kcal/mol by Berkowitz, *et al.*,[18] 158.62 kcal/mol by Wheatley,[19] 157 kcal/mol by Herzberg,[20] and 129 kcal/mol by Carlson, *et al.*[12] In the present communication an attempt has been made to clarify the exact value of D_0(TiO) using the potential energy curve of the ground state of TiO and the chemical energy available in a chemiluminescent reaction.

Experimental Section

Construction of the Potential Energy Curves. The potential energy curves have been calculated from the experimental energy levels, using the method of Rydberg–Klein–Rees,[21-23] as modified by Vanderslice,[24] known as the RKRV method. This is a WKB method where one starts with the observed energy level E and from this calculates the maximum and minimum points of vibration. This method gives the potential function very accurately but it is restricted to known energy levels. Ginter and Battino[25] have suggested an extrapolation of the RKRV curves which are best for the region of the potential curve immediately beyond the last point determined from the experimental data, but they often can be extended meaningfully to as many as twice the number of vibrational levels known experimentally or to the dissociation limit, whichever is reached first energetically. The spectroscopic data used in the calculation are given in Table I and the results of the calculation are given in Table II.

Determination of the Ground-State Dissociation Energy. (1) Curve-Fitting Method. The method of curve fitting has been used to estimate the ground-state dissociation energy of a number of molecules. This method involves the comparison of the RKRV curves for the ground state of the molecule to an empirical potential function with different values of dissociation energies. The value of the

TABLE I: Molecular Constants (cm^{-1}) Used in the Calculation

State	T_e	ω_e	$\omega_e x_e$	α_e	B_e	r_e, Å
$C^3\Delta$	19434.6	837.9	4.55	0.0029	0.4889	1.695
$A^3\phi$	14242.6	866.3	3.83	0.0032	0.5074	1.664
$X^3\Delta_r$	0	1008.4	4.61	0.0030	0.5355	1.620

dissociation energy giving the best fit is taken to be an estimate of the actual dissociation energy.

The Lippincott potential function in the modified form

$$U(r) = D_e\left[1 - \exp\left\{-\frac{n(r - r_e)^2}{2r}\right\}\right] \times \left[1 - a\left(\frac{b^2 n}{2r}\right)^{1/2}(r - r_e)\exp\left\{-\left(\frac{b^2 n}{2r_e}\right)^{1/2}(r - r_e)\right\}\right]$$

has been shown to fit the RKRV potential energy curves of a large number of molecules to a very great extent. According to Steele and Lippincott,[26] the factors inside the squared brackets are independent of D_e if we put

$$a = F/1 + \frac{5}{4}F; n = \frac{2}{r_e}\left(\frac{F}{ab}\right)^2; b = 1.065; F = \frac{\alpha_e\omega_e}{6B_e^2}$$

Now in the above expression D_e is varied till a good fit to the RKRV curve is obtained. This value of D_e is a good estimate to the dissociation energy. The result of such calculation for TiO is given in Table III.

(*ii*) *Chemical Excitation of TiO.* Pathak and Palmer[14] have reported the electronic excitation of TiO in a low pressure diffusion flame of a mixture of $TiCl_4 + O_2$ burning in the presence of potassium vapor. The authors[14] have reported a band system in TiO in the region 2900–3200 Å which involves the ground state of TiO and a new upper electronic state *D*. On the basis of some previous observations on BO[27] and GeO,[30] they have proposed the following reaction primarily responsible for exciting TiO to the new energy state *D*.

$$TiCl(G.S) + KO(G.S) \longrightarrow TiO^* + KCl(G.S.) \quad (I)$$

where (G.S) and the superscript asterisk refer to the ground state and the electronically excited molecule, respectively.

The above reaction assumes a two-body collision process between TiCl and KO in their ground states which is a valid assumption in view of the fact that no emission was recorded by Pathak and Palmer[14] from TiCl, KO, or KCl. Furthermore, at the temperature (~400°K) of the reaction, one estimates that nearly 70% of the reacting molecules would be in their ground state. Thus eq I would be quite likely.

It is to be noted that Pathak and Palmer[14] have observed an abrupt cutoff in the emission of $TiCl_4 + O_2 +$ K at 2920 Å. This cutoff of the emission clearly gives the upper limit of the chemical energy available in the reaction and correspond to the exothermicity of the reaction. From this observation the ground state dissociation energy of TiO can be calculated. Writing the reaction I in equilibrium condition we have

$$D_0(TiO) + D_0(KCl) - D_0(TiCl) - D_0(KO) = \Delta H_0 \quad (II)$$

where D_0 and ΔH_0 represent the ground-state dissociation energy and the exothermicity of the reaction at 0°K, respectively. Substituting $D_0(TiCl) = 101 \pm 20$ kcal/mol,[28] $D_0(KO) = 70$ kcal/mol,[29] $D_0(KCl) = 101$ kcal/mol,[29] and $\Delta H_0 = 34239\ cm^{-1} = 97.82$ kcal/mol in eq II, we have $D_0(TiO) = 167.82 \pm 20$ kcal/mol.

TABLE II: RKRV Potential Curves for the Grourd and Excited States of TiO

State	v	$U(r)$, cm^{-1}	r_{min}, Å	r_{max}, Å	$T_e + U$, cm^{-1}
$X^3\Delta_r$	0	503.05	1.5936	1.6558	503.05
	1	1,502.23	1.5592	1.7095	1,502.23
	2	2,492.19	1.5358	1.7491	2,492.19
	3	3,472.93	1.5195	1.7818	3,472.93
	4	4,444.48	1.5068	1.8109	4,444.48
	5	5,406.75	1.4965	1.8378	5,406.75
	6	6,359.83	1.4878	1.8632	6,359.83
	7	7,303.69	1.4804	1.8875	7,303.69
	8	8,238.33	1.4740	1.9110	8,238.33
	9	9,163.75	1.4684	1.9339	9,163.75
	10	10,079.95	1.4636	1.9563	10.079.95
	11	10.986.93	1.4593	1.9782	10.986.93
	12	11,884.69	1.4556	1.9999	11,884.69
	13	12,773.23	1.4524	2.0212	12,773.23
	14	13,652.55	1.4495	2.0424	13,652.55
	15	14,522.65	1.4471	2.0635	14,522.65
	16	15,383.53	1.4450	2.0844	15,383.53
	17	16,235.32	1.4432	2.1052	16,235.19
	18	17,077.63	1.4418	2.1260	17,077.63
	19	17,910.85	1.4406	2.1467	17,910.85
	20	18,734.85	1.4397	2.1674	18,734.85
	21	19,549.63	1.4390	2.1882	19,549.63
$A^3\phi$	0	417.82	1.6392	1.7011	14,660.42
	1	1,290.83	1.5997	1.7618	15,533.43
	2	2,141.81	1.5751	1.8052	16.384.41
	3	2,985.13	1.5581	1.8410	17,227.73
	4	3,820.79	1.5451	1.8730	18.063.39
	5	4,648.79	1.5347	1.9027	18,891.39
	6	5,469.13	1.5260	1.9307	19,711.73
	7	6,281.81	1.5187	1.9576	20,524.41
	8	7,086.83	1.5126	1.9836	21,329.43
	9	7,884.19	1.5074	2.0089	22,126.79
	10	8,673.89	1.5029	2.0337	22,916.49
	11	9,455.93	1.4991	2.0581	23,698.53
	12	10,230.31	1.4960	2.0821	24,472.91
	13	10,997.03	1.4933	2.1059	25,239.63
	14	11,756.09	1.4912	2.1295	25,998.69
	15	12,507.49	1.4894	2.1530	26,750.09
	16	13,251.23	1.4881	2.1763	27,493.83
	17	13,987.31	1.4872	2.1995	28,229.91
	18	14,715.73	1.4866	2.2228	28,958.33
	19	15,436.49	1.4864	2.2460	29,679.09
$C^3\Delta_r$	0	419.08	1.6666	1.7493	19,853.68
	1	1,246.61	1.6288	1.7939	20,681.21
	2	2,066.31	1.6033	1.8378	21,500.91
	3	2,876.91	1.5854	1.8739	22,311.51
	4	3,678.41	1.5715	1.9062	23,113.01
	5	4,470.81	1.5602	1.9362	23,905.41
	6	5,254.11	1.5506	1.9646	24,688.71
	7	6,028.31	1.5425	1.9918	25,462.91
	8	6,793.41	1.5355	2.0181	26,228.01
	9	7,549.41	1.5293	2.0438	26,984.01
	10	8,296.31	1.5240	2.0690	27,730.91
	11	9,034.11	1.5192	2.0937	28,468.71
	12	9,762.81	1.5151	2.1182	29,197.41
	13	10,482.41	1.5114	2.1425	29,917.01
	14	11,192.91	1.5083	2.1665	30,627.51
	15	11,894.31	1.5055	2.1905	31,328.91
	16	12,686.61	1.5031	2.2143	32,021.21
	17	13,269.81	1.5011	2.2382	32,704.41
	18	13,943.91	1.4994	2.2620	33,378.51
	19	14,608.91	1.4980	2.2858	34,043.51
	20	15,264.81	1.5968	2.3097	34,699.41
	21	15,911.61	1.4960	2.3337	35,346.21

TABLE III: Calculations for the Ground-State Dissociation Energy of the TiO Molecule Using the Lippincott Function (Three-Parameter Form)

r, Å	D_e = 60,000, cm^{-1}	D_e = 58,500, cm^{-1}	D_e = 56,000, cm^{-1}	RKRV, cm^{-1}
1.6558	533.13	506.21	441.15	503.05
1.7095	1,559.28	1,525,31	1,420.10	1,502.23
1.7818	3,551.91	3,501.81	3,380.32	3,472.93
1.8109	4,573.45	4,511.35	4,354.71	4,444.45
1.8632	6,478.61	6,398.20	6,240.38	6,359.83
1.9110	9,382.35	8,290.51	8,108.67	8,238.33
1.9563	10,288.71	10,103.62	9,882.25	10,079.95
1.9782	11,352.63	11,054.43	10,663.35	10,986.93
2.0212	13,086.92	12,821.21	12,493.82	12,773.23
2.0635	14,769.81	14,572.74	14,222.65	14,522.60
1.5358	2,610,73	2,512.62	2,422.53	2,492.19
1.4965	5,521.37	5,441.32	5,319.62	5,406.75
1.4804	7,414.81	7,343.29	7,228.84	7,303.69
1.4684	9,275.38	9,180.87	9,092.63	9,163.75
1.4556	12,165.91	11,921.37	11,312.80	11,884.69
1.4495	13,858.72	13,691.38	13,198.61	13,652.55
1.4450	15,585.23	15,431.03	15,065.39	15,383.53
1.4432	16,462.11	16,275.61	15,876.27	16,235.19
1.4406	18,186.25	17,971.64	17,501.72	17,910.85
1.4390	19,814.61	19,580.52	19,336.11	19,549.63

Results and Discussion

The experimental potential energy curves for the three states of TiO are shown in Figure 1. The most prominent feature of these curves is that these are narrow well type potentials which indicate that the molecule behaves approximately like a harmonic oscillator rather than an anharmonic oscillator. The ground-state potential curve is comparatively narrower than the upper state potential curve and therefore, one should expect a large value of ω_e in the ground state than in the upper states which explains the observed ω_e value for the lower and the upper states. The three curves are lying approximately one above the other which indicates that the structure of the molecule in the ground and in the upper states should be nearly the same. The observed r_e values corresponding to the $X^3\Delta_r$, $A^3\phi$, and $C^3\Delta_r$ states are nearly equal and support the predicted structure of the molecule. In addition, the Franck-Condon principle is also satisfied and thus it explains the maximum intensity of the (0,0) band and slightly lesser intensity of the (0,1) and (1,0) bands observed in the A-X and C-X band systems of TiO. The most interesting feature would be due to the presence of the potential curve of the $C^3\Delta$ state which is inside the potential curve of the $A^3\phi$ state. Because of the presence of this potential curve a strong perturbation should be observed in the A-X and C-X systems. This explains the perturbation observed by Phillips[7] in the A-X system but such perturbation has not been observed in the C-X system. In the analogous molecule ZrO, similar perturbations have been observed in the A-X and C-X systems.[9]

The results of calculation for the ground-state dissociation energy of TiO is given in Table III. This table shows that the best fit to the RKRV curve is obtained when we put D_e = 58,500 cm^{-1}. The most probable value of D_e from our calculations is 166.75 kcal/mol from which we get D_0(TiO) = 165.37 kcal/mol. From the consideration of the chemical energy available in the chemiluminescent reaction, we have observed a value D_0(TiO) = 167.82 ± 20 kcal/mol. The magnitude of the two results is in very good agreement, but each of them is larger than the spectroscopic value[20] of 157 kcal/mol derived from the linear Birge-Sponer extrapolation of the ground state and also larger than the theoretical value[12] of 129 kcal/mol. However, the present values are nearly equal to the value 167.38 ± 2.30 kcal/mol reported by Wahlbeck, *et al.*[16] The spectroscopic value is based on only five vibrational spacings which add to about one-tenth the dissociation energy and the theoretical result is low because of the limited basis set and the uncertainty in the correlation data.

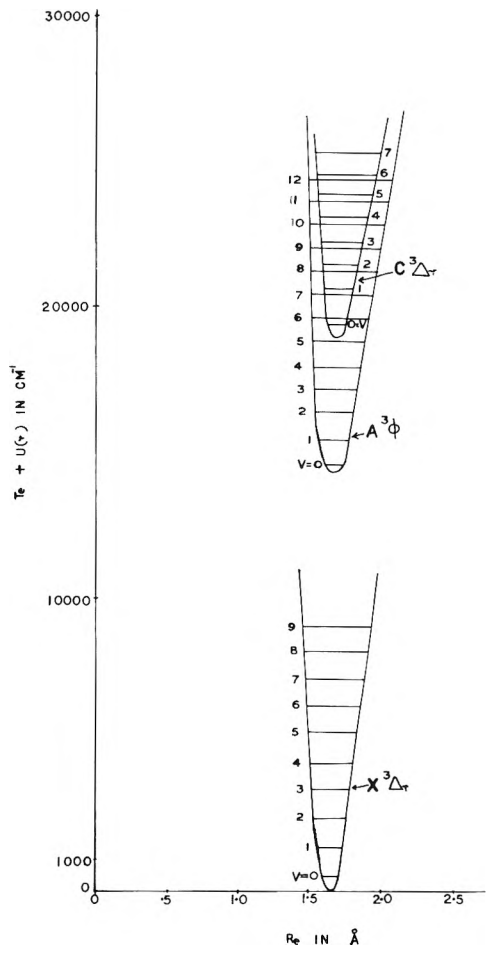

Figure 1. Potential energy curves for TiO.

The value of D_0(TiO) reported by Hampson, *et al.*,[15] depends directly on the dissociation energy of ScO(g), which in turn depends on mass spectroscopic measurements involving numerous other oxides and metal species, notably those of lanthanum, yttrium, germanium, and silicon. In the abscence of a spectroscopic dissociation energy for a gaseous metal monoxide, the authors[15] have reported that the dissociation energy of TiO is less satisfactory. Moreover, they have also admitted that there could be an error in D_0(ScO) and hence in D_0(TiO), due to an inaccurate relative ionization cross section of TiO(g) and TiO_2(g). The result of Walhbeck, *et al.*,[16] seems to be more accurate than any other value of D_0(TiO) reported previously, but it is to be noted that these authors[16] were unable to pin down the principal reaction responsible for the vaporization of Ti_3O_5(S). Of course, they performed some relatively crude mass spectroscopic measurements to identify the principal species but all these measurements were not in agreement and therefore the dissociation ener-

gy of TiO(g) obtained using such measurements may not be very accurate.

In the present work, we have obtained a value $D_0(TiO)$ = 167.82 ± 20 kcal/mol using the position of a band head which corresponds to the highest value of the chemical energy available in the reaction and the precision of measurement of this band head is ±5 cm^{-1}.[14] The value of the ground-state dissociation energy of TiO reported in this work may therefore be regarded as much more reliable than any other value.

We have obtained $D_0(TiO)$ experimentally as well theoretically, which matches very well with the value of $D_0(TiO)$[16] obtained using entirely different experimental procedure. This agreement provides strong evidence in support to the high value of $D_0(TiCl)$ = 101 ± 20 kcal/mol[28] rather than a low value $D_0(TiCl)$ = 25 kcal/mol derived from a linear Birge–Sponer extrapolation of the ground state. Also, a comparison of $D_0(TiO)$ = 167.82 ± 20 kcal/mol (present work) and $D_0(TiO)$ = 167.38 ± 2.3 kcal/mol[16] shows that the uncertain value (±20 kcal/mol) in the present work (this is due to $D_0(TiCl)$) should be the same as in Wahlbeck's[16] result since the magnitude of the certain value is equal, and thus the $D_0(TiCl)$ and $D_0(TiO)$ may be equal to 101 ± 2 and 167.82 ± 2 kcal/mol, respectively.

Acknowledgments. The author is thankful to Dr. C. M. Pathak for valuable suggestions and criticisms and to Mr. B. P. Asthana for help in some portions of the calculations. The financial support received from the C.S.I.R., India, is gratefully acknowledged.

References and Notes

(1) A. Fowler, *Proc. Phys. Soc., London*, **19A**, 509 (1907).
(2) F. Lowater, *Proc. Phys. Soc., London*, **41**, 557 (1929).
(3) K. Wurn and M. J. Meister, *Z. Astrophys.*, **13**, 199 (1937).
(4) C. C. Kiess, *Publ. Astron. Soc. Pac.*, **60**, 252 (1937).
(5) F. P. Coheur, *Bull. Soc. Roy. Sci. Liege*, **12**, 98 (1943).
(6) J. G. Phillips, *Astrophys. J.*, **111**, 314 (1950).
(7) J. G. Phillips, *Astrophys. J.*, **114**, 152 (1951).
(8) J. G. Phillips, *Astrophys. J.*, **115**, 567 (1952).
(9) U. Uhler, Ph.D. Thesis, University of Stockholm, Sweden, 1954.
(10) A. V. Petterson, *Ark. Fys.*, **16**, 185 (1959).
(11) A. V. Petterson and B. Lindgren, *Naturwissenschaften*, **48**, 128 (1961).
(12) K. D. Carlson and R. K. Nes, *J. Chem. Phys.*, **41**, 1051 (1964).
(13) I. Kovacs and V. M. Korwar, *Acta. Phys. Hung.*, **29**, 399 (1970).
(14) C. M. Pathak and H. B. Palmer, *J. Mol. Spectrosc.*, **33**, 137 (1970).
(15) P. J. Hampson and P. W. Gilles, *J. Chem. Phys.*, 55, 3712 (1971).
(16) P. G. Wahlbeck and P. W. Gilles, *J. Chem. Phys.*, **46**, 2465 (1967).
(17) W. O. Groves, M. Hoch, and H. L. Johnston, *J. Phys. Chem.*, **59**, 127 (1955).
(18) J. Berkowitz, W. A. Chupka, and M. G. Inghram, *J. Phys. Chem.*, **61**, 1569 (1957).
(19) Q. D. Wheatley, Ph.D. Thesis, University of Kansas, 1954.
(20) G. Herzberg, "Spectra of Diatomic Molecules," D. Van Nostrand, Princeton, N. J., 1950.
(21) R. Rydberg, *Z. Phys.*, **73**, 376 (1931); **80**, 514 (1933).
(22) O. Klein, *Z. Phys.*, **76**, 226 (1932).
(23) A. L. G. Rees, *Proc. Roy. Soc., Ser. A*, **59**, 998 (1947).
(24) J. T. Vanderslice, E. A. Mason, W. G. Maisch, and E. R. Lippincott, *J. Mol. Spectrosc.*, **3**, 17 (1959); **5**, 83 (1960).
(25) M. L. Ginter and R. Battino, *J. Chem. Phys.*, **42**, 3222 (1965).
(26) D. Steele, E. R. Lippincott, and J. T. Vanderslice, *Rev. Mod. Phys.*, **34**, 239 (1962).
(27) D. W. Naegli, Ph.D. Thesis, Pennsylvania State University, 1967.
(28) V. I. Vedeneyev, *et al.*, "Bond Energies, Ionization Potentials and Electron Affinities," U.S.S.R. Academy of Sciences, 1962.
(29) A. G. Gaydon, "Dissociation Energies," 3rd ed, Chapman and Hall, London, 1968.
(30) H. B. Palmer, A. Tewarson, D. W. Naegeli, and C. M. Pathak, "Molecular Luminescence," E. C. Lim, Ed., W. A. Benjamin, New York, N. Y., 1969, p 493.

CNDO/2 Studies on Ion Solvation

Abha Gupta and C. N. R. Rao*
Department of Chemistry, Indian Institute of Technology, Kanpur-16, India *(Received April 18, 1973)*

CNDO/2 calculations on the interaction of Li^+ with a variety of donor molecules such as H_2O, ether, carbonyl compounds, NH_3, acetonitrile, pyridine, and HF to give complexes of the type $Li^+(donor)_n$ show that the binding energy decreases while the Li^+–donor distance increases with increase in n. These calculations satisfactorily describe the nature of charge transfer in these complexes as well as their stereochemistry. The changes in bond distances and spectral properties of carbonyl donors due to complexation are also predicted. The potential energy surfaces obtained from the study can be fitted into the Lennard-Jones 6–12 potential function. Based on the CNDO/2 calculations, comments have been made regarding the nature of the second hydration layer, different types of ion pairs, and the quantized vibrations of Li^+ in solvent cages.

Solvation of ions in aqueous and nonaqueous media is of primary importance in the theory of polar liquids. It appeals to reason that in the region of the primary solvation sphere where the ion is closest to solvent molecules there will be strong interaction, while at large distances the solvent is essentially unperturbed. We can also visualize an intermediate region where the solvent molecules are slightly perturbed and there is some disorder in the solvent structure. Although classical models[1,2] are somewhat successful in the study of ion–dipole interactions, they provide little information on the electronic structure of the solvated ions and on the nature of binding forces. However, semiempirical LCAO MO SCF methods would be particularly useful in examining ion–solvent complexes,

$M(S)_n$, which approximate the primary solvation sphere since such methods have been successful in providing fairly satisfactory descriptions of hydrogen-bonded systems.[3-5]

In the present study, we have employed Pople's CNDO/2 method[6] to investigate the potential energy surfaces for the interaction of lithium ion with water and other oxygen donors such as ether, formaldehyde, formamide (FA), *N*-methylacetamide (NMA), *N,N*-dimethylformamide (DMF), and cytosine, nitrogen donors such as ammonia, acetonitrile, and pyridine as well as HF to yield complexes of the general formula $Li^+(donor)_n$. In the case of 1:1 complexes we have investigated the stereochemistry in some detail. Further, we have examined the nature of the second solvation sphere in the case of $Li^+(H_2O)_n$ and various types of ion pairs formed by Li^+F^-. Although the CNDO/2 method does not provide good values of binding energies in such calculations, the results are expected to show reliable trends of binding energies and bond distances with changes in donor and stoichiometry. Based on the potential energy curves from the CNDO/2 calculations, we have arrived at an empirical potential function which is applicable to the large variety of systems examined by us. We have also predicted changes in the structure and spectra of the donors in these ion complexes and the nature of the quantized vibration of lithium ion in solvation spheres and complexes.

Method

In the CNDO/2 calculations, we have made use of the following Slater exponents in the calculation: H, 1.2; Li, 0.65; C, 1.625; N, 1.950; O, 2.275, and F, 2.600. In the case of water and other oxygen donor molecules except dimethyl ether we have employed CNDO/2 minimized geometries: H_2O, r_{O-H} = 1.03 Å, ∠HOH = 107.1°; H_2CO, r_{C-H} = 1.11 Å, $r_{C=O}$ = 1.25 Å, ∠HCO = 120°; NH_2HCO, r_{C-N} = 1.37 Å, $r_{C=O}$ = 1.26 Å, r_{N-H} = 1.02 Å, r_{C-H} = 1.09 Å, all angles 120°; *N*-methylacetamide (NMA), r_{C-N} = 1.38 Å, r_{N-C} = 1.44 Å, r_{C-C} = 1.53 Å, $r_{C=O}$ = 1.27 Å, r_{N-H} = 1.06 Å, r_{C-H} = 1.09 Å, ∠H_3CNH = 107°, ∠NCO = ∠OCC = 120°; *N,N*-dimethylformamide (DMF), r_{C-N} = 1.38 Å, r_{N-C} = 1.44 Å, $r_{C=O}$ = 1.27 Å, r_{C-H} = 1.09 Å, all angles 120°. The geometries of various 1:1 complexes of Li^+ are shown in Figure 1. Geometries of 1:2, 1:3 and 1:4 complexes were generally symmetrical structures and are described in appropriate tables or in the text.

The geometries of dimethyl ether, cytosine, and nitrogen donors were taken from Sutton's compilations of structural data.[7] In the 1:2 complex of acetonitrile, Li^+ is situated in a position ϕ = 60° with respect to both the CH_3CN molecules and the CH_3 groups are trans with respect to Li^+. The 1:2 complex with NH_3 is linear with ∠NLi^+N of 180°. In the 1:4 complex, the four nitrogens and Li^+ are in the same plane and the complex is square-planar; a tetrahedral configuration is not more stable than this structure. In the case of cytosine, Li^+ was taken along the carbonyl bond. In the case of HF complexes, the H-F distance was minimized by the CNDO/2 method (r_{H-F} = 0.915 Å). The various possible geometries of 1:2 and 1:4 complexes with H-F are described in the text.

Results and Discussion

Li^+ Complexes with Water. After we initiated this study, there were several molecular orbital calculations reported in the literature[8-14] on $Li^+(H_2O)_n$ complexes. We will, however, indicate our results briefly since they are pertinent to the discussion of other systems investigated by us. A typical potential energy curve showing the variation of the binding energy, ΔE, with the $Li^+\cdots O$ distance, r, is shown in Figure 2. The variation of ΔE with ϕ (Figure 3) is roughly comparable to that predicted by *ab initio* calculations[8] although the actual values of binding energies differ. The results of our calculations on $Li^+(H_2O)_2$, $Li^+(H_2O)_3$, $Li^+(H_2O)_4$, and $Li^+(H_2O)_6$ are summarized in Table I. The stabilization energy is not additive in these complexes and our results are in general agreement with the CNDO/2 calculations recently published on these systems by other workers.[9-12]

We are in a position to compare our results with those from the recent *ab initio* calculations[13,14] and with the experimental equilibrium interaction energies (in the gas phase) between Li^+ and H_2O to give different $Li^+(H_2O)_n$ complexes ($1 \leq n \leq 6$) reported by Dzidic and Kebarle.[15] The CNDO/2 binding energies are much higher than the values from experiment and *ab initio* calculations: the CNDO/2 binding energy, however, decreases with increase in n just as in the case of $H^+(H_2O)_n$ complexes.[16] The

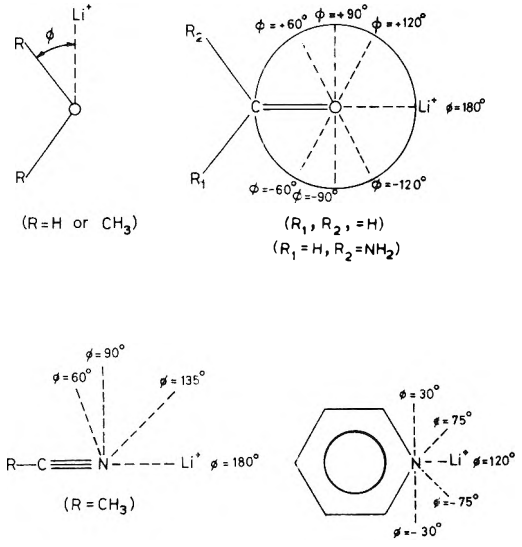

Figure 1. Geometry of 1:1 Li^+ donor complexes.

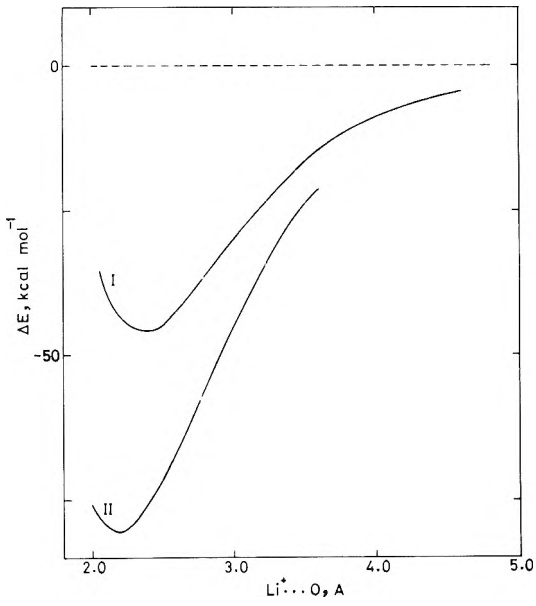

Figure 2. Typical potential energy curves showing the variation of ΔE with $Li^+\cdots O$ distance (r), in Li^+–H_2O, I (ϕ = 126.5°), and Li^+–ether, II (ϕ = 124.5°).

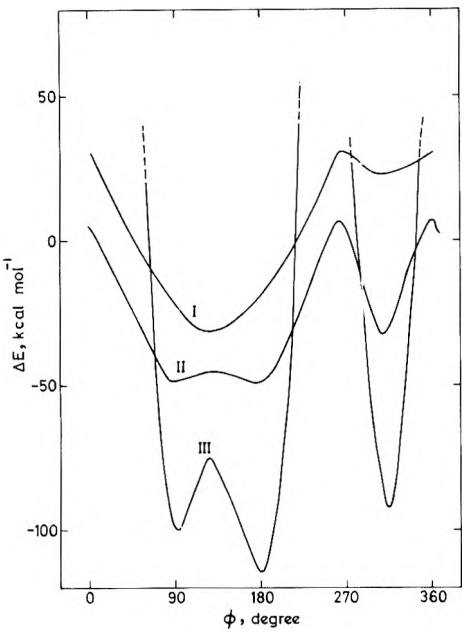

Figure 3. Variation of ΔE with ϕ in planar 1:1 Li^+-H_2O (II) and Li^+-ether (III) complexes at $Li^+ \cdots O$ distance of 2.3 and 2.4 Å, respectively. Curve I shows the *ab initio* results on the 1:1 Li^+-H_2O complex.

TABLE I: CNDO/2 Calculations on Interaction of Water with Li^+

Adducts	E_T, au	$-\Delta E$, kcal/mol[a]	$Li^+ \cdots O$, Å	Δq_T	μ, D	k, mdyn/Å
1:1[b]	−19.9636	46	2.36	−0.16	7.9	0.9
1:1[c]	−19.9670	48	2.36	−0.17	9.2	1.0
2:1[b]	−39.9219	44	2.37	−0.16	0.0	0.9
2:1[c]	−39.9297	46	2.37	−0.17	0.0	1.0
3:1[b]	−59.8705	41	2.41	−0.14	3.3	...
3:1[c]	−59.8821	44	2.41	−0.15	3.0	...
4:1[b,d]	−79.8151	39	2.43	−0.13	0.0	0.9
4:1[c,d]	−79.8312	42	2.43	−0.14	0.0	1.0
6:1[c,e]	−119.7146	39	2.47	−0.12	0.0	...
6:1[b,f]	−119.5985	44	2.37	−0.16	0.0	...
6:1[b,g]	−119.6513	39	2.43	−0.14	0.0	...

[a] ΔE is the average stabilization energy per $Li^+ \cdots O$ bond of the complex (H_2O energy = −19.8909 au). [b] Li^+ along the bisector of the HOH angle (in the plane of HOH and away from hydrogens). [c] Li^+ along the lone pair of oxygen. [d] Tetrahedral arrangement of H_2O molecules. [e] Octahedral arrangement of H_2O molecules. [f] To examine the effect of second sphere of hydration, we have taken two H_2O molecules bonded to Li^+ and four H_2O molecules hydrogen bonded to the two inner H_2O molecules. [g] Here, the second sphere of coordination is formed by two outer H_2O molecules hydrogen bonded to two of the water molecules in $Li^+(H_2O)_4$.

equilibrium $Li^+ \cdots O$ distance also increases with n, but the CNDO/2 value (~2.35 Å) is much higher than the value from *ab initio* calculations (~1.85 Å) reported by Clementi and others.[13,14] The equilibrium distance expected from the sum of the van der Waals radius of H_2O and ionic radius of Li^+ is between these two values (~2.0 Å). The charge transfer associated with the formation $Li^+(H_2O)_n$ complexes is shown in Figure 4. We see that the charge of hydrogens is transferred to the Li^+ ion. The net charge transfer, Δq_T, to the cation in the various complexes is given in Table I; Δq_T decreases as n increases in accordance with the other changes.

In order to examine the effect of the second layer of hydration on the Li^+-H_2O interaction, we have calculated

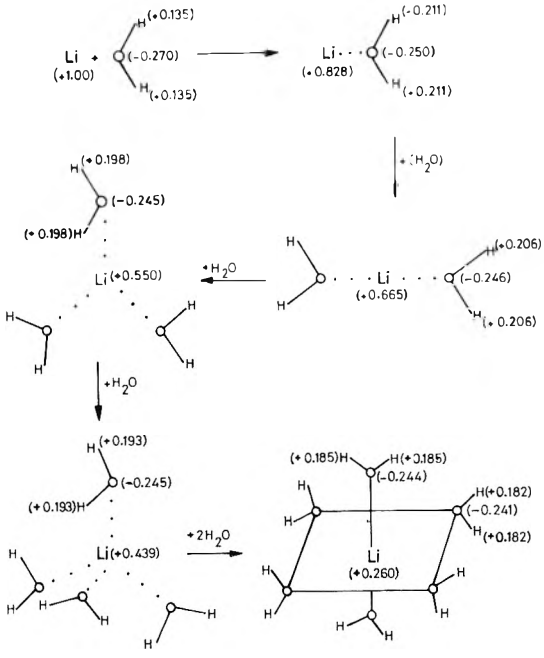

Figure 4. CNDO/2 charges in $Li(H_2O)_n$ complexes.

the energies of $Li^+(H_2O)_6$ where two or four molecules of water are in the outer layer as shown below.

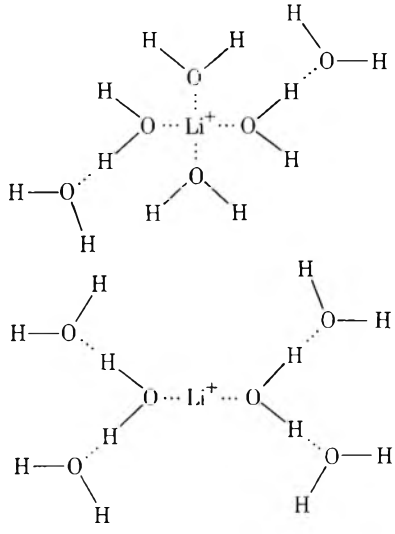

We see from Table I that the binding energy of $Li^+(H_2O)_n$ is not affected by the water molecules in the second hydration sphere. However, the hydrogen bond energy in both these systems is considerably higher (17 kcal mol^{-1} per hydrogen bond) than in the corresponding hydrogen bonded trimer or dimer of water (6–10 kcal mol^{-1}). The O···O distance here is 2.5 Å compared to 2.6 Å in the simple hydrogen bonded species.[3,17] This is what we would expect considering the nature of charge transfer; water molecules polarized by Li^+ form stronger hydrogen bonds than ordinary water molecules. This effect would be expected to diminish as we add water molecules in successive layers. Preliminary calculations show that beyond the fourth layer we will essentially have unperturbed hydrogen bonds similar to those in bulk water.

Complexes of F^- with Water. Halide ions form strong hydrogen bonds with water. Our CNDO/2 calculations give ΔE values of 77 and 58 kcal mol^{-1} per $F^- \cdots O$ bond in $F^-(H_2O)$ and $F^-(H_2O)_2$ complexes, respectively. Extensive CNDO/2 calculations on $F^-(H_2O)_n$ complexes by

TABLE II: CNDO/2 Calculations on Hydration of Ion Pairs[a]

System	$-\Delta E$, kcal mol^{-1}	O···F$^-$ or O···Li$^+$, Å
$H_2O\cdots F^-\cdots Li^+$	20[d]	2.2[b,c]
$H_2O\cdots Li^+\cdots F^-$	30[e,f]	2.4
$H_2O\cdots Li^+\cdots F^-\cdots H_2O$	94[e]	2.4
$Li^+\cdots H_2O\cdots F^-$	181[e]	2.4
$H_2O\cdots Li^+\cdots H_2O\cdots F^-\cdots H_2O$	69[e]	2.3
$Li^+\cdots H_2O\cdots H_2O\cdots F^-$	144[e,g]	2.2

[a] Equilibrium $Li^+\cdots F^-$ distance is 2.2 Å in the minimum energy configuration. [b] O···F$^-$ distance in the minimum energy structure. [c] The O–H distance hydrogen bonded to F$^-$ is about 1:1 Å. [d] Per F$^-\cdots H_2O$ bond. [e] Per $Li^+\cdots OH_2$ bond. [f] Similar calculations with $H_2O\cdots Li^+\cdots NO_3^-$ gave a ΔE value of -32 kcal mol^{-1}. [g] The hydrogen bond energy of $H_2O\cdots H_2O$ in $H_2O\cdots H_2O\cdots F^-$ is 25 kcal mol^{-1} (O···O distance = 2.4 Å).

other workers[10,12] show a decrease in ΔE with n. The calculated E values are generally much higher than the experimental values[18] just as in the case of $Li^+(H_2O)_n$ complexes. Our calculations on $F^-\cdots H_2O\cdots H_2O$ show that the hydrogen bond energy between the two water molecules is much higher (25 kcal mol^{-1}) than the ordinary water dimers, a situation similar to that encountered with the second solvation sphere of $Li^+(H_2O)_n$ complexes.

Hydration of Ion Pairs. We have examined the hydration of the Li^+–F^- ion pairs to see the effect of the counteranion in different types of ion pairs on the energy of hydration of Li^+. We have considered three types of ion pairs:[19] hydrated cage pairs, $H_2O\cdots F^-Li^+$, $H_2O\cdots Li^+\cdots F^-$ and $H_2O\cdots Li^+\cdots F^-\cdots H_2O$; extended cage pairs, $Li^+\cdots H_2O\cdots F^-$ and $H_2O\cdots Li^+\cdots H_2O\cdots F^-\cdots H_2O$ and the solvent-separated pair, $Li^+\cdots H_2O\cdots H_2O\cdots F^-$. The results of our calculations are summarized in Table II. We see that the binding energy of the $Li^+\cdots O$ bond or the $F^-\cdots O$ hydrogen bond is lower in the cage pair compared to that found in the interaction of Li^+ or F^- alone. This is understandable since the H_2O molecule competes with the counter anion or cation for bonding in the cage pair. In the extended cage pair, $Li^+\cdots H_2O\cdots F^-$, the stabilization energy of the $Li^+\cdots O$ bond is very large; this is in the expected direction since hydrogen bonding of H_2O with the anion would make the oxygen more negative. When extra water molecules surround such an extended cage pair as in $H_2O\cdots Li^+\cdots H_2O\cdots F^-\cdots H_2O$, the stabilization energy comes down considerably, but is still higher than in an isolated 1:1 $Li^+\cdots H_2O$ complex. In the solvent separated pair, $Li^+\cdots H_2O\cdots H_2O\cdots F^-$, the stabilization energy is lower than in the extended cage pair as expected. We can readily visualize that as the number of water molecules separating the ion pair (as well as the number of H_2O molecules surrounding each ion) increases, ΔE will approach the value in the isolated $Li^+(H_2O)_n$ or $F^-(H_2O)_n$ complexes. An examination of the CNDO/2 charges of the ion pairs shows that the variations in charges are in the expected direction and consistent with the energy changes discussed above.

Li^+ Complexes with Other Oxygen Donors. We have calculated the energies of a variety of Li^+–O donor complexes as functions of the $Li^+\cdots O$ distance. Typical potential energy curves for 1:1 complexes with dimethyl ether, formaldehyde, formamide, and *N*-methylacetamide are shown in Figures 2 and 5. In the 1:1 complexes (Figure 1), we have studied the variation of binding energies with

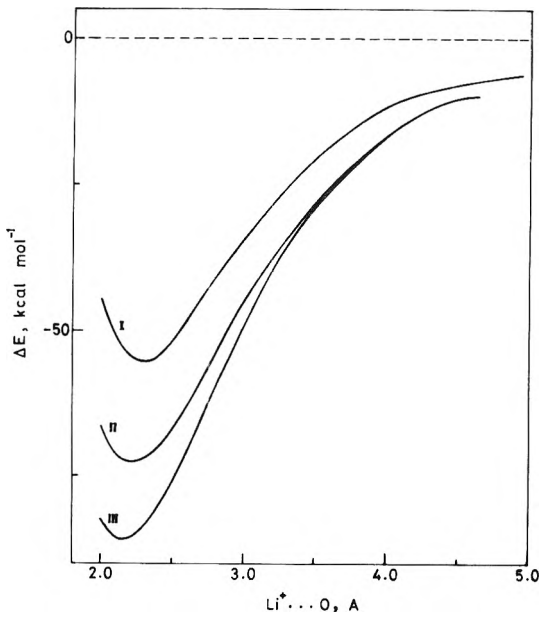

Figure 5. Typical potential energy curves showing the variation of ΔE with $Li^+\cdots O$ distance in (I) Li^+–formaldehyde (ϕ = 180°), (II) Li^+–formamide (ϕ = 180°), and (III) Li^+–*N*-methylacetamide (ϕ = 180°).

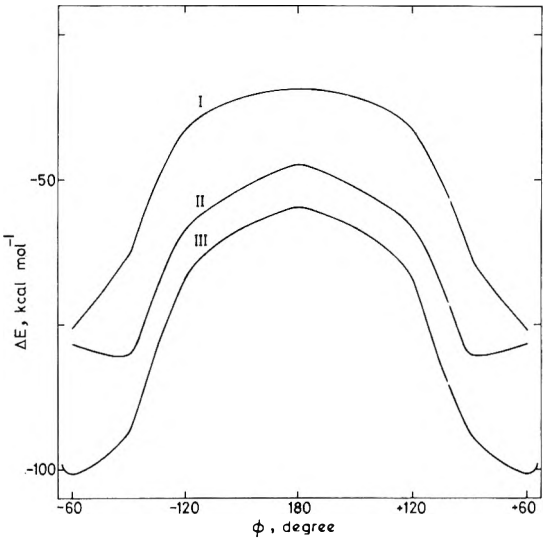

Figure 6. Variation of ΔE with ϕ in planar 1:1 Li^+–formaldehyde complex at $Li^+\cdots O$ distances of 3.0 Å (I), 2.0 Å (II), and 2.3 Å (III).

the orientation of Li^+ with respect to the oxygen donor. Variation of ΔE with ϕ in the Li^+–ether system is compared with that in Li^+–H_2O in Figure 3. We see that the orientational dependence in the two systems is quite similar. The ΔE in the ether complex is highest when <LiOC is between 90 and 180°; when Li^+ is along the lone-pair direction ΔE was 103 kcal mol^{-1}, which is less than that found in the most stable planar structure. In the case of the Li^+–formaldehyde complex (Figure 6), the binding energy is maximum when Li^+ is located at the center of the C=O bond ($\angle$LiOC = ±60°). In the case of planar Li^+–formamide (Figure 7), however, the most stable configuration is one where the NH_2 group is trans with respect to Li^+ and ϕ is −60°. A slightly more stable configuration is found when Li^+ is above the plane (ϕ = 60°) of formamide. It is interesting that in all these Li^+–oxygen donor

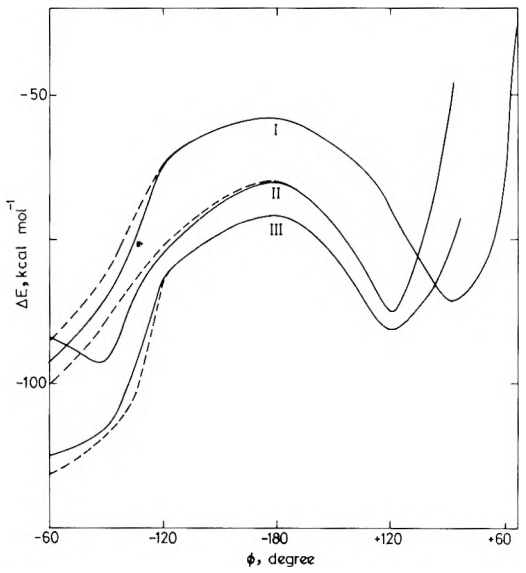

Figure 7. Variation of ΔE with ϕ in planar 1:1 Li^+–formamide complex (solid curves) at $Li^+\cdots O$ distances of 2.8 Å (I), 2.0 Å (II), and 2.3 Å (III). Angle ϕ is positive when the NH_2 group is cis to Li^+ and negative when NH_2 group is trans to Li^+. Dashed curves show the variation of ΔE with ϕ when Li^+ is in a plane perpendicular to that of formamide.

TABLE III: CNDO/2 Results on the Most Stable Configurations of Complexes of Li^+ with Oxygen Donors[a]

	$Li^+\cdots O$, Å	$-\Delta E$, kcal mol^{-1}	Δq_T	μ, D	k, mdyn/Å
		1:1 Complexes			
H_2O[b]	2.36	48	−0.17	9.2	1.0
$(CH_3)_2O$[c]	2.40	125	−0.35	8.1	1.1
H_2CO[d,e]	2.28	102	−0.30	9.5	1.1
H_2NHCO[f]	2.32	116	−0.32	9.5	1.4
NMA[f]	2.30	152	−0.40	9.6	1.1
DMF[d]	2.35	116	−0.34	7.1	1.1
Cytosine	2.20	99	−0.27	21.8	...
		1:2 Complexes			
H_2O[b]	2.37	46	−0.17	0.0	1.0
$(CH_3)_2O$[b]	2.22	94	−0.25	6.1	1.1
H_2CO[d]	2.40	99	−0.30	0.0	1.1
H_2NHCO[f]	2.40	113	−0.31	0.0	1.1
		1:4 Complexes			
H_2O[b,g]	2.43	42	−0.14	0.0	1.0
H_2CO[b,h]	2.40	53	−0.15	0.0	1.0

[a] Data for the most stable configurations. ΔE is the stabilization energy per $Li^+\cdots O$ bond of the complex compared to the components. [b] Along the lone pair direction. [c] ∠ L OC = 180° planar arrangement. [d] ∠ LiOC = 60° (Li^+ in the plane of the carbonyl skeleton); C=O distance increases on complexation. [e] There is an increase in C=O distance by 0.01 Å. [f] ∠ LiOC = 60°; Li^+ in the direction perpendicular to the molecular plane; C=O distance increases on complexation. [g] Tetrahedral arrangement. [h] ∠ LiOC = 120°.

systems, the configurations where Li^+ is along the direction of the oxygen lone pair are not the most stable ones. This is in accordance with a similar observation made in hydrogen-bonded systems where also there is no preference for bonding along the lone-pair vector.[20,21]

In Table III, we have summarized the results of our CNDO/2 calculations for the most stable configurations of 1:1, 1:2, and 1:4 complexes of Li^+ with oxygen donors. The results clearly show that of all the oxygen donors,

TABLE IV: CNDO/2 Charges in Li^+–Oxygen Donor Complexes[a]

	Li	O	Other sites	
		1:1 Complexes		
H_2O	0.828	−0.250	H	0.211
	(1.000)	(−0.270)		(0.135)
$(CH_3)_2O$	0.650	−0.185	C	0.135
	(1.000)	(−0.209)		(0.138)
			H	0.062 to 0.021
				(−0.015 to −0.008)
H_2CO	0.698	−0.095	C	0.250
	(1.000)	(−0.195)		(0.206)
			H	0.056, 0.090
				(−0.005)
H_2NHCO[b]	0.683	−0.253	C	0.362, N −0.209
	(1.000)	(−0.320)		(0.345) (−0.245)
			H	0.045
				(−0.037)
NMA[c]	0.597	−0.293	C	0.363, C′ −0.093
	(1.000)	(−0.374)		(0.353) (−0.099)
			N	−0.183, H 0.153
				(−0.190) (+0.098)
DMF[b]	0.658	−0.282	C	0.371
	(1.000)	(−0.338)		(0.324)
			N	−0.103, H 0.019
				(−0.140) (−0.030)
		1:2 Complexes		
H_2O	0.665	−0.246	H	0.206
$(CH_3)_2O$	0.499	−0.186	C	0.134
			H	0.034 to 0.019
H_2CO	0.397	−0.098	C	0.254
			H	0.080, 0.066
H_2NHCO	0.368	−0.261	C	0.373, N −0.203
			H	0.042
		1:4 Complexes		
H_2O	0.439	−0.245	H	0.193
H_2CO	0.386	−0.162	C	0.252
			H	0.045 to 0.018

[a] Charges in the parentheses are for the parent system. [b] The hydrogen atom is the C–H hydrogen. [c] The hydrogen atom is the N–H hydrogen; C′ is the carbon of the CH_3 group linked to C=O and C is the carbonyl group.

amides by far have the strongest interaction with Li^+. Accordingly, the net charge transfer, Δq_T, between the ion and the oxygen donor is also highest in amides. The stabilization energy (ΔE per $Li^+\cdots O$ bond) and Δq_T in all the complexes decreases with increase in n just as in the case of $Li^+(H_2O)_n$ complexes. Accordingly, with increase in , the $Li^+\cdots O$ bond becomes weaker and hence the $Li^+\cdots O$ distance becomes longer. The most significant change in CNDO/2 charges on complexation is the transfer of charge from oxygen to Li^+ (Table IV). In addition, there seems to be small charge transfer from some of the atoms adjacent to the donor atom as well.

With the carbonyl donors, the carbonyl distance is slightly higher in Li^+ complexes. In the case of formaldehyde, the increase in C=O distance is 0.01 Å and in amides it is 0.03 Å. In amides, there is also a shortening of the central C–N bond by 0.03 Å. The bond distance changes would be expected to result in significant changes in the vibrational and nmr spectra of these complexes. Such changes in spectra are indeed observed. Thus, in the case of the acetone–Li^+ complex, a decrease in C=O frequency is reported,[22] while in amide complexes, a de-

TABLE V: CNDO/2 Calculations on Li^+–Amide Complexes

Amide[a]	$-\Delta E$, kcal mol^{-1}	Li···O, Å	Δq_T	E_a, kcal mol^{-1}
FA[b]	72	2.20	−0.24	25 (16.0)
NMA[c]	88	2.20	−0.28	31 (16.0)
DMF[d]	83	2.20	−0.27	31 (16.5)

[a] In all these cases, ∠LiOC = 180°. This is not the most stable configuration (see Table III), but the trends in properties remain similar in other configurations as well. Values of barrier height, E_a, given in brackets are for parent amides. [b] Δ(C=O) = 0.02 Å and Δ(C–N) = −0.02 Å. [c] Δ(C=O) = 0.02 Å and Δ(C–N) = −0.03 Å. [d] Δ(C=O) = 0.02 Å, and Δ(C–N) = −0.03 Å.

crease in the amide I frequency and an increase in the amide II frequency have been noted.[23] Nmr studies on tertiary amides like DMF or *N,N*-dimethylacetamide in the presence of Li^+ salts have shown an increase in the coaelesence temperature of CH_3 signals.[23] This is consistent with the higher C–N bond order in the complexes. CNDO/2 calculations also predict an increase in the barrier to rotation, E_a, in these amide complexes (Table V). The changes in bond distances and spectra found in Li^+ complexes of carbonyl compounds are comparable to those found in protonated amides.[24,25]

Solubility of lithium salts in amides is known to be appreciable.[26] It is also known that polypeptides and proteins undergo conformational changes in aqueous lithium salt solutions.[27] Although there are a few reports on the nature of interaction of Li^+ with amides,[28] polypeptides,[29,30] and proteins,[31] it is not clear whether the interaction involves Li^+ binding to specific sites. The present studies indicate strong binding of Li^+ to the carbonyl oxygen of the peptide bond. Swenson[32] as well as Johnston and Krimm[33] have found alterations in the amide I bond of poly-L-proline in the presence of lithium salts suggesting ion-induced changes in the peptide geometry. Our calculations on the interaction of Li^+ with cytosine (Table III) show that the interaction with the carbonyl group is strong just as with amides.

There are no experimental data on the binding energies of Li^+ with any of the oxygen donors discussed here. The only case where we can roughly estimate the binding energy is in amide complexes. The enthalpies of solvation of formamide and *N,N*-dimethylformamide are around 215 kcal mol^{-1} and the enthalpy of solvation of lithium ion in these amides is ~130 kcal mol^{-1} (compared to 106 kcal mol^{-1} in the case of Na^+).[34] Assuming 1:4 coordination and correcting for Born energy, this gives an estimate of 25–30 kcal mol^{-1} for the energy of one Li^+–amide bond. Just as in the $Li^+(H_2O)_n$ complexes this estimated value of the binding energy is much smaller than the calculated values.

Interaction of carbonyl compounds with Li^+ is in many ways comparable to protonation of these compounds. CNDO/2 calculations as well as spectroscopic studies have shown that the site of protonation in carbonyl compounds is the carbonyl oxygen.[24,25] In the case of formaldehyde, protonation increases the C=O distance by 0.3 Å. In amides, the increase in C=O distance is around 0.06 Å, while the decrease in C–N distance is about 0.05 Å. Barrier heights to rotation, E_a, in protonated amides are considerably higher than in the parent amides.

Li^+ Complexes with Nitrogen Donors. The geometry of 1:1 complexes of Li^+ with acetonitrile and pyridine are shown in Figure 1. In the case of the Li^+–NH_3 complex,

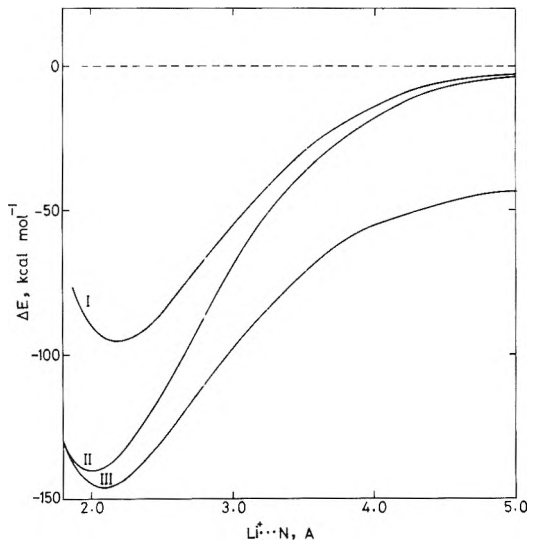

Figure 8. Potential energy curves showing the variation of ΔE with $Li^+\cdots N$ distance in I, NH_3–Li^+, II, C_5H_5N–Li^+ (ϕ = 60°), and III, CH_3CN–Li^+ (ϕ = 75°) systems.

TABLE VI: CNDO/2 Calculations on Li^+–Nitrogen Donor Complexes

Donor	E_T, au	$-\Delta E$, kcal mol^{-1} [a]	$Li^+\cdots N$, Å	Δq_T	k, mdyn/Å	μ, D
		1:1 Complexes				
NH_3	−14.0164	95	2.18	−0.29	1.7	7.6
CH_3CN[b]	−28.1356	193	2.20	−0.39	1.8	10.6
C_5H_5N[c]	−51.1273	164	2.20	−0.48	1.7	5.1
		1:2 Complexes				
NH_3	−28.0280	94	2.20	−0.28	...	0.0
CH_3CN[b]	−56.1989	171	2.15	−0.39	...	10.5
		1:4 Complexes				
NH_3	−55.9737	81	2.30	−0.22	...	0.0

[a] ΔE is the average stabilization energy per $Li^+\cdots N$ bond of the complex. E_T of NH_3, CH_3CN, and C_5H_5N are −13.8644, −27.8268, and −50.8660 au, respectively. [b] This is the most stable configuration, ϕ = 60°. [c] This is the most stable configuration, ϕ = 75°.

the Li^+ was along the lone-pair direction. Typical potential energy curves for these 1:1 complexes are shown in Figure 8. We see that the binding energies with nitrogen donors (Table VI) are somewhat higher than with the oxygen donors (Table III). The variation of binding energies with ϕ in the case of 1:1 acetonitrile and pyridine complexes are shown in Figure 9. In the case of Li^+–CH_3CN, the orientation where Li^+ is above the center of the C≡N bond (ϕ = ±60) is most stable. In the planar Li^+–pyridine complex, the most stable configuration is one where ϕ = 75°.

The stabilization energy per $Li^+\cdots N$ bond decreases as the number of coordinating donor molecules, n, increases just as in the oxygen donor complexes (Table VI). The CNDO/2 charges in these complexes show that the charge is transferred from the nitrogen to Li^+; there is also some charge transfer from other atoms such as the hydrogen atoms in the case of NH_3, the nitrile carbon atom in CH_3CN, and the α-carbon atom in the case of pyridine.

Recently, Yamdagni and Kebarle[35] have experimentally determined the binding energy of K^+–CH_3CN to be 24 kcal mol^{-1}. Considering the trends in the water–alkali

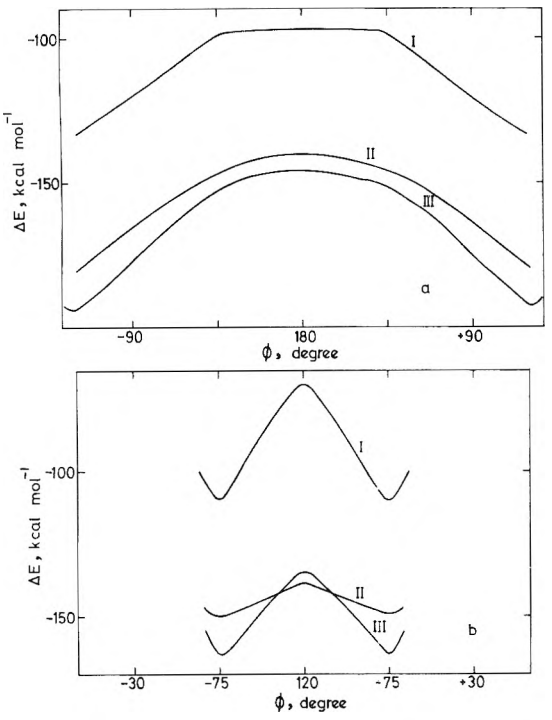

Figure 9. (a) Variation of ΔE with ϕ in CH_3CN–Li^+ at N···Li^+ distances of 3.0 Å (I), 1.9 Å (II), and 2.1 Å (III). (b) Variation of ΔE with ϕ in C_5H_5N–Li^+ at N···Li^+ distance of 3.0 Å (I), 1.9 Å (II), and 2.2 Å (III).

TABLE VII: CNDO/2 Calculations on $Li^+(HF)_n$ Complexes

System	E_T, au	$-\Delta E$, kcal mol^{-1}	Li^+···F, Å	μ, D
	1:1 Complexes			
HF[a]	−28.4462	16	2.7	10.4
HF[b]	−28.4461	16	2.7	11.1
	1:2 Complexes			
HF[a]	−56.8905	17	2.7	0.0
HF[b]	−56.8905	17	2.7	0.0
	1:4 Complexes			
HF[a]	−113.7732	16	2.8	0.0
HF[b]	−113.7728	16	2.8	0.0

[a] ϕ = 180° (linear arrangement) and Li^+ is at the fluorine end; E_T = −28.4179 au and μ = 1.85 D for H–F molecule. [b] ϕ = 135°.

metal ion complexes (where ΔE decreases going from Li^+ to Na^+ or K^+), we would estimate the binding energy of Li^+–CH_3CN to be around 45 kcal mol^{-1}, which is again lower than the calculated value. Searles and Kebarle[36] have determined the thermodynamics of association of NH_3 with NH_4^+ giving rise to the complexes of the type $NH_4^+(NH_3)_n$ and ΔE in these complexes decreases with n.

Li^+ Complexes with HF. The results of the CNDO/2 calculations on $Li^+(HF)_n$ complexes are summarized in Table VII. The bonding energies in these complexes are smaller as compared to the values in oxygen or nitrogen donor complexes. Accordingly, the Li^+···F distance is also much longer than the Li^+···O or Li^+···N distance in complexes. A similar result is found in mixed hydrogen-bonded dimers of H_2O, NH_3, and HF; the hydrogen bond energies of dimers where the hydrogen bond is formed between the fluorine of HF and the proton of another donor is generally weak compared to other dimers.[37] Further, ΔE does not change with n in these HF complexes and charge is transferred from both H and F atoms to Li^+.

CNDO/2 Binding Energies and Potential Function for Li^+–Donor Interactions. In the previous sections it was pointed out that the values of binding energies calculated by the CNDO/2 method are generally much higher than the experimental values. The equilibrium distances also differ from experiment. These discrepancies arise from limitations of the CNDO/2 method. The basis sets in the CNDO/2 method are small, valence basis sets; inclusion of 1s and 3d orbitals in some form would probably improve the results.[38] Further, the parameters in the CNDO/2 program were not optimized in our calculations; reparameterisation is likely to yield better agreement with experiment.

In spite of the disagreement of absolute values of binding energies with experiment, the CNDO/2 binding energies and equilibrium distances exhibit the correct trends with n in $Li^+(donor)_n$ complexes. We therefore feel that the CNDO/2 method rightly predicts the form of the potential curve (variation of ΔE with distance) for Li^+–donor interaction. Assuming that the form of the potential function for the variation of ΔE with r is rightly given by the CNDO/2 method, we next attempted to see if the function can be fitted to the empirical equation of the type

$$\Delta E = \frac{A}{r^a} - \frac{B}{r^b}$$

where a and b are constants. Here, ΔE is the interaction energy of the complex $Li^+(donor)_n$ where Li^+ is at the same distance r from all the donor molecules. We used the CNDO/2 stabilization energies, ΔE, at the equilibrium distances to calculate A and B for different values of a and b. We find that for all the systems studied here, the best values of a and b are 12 and 6, respectively. We thus see that the classical Lennard-Jones potential holds good for the ion–dipole interactions studied presently, a conclusion which has also been arrived at by Saluja and Scheraga.[12] Once having obtained the correct potential function, we can evaluate A and B if we know the correct values of ΔE. Unfortunately, experimental ΔE values are available only for $Li^+(H_2O)_n$ and A and B have been evaluated for this system.[12]

Stretching Vibrations Involving Li^+ in $Li^+(donor)_n$ Complexes. The Li···donor (Li···O or Li···N) stretching force constants calculated from the CNDO/2 potential energy curves are given in Tables I, III, and VI. We see that the force constant is of the order of 1 mdyn/Å in all the complexes studied by us. The essential constancy of the Li···donor distances and the stretching force constant in these complexes indicates that the Li···donor stretching frequency must be about the same. We have calculated the asymmetric stretching frequency in linear $Li(donor)_2$ as well as tetrahedral and planar $Li(donor)_4$ complexes employing standard relations[39-41] with stretching force constants of 1.0 and 0.6 mdyn/Å, the latter being taken as a likely lower limit. The donors employed for the calculations are oxygens (as may be present in oxides or oxyanion salts), water, and dimethyl ether.

The results of these calculations show that the asymmetric stretching frequency in these systems is between 440 and 750 cm^{-1} immaterial of the donor when the

stretching force constant is 1 mdyn/Å; with 0.6 mdyn/Å the range is 350–590 cm^{-1}. It appears that a value of 500 ± 100 cm^{-1} would cover the likely range for the $Li(O)_n$ asymmetric stretching frequency if the force constant is in this range. A force constant of 0.7 mdyn/Å has indeed been suggested by Edgell and coworkers[41] for the Li^+ vibration in the solvent cage of oxygen donors.

It would be relevant to discuss briefly the nature of cation vibrations in the oxygen polyhedra formed by the coordinating solvent molecules. Alkali metal salts dissolved in oxygen donor solvents such as ethers, ketones, and amides exhibit broad low-frequency absorption band characteristic of alkali metal ions in the infrared spectra.[22,41-43] In the case of lithium salts, this band appears at around 400 cm^{-1}. This is essentially independent of the anion and the solvent in polar solvents and the solvation number is 4.[22,42,44] The lithium cation–solvent cage band around 400 cm^{-1} has a corresponding band in well-defined 1:4 coordination compounds of Li^+ with amides as well as in lithium oxide glasses.[45] These bands appear to be characteristic of specific cation–oxygen coordination polyhedra ($Li^+(O)_4$ in the case of Li^+), similar to those found in the spectra of crystalline oxyanion salts by Tarte.[46,47] Lithium salts also exhibit a band at around 400 cm^{-1} in nitrogen-donor solvents such as pyridine and acetonitrile[41,45,48] just as in oxygen-donor solvents. Accordingly, the force constants for the $Li^+\cdots N$ and $Li\cdots O$ vibrations in Li^+–donor complexes are of the same order. It is remarkable that the low-frequency bands characteristic of quantized vibrations of cations in different systems require only the short range order of the first coordination sphere. These bands will undoubtedly serve as useful probes in the study of coordination of cations in solutions, glasses, crystals, and other systems and also ion–solvent interactions.

Concluding Remarks

Although CNDO/2 calculations do not provide correct values of interaction energies, ΔE, between Li^+ and donor molecules to give $Li^+(donor)_n$ complexes, the calculated ΔE values show a decreasing trend with increase in n as expected. Accordingly, the $Li^+\cdots$donor distance increases with n. Assuming that the CNDO method rightly predicts the form of variation of ΔE with $Li^+\cdots$donor distance, we find that the CNDO results can be fitted into a 6–12 potential function.

In the case of Li^+ complexes with water, the calculations show that the molecules in the second hydration layer are very strongly hydrogen bonded to the molecules in the first layer; this hydrogen bond energy will approach the normal value in water as we go to successive layers of hydration. A similar situation seems to be present in the case of F^- complexes with water. Properties of hydrated ion pairs predicted by the CNDO method appeal to reason. Thus, in the case of solvent-separated ion pairs, as the number of water molecules separating the ion pair increases, the stabilization energy, ΔE, approaches the value for the isolated $Li^+(H_2O)_n$ or $F^-(H_2O)_n$ complex.

Based on CNDO calculations, the orientations of donor molecules with respect to Li^+ in $Li^+(donor)_n$ complexes have been predicted. In all of the cases examined, the most stable orientation is not along the direction of the lone-pair orbital of the donor, a situation similar to hydrogen-bonded systems. The present calculations correctly predict the trends in the variations of bond distances in the donor due to interaction with Li^+. The predicted bond distance changes can be experimentally verified in terms of infrared band shifts as well as nmr spectra. For example, in the case of carbonyl donors, the predicted increase in the C=O distance in carbonyl donors causes a lowering of the C=O stretching frequency. In amides, a decrease in the C–N bond distance increases the barrier to rotation about the C–N bond. In this regard, interaction of Li^+ with donors is comparable to the protonation of donors. Based on CNDO calculations we can predict the nature of the quantized vibration of Li^+ in $Li^+(donor)_n$ polyhedra. Characteristic infrared bands due to such vibrations have indeed been reported.

It is heartening that in spite of the approximations of the CNDO method, the calculations are able to describe the gross features of ion solvation to some extent. The main shortcoming, however, is that these calculations do not provide the right values of interaction energies and bond distances.

Acknowledgments. The authors are thankful to the Council of Scientific and Industrial Research (India) and the National Institutes of Health (01-078-1) for support of this research.

References and Notes

(1) J. D. Bernal and R. H. Fowler, *J. Chem. Phys.*, **1**, 515 (1933).
(2) D. F. C. Morris in "Structure and Bonding," Vol. 4, C. K. Jorgensen, *et al.*, Ed., Springer-Verlag, Berlin, 1968.
(3) A. S. N. Murthy and C. N. R. Rao, *J. Mol. Struct.*, **6**, 253 (1970); C. N. R. Rao in "Water—A Treatise," F. Franks Ed., Plenum Press, New York, N. Y., 1972.
(4) J. R. Hoyland and L. B. Kier, *Theoret. Chim. Acta*, **15**, 1 (1969).
(5) P. Schuster, *Int. J. Quantum Chem.*, **3**, 851 (1969).
(6) J. A. Pople, D. P. Santry, and G. A. Segal, *J. Chem. Phys.*, **43**, S129 (1965); J. A. Pople and G. A. Segal, *ibid.*, **43**, S136 (1965); **44**, 3289 (1966).
(7) L. E. Sutton, Ed., "Tables of Interatomic Distances and Configurations in Molecules and Ions," The Chemical Society, London, 1958, 1965.
(8) K. G. Breitschwerdt and H. Kistenmacher, *Chem. Phys. Lett.*, **14**, 286 (1972).
(9) H. Lischka, Th. Plesser, and P. Schuster, *Chem. Phys. Lett.*, **6**, 263 (1970).
(10) P. Russegger, H. Lischka, and P. Schuster, *Theoret. Chim. Acta*, **24**, 191 (1972).
(11) R. E. Burton and J. Daly, *Trans. Faraday Soc.*, **66**, 1281 (1970); **67**, 1219 (1971).
(12) P. P. S. Saluja and H. A. Scheraga, unpublished results.
(13) E. Clementi and H. Popkie, *J. Chem. Phys.*, **57**, 1077 (1972).
(14) G. H. F. Diercksen and W. P. Kraemer, *Theoret. Chim. Acta*, **23**, 387 (1972); W. P. Kraemer and G. H. F. Diercksen, *ibid.*, **23**, 393 (1972).
(15) I. Dzidic and P. Kebarle, *J. Phys. Chem.*, **74**, 1466 (1970).
(16) (a) M. De Paz, S. Ehrenson, and L. Friedman, *J. Chem. Phys.*, **52**, 3362 (1970); (b) A. J. Cunningham, J. D. Payzant, and P. Kebarle, *J. Amer. Chem. Soc.*, **94**, 6727 (1972).
(17) A. Goel, A. S. N. Murthy, and C. N. R. Rao, *Indian J. Chem.*, **9**, 56 (1971).
(18) M. Arshadi, R. Yamacagni, and P. Kebarle, *J. Phys. Chem.*, **74**, 1475 (1970).
(19) E. M. Kosower, "Physical Organic Chemistry," Wiley, New York, N. Y., 1968, p 353.
(20) A. Goel, A. S. N. Murthy, and C. N. R. Rao, *J. Chem. Soc., A*, 190 (1971).
(21) C. N. R. Rao, A. Goel, K. G. Rao, and A. S. N. Murthy, *J. Phys. Chem.*, **75**, 1744 (1971).
(22) M. K. Wong, M. J. McKinney, and A. I. Popov, *J. Phys. Chem.*, **75**, 56 (1971).
(23) D. Balasubramanian, A. Goel, and C. N. R. Rao, *Chem. Phys. Lett.*, **17**, 482 (1973).
(24) A. S. N. Murthy, K. G. Rao, and C. N. R. Rao, *J. Amer. Chem. Soc.*, **92**, 3544 (1970).
(25) C. N. R. Rao, K. G. Rao, A. Goel, and D. Balasubramanian, *J. Chem. Soc., A*, 3077 (1971).
(26) J. W. Vaughn in "The Chemistry of Non-aqueous Solvents," Vol. II, J. J. Lagowski, Ed., Academic Press, New York, N. Y., 1967.
(27) P. Von Hippel and T. Schleich in "Biological Macromolecules," Vol. II, S. N. Timasheff and G. D. Fasman, Ed., Marcel Dekker, New York, N. Y., 1968.
(28) J. Bello, D. Haas, and H. R. Bello, *Biochemistry*, **5**, 2510 (1966).

(29) J. Kurtz and W. H. Harrington, *J. Mol. Biol.*, **17**, 440 (1966).
(30) C. B. Baddiel, D. Chaudhuri, and B. C. Stace, *Biopolymers*, **10**, 1169 (1971).
(31) M. E. Noelken, *Biochemistry*, **9**, 4122 (1970).
(32) C. A. Swenson, *Biopolymers*, **10**, 2591 (1971).
(33) N. Johnston and S. Krimm, *Biopolymers*, **10**, 2597 (1971).
(34) D. V. S. Jain, B. S. Lark, S. P. Kochar, and V. K. Gupta, *Indian J. Chem.*, **7**, 256 (1969).
(35) R. Yamdagni and P. Kebarle, *J. Amer. Chem. Soc.*, **94**, 2940 (1972).
(36) S. K. Searles and P. Kebarle, *J. Chem. Phys.*, **72**, 742 (1968).
(37) P. A. Kollman and L. C. Allen, *J. Amer. Chem. Soc.*, **92**, 753 (1970).
(38) D. P. Santry and G. A. Segal, *J. Chem. Phys.*, **47**, 158 (1967).
(39) A. G. Meister and F. F. Cleveland, *Amer. J. Phys.*, **14**, 13 (1946).
(40) K. Nakamoto in "Infrared Spectra of Inorganic and Coordination Compounds," Wiley, New York, N. Y., 1962, Appendix II.
(41) W. F. Edgell, J. Lyford, R. Wright, W. Risen, and A. Watts, *J. Amer. Chem. Soc.*, **92**, 2240 (1970).
(42) J. L. Wuepper and A. I. Popov, *J. Amer. Chem. Soc.*, **91**, 4352 (1969); **92**, 1493 (1970).
(43) C. Lasserigne and P. Baine, *J. Phys. Chem.*, **75**, 3188 (1971).
(44) R. M. Erlich and A. I. Popov, *J. Amer. Chem. Soc.*, **93**, 5620 (1971).
(45) C. N. R. Rao, V. V. Bhujle, A. Goel, U. R. Bhat, and A. Paul, *Chem. Commun.*, 161 (1973), and the references cited therein.
(46) P. Tarte, *Acad. Roy. Belg., Cl. Sci. Mem.*, **35**, 1 (1965).
(47) P. Tarte, *Spectrochim. Acta*, **20**, 238 (1964); **21**, 313 (1965); **26A**, 747 (1970).
(48) W. J. McKinney and A. I. Popov, *J. Phys. Chem.*, **74**, 535 (1970).

Electron Spin Resonance Studies of the Reduced Molybdovanadophosphoric Heteropoly Acids. I

Masayuki Otake,* Yukie Komiyama, and Tadaaki Otaki

The Central Research Laboratories, Mitsubishi Chemical Industries Co., Hisamoto, Takatsu-ku, Kawasaki, Japan

(Received March 26, 1973)

Publication costs assisted by Mitsubishi Chemical Industries Co.

Esr spectra of the reduced forms of the molybdovanadophosphoric heteropoly acids ($H_{3+x}Mo_{12-x}V_xPO_{40}\cdot nH_2O$, where x = 0, 1, and 2) have been observed in their solid state, and exhibit well-resolved anisotropic hyperfine structure. From the analysis based on the second-order perturbation theory, it was found that replacements of molybdenum by vanadium ions afforded a very promising way to clarify the nature of the reduced form of the heteropoly compounds. The hyperfine coupling constants of the vanadium(IV) observed for x = 1, 2 are almost the same as those of organic vanadyl complexes, which indicates localization of one electron on the vanadium ion. A mechanism for this localization in the heteropoly acids is proposed. Several parallel lines of the x = 1 and 2 species were found to be split by about 15 G, due presumably to interactions with neighboring hydroxylated molybdenum anions. The narrow line width of the peaks is attributable to the separation of the paramagnetic ions in the heteropoly cage, large enough to remove dipolar broadening. By the estimation of the line width with a cubic lattice model, it was found that only one paramagnetic ion existed in one molecule. Mo(V) is the sole paramagnetic species in the x = 0 acid, whereas V(IV) is assumed to be that in the x = 1 and 2 acids. The possibility of the existence also of Mo(V) components in the esr signal of the latter acids remains, because of the obscuring effect of the stronger intensity of the vanadium(IV) lines.

The reduction of molybdenum and vanadium compounds generally gives rise to blue products associated with molybdenum(V) and vanadium(IV), respectively. Many esr studies of the reduced states have been reported,[1-4] sometimes with an interest in their relation to catalytic activity.[1,4] In the case of the reduction of oxides of vanadium[5] and its mixed oxides with molybdenum,[5,6] the esr spectra usually show a broad line (with no hyperfine structure and apparently small anisotropy), due to the large line width caused by fast spin–lattice relaxation[6] or dipole–dipole interaction.[7]

In the study of such oxides, it is often observed that the esr spectrum is strongly affected by the conditions of sample preparation. A single crystal of V_2O_5, prepared by crystallization after zone melting, for instance, gives several kinds of paramagnetic species, dependent on small changes in the cooling rate or in the atmosphere. Mixed oxides with completely identical chemical and physical properties are difficult to produce. Thus, Mann and Khulbe[1] observed a complicated structure in the esr spectrum of a low V_2O_5 content V_2O_5–MoO_3 system, whereas Yoshida[5,6] reported only a broad singlet throughout the composition range. One of the most promising ways to achieve reproducibility is to prepare pure compounds, with definite molecular or crystal structure. In the present study, a series of molybdovanadophosphoric heteropoly acids was selected as a model compound for the V_2O_5–MoO_3 composite oxides. These heteropoly acids are, in general, prepared by the condensation of aqueous solutions containing VO_3^-, MoO_4^{2-}, and PO_4^{3-} oxyanions with sulfuric acid. The famous Keggin structure[8,9] is generally accepted for the 12-molybdophosphoric heteropoly acid and the identical structure[10] was proposed for all the molybdovanadophosphoric acids with the general formula $H_{3+x}Mo_{12-x}V_xPO_{40}\cdot nH_2O$, where x is a number from 0 to 12, and n is the number of waters of crystallization.

The reduced form of molybdophosphoric heteropoly acid is generally used in analytical chemistry for the detection of trace amounts of phosphorus, utilizing the strong blue colorization generally called heteropoly blue. This colorization is associated with the formation of lower valent molybdenum ions among the polymeric units in the heteropoly cage, but the valency of such reduced ions is not yet identified. Several polarographic[11] and spectroscopic[12] studies of the reduction of heteropoly tungstates have shown that the compounds have low reduction potentials and the addition of electrons is so fast that it is sometimes difficult to discriminate between one and two electron transfers. Esr spectra of such a reduced phosphotungstate[11] have shown the applicability of this technique to the study of the mechanism of the reduction, but the spectral pattern is a broad singlet with little anisotropy and hyperfine structure, so that the usefulness is only a limited one. In the present study it will be shown how vanadium substitution into the molybdophosphoric heteropoly acid is a promising way for the elucidation of the reduction process and the chemistry of the reduced compounds. The heteropoly acids with the above formula have a stability against reduction and thus were useful in the present study.

Experimental Section

Dodecamolybdophosphoric acid was prepared from aqueous solution of the stoichiometric mixture of $Na_2MoO_4 \cdot 2H_2O$ and $Na_2HPO_4 \cdot 12H_2O$ by condensation with sulfuric acid (d = 1.84), followed by extraction with ether. All these were analogous to the method for preparation of the vanadium-substituted heteropoly molybdates proposed in ref 13. Commercial grade dodecamolybdophosphoric acid ($H_3MO_{12}PO_{40} \cdot 24H_2O$) was also used in the experiment with the same results. 11-Molybdo-1-vanadophosphoric and 10-molybdo-2-vanadophosphoric acids were prepared following the method of Tsigdinos and Hallada.[13] The vanadium and molybdenum condensation ratio was confirmed by X-ray fluorescence analysis. The mixed oxides of the MoO_3-V_2O_5-P_2O_5 system were used in order to compare with the results of the heteropoly acids. They were prepared by mixing the aqueous solution containing calculated amounts of the corresponding ammonium salt, *i.e.*, $(NH_4)_6Mo_7O_{24} \cdot 4H_2O$, NH_4VO_3, and $(NH_4)_2HPO_4$, respectively. The mixed solution was evaporated to dryness under vacuum (20 Torr) at 40°, and further dried in an oven at 150°. The dry mass was ground in an agate mortar and the powder was placed as a thin layer (2~3 mm) in a Pyrex tube. It was heated under flowing dried air in an electric furnace, with the programed heating rate of 1°/min from room temperature to 600° followed by 2 hr of calcination at that temperature. Several molybdenum compounds were also selected for the esr study of their reduced oxyanions. The reduction of these compounds was carried out in a dual quartz tube, the inner diameters being 4 and 2 mm, respectively. The sample powder was placed in the inner tube to about 20 mm height, the bottom being stuffed with a small amount of quartz wool, through which hydrogen gas preheated in the outer tube flows. The reduction of the heteropoly acids was carried out below 300° for less than 10 min, whereupon a strong esr signal with resolved hyperfine splitting (hfs) was observed. All the spectra were recorded at 77°K, after rapidly evacuating the sample to less than 10^{-4} Torr at 100°. An X-band spectrometer JES-P-10, Japan Electron Optics Co., was used throughout the present investigation. The analysis of the anisotropic hfs signals was carried out by the parameter optimization technique explained in the Appendix. In this paper the direction of the magnetic field has been indicated in the figures by an arrow, whose length corresponds to 250-G width.

Results

(*A*) *Dodecamolybdophosphoric Acid.* The fresh compound dodecamolybdophosphoric acid is a yellow microcrystalline powder, and does not give any esr signals. Reduction (5 min) at 280° in H_2 caused no apparent color change but gave an esr spectrum with the anisotropic hfs shown in Figure 1. Further reduction caused the formation of black portions in the sample, and the complete reduction required 1 hr, accompanied by a uniform color change to black. The higher the degree of reduction, the less resolved were the esr observed, and another signal with broader line width appeared with increasing intensity. The spectrum in Figure 1 is quite different from that of the molybdenum oxide supported on alumina,[4] in its sharp line width and the clear resolution of hfs components. The signals in Figure 1 are grouped into two sets, one being the perpendicular and the other the parallel components. The assignment of the second derivative spectrum is given in Table I. It was found that the reduced sample was very soluble in water, just as the original heteropoly acid. This fact indicates that the sample is not decomposed to the composite oxide by the present treatment. The stability was also confirmed by X-ray diffraction and ir spectroscopy.

(*B*) *Undecamolybdovanadophosphoric Acid.* The orange-colored sample showed an esr signal even before reduction with H_2. The reduction in H_2 at 280° was very fast, with colorization to dark blue, but the esr spectral pattern was almost unchanged except for the larger signal intensity and the broader line width and, hence, decreased resolution. The partial reduction of the original heteropoly acid seemed to have occurred in the synthetic stage, possibly due to the presence of sulfur compounds in the ether,[13b] for which the commercially available G.R. grade sample was used without further purification. The spectrum in Figure 2 was obtained from the original heteropoly acid at 77°K after evacuation at 100° to below 10^{-4} Torr. It is remarkably similar to that of oxovanadium(IV) in frozen glasses[14] or vanadium pentoxide supported on alumina,[5] and thus the signal is reasonably assigned to the vanadium(IV) ion substituting for one of the 12 octahedral molybdenum(VI) oxyanions in the heteropoly cage. The spectrum seems not to retain even a trace of the signal pattern of the dodecamolybdophosphoric acid shown in Figure 1. Thus, the analysis of Figure 2 given in Table I is based completely on the anisotropic hfs of vanadium(IV). The sample reduced in H_2 to a dark mass was soluble in water, just as the original heteropoly acid. The stability of the compound against reduction was further confirmed by the ir spectroscopy.

(*C*) *Decamolybdodivanadophosphoric Acid.* The reddish-orange powder was very easily reduced at 280° in H_2 and was changed to a dark mass. The esr signal was, however, observed even in an original sample before H_2 reduction, which is quite similar to the case of B (the same method of preparation).

The spectral pattern of such a partly reduced sample (Figure 3) resembles that of the H_2-reduced one, and the

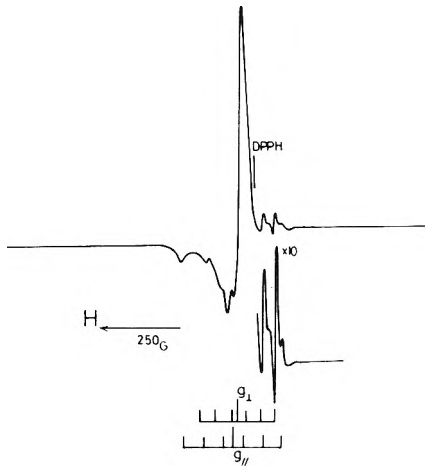

Figure 1. Esr (first derivative) spectrum of reduced $H_3Mo_{12}PO_{40}$ (solid, 77°K).

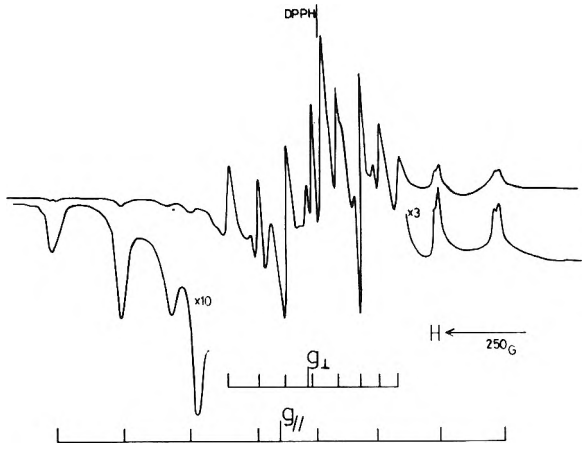

Figure 2. Esr (first derivative) spectrum of reduced $H_4Mo_{11}VPO_{40}$ (solid, 77°K).

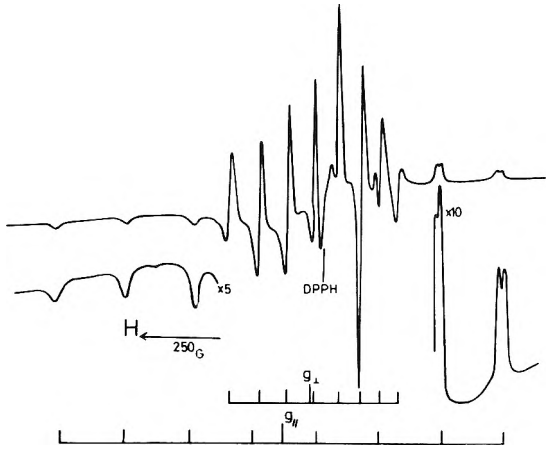

Figure 3. Esr (first derivative) spectrum of reduced $H_5Mo_{10}V_2PO_{40}$ (solid, 77°K).

change in the spectrum was also consistent with B. Its analysis was based on the assumption that vanadium(IV) substitutes for one of the 12 octahedra in the heteropoly cage, and that there is no interaction between vanadium(IV) and vanadium(V). The results are shown in the figure and in Table I. Just as in the previous two heteropoly acids, the original and the reduced samples were equally very soluble in water, from which it was reasonably concluded that the heteropoly acid was not decomposed on reduction. This point was further confirmed by the ir spectroscopy.

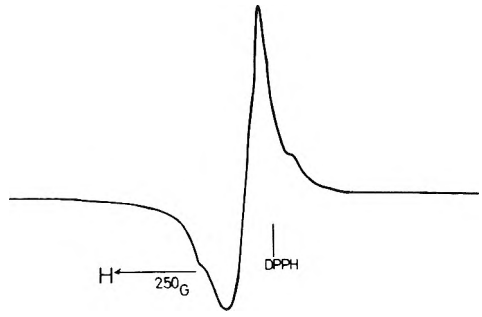

Figure 4. Esr (first derivative) spectrum of reduced $(NH_4)_3Mo_{12}PO_{40}$ (solid, 77°K).

(*D*) *Dodecamolybdophosphoric Acid Ammonium Salt.* The commercially available ammonium dodecamolybdophosphate ($(NH_4)_3Mo_{12}PO_{40}\cdot 3H_2O$, Guaranteed Grade, Kishida Chemicals) was reduced at 350° with a 30-min treatment under a stream of hydrogen. The esr spectrum thus obtained is given in Figure 4. It resembles the signal pattern of the free dodecamolybdophosphoric heteropoly acid in Figure 1, but with a little poorer resolution. The analysis was carried out from the second-derivative spectrum, and the results given in Table I were obtained.

(*E*) *Ammonium Heptamolybdate.* The commercially available ammonium heptamolybdate ($(NH_4)_6Mo_7O_{24}\cdot 4H_2O$, Guaranteed Grade, Kishida Chemicals) was powdered in an agate mortar and reduced under the same conditions as in D. The white powder, when reduced in a stream of hydrogen, turned grey and gave an esr spectrum shown in Figure 5a. However, this compound gave a quite different esr signal (Figure 5b) when decomposed in a stream of air (and hence in an oxidative atmosphere) and with a programed temperature treatment described in the Experimental Section (see section G). The spectrum of the reduced sample in Figure 5a is apparently composed of two kinds of lines, one with anisotropic hfs lines and the other probably with isotropic hfs lines.

(*F*) *Sodium Molybdate Dihydrate.* The commercially available microcrystalline sample of sodium molybdate dihydrate ($Na_2MoO_4\cdot 2H_2O$, Guaranteed Grade, Kishida Chemicals) was powdered and reduced as described in D and E. The white powder maintained its original color and gave no esr signal.

(*G*) *Molybdenum Trioxide.* The commercially available sample of molybdenum trioxide (MoO_3, Commercial Grade, Kishida Chemicals) was a mixture of variously shaped crystals (approximately 2 × 1 × 1 mm) with extremely pale greenish yellow color. This sample was powdered and reduced as described in D, but there appeared only very weak esr signals. The grey sample obtained after reduction at 400° for 30 min in a stream of hydrogen gave no esr signals. The alternative method was applied for preparing MoO_3, utilizing ammonium heptamolybdate powdered and calcined in a thin layer in flowing air with the programmed temperature elevation. The powder thus obtained was pale grey, which was confirmed to be MoO_3 by X-ray diffraction and infrared spectrum. This sample gave an esr signal shown in Figure 5b even before reduction.

(*H*) *Mixed Oxides of the MoO_3-V_2O_5-P_2O_5 System.* Three mixed oxide samples of the MoO_3-V_2O_5-P_2O_5 system showed esr signals even without reduction. The spec-

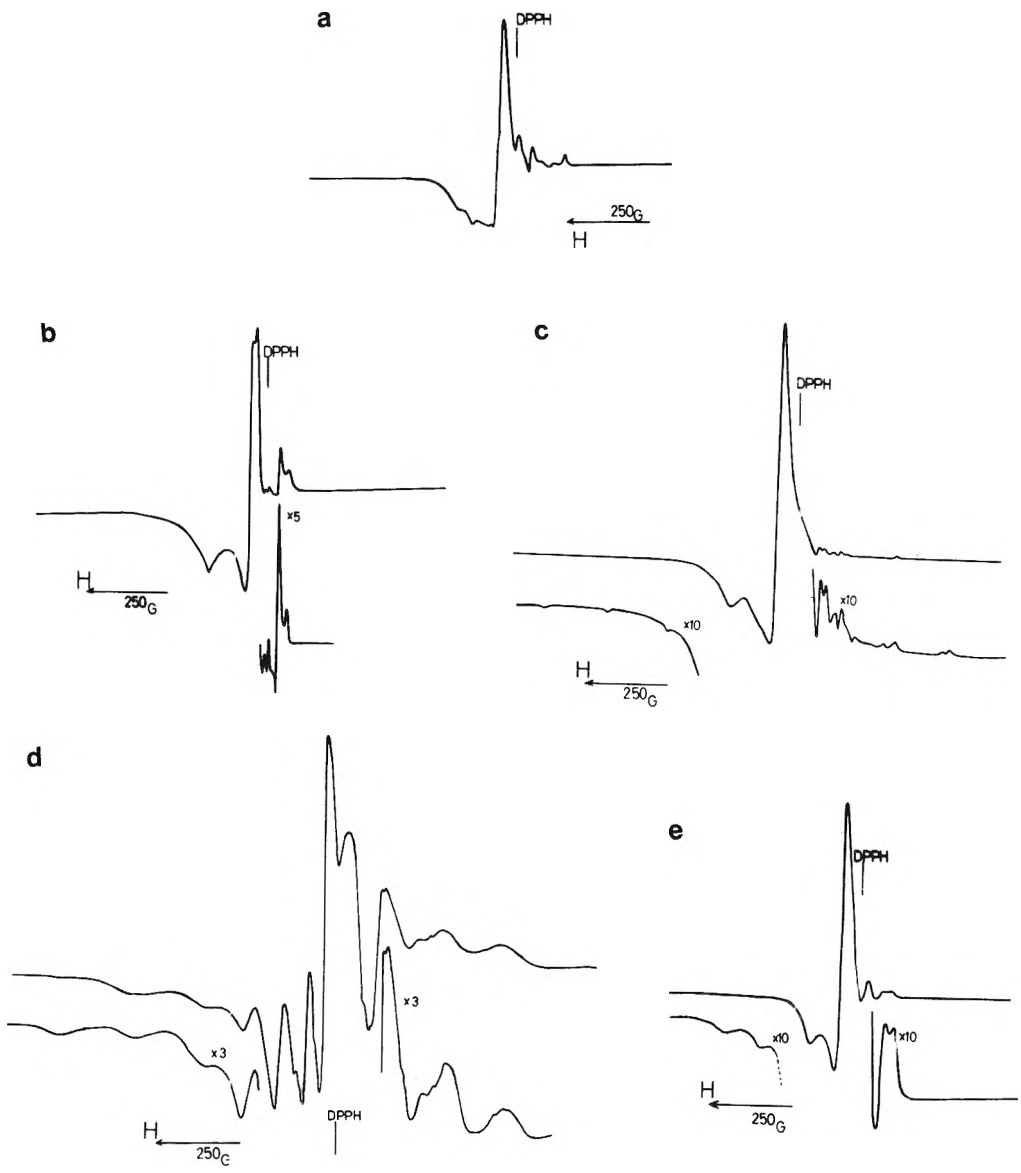

Figure 5. Esr (first derivative) spectra (solid, 77°K) of (a) reduced ammonium heptamolybdate, (b) molybdenum trioxide, and the composite oxides with (c) Mo:V = 10:2 (d) Mo:V:P = 10:2:1, and (e) Mo:P = 12:1 atomic ratios.

TABLE I: *g* and *T* Tensor Parameters for the Reduced Molybdovanadophosphoric Heteropoly Acids

Compounds	Paramagnetic ion	$g_\perp$	$g_\parallel$	$\langle g \rangle$	$T_\perp$ [a]	$T_\parallel$ [a]	$\langle T \rangle$ [a]
$H_3Mo_{12}PO_{40}$	Mo(V)	1.953	1.947	1.951	−0.416	−0.534	−0.455
$H_4Mo_{11}VPO_{40}$	V(IV)	1.982	1.923	1.962	−0.690	−1.751	−1.043
			(1.919)	(1.961)		(−1.724)	(−1.034)
$H_5Mo_{10}V_2PO_{40}$	V(IV)	1.982	1.928	1.964	−0.678	−1.730	−1.029
			(1.924)	(1.962)		(−1.702)	(−1.019)
$H_5Mo_{10}V_2PO_{40}$ [b]	V(IV)			1.965			−1.037
$(NH_4)_3Mo_{12}PO_{40}$	Mo(V)	1.95	1.95	1.95	−0.387	−0.711	−0.495
Oxide [c]	V(IV)	1.99	1.89	1.96	−0.675	−1.708	−1.019
Mo(V) complex [d]	Mo(V)			1.975			−0.32
V(IV) complex [e]	V(IV)	1.980	1.945	1.972	−0.618	−1.674	−0.974

[a] 10^{-2} cm^{-1}. [b] Acetonitrile solution; room temperature (ref 21). [c] Composite oxide with Mo:V:P = 10:2:1 atomic ratio, second-order correction was not made because of the broad line width. [d] Cysteine complex (pH 9, in the 0.2 *M* phosphate buffer) (ref 26). [e] Vanadyl acetylacetonate in pyridine–toluene glass (ref 14).

trum of the mixed oxide with the atomic composition Mo:V = 10:2 is shown in Figure 5c. The first-derivative spectrum is approximately regarded as a broad doublet, but its second-derivative showed the more complicated nature of the anisotropic hfs lines. The spectral pattern resembles that of MoO_3 in Figure 5b, but it has weak sup-

plementary hfs signals originating from V(IV). The sample with Mo:V:P = 10:2:1 showed the spectrum in Figure 5d. This pattern is completely different from that of the sample without phosphorus, and rather resembles that of the vanadium-substituted heteropoly acid given in B of this section. It was composed of two kinds of lines, one with a broader line width, and was assigned as in Table I. The latter and sharper lines are too weak for detailed analysis. The esr signal of the sample with Mo:P = 12:1 is very similar to that of the molybdenum trioxide prepared by the oxidative decomposition of the ammonium heptamolybdate (see F). It was composed of lines from anisotropic origin and had only parallel hfs components resolved (Figure 5e).

These mixed oxides were further investigated by X-ray diffraction and infrared spectroscopy, but both analytical tools indicated only the presence of MoO_3, with only one exceptional compound MoV_2O_6 in the X-ray diffraction of the Mo:V = 10:2 sample. The appearance of the Mo:V:P = 10:2:1 sample was, however, quite different from the other two; *i.e.*, it was yellowish brown whereas the others were grey. The former sample was further found to be completely soluble in water to give an orange-colored solution. The last behavior is quite unexpected for the ordinary oxides after heat treatment at 600°.

Discussion

The molybdophosphoric heteropoly compounds contain a complex and high-molecular weight anion which contains 12 hexavalent molybdenum atoms around one central phosphorus. Pentavalent vanadium or niobium can replace some of the molybdenum atoms in the heteropoly structure, and this property provided a promising hint for the present study. Many successful esr studies have been made on the vanadium compounds, in which the strong anisotropy and the large hyperfine coupling constants of the $^{51}V(IV)$, $I = 7/2$, have been used to elucidate the detailed electronic structure. The information from these studies was found to be applicable to the heteropoly anions replaced by vanadium. The esr spectrum[11] of the electrochemically reduced tungstophosphoric heteropoly acid, $H_3W_{12}PO_{40}$, has been reported, but it contains no hyperfine structures from the $^{183}W(V)$, $I = 1/2$, due to the masking by the large signals from the natural tungsten isotopes with a nuclear spin of zero. In the case of the molybdophosphoric heteropoly acid, the situation becomes a little better thanks to the greater natural abundance of $^{95}Mo(15.70\%)$ and $^{97}Mo(9.45\%)$, both with a nuclear spin 5/2. The anisotropic hyperfine structure in Figure 1 is resolved fairly well. However, the coupling constants are not large enough for accurate analysis and the higher field perpendicular components are overlapped with the parallel hfs signals. Furthermore, in the case of the ammonium salt of this acid, the resolution of the hfs components is incomplete due to the broader line width. In the present esr study of the reduced form of the molybdovanadophosphoric acids, vanadium(IV) signals were used as markers reflecting the electronic properties in relation to their heteropoly structure. The esr parameters of the $x = 1$ and $x = 2$ acids, listed in Table I, were found to be comparable in magnitude to those of the oxovanadium(IV) chelates.[14] This clearly proves the localization of one electron on the vanadium ion in the heteropoly cage. However, the preferential occurrence of the electron on the vanadium ion could not be anticipated, *i.e.*, if it is assumed that the reaction proceeds in order of the ionization potential, V(V–IV) = 65 eV and Mo(VI–V) = 68 eV and Mo(V–IV) = 61.2 eV, or the electronegativity, V(V) = 17.6 and Mo(VI) = 23.4, Mo(V) = 19.8, and Mo(IV) = 16.2. Since both of these parameters suggest the preferential reduction of Mo(VI), it is reasonable to conclude that the V(IV) is not formed by the first electron introduced into the molecule. If the reduction proceeds *via* a two or multielectron process, as have been observed electrochemically in tungstophosphoric acid,[11] these electrons should be distributed among the molybdenum–vanadium cluster. In this case, a larger probability would be expected for the vanadium(V) ion to abstract one electron from the system, although it remains uncertain which of the reactions would occur prior to the other, V(V) → V(IV) or Mo(V) → Mo(IV). These considerations suggest a mechanism of the formation of vanadium(IV) in the $x = 1$ acid. There, however, remain two other questions still to be solved. The first is whether or not molybdenum(V) coexists with vanadium(IV) among the $x = 1$ molecules. From the spectrum of the reduced $x = 1$ acid alone, possible superimposing by the $x = 0$ spectrum (Figure 1) of molybdenum(V) cannot be excluded. The spectrum of the $x = 2$ species was observed, in expectation of information on this question. The spectrum in Figure 3 was slightly different from that of the $x = 1$ species, but it was successfully analyzed on the assumption that there is only one vanadium(IV) in the heteropoly cage and there is no interaction between vanadium(IV) and vanadium(V). Another explanation, that there are two identical vanadium(IV) ions which do not interact each other, will give the same result. However, the coexisting of two paramagnetic ions in one molecule will be excluded by a linewidth analysis which will be described later. Hence one possible solution to the first question is that heteropoly molecules with molybdenum(V) ion in the heteropoly cage may exist among the $x = 1$ and 2 species, just as in the case of the $x = 0$ species, but that it must be a sole paramagnetic ion in the molecule and it should have little electronic interaction with the neighboring vanadium(V) ion. This model is related to the second question, namely, what is the chemical structure of the reduced heteropoly acid? Recently, Pottkamp and Umland[15] proposed, from their polarographic study of the reduction of the $x = 0$ heteropoly acid, the following scheme of the reaction; *i.e.*

$$H_3PMo_{12}O_{40} \longrightarrow H_3PMo_{12}O_{38}(OH)_2 \longrightarrow H_3PMo_{12}O_{36}(OH)_4, H_3PMo_{12}O_{34}(OH)_6$$

Their intermediate compounds correspond to the simultaneous reduction of two Mo(VI)–O bonds to Mo(V)–OH. If it is assumed that the two Mo(VI)–O bonds are of a double bond nature, this corresponds to the disappearance of a π-electron system on these molybdenum(V) ions, and thus they will be electronically isolated by taking the σ-bonding framework, as above. This model is convenient for the explanation of the analysis of the first question. In this respect, however, it would be useful to take into consideration the chemistry of the oxygen atom coordination to the molybdenum and vanadium ions.

It is well known that there are two possible structures for molybdenum oxyanions, one is Mo(VI) surrounded by four O^{2-} in the tetrahedral configuration and the other Mo(VI) surrounded by six O^{2-} in the octahedral configuration. Sodium molybdate is one of the representative tetrahedral compounds, whereas the octahedral coordination

is usually found in the polymeric state. Molybdenum oxyanions are easily condensed under proper conditions to form many isopoly or heteropoly compounds,[16] and both tetrahedral and octahedral oxyanions are known to take part in the reaction. The interconversion between the tetrahedral and the octahedral state is extremely fast;[17] the pH of the aqueous solution is the predominant factor affecting it. The tetrahedral anion is condensed to the octahedral anion, usually by sharing its corner oxygen as a bridging ion. Octahedral anions have two additional ways of condensation. One is to share its corner oxygen with the neighboring octahedral ions, in the same way as stated above. The other is to simultaneously share its two corner oxygen ions with the neighboring octahedral ions. The latter type is regarded as an edge-sharing condensation. The oxygen-containing molybdenum compounds are generally composed of the regular arrangement of these oxyanions or of their condensed polymeric anions.

Several molybdovanadophosphoric heteropoly compounds and their analogs, dealt with in the present study, have structural characteristics as shown in Table II. Among these compounds, the heteropoly acids are characterized by their easy reducibility and stability in the reduced state, while Na_2MoO_4 is reduced less easily by hydrogen at 350 or 400°. This difference toward reduction may reasonably be attributed to such structural differences as (A) whether the environment of Mo(VI) is tetrahedral (MoO_4) or octahedral (MoO_3), and (B) whether the Mo(VI) oxyanion is isolated (Na_2MoO_4) or condensed. The former is presumably a minor factor, since the ionic radii of Mo(VI) ions in the tetrahedron (0.59 Å) is smaller than in the octahedron (0.62 Å), implying more abundant outer shell electrons and hence smaller electron affinity in the octahedral ions. As to the latter point it is more interesting to know how the type and the degree of condensation affect their reduction–oxidation properties. Thus, the sample compounds selected for the present study have seven, twelve, and infinite numbers of octahedra, all of which have, however, different types of condensation. All the samples with octahedral oxyanions were reduced under the stream of hydrogen at 350°, to give an esr signal originating from Mo(V). One exception is the case of crystalline MoO_3 in which, as discussed in ref 6, it was usually impossible to detect the esr signal even after reduction at 400°. In the present study, however, a complicated esr signal was observed in the MoO_3 prepared by the calcination of ammonium heptamolybdate in an oxygen environment, while this sample gave an identical X-ray diffraction pattern with that of a well-developed single crystal. The present esr study of the reduction of the compounds in Table II clearly indicated the importance of the terminal oxygen (Ot) ligand of molybdenum and vanadium ions in an octahedral environment. The localization of the electron on Mo and V was observed only in compounds with this type of oxygen. The terminal oxygen atoms presumably favor localization of electrons introduced by reduction, whereas the bridging oxygen atoms may cause electron transfer from one molybdenum ion to another, *i.e.*, fast spin–lattice relaxation. The double-bond nature and the catalytic importance of the terminal oxygen atoms have been pointed out by Trifiro and Mitchell,[18a] and this property would be convenient for the localization of electrons by the mechanism described earlier. On the other hand, an electron transfer through an outer-sphere cage structure into the central CoO_4 tetrahedron has been observed in the reduction process of the dodecatungstocobaltate anion,[18b] which implies that the existence of such terminal oxygen with double-bond nature is not a satisfactory condition for this electron localization phenomenon. Thus the crystalline MoO_3 has one terminal oxygen in each of their molybdenum oxyanions, but no esr spectrum has been observed after reduction by hydrogen at 400°.

TABLE II: Molecular and Crystal Structure of Several Molybdenum Oxyanions

Compounds	Structure of unit molybdenum oxyanions	Type of condensation and oxygen[a]	Ref
$Na_2MoO_4 \cdot 2H_2O$	1 tetrahedron	No Condensation (4 Ot)	18
MoO_3	Octahedra	2 edge sharing (3 Ob) +2 corner sharing (2 Ob)[b] (5 Ob + 1 Ot)	19
$(NH_4)_6Mo_7O_{24} \cdot 4H_2O$	7 octahedra	3 edge sharing (4 Ob + 2 Ot)	20
$H_3Mo_{12}PO_{40}$	12 octahedra	2 corner sharing (2 Ob)	8
$H_5Mo_{10}V_2PO_{40}$		+ 2 edge sharing (3 Ob) (5 Ob + 1 Ot)	20

[a] Ob for bridging (both corner and edge sharing) and Ot for terminal oxygen anion; the number of these anions per molybdenum is also given. [b] There are three different types for the sharing oxygen, which are shared by 2, 3, and 4 octahedra, respectively

In the case of heteropoly compounds presumably another type of electron transfer is possible, which has been confirmed experimentally by nmr spectroscopy of the crystalline dodecamolybdophosphoric acids.[18c] In the case of dodecatungstocobaltate, the transfer was through the cage structure, while the proposed is based on the surface structure of these heteropoly compounds that contains many lone-pair electron clouds of the sp^2-hybridized oxygen atom of the Mo(VI)=O and V(V)=O bonds. Several -OH bonds that exist in the free heteropoly molecule would cause hydrogen bonding with these lone-pair electrons, which causes dissociation and apparent electron transfers by leaving one Mo(VI)=O to make one new -OH bond. The possibility of this affecting the electronic state of V(IV) will be discussed later.

The molybdovanadophosphoric heteropoly acids gave esr spectra with resolved hfs originating from V(IV). It should be emphasized that even when two vanadium ions occupy two sites of the 12 possible molybdenum octahedra, they will tend not to occupy neighboring positions, thus escaping from the increase of structural and electrostatic strains caused by ions with different radius and different charge (0.59 Å for V(V) and 0.62 Å for Mo(VI)). This makes the distance between two intramolecular vanadium ions large enough to minimize the dipolar interaction, thus leading to the narrower line width. In the case of undecamolybdovanadophosphoric acid, this separation is the order of one molecule, across which only negligible electron transfer can occur. If the line width of the esr signal is determined by the dipole–dipole interaction alone, as was assumed by Van Vleck,[22] the half-width, ΔH, for the spin quantum number S is given by the equation

$$\Delta H = \frac{2.35}{g\beta}\sqrt{\frac{1}{3}S(S+1)}\sqrt{\sum_j B_{jk}^2}$$

where $B_{jk} = (3/2)g^2\beta^2(3\cos^2\theta_{jk} - 1)/r_{jk}^3$.

The observed half-width ($\Delta H = 1.177\Delta H_{msl}$) was nearly

13.2 G for the heteropoly acids with $x = 0$, 1, and 2, which for a simple cubic lattice model corresponds to 14.2 Å for the average distance between the paramagnetic ions. This supports the above-mentioned assumption that the paramagnetic species are formed independently of each other since the size of the heteropoly molecule is about 10 Å in diameter. The distance makes unlikely existence of two or more paramagnetic ions in the same heteropoly cage, and rather suggests the formation of one paramagnetic ion and tetravalent molybdenum ions in the $x = 0$ and 1 species when they are reduced by adding a number of electrons. This is also applicable to the $x = 2$ species, in which only one electron is introduced to vanadium ions. The average distance becomes shorter with increasing degree of reduction, causing broader line widths. In the case of the heteropoly acids, however, it is to be noted that the line width of the slightly reduced solid sample is nearly equal to that of vanadyl(IV) ion in aqueous solution.[23] Furthermore, ΔH in the solid heteropoly acids remained roughly constant at both room and liquid nitrogen temperatures, hence the spin exchange interaction[24] or the motional narrowing are presumably less effective factors.

Completely random electronic interactions are expected in the case of MoO_3–V_2O_5 and MoO_3–V_2O_5–P_2O_5 composite oxide system. These oxides are constructed from clusters with random condensation of the composite oxyanions, whose polymeric unit is much larger than that of the heteropoly anions. Since the average intervanadium(IV) distance is a little shorter than that of the heteropoly acid with the same atomic composition, it causes random but possibly larger magnetic interactions. Almost all of the hfs lines dissappeared in the spectrum (Figure 5c) of the composite with Mo:V = 10:2 atomic ratio. A broader line width (~50 G) was observed for almost all the lines in the spectrum (Figure 5d) of the composite with Mo:V:P = 10:2:1 atomic ratio.

In the esr spectra of the two molybdovanadophosphoric heteropoly acids, parallel components of the hfs lines were found to be split. It has been shown that split spectral patterns can be explained by D_4, but not by C_{4v} symmetry. In the latter, the approximation that $g_{xx} = g_{yy}$ and $T_{xx} = T_{yy}$ is not allowed and hence splitting of the three hfs components occurs. The present splitting of the parallel components cannot be explained by this type of symmetry lowering, except for the possibility of interchange of parallel and perpendicular components, which cannot be excluded, judging from the following estimation of the energy differences. In a rhombic field, with compression along the Z axis, g values are related to the energy levels by

$$g_{\parallel} = g_e(1 - 4\lambda/\Delta)$$

and

$$g_{\perp} = g_e(1 - \lambda/\delta)$$

where g_e is the g value of the free electron, λ is the spin-orbit coupling constant, Δ and δ are the energy differences

$$\Delta = d(x^2 - y^2) - d(xy)$$

$$\delta = d(yz,zx) - d(xy)$$

Assuming $\lambda = 209$ cm^{-1} for vanadium(IV),[25] δ is estimated to be 20,400 cm^{-1}, whereas Δ is estimated to be 21,000~22,500 cm^{-1}, almost equal in magnitude to δ. In the present case, another explanation of the splitting of the parallel components is given by considering two kinds of vanadium(IV) species in the reduced cage structure. The plausibility of this is not small if we refine the mechanism of reduction suggested by Pottkamp, that is, their difference depends on the distance of the reduced molybdenum (Mo(IV)–OH) from the reduced vanadium (V(IV)=O or V(IV)–OH). Here the valency of this molybdenum ion would rather be Mo(IV) from the line-width analysis. If the reduction of molybdenum occurs at the nearest neighbor of vanadium, the hydrogen bonding between Mo(IV)–OH and one or two of the lone-pair electron clouds on the sp^2-hybridized oxygen of V=O would cause some perturbation on the electronic state of the V(IV) ion. Here it must be recalled (Results section) that the vanadium-substituted heteropoly acids gave weak esr signals even before reduction. The esr spectral pattern was, however, quite similar to that of the H_2-reduced sample except for the signal intensity and the increase of the intensity was found quite parallel for the two splitting lines (those in the parallel and lower field $m_n = -7/2$ and $-5/2$ lines). Hence the splitting observed in Figures 2 and 3 should be indifferent to the degree of reduction. Another assumption that some contaminants have given one or other of the split lines or vanadium species is similarly excluded. Furthermore the intensity ratio of the two splitting lines is nearly identical in the $x = 1$ (Figure 2) and $x = 2$ (Figure 3) species, while the content of vanadium ions in the heteropoly cage is twice as large in the latter species, so that the splittings observed in these species are concluded to be indifferent to the vanadium content. Although the stoichiometry of condensation (Mo:V ratio) of the $x = 1$ and $x = 2$ species has been confirmed, with a similar result as in ref 13a, this would have, hence, little effect on this observation. Further discussion on this geometric charge isomerism will be given in our forthcoming paper.

Acknowledgment. The authors are indebted to the Director of the Central Research Laboratories, Mitsubishi Chemical Industries Co., for allowing the publication of this paper. They are also grateful to Dr. K. Wada for helpful discussions and encouragement throughout the work.

Appendix

Analysis of the Anisotropic Hfs Signals. The analysis of the anisotropic hfs signals was carried out by the approximate solution, correct to second-order perturbation, of the spin Hamiltonian

$$\mathcal{H} = \beta[g_{xx}H_xS_x + g_{yy}H_yS_y + g_{zz}H_zS_z] + T_{xx}I_xS_x + T_{yy}I_yS_y + T_{zz}I_zS_z + Q'[I_z^2 - (1/3)I(I+1)] \quad (1)$$

The solution[14] is given by

$$H_z = \frac{h\nu}{g_{zz}\beta} - \frac{hc}{g_{zz}\beta}T_{zz}m_n - \frac{hc^2}{4g_{zz}\beta\nu} \times [T_{xx}^2 + T_{yy}^2][I(I+1) - m_n^2] \quad (2)$$

$$H_\perp = \frac{h\nu}{g_{xx}\beta} - \frac{hc}{g_{xx}\beta}T_{xx}m_n - \frac{hc^2}{4g_{xx}\beta\nu} \times [T_{yy}^2 + T_{zz}^2][I(I+1) - m_n^2] - \frac{hc}{2g_{xx}\beta T_{xx}}(Q')^2[2I(I+1) - 2m_n^2 - 1]m_n \quad (3)$$

Here ν is the microwave frequency, and the T tensor components are in units of cm^{-1}. H_y is obtained from (3) by interchanging subscripts x and y, but in the present case, axial symmetry was assumed. The least-squares fit of the data was carried out by initial estimation of the second-order terms, $\Delta H_{\parallel}^{(2)}(m_n)$ and $\Delta H_{\perp}^{(2)}(m_n)$, from data in the literature[14] and then determination of g_i and T_i by assuming the following linear equations

$$H_i^{obsd}(m_n) + \Delta H_i^{(2)}(m_n) = \frac{h\nu}{g_i\beta} - \frac{hc}{g_i\beta}T_i m_n \quad (4)$$

$$\Delta H_{\parallel}^{(2)}(m_n) = \frac{hc^2}{2g_{\parallel}\beta\nu}T_{\perp}^2[I(I+1) - m_n^2]$$

$$\Delta H_{\perp}^{(2)}(m_n) = \frac{hc^2}{4g_{\perp}\beta\nu}[T_{\parallel}^2 + T_{\perp}^2][I(I+1) - m_n^2] + \frac{hc}{2g_{\perp}\beta T_{\perp}}(Q')^2[2I(I+1) - 2m_n^2 - 1]m_n \quad (5)$$

All the g_i and T_i (where the subscript i stands for parallel and perpendicular components) values were compared with their previous estimation and the calculation recycled until convergence was attained. The value Q' for V(IV) is fixed to 0.0002 cm^{-1},[14] whereas that for Mo(V) is assumed to be zero. The negative sign of T_i's was assumed, following ref 14. In the present case, the analysis of the $x = 1$ and 2 species was based on the assumption that there are two kinds of radicals, both exhibiting the same (*i.e.*, indistinguishably superimposed on each other) perpendicular but different parallel signal patterns, causing the apparent splitting of the $m_n = -7/2$, $-5/2$, and $-3/2$ lines.

References and Notes

(1) R. S. Mann and K. C. Khulbe, *Bull. Chem. Soc. Jap.*, **45**, 2929 (1972).
(2) K. Hirota and K. Kuwata, *Bull. Chem. Soc. Jap.*, **36**, 227 (1963).
(3) V. B. Kazanskii, *et al.*, *Kinet. Katal.*, **2**, 862 (1961); **3**, 194 (1962); **5**, 861 (1964).
(4) K. S. Seshadri and L. Petrakis, *J. Phys. Chem.*, **74**, 4102 (1970).
(5) K. Tarama, S. Teranishi, S. Yoshida, and H. Yoshida, *Bull. Chem. Soc. Jap.*, **34**, 1195 (1961).
(6) S. Yoshida, *Shokubai*, **10(2)**, 90 (1968).
(7) H. Takahashi, M. Shiotani, H. Kobayashi, and J. Sohma, *J. Catal.*, **14**, 134 (1969).
(8) J. F. Keggin, *Proc. Roy. Soc., Ser. A*, **144**, 75 (1934).
(9) A. J. Bradley and J. W. Illingworth, *Proc. Roy. Soc., Ser. A*, **157**, 113 (1936).
(10) A. V. Ablov, T. I. Malinovskii, and V. I. Dedyu, *Russ. J. Inorg. Chem.*, **4**, 176 (1959).
(11) P. Stonehart, J. G. Koren, and J. S. Brinen, *Anal. Chem. Acta*, **40**, 65 (1968).
(12) M. T. Pope and G. M. Varga, Jr., *Inorg. Chem.*, **5**, 1249 (1966).
(13) (a) G. A. Tsigdinos and C. J. Hallada, *Inorg. Chem.* **7**, 437 (1968); (b) *Inorg. Syn.*, **1**, 127 (1939).
(14) C. P. Stewart and A. L. Porte, *J. Chem. Soc., Dalton Trans.* 1661 (1972).
(15) F. Pottkamp and F. Umland, *Fresenius' Z. Anal. Chem.*, **260**, 185 (1972).
(16) D. S. Honig and K. Kustin, *Inorg. Chem.*, **11**, 65 (1972).
(17) G. Schwarzenbach and J. Meier, *J. Inorg. Nucl. Chem.*, **8**, 302 (1958).
(18) (a) P. C. H. Mitchell and F. Trifiro, *J. Chem. Soc. A*, 3183 (1970); (b) A. W. Chester, *J. Org. Chem.*, **35**, 1797 (1970); (c) T. Wada, *C. R. Acad. Sci.*, **259**, 553 (1964).
(19) G. Andersson and A. Magnéli, *Acta Chem. Scand.*, **4**, 793 (1950); **7**, 154 (1953).
(20) G. A. Tsigdinos, Molybcenum Chemicals Bulletin (db-12a), Climax Molybdenum Co., 1969.
(21) M. Otake and T. Otaki, unpublished results.
(22) J. H. Van Vleck, *Phys. Rev.*, **74**, 1168 (1948).
(23) R. N. Rogers and G. E. Pake, *J. Chem. Phys.*, **33**, 1107 (1960).
(24) P. W. Anderson and P. R. Weiss, *Rev. Mod. Phys.*, **25**, 269 (1953).
(25) J. S. Griffith, "The Theory of Transition-Metal Ions," Cambridge University Press, Oxford, 1961.
(26) T. S. Huang and G. P. Haight, Jr., *J. Amer. Chem. Soc.*, **92**, 2336 (1970).

The Vibrational Spectrum of Naphthalene Anion

Charles L. Dodson* and James F. Graham

Chemistry Department University of Oxford, Oxford OX1 3TG, England

(Received June 12, 1973)

Publication costs assisted by the University of Alabama in Huntsville, Huntsville, Alabama 35807

An investigation of the vibrational spectrum of the naphthalene anion radical is reported. Infrared data were obtained at 295 and 77°K; Raman, at 295°K. Six of the required twenty-four Raman fundamentals were observed as well as thirteen of the expected twenty infrared modes. Tentative assignments were based upon analogy with the spectrum of the parent molecule, neutral naphthalene, and comparison of band intensities and spectral shifts between naphthalene and its anion. It is suggested that, for appropriate molecules, additional aids for vibrational assignments are provided by the examination of ions of the neutral species together with isotopic variants of both compounds.

Introduction

An investigation of the vibrational spectrum of the naphthalene anion radical is reported. Six of the required twenty-four Raman active fundamentals were observed while the infrared spectrum provided thirteen of the expected twenty bands. Infrared data were obtained at 295 and 77°K; Raman, at 295°K. Tentative assignments were based upon analogy with the spectrum of the parent molecule, neutral naphthalene, and comparison of band intensities and spectral shifts between naphthalene and its anion, the assumption being that the mechanical descriptions of the normal modes for both species are approximately equivalent. This assumption is supported by the fact that both compounds possess D_{2h} symmetry, spectral

shifts are small, and bond lengths and angles change only slightly.

This experiment was encouraged by (1) a suggestion that out-of-plane bending vibrations might be responsible for some of the observed effects of temperature on esr coupling constants[1,2] of certain aromatic radical ions; (2) the opportunity of studying directly the effect of an added π antibonding electron on the fundamental modes of an otherwise unchanged aromatic structure; and (3) the possibility of obtaining evidence useful for the clarification of the vibrational spectrum of aromatic molecules by an examination of their ions, naphthalene itself having a substantial history in the spectroscopic literature.[3-28] To our knowledge, Kachkurova[29,30] has reported the only work of this type on aromatic radicals.

Experimental Section

Standard techniques from the esr literature have been used to prepare the naphthalene anion by alkali metal reduction in highly purified solvents, tetrahydrofuran (THF), and dimethoxyethane (DME).[1] An initial 99.9% commercially pure sample of naphthalene was zone refined by 24 passes. All alkali metals used in the preparation were twice distilled *in vacuo*. All solvents were vacuum distilled, refluxed over an Na–K mixture with an aromatic hydrocarbon, which established solvent purity by forming an anion as signified by known color changes. The solvent was distilled into a storage container equipped with a helium leak-tested stopcock, and used as required. Each withdrawn solvent sample was initially used to form the naphthalene anion and then redistilled into a final reaction tube for preparation of the spectral samples. No solvent so stored for 8 months has failed to give the hydrocarbon-to-anion reaction.

Five-mm round Pyrex tubing or 8-mm square tubing was attached directly to the U-shaped preparation tube and served as the Raman cell. These tubes contained a fine porosity (4–5.5-μ pore diameter) or medium porosity (10–15-μ pore diameter) fritted filter which largely removed suspended and unreacted metal particles, thereby reducing light scattering from this source. THF was used as the solvent for all Raman work and presented no spectral interference since only one THF bond is observed 914.8 cm^{-1} from the Raman excitation frequency.

Infrared spectra were obtained from samples which had been transferred under vacuum to cells equipped with NaCl or KBr windows. Vacuum preparation and transfer are necessary since the naphthalene anion is very sensitive to both oxygen and water. A cell for use at room temperature consisted of a conventional liquid cell inside a conventional gas cell with appropriate interior and exterior connections for transference of sample from the reaction tube to the liquid cell under vacuum conditions. A cell for use at liquid nitrogen conditions was of a slightly modified Walsh–Willis type[31] and adapted for the transfer of samples under vacuum conditions. An anion sample was obtained on a single KBr window precooled by liquid nitrogen, warmed to about 150°K, which permitted removal of solvent by a mechanical vacuum pump, recooled with liquid nitrogen to 85°K, and the infrared spectrum was then obtained. Spectra of the better samples so prepared showed no evidence of solvent although traces of neutral naphthalene were present.

Infrared spectra were obtained on a standard Beckmann IR-10 spectrometer equipped with a 10-in. strip chart recorder. Calibration of the system incorporated molecules and data provided by IUPAC tables.[32] The Raman spectrometer consisted of a Spectra-Physics, Model 125, helium–neon laser; Spex Industries Model 1400 Czerny-Turner double monochromator; RCA C3100E photomultiplier tube; Princeton Applied Research Corporation HR-8 lock-in amplifier; and the necessary associated electronics and recorder. This instrument was calibrated by the 6328-Å He–Ne laser line and the Raman spectra of CCl_4, $CHCl_3$, and benzene utilizing data given by Herzberg.[33] Precision of the infrared data is ± 2 cm^{-1} at 1000 cm^{-1}; the Raman data, ± 4 cm^{-1}.

An intensity problem arises in the Raman spectrum of naphthalene anion since the 6328-Å He–Ne laser line lies in the wing of an electronic transition, *i.e.*, the resonance Raman effect is present. The signal to noise ratio is about optimal at an anion concentration of $\approx 8 \times 10^{-3} M$ rather than 0.5 M which was used initially. A better approach, however, may be to incorporate a rotating Raman cell as discussed by Bernstein and Kiefer.[34]

Table I contains a summary of all the data obtained together with a tentative assignment. Thirteen infrared bands and six Raman bands were observed. Comparisons are made, where applicable, with the data of Kachkurova and with data from the literature for the parent molecule. All naphthalene data in columns II and III were obtained in this work under the same environmental conditions ensuring the validity of the comparison between anion and neutral species. Raman data in column I were taken from the work of Stenman;[12] similar infrared data, from Mitra and Bernstein.[3] The naphthalene assignment follows that of Scully and Whiffen.[8]

Results and Discussion

Normal modes for naphthalene have been computed from rather different force fields by Schmid,[10] Luther and Drewitz,[6] and Freeman and Ross.[16] Comparison of these demonstrates such equivalence that the last authors conclude compellingly that the forms of the normal modes are qualitatively secure. Since the frequency shifts from neutral to anionic naphthalene are small, it is assumed that normal modes of both species are approximately equivalent.

This assumption combined with Table I allows the following observations on the frequency shifts, $\Delta\nu$, from neutral to anionic naphthalene.

(1) $\Delta\nu$ for the observed Raman active modes, 0–7 cm^{-1}, is smaller than those for infrared active modes, 10–75 cm^{-1}. (This statement may be artificial in that the six observed Raman modes are similar in type to the ir modes with small $\Delta\nu$, and since the Raman spectrum was obtained in a solvent at 295°K while the ir spectrum was obtained at 77°K in no solvent.)

(2) $\Delta\nu$ increases for normal modes in a manner described by their *predominant* component as follows: hydrogen stretching, 4 cm^{-1}; skeletal carbon motions, 10–30 cm^{-1}; bending hydrogen motions, 40–60 cm^{-1}; combined hydrogen and carbon motions, 70–80 cm^{-1}. It is clear that the normal modes consist of composite contributions in terms of the standard usage of stretches and bends, *i.e.*, the comment in (2) above is idealized. However, stretching and bending motions do predominate in many modes and thereby provide consistency for the statement.

The criteria for the recommended assignment are (a) fit with the parent molecule's assignment (Scully and Whif-

TABLE I: Comparative Vibrational Data for Naphthalene and Its Anion

Symmetry species[a]	Assignment[b]	(I) $C_{10}H_8$, literature values,[c] cm^{-1}	(II) $C_{10}H_8$, this work,[d] cm^{-1}	(III) $C_{10}H_8^-$ this work,[d] cm^{-1}	(IV) $C_{10}H_8^-$, Kachkurova,[e] cm^{-1}	$\Delta\nu$, II − III, cm^{-1}
A_g	ν_1	3056	3062			
	ν_2	3021				
	ν_3	1576	1585			
	ν_4	1464	1470	1471		1
	ν_5	1383	1384			
	ν_6	1147				
	ν_7	1021	1028	1026		2
	ν_8	764	764			
	ν_9	513	516			
B_{1u}	ν_{17}	3060		(3052)	3050	8[h]
	ν_{18}	3027		(3024)	3023	3[h]
	ν_{19}	1592	1595			59
	ν_{20}	1387	1379	1320 vw		
	ν_{21}	1267	1249	1195 m	1190	54
	ν_{22}	1128	1140	1093 vw		47
	ν_{23}	877	877	840 vw	840	37
	ν_{24}	359				
B_{2u}	ν_{29}	3076				
	ν_{30}	2987				
	ν_{31}	1506	1510	1485 m	1485	25
	ν_{32}	(1361)[f]	1369	1291 mw		78
	ν_{33}	1210	1220	1174 vw		46
	ν_{34}	(1144)[e]				
	ν_{35}	1011		1001 m	1003	10
	ν_{36}	618			595	(24)
B_{3g}	ν_{37}	3051	2967[g]	2062		5
	ν_{38}	3006	2878	2876		2
	ν_{39}	1628				
	ν_{40}	1443	1445	1446		0
	ν_{41}	1244	1242	1235		7
	ν_{42}	1168				
	ν_{43}	951				
	ν_{44}	509				
B_{3u}	ν_{45}	958	968	928 mw		40
	ν_{46}	782	789	715 m	727	74
	ν_{47}	476	481	461 vw	466	20
	ν_{48}	176				

[a] Species designations follow the recommendations of Mulliken on coordinate axis definition[35]. [b] No bands in species B_{1g} or B_{2g} were observed and consequently omitted from the table. Species A_u modes are inactive in both Raman and infrared spectroscopy. The assignments follows those of Scully and Whiffen[8] and essentially those of Loise[15] who disagrees with the former in ν_{12}, ν_{14}, ν_{16}, ν_{27}, ν_{28}, and ν_{38}. Only ν_{38} was observed in this work. [c] Raman data from ref 12; infrared, ref 3. [d] All data for B_{1u}, B_{2u}, and B_{3u} were obtained at liquid nitrogen temperature; for A_g and B_{3g}, at room temperature. [e] References 29 and 30. Kachkurova assigned bands 1190 and 840 cm^{-1} as ν_{33} and ν_{35}, respectively, rather than as ν_{21} and ν_{23}. See discussion for explanation. [f] Reference 8. [g] These large melt to THF solution shifts were consistently obtained from all samples regardless of origin of naphthalene or solvent. [h] These values are obtained as the difference between columns I and III.

fen); (b) relative changes in dipole moments and therefore infrared band intensities; (c) relative changes in primary force constants (diagonal elements of the F matrix); (d) the reduction of all force constants relative to the neutral parent when an electron is added to an antibonding molecular orbital, and the subsequent decrease in frequency for all modes of the anion; (e) the established electron densities by esr at the α and β carbons as 0.180 and 0.069, respectively, thereby providing a measure of overall force constant relaxation, and insight on relative dipole moment changes; (f) and a somewhat crude force constant rule analogous with the Teller-Redlich isotopic rule. Recognizing that the product of all roots, $\lambda_i = 4\pi\nu$, of the secular equation are equal to the product of the determinants of the Wilson G and F matrices

$$\prod_i \lambda = |G||F|$$

one obtains the Teller-Redlich product rule by accepting $|F|$ as equivalent for both isotopic species, *i.e.*

$$\prod_i \frac{\lambda_i}{\lambda_i'} = \frac{|G|}{|G'|}$$

where the presence and absence of primes distinguish the two isotopic species.

Analogously

$$\prod_i \frac{\lambda_i}{\lambda_i'} \approx \frac{|F|}{|F'|}$$

for cases where masses of the two chemical species are the same, symmetry is preserved, and bond lengths and angles vary slightly. This is the case for neutral and charged species of the type considered here since the addition of an electron is a trivial change in mass, symmetry is preserved, and although bond lengths and angles change somewhat, their ratios in $|G|/|G'|$ do not markedly deviate from unity. (Mass, symmetry, and geometry are also approximately preserved by some excited electronic states relative to the ground state of selected molecules.)

These concepts are given meaning by an initial examination of the B_{3u} fundamentals since their assignments for the neutral molecule are generally agreed to be most satisfactory.

Table II provides a resume of the relevant information. The relative intensities decrease in the order $\nu_{46} > \nu_{45} > \nu_{47}$ indicating a corresponding trend for the changes in dipole moment. Examination of the normal modes suggests this is reasonable. Mode ν_{47} consists of essentially nonplanar carbon motions which involve small excursions relative to hydrogen, and since α and β carbons move in opposite directions the overall change in the center of negative charge and therefore the dipole moment, will be slight. (Recall the charge distribution of the unpaired electron at the α and β positions is 0.180 and 0.069, respectively.) Whereas ν_{46} consists of all positive centers (hydrogen) moving oppositely to all negative centers (carbons) resulting in a much larger change in the dipole moment. ν_{45} is an intermediate case. Also, ν_{46} with a $\Delta\nu$ of 74 cm^{-1} is a composite of the *types* of motion for ν_{45} and ν_{47}, *i.e.*, 40 + 20 cm^{-1} shifts.

These arguments applied to B_{1u} and B_{2u} modes determine the asignments of ν_{21} as 1195 cm^{-1} and ν_{33} as 1174 cm^{-1} rather than the reverse which would contradict the observed intensity relationship for ν_{21} and ν_{33} and require two modes of similar type to have $\Delta\nu_{21}/\Delta\nu_{33}$ equal to 3:1 rather than the observed 1:1. The remaining infrared assignments are similarly derived including those not observed, *i.e.*, comparative changes in dipole moments indicate that those of unobserved bands are smaller than those of observed bands.

Unfortunately, similar intensity comparisons between neutral and anionic species could not be made due to large differences in concentrations which were known only approximately.

No Raman bands below 1000 cm^{-1} were observed. This eliminates from consideration all B_{1g} and B_{2g} modes

TABLE II: Summary of Data For the B_{3u} Normal Modes

Assignment	$C_{10}H_8$ frequency, cm^{-1}	$C_{10}H_8^-$ frequency, cm^{-1}	$\Delta\nu$	Rel intensity	Normal mode[a]	Remark
ν_{45}	968	928	40	mw	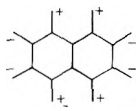	Predominantly hydrogen bending
ν_{46}	789	715	74	m	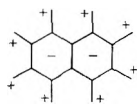	Carbon and hydrogen bending
ν_{47}	481	461	20	vw	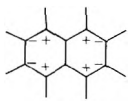	Predominantly carbon bending

[a] A + refers to motion above the plane of the drawing; −, below. ν_{48} at 176 cm^{-1} is outside the range of our instrumentation.

which contain only nonplanar bends of such type as to suggest small changes in polarizability. (Indeed this correlates with the Raman spectrum of the parent molecule as given by Mitra and Bernstein[3] on naphthalene melt at 90°.) The absence of bands below 1000 cm^{-1} also eliminates from consideration the two lowest modes in both A_g and B_{3g} species. Of the remaining 13 bands, the tentative assignment depends primarily on nearness of fit with the parent molecule. A number of alternative assignments to that suggested here were considered, but all of them required Raman shifts markedly larger than those in the infrared.

Application of intensity arguments to the Raman bands is difficult. In general, the polarizability of the anion should be larger than the neutral compound. This is supported experimentally since a Raman spectrum was obtained from a solution of about 8×10^{-3} M in anion. Beyond this, little can be said even though marked differences in intensities between neutral and anionic species were observed, *e.g.*, ν_5 is much reduced in the anion while ν_7 increases considerably. The presence of a resonance Raman effect is known to complicate intensities relative to their normal Raman values, and the nature of these changes in specific cases is unclear.[36] When such difficulties are absent, it may be possible to take advantage of the variations in polarizability suggested by the different symmetries and charge distributions between the highest occupied molecular orbitals of neutral and charged species. A survey spectrum of the benzophenone anion in the Raman suggests that such intensity considerations can be utilized but with difficulty nevertheless.

Conclusions

Only three nonplanar vibrations were observed. The shifts in frequency for ν_{45} and ν_{46} are not sufficiently large to explain temperature variations of esr coupling constants. It does not appear likely that those which were not observed would have much larger shifts.

Although obviously limited in scope, these results suggest that ions of the same symmetry as the parent molecule may be useful in clarifying vibrational assignments of the parent molecule. Both frequency shifts and intensity variations occur upon moving from the neutral molecule to the ion. Finally the advantages provided by isotopic substitutions may be applied equally well to the ionic molecule. This provides normal and isotopically substituted neutral and radical species, all of which are interrelated by symmetry, basic geometry, and known mass relationships.

Acknowledgment. We express our appreciation for the financial support of this project to the University of Alabama in Huntsville Research Committee.

References and Notes

(1) C. L. Dodson and A. H. Reddoch, *J. Chem. Phys.*, **48**, 3226 (1968).
(2) A. H. Reddoch, C. L. Dodson, and D. H. Paskovich, *J. Chem. Phys.*, **52**, 2318 (1970).
(3) S. S. Mitra and H. J. Bernstein, *Can. J. Chem.*, **37**, 553 (1959).
(4) A. L. McClellan and G. C. Pimentel, *J. Chem. Phys.*, **23**, 245 (1955).
(5) E. R. Lippincott and E. J. O'Reilly, *J. Chem. Phys.*, **23**, 238 (1955).
(6) H. Luther and H. J. Drewitz, *Z. Elektrochem.*, **66**, 546 (1962).
(7) G. V. Peregudov, *Opt. Spectrosc. (USSR)*, **11**, 397 (1961).
(8) D. B. Scully and D. H. Whiffen, *Spectrochim. Acta*, **16**, 1409 (1960).
(9) D. B. Scully and D. H. Whiffen, *J. Mol. Spectrosc.*, **1**, 257 (1958).
(10) E. Schmid, *Z. Electrochem.*, **62**, 1005 (1958).
(11) D. M. Hanson and A. E. Gee, *J. Chem. Phys.*, **51**, 5052 (1969).
(12) F. Stenman, *J. Chem. Phys.*, **54**, 4217 (1971).
(13) M. Ito and T. Shigeoka, *Spectrochim. Acta*, **22**, 1029 (1966).
(14) M. Suzuki, T. Yokoyama, and M. Ito, *Spectrochim. Acta*, **24**, 1091 (1968).
(15) J. Loisel, *C. R. Acad. Sci., Ser. B*, **266**, 330 (1968).
(16) D. E. Freeman and I. G. Ross, *Spectrochim. Acta.*, **16**, 1393 (1960).
(17) G. W. Chantry, A. Anderson, and H. A. Gebbie, *Spectrochim. Acta*, **20**, 1465 (1964).
(18) I. Harada and T. Shimanouchi, *J. Chem. Phys.*, **44**, 2016 (1966).
(19) S. C. Wait, Jr., and F. E. Schaffer, *J. Mol. Spectrosc.*, **10**, 78 (1963).
(20) H. Yamada and K. Suzuki, *Spectrochim. Acta., Sect. A*, **23**, 1735 (1967).
(21) B. Wyncke, A. Hadni, D. Chanal, and E. Decamyss., *Ann. Phys.*, **2**, 123 (1967).
(22) W. B. Person, G. C. Pimentel, and O. Schnepp, *J. Chem. Phys.*, **23**, 230 (1955); G. C. Pimentel, A. L. McClellan, W. B. Person, and O. Schnepp, *ibid.*, **23**, 234 (1955).
(23) J. R. Scherer, *J. Chem. Phys.*, **36**, 3308 (1962).
(24) J. M. Hollas, *J. Mol. Spectrosc.*, **9**, 138 (1962).
(25) E. P. Krainov, *Opt. Spectrosc. (USSR)*, **15**, 415 (1963).
(26) R. Mecke, W. Bruhn, and A. Chafik, *Z. Electrochem.*, **67**, 85 (1963).
(27) B. Schrader, *Z. Phys.*, **197**, 295 (1963).
(28) D. H. Eargle, Jr., and E. W. Cox, *Chem. Soc., Special Publ.*, **No. 22**, 116 (1967).
(29) I. Y. Kachkurova, *Dokl. Akad. Nauk SSSR*, **163**, 1198 (1965).
(30) I. Y. Kachkurova, *Teor. Eksp. Khim.*, **3**, 498 (1967).
(31) A. Walsh and J. B. Willis, *J. Chem. Phys.*, **18**, 552 (1950).
(32) "Table of Wavenumbers for the Calibration of Infrared Spectrometers," International Union of Pure and Applied Chemistry, Butterworths, New York, N. Y., 1961.
(33) G. Herzberg, "Infrared and Raman Spectra of Polyatomic Molecules," Van Nostrand, New York, N. Y., 1945.
(34) W. Kiefer and J. H. Bernstein, 26th Symposium on Molecular Structure and Spectroscopy, The Ohio State University, June 1971. H. J. Bernstein, private communication.
(35) R. S. Mulliken, *J. Chem. Phys.*, **23**, 1997 (1955).
(36) J. Behringer, "Raman Spectroscopy," Vol. I, H. A. Szymanski, Ed., Plenum Press, New York, N. Y., 1967.

Sedimentation Equilibrium Studies on Indefinitely Self-Associating Systems. *N*-Methylacetamide in Carbon Tetrachloride

G. J. Howlett, L. W. Nichol,* and P. R. Andrews

Department of Physical Biochemistry, John Curtin School of Medical Research, Australian National University, Canberra, A.C.T., 2601, Australia *(Received December 4, 1972; Revised Manuscript Received June 4, 1973)*

Theory is developed to permit simulation by numerical integration of sedimentation equilibrium distributions pertaining to systems undergoing indefinite self-association. The treatment includes consideration of volume changes on reaction, nonideality effects, and density variations with radial distance arising as a result of solute redistribution and compressibility effects. The development, initially in terms of an isodesmic association, is extended to cases where two equilibrium constants apply. For both models, expressions for the second derivative of the concentration distribution are obtained and discussed in relation to the evaluation of nonideality coefficients corresponding to the conventional second and third virial coefficients, and to the appearance of maxima in schlieren records. The theory is applied to the analysis of sedimentation equilibrium results obtained with *N*-methylacetamide in carbon tetrachloride. It is shown that the distributions may be described in terms of an isodesmic indefinite association characterized by an equilibrium constant of $2 \times 10^3\ M^{-1}$, in agreement with previous findings. However, it is also shown that this solution is not unique and, indeed, the same experimental results are fitted with a distribution computed on the basis of a model in which dimer formation is governed by an equilibrium constant of $1\ M^{-1}$ and addition of monomer to higher polymers by an association constant of $50\ M^{-1}$. These values are in substantial agreement with those used to interpret previous infrared and nuclear magnetic resonance results obtained with the same system. Accordingly, the work resolves the apparent controversy between previous interpretations given to spectrophotometric and sedimentation equilibrium results.

Introduction

Sedimentation equilibrium results obtained with several systems[1-5] have been analyzed successfully in terms of an indefinite self-association, for which a single equilibrium constant suffices to describe the formation of a series of polymers. The treatments have included the dependence of the activity coefficients of the solute species on total concentration, but have not accounted for possible volume changes on reaction or effects due to density variation with radial distance. One purpose of the present work is to present equations which account for these effects and which permit computer simulation of equilibrium distributions pertaining to indefinitely self-associating systems. Such simulations have proved useful in analyzing results obtained with systems undergoing discrete self-associations[6] and heterogeneous associations.[7,8] In addition, an expression is obtained defining the appearance of a maximum in the schlieren record of a sedimentation equilibrium experiment conducted with an indefinitely self-associating system. In previous work,[9] with the single solute hyaluronic acid, the position of a maximum of this type proved useful in estimating the nonideality coefficient corresponding to the conventional third virial coefficient.

Although the relations to be presented are applicable to any indefinite self-association, they are used herein to reexamine the association of *N*-methylacetamide in carbon tetrachloride under conditions where the schlieren plot of the equilibrium distribution exhibits a maximum.[10] The self-association is thought to occur by linear hydrogen bonding, the system serving as a useful model in the investigation of the contribution of peptide hydrogen bonds to protein and polypeptide stability.[11-13] Previous sedimentation equilibrium results[10] have been interpreted in terms of an indefinite self-association described by a single equilibrium constant (an isodesmic association[4]) of approximately $2 \times 10^3\ M^{-1}$, in marked contrast to lower values found from infrared[14] and nuclear magnetic resonance[15] studies. In the latter work, a model was preferred in which dimer formation was characterized by an equilibrium constant of $\sim$1–1.5 M^{-1} and higher polymer formation by a constant of $\sim$24–38 M^{-1}. In an attempt to correlate these findings, the present experimental results are analyzed in terms of both models, with allowance for nonideality, density variation, and possible volume changes in the isodesmic case.

Theory

Isodesmic Indefinite Self-Association. Consider first the system, $A_{i-1} + A \rightleftharpoons A_i$ ($i = 1, 2, \ldots$), each equilibrium being governed by the equilibrium constant

$$K_i = \frac{\gamma_{A_i}}{\gamma_{A_{i-1}}\gamma_A}\frac{m_{A_i}}{m_{A_{i-1}}m_A} \qquad (1)$$

where m denotes the molar concentration and γ the activity coefficient on the same scale. The activity coefficient of each species A_i may be expressed as a virial expansion of the form[9,16]

$$\ln \gamma_{A_i} = M_{A_i}(B\bar{c} + C\bar{c}^2 + \cdots) \qquad (2)$$

where $\bar{c}$ is the total weight concentration (g l.$^{-1}$), M_{A_i} is the molecular weight ($= iM_A$) of species A_i and the nonideality coefficients, B, C, etc., are assumed identical for each species. It follows that $\gamma_{A_i}/\gamma_{A_{i-1}}\gamma_A = 1$ and from eq 1 that $m_A = K_i m_{A_{i-1}} m_A$. If all K_i are set equal, $K_i = K$ (an isodesmic indefinite self-association) the latter relation becomes $m_{A_i} = K^{i-1}m_A{}^i$. This equation has been derived on the basis of a model involving successive addi-

tions of monomer to polymeric species, but is valid regardless of the pathway of formation of A_i provided any polymer-polymer interaction is also described by K. The following useful relations may now be derived[2] on the basis of sums of geometrical progressions since the common ratio $Km_A < 1$.

$$\sum_{i=1}^{x} m_{A_i} = \sum_{i=1}^{\infty} c_{A_i}/M_{A_i} = m_A/(1-Km_A) \quad (3a)$$

$$\bar{c} = \sum_{i=1}^{x} c_{A_i} = M_A m_A/(1-Km_A)^2 \quad (3b)$$

$$\sum_{i=1}^{\infty} M_{A_i} c_{A_i} = M_A{}^2 m_A(1+Km_A)/(1-Km_A)^3 \quad (3c)$$

$$\sum_{i=1}^{\infty} c_{A_i}/\sum_{i=1}^{\infty} M_{A_i} c_{A_i} = (1-Km_A)/M_A(1+Km_A) \quad (3d)$$

At equilibrium in a sedimentation equilibrium experiment conducted at constant angular velocity ω and temperature T each species, A_i, distributes with radial distance r according to[17]

$$\mathrm{d} \ln a_{A_i}(r)/\mathrm{d}(r^2) = \phi_{A_i}(r) M_{A_i} \quad (4a)$$

$$\phi_{A_i}(r) = (1-\bar{v}_{A_i}(r)\rho(r))\omega^2/2RT \quad (4b)$$

where $a_{A_i}(r)$ and $\bar{v}_{A_i}(r)$ are the activity and partial specific volume of A_i, respectively, and $\rho(r)$ is the solution density at r. Equation 4 may be rewritten as

$$\frac{\mathrm{d} \ln c_{A_i}(r)}{\mathrm{d}(r^2)} = \frac{\mathrm{d} \ln m_{A_i}(r)}{\mathrm{d}(r^2)} = \phi_{A_i}(r) M_{A_i} - \frac{\mathrm{d} \ln \gamma_{A_i}(r)}{\mathrm{d}(r^2)} \quad (5a)$$

where from eq 2

$$\frac{\mathrm{d} \ln \gamma_{A_i}(r)}{\mathrm{d}(r^2)} = M_{A_i}\left(B \frac{\mathrm{d}\bar{c}(r)}{\mathrm{d}(r^2)} + 2C\bar{c}(r) \frac{\mathrm{d}\bar{c}(r)}{\mathrm{d}(r^2)} + \cdots\right) \quad (5b)$$

Combination of eq 5a and 5b yields on summation over all i

$$\frac{\mathrm{d}\bar{c}(r)}{\mathrm{d}(r^2)} = \frac{\sum^{i} \phi_A(r) M_{A_i} c_{A_i}(r) / \sum^{i} M_{A_i} c_{A_i}(r)}{\left(1/\sum^{i} M_{A_i} c_{A_i}(r)\right) + B + 2C\bar{c}(r) + \cdots} \quad (6)$$

In order to proceed it is necessary to examine the quantity $\phi_{A_i}(r)$ defined in eq 4b. An expression for $\rho(r)$ is available as follows[17]

$$\rho(r) = \rho_0(r) + \left\{\sum^{i} (1-\bar{v}_{A_i}(r)\rho_0(r)) c_{A_i}(r)/1000\right\} \quad (7a)$$

where $\rho_0(r)$ is the density of pure solvent in g ml^{-1} at r given by[18]

$$\rho_0(r) = \rho_0(r_m)/\{1-0.5\chi_1\omega^2\rho_0(r_m)(r^2-r_m^2)\} \quad (7b)$$

$\rho_0(r_m)$ is the solvent density at the meniscus r_m (1 atm) and χ_1 is the isothermal compressibility of solvent. Similarly, the variation of $\bar{v}_{A_i}$ for each species with radial distance may be written in terms of the isothermal compressibility of the species, χ_{A_i}

$$\bar{v}_{A_i}(r) = \bar{v}_{A_i}(r_m) + 0.5\chi_{A_i}\omega^2(r_m{}^2 - r^2) \quad (8)$$

Provided the reasonable assumptions are made that all χ_{A_i} are identical ($\chi_{A_i} = \chi_2$) and the molar volume changes, ΔV_i, associated with each successive equilibrium are also equal ($\Delta V_i = \Delta V$), it follows that ΔV is a constant independent of r given by

$$\Delta V = iM_A\bar{v}_{A_i}(r) - (i-1)M_A\bar{v}_{A_{i-1}}(r) - M_A\bar{v}_A(r) \quad (9a)$$

or

$$\bar{v}_{A_i}(r) = \bar{v}_A(r) + \{(i-1)\Delta V/iM_A\} \quad (9b)$$

To complete the basic equations, it need only be noted that if $\Delta V \neq 0$, $K(r)$ varies with r according to[19]

$$\mathrm{d}K(r)/\mathrm{d}(r^2) = -\Delta V\omega^2\rho(r)K(r)/2RT \quad (10)$$

Combination of eq 3, 4b, 6, and 9b yields

$$\mathrm{d}\bar{c}(r)/\mathrm{d}(r^2) = \psi = \alpha/\beta \quad (11a)$$

$$\alpha = \omega^2 - \omega^2\rho(r)\{\bar{v}_A(r) + [2\Delta VKm_A/M_A(1+Km_A)]\} \quad (11b)$$

$$\beta = \frac{2RT(1-Km_A)^3}{M_A{}^2 m_A(1+Km_A)} + 2RTB + \frac{4RTCM_A m_A}{(1-Km_A)^2} \quad (11c)$$

In writing eq 11c the expansion in eq 2 has been truncated after the second term. It is now possible to describe the method by which a sedimentation equilibrium distribution, ψ *vs.* r, may be computed with known values of ω, T, M_A, $\bar{v}_A(r_m)$, $\rho_0(r_m)$, χ_1, χ_2, $K(r_m)$, ΔV, B, C, and $m_A(r_m)$. Equation 3b is used directly to obtain $\bar{c}(r_m)$, while $\rho(r_m)$ is obtained from eq 12, a combination of eq 3a, 7a, and 9b.

$$\rho(r) = \rho_0(r) + \frac{\bar{c}(r)(1-\bar{v}_A(r)\rho_0(r))}{1000} - \frac{\rho_0(r)\Delta V\bar{c}(r)}{1000M_A} + \frac{\rho_0(r)\Delta V m_A}{1000(1-Km_A)} \quad (12)$$

Equation 11 now yields $\psi(r_m)$, which is used to calculate $\mathrm{d}m_A(r_m)/\mathrm{d}(r^2)$ from eq 13, a rearrangement of eq 5

$$\mathrm{d}m_A(r)/\mathrm{d}(r^2) = \phi_A(r)M_A m_A(r) - M_A m_A(r)\{B\psi(r) + 2C\bar{c}(r)\psi(r)\} \quad (13)$$

The value of $\phi_A(r)$ required follows by setting $i = 1$ in eq 14 obtained from eq 4b and 9b

$$\phi_{A_i}(r) = \omega^2\{1-\rho(r)[\bar{v}_A(r) + (\Delta V/M_A) - (\Delta V/iM_A)]\}/2RT \quad (14)$$

A value of $\mathrm{d}K(r_m)/\mathrm{d}(r^2)$ is also available from eq 10. The improved Euler method[20] may now be used to calculate K and m_A at a small increment Δr from r_m. Reiteration of the above procedure therefore yields $\mathrm{d}m_A(r_m + \Delta r)/\mathrm{d}(r^2)$ and $\mathrm{d}K(r_m + \Delta r)/\mathrm{d}(r^2)$ which provide the starting points for the application of the predictor-corrector method[20] to the determination of the variation of m_A (and hence $\bar{c}$) and of K (and hence all m_{A_i}) with radial distance. In attempting to simulate an actual experimental distribution two basic problems arise. First, even if values may be assigned to parameters characterizing the system, the value of $m_A(r_m)$ is not known. This problem may be overcome by refining chosen values of $m_A(r_m)$ in successive simulations until the area under the computed $\bar{c}(r)$ *vs.* r^2 curve conforms to the conservation of mass requirement. Secondly, while values of ω, T, M_A, $\bar{v}_A$ (1 atm), ρ_0 (1 atm), χ_1, and χ_2 are either known or available from separate experiments, attempts to fit an experimental result by the simulation procedure involve assignment of values to the parameters $K(r_m)$, ΔV, B, and C.

In this connection, differentiation of eq 11 with respect to r^2 is useful since it provides a relation which permits calculation of C for particular values of $K(r)$ and ΔV. The differentiation after extensive rearrangement leads to

$$C = \frac{(1-Km_A)^5(K^2m_A^2+4Km_A+1)}{2M_A^3m_A^2(1+Km_A)^3} + \frac{\omega^2\rho\Delta VK(1-Km_A)}{RT\psi M_A(1+Km_A)^3}\left\{\frac{\omega^2\rho\Delta Vm_A}{4RT\psi} - \frac{(1-Km_A)^2}{M_A}\right\} - \frac{\omega^2}{4RT\psi^2}\left\{\frac{d\bar{v}_A\rho}{d(r^2)} + (1-\bar{v}_A\rho)\frac{d\ln\psi}{d(r^2)}\right\} - \frac{\omega^2\Delta VKm_A}{2RT\psi^2M_A(1+Km_A)}\left\{\frac{d\rho}{d(r^2)} - \rho\frac{d\ln\psi}{d(r^2)}\right\} \quad (15)$$

where all quantities refer to radial position r. In general, corresponding values of $\bar{c}$ and $d\bar{c}/dr$ ($= 2r\psi$) are available from an experimental record whereupon $d\ln\psi/d(r^2)$ may readily be calculated. For a selected value of $K(r)$ eq 3b gives $m_A(r)$. With assigned ΔV, the solution of eq 15 for C requires only estimation of $\bar{v}_A$, ρ, and their differentials with respect to r^2 at the same value of r; eq 8 yields $\bar{v}_A(r)$, eq 7b gives $\rho_0(r)$, and eq 12 then permits calculation of $\rho(r)$. The required differentials are given by

$$d\bar{v}_A/d(r^2) = 0.5\chi_2\omega^2 \quad (16a)$$

$$d\rho/d(r^2) = \frac{(1-\bar{v}_A\rho_0)\psi}{1000} - \frac{\rho_0\Delta VKm_A\psi}{500M_A(1+Km_A)} + \frac{\rho_0\Delta V^2\omega^2Km_A^2\rho}{2000RT(1-K^2m_A^2)} + \frac{\chi_1\rho_0^2\omega^2}{2}\left\{1 - \frac{\bar{v}_A\bar{c}}{1000} - \frac{\Delta V\bar{c}}{1000M_A} + \frac{\Delta Vm_A}{1000(1-Km_A)}\right\} + \frac{\chi_2\omega^2\bar{c}\rho_0}{2000} \quad (16b)$$

Once a value of C has been obtained, eq 11a and 11b may be used to find the corresponding value of B whereupon the improved Euler method and the predictor–corrector method may be used to generate the entire distribution around the value of r selected. If this value of r is not r_m, the simulation procedure itself gives $K(r_m)$ corresponding to the selected $K(r)$. Indeed, if a maximum is observed in the schlieren plot, the experimenter may choose to utilize the point (r_{max}, ψ_{max}) which leads to the simplification in eq 15 that $d\ln\psi/d(r^2)$ equals zero. Moreover, further simplification of eq 15 is possible for particular systems. For example, Nichol, *et al.*,[9] considered the sedimentation equilibrium of a single noninteracting solute ($K = 0$, $\Delta V = 0$), where $\bar{v}_A$ and ρ were independent of radial distance. With these substitutions eq 15 becomes $C = 1/[2M_A^3\cdot(m_A)^2_{max}]$, in agreement with eq 6a of the previous workers.[9] In studies with polymerizing protein systems in aqueous solutions the following frequently employed approximations may prove reasonable: $\Delta V = 0$, $\chi_1 = 0$ (ρ_0 = constant), $\chi_2 = 0$ ($\bar{v}_A$ = constant). In these cases, C may be evaluated from eq 17 employing the maximum, which may be observed at high total protein concentrations.

$$C = \frac{(1-Km_A)^5(K^2m_A^2+4Km_A+1)}{2M_A^3m_A^2(1+Km_A)^3} - \frac{\omega^2\bar{v}_A(1-\bar{v}_A\rho_0)}{4000RT\psi_{max}} \quad (17)$$

where the second term accounts for the variation of density with radial distance given by eq 16b.

A Model Involving Two Equilibrium Constants. In view of the conflicting results obtained with *N*-methylacetamide it is necessary to formulate equations applicable when the dimerization equilibrium constant K_1 differs from that describing the addition of monomer to higher polymers, K_2. The expressions analogous to eq 3b and 3c are

$$\bar{c} = \frac{M_Am_A\{1+2m_A(K_1-K_2)+K_2m_A^2(K_2-K_1)\}}{(1-K_2m_A)^2} \quad (18a)$$

$$\sum_i M_{A_i}c_{A_i} = \frac{M_A^2m_A\{1+m_A(4K_1-3K_2)+3K_2m_A^2(K_2-K_1)+K_2^2m_A^3(K_1-K_2)\}}{(1-K_2m_A)^3} \quad (18b)$$

The basic eq 4–10 continue to apply, but for simplicity in what follows second-order effects contributing to the distribution will be neglected by assuming $\Delta V = 0$, ρ_0 = constant, and $\bar{v}_A$ = constant. In these terms eq 11 becomes

$$\psi = \frac{d\bar{c}(r)}{d(r^2)} = \frac{\omega^2\{1-\bar{v}_A\rho_0-[\bar{v}_A(1-\bar{v}_A\rho_0)\bar{c}(r)/1000]\}}{2RT\{(1/\Sigma M_{A_i}c_{A_i}(r)) + B + 2C\bar{c}(r)\}} \quad (19)$$

As before eq 18 and 19 could be used to simulate a distribution for comparison with an experimental result and it thus remains to comment on the evaluation of C for given values of K_1 and K_2 from an observed maximum. For such a maximum, $d\psi/d(r^2) = 0$ and thus from eq 19

$$C = \frac{-\omega^2\bar{v}_A(1-\bar{v}_A\rho_0)}{4000RT\psi_{max}} - \frac{d(1/\Sigma M_{A_i}c_{A_i}(r))}{d(r^2)}\frac{1}{2\psi_{max}} \quad (20a)$$

where from eq 18a and 18b

$$\frac{d(1/\Sigma M_{A_i}c_{A_i}(r))}{d(r^2)} = \frac{M_A\psi_{max}F(m_A)}{(\Sigma M_{A_i}c_{A_i})^2} \quad (20b)$$

$$F(m_A) = \{1+4m_A(2K_1-K_2)+K_2m_A^2(6K_2-5K_1)+4K_2^2m_A^3(K_1-K_2)+K_2^3m_A^4(K_2-K_1)\}/\{1+4m_A(K_1-K_2)+K_2m_A^2(6K_2-7K_1)+4K_2^2m_A^3(K_1-K_2)+K_2^3m_A^4(K_2-K_1)\} \quad (20c)$$

Use of eq 20 to evaluate C requires only evaluation of ψ and $\bar{c}$ at the maximum; m_A may be found from $\bar{c}$ using eq 18a by the Newton–Raphson method. It could be noted that when $K_1 = K_2$, eq 20 simplifies to eq 17.

Experimental Section

N-Methylacetamide (Fluka) was distilled before use, while carbon tetrachloride (Mallinckrodt) was used as obtained. Sedimentation equilibrium experiments were conducted at 25 ± 0.1° using a Spinco Model E ultracentrifuge (fitted with an electronic speed control) and a cell comprising a 12-mm double sector filled-epon centerpiece and sapphire windows. Experimental records were obtained using a schlieren optical system and measured with a two-coordinate comparator (Gaertner Scientific Corp.).

At low speeds the baselines of the solution and solvent were coincident, both being elevated as the speed increased until at the time the operating speed was reached that of the solvent was above that of the solution; similar effects were observed by Albers, *et al.*[10] The observed elevations were used to calculate the compressibilities[21] of the solutions employed and hence the isothermal compressibility of *N*-methylacetamide ($\chi_2 = 5.3 \times 10^{-11}$ cm^2 dyn^{-1}). The calculation involved the use of the following parameters obtained from standard tables: χ_1 for carbon tetrachloride 10.67×10^{-11} cm^2 dyn^{-1} and refractive indices of 1.4631 and 1.4301 for carbon tetrachloride and *N*-methylacetamide, respectively. After the initial photographs had been obtained, the operating speed was maintained for 30 hr, a time sufficient to attain equilibrium as was confirmed by the identity of the patterns ob-

tained after 24 and 30 hr. The procedure described by Albers, *et al.*,[10] was used to correct the equilibrium distributions for the effects of compressibility. The first step involved the calculation of the apparent concentration distribution (in refractometric units) of *N*-methylacetamide employing the observed baseline of carbon tetrachloride, this calculation followed the procedure described by Schachman.[22] Secondly, at each radial position, the apparent solute concentration was employed, together with the dependence on *N*-methylacetamide concentration of the difference in baseline elevations obtained in separate experiments at zero time to obtain a first estimate of the baseline corrected for compressibility and therefore appropriate to the solution channel. This led to a revised estimate of the solute concentration distribution, permitting reiteration of the procedure until the values used for the baseline at each radial position converged.

The initial concentrations of *N*-methylacetamide solutions were obtained in the required refractometric units from separate experiments conducted with a capillary-type synthetic boundary cell. In these experiments the rotor was initially accelerated to 10,000 rpm to equalize the menisci, whereupon the speed was reduced to 3000 rpm to minimize compressibility effects. As noted previously,[10] the areas under the schlieren peaks so obtained were, within experimental error, directly proportional to the known weight concentrations of the solutions. The other parameters required in the calculations to be presented were the density of carbon tetrachloride, taken as 1.583 $cm^3\ g^{-1}$ and the partial specific volume of the *N*-methylacetamide monomer, $\bar{v}_A$. For an isodesmic indefinite self-association, the weight-average partial specific volume may be related to $\bar{v}_A$ by use of eq 3a, 3b, and 9b

$$\sum^{i} \bar{v}_{A_i} c_{A_i} / \sum^{i} c_{A_i} = \bar{v}_A + (\Delta V K m_A / M_A) \qquad (21)$$

The concentration independence of the weight-average quantity previously observed[10] may, therefore, be taken as an indication that $\Delta V \sim 0$ and that the reported value of 1.042 $cm^3\ g^{-1}$ equals $\bar{v}_A$. On the other hand, Km_A remains essentially unchanged approximating unity over the concentration range studied,[10] and thus the possibility cannot be excluded that ΔV is nonzero; in this case, eq 21 permits estimation of $\bar{v}_A$ for any assigned value of ΔV.

Results

Figures 1 and 2 summarize the results of sedimentation equilibrium experiments conducted with solutions of *N*-methylacetamide of concentrations 103 g $l.^{-1}$ and 158 g $l.^{-1}$, respectively (other experimental detail being reported in the captions). The solid points represent the experimental results corrected for the effects of compressibility. The solid lines in each figure were computed assuming a model involving isodesmic indefinite self association and a zero volume change. These simulations commenced by using eq 15 and 16 to calculate C from the observed maxima and an assigned value of K. The corresponding value of the nonideality coefficient B was then computed using eq 11, which permitted calculation of an entire distribution by the predictor-corrector method as described in the theory section. A range of values of K was searched by this procedure, a value of $2 \times 10^3\ M^{-1}$ being found to best fit both sets of data. The solid lines in Figure 1 and 2 were computed using this value of K and values of B and C reported in Table I. The value of K reported is in excellent agreement with that ($1.96 \times 10^3\ M^{-1}$) found by Albers, *et al.*,[10] who assumed the same model but neglected variations of density with radial distance in treating their

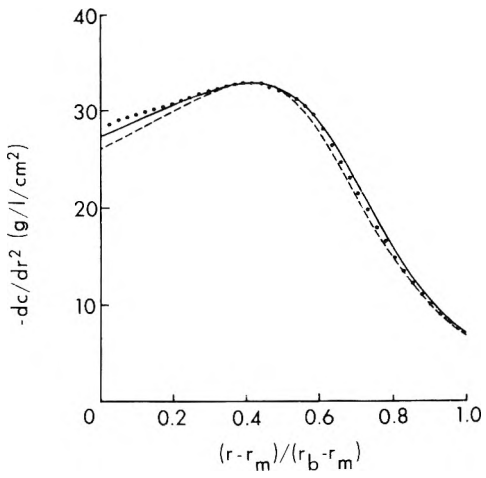

Figure 1. Sedimentation equilibrium results obtained from a schlieren record of an experiment conducted at an angular velocity of 30,000 rpm with a solution of *N*-methylacetamide in carbon tetrachloride of initial concentration 103 g $l.^{-1}$. At equilibrium the concentrations at the meniscus (r_m = 6.64 cm) and base (r_b = 7.20 cm) were 208 and 19.6 g $l.^{-1}$, respectively. Experimental points are designated ●. The solid line was calculated on the basis of an isodesmic indefinite self-association ($K = 2 \times 10^3\ M^{-1}$) and was virtually identical with that calculated for a model described by the equilibrium constants, $K_1 = 1\ M^{-1}$ and $K_2 = 50\ M^{-1}$. The broken line refers to a model for which $K_1 = 1\ M^{-1}$ and $K_2 = 38\ M^{-1}$.

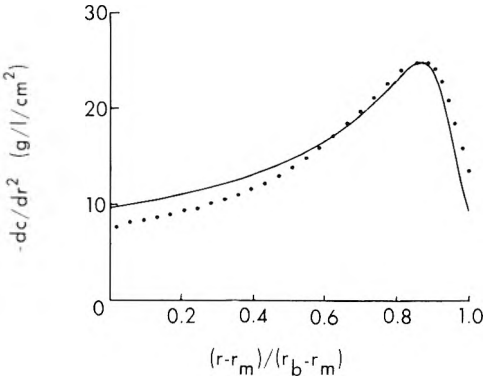

Figure 2. A sedimentation equilibrium distribution obtained with a solution of *N*-methylacetamide in carbon tetrachloride of initial concentration 158 g $l.^{-1}$. A column length of 1.2 cm was used and an angular velocity of 44,000 rpm. At equilibrium the meniscus concentration was 251 g $l.^{-1}$ and that at the base 10 g $l.^{-1}$. Experimental points, ●, are compared with the solid line computed for an isodesmic association ($K = 2 \times 10^3\ M^{-1}$) and for a model described by the equilibrium constants, $K_1 = 1\ M^{-1}$ and $K_2 = 50\ M^{-1}$.

TABLE I: Values of Nonideality Coefficients Derived from Analyses of Sedimentation Equilibrium Results[a] Obtained with *N*-Methylacetamide in Carbon Tetrachloride at 25°

Equilibrium constants, M^{-1}	B, mol $l.\ g^{-2} \times 10^5$		C, mol $l.^2\ g^{-3} \times 10^8$	
	1	2	1	2
$K = 2 \times 10^3$	0.1	0.4	0.5	3.0
$K_1 = 1$, $K_2 = 50$	0.2	0.4	0.4	3.1

[a] The columns headed 1 and 2 refer respectively to the results shown in Figures 1 and 2.

results by a differential procedure.[2] Estimation of values of nonideality coefficients is subject to greater uncertainty and thus the values of B reported in Table I are considered to compare favorably with the average value of 0.3×10^{-5} M g^{-2} found by the previous workers.[10,23] Similarly, the value of C found from Figure 1 is in approximate agreement with the average value[25] 0.97×10^{-8} mol l.[2] g^{-3}, while that found from Figure 2 is somewhat higher. This could arise from the neglect of higher order virial coefficients, which may also explain the relatively poor fit in Figure 2 of the solid line to the experimental points near the meniscus, where the concentration of N-methylacetamide is highest. Accordingly, it would appear that there is substantial agreement between the present and previous analyses of results based on the model involving isodesmic association, a mechanism which at first sight seems to describe quite satisfactorily the interactions occurring in solution.

The problem remains however that other results[14,15] involving spectrophotometric determination of the weight fraction of monomer as a function of total concentration have indicated that the indefinite self-association may not be isodesmic. The alternative model proposed involves two equilibrium constants and the present results have also been explored in this light by utilizing eq 18–20. The use of eq 20 to find C (and hence B) requires specification of the constants K_1 and K_2 and implicitly assumes that $\Delta V = 0$ and compressibility effects are negligible ($\chi_1 = \chi_2 = 0$). Guided by previous work,[14,15] a value of 1 M^{-1} was selected for the dimerization constant K_1, and a range of values of K_2 were examined by computing entire distributions on the basis of the derived values of B and C. It was found that the values of the parameters reported in the second row of Table I best fitted the results, the sign and magnitudes of the nonideality coefficients being similar to those obtained with the isodesmic model. The computed distributions corresponding to the parameters reported in Table I are again shown by the solid lines in Figures 1 and 2. It is immediately apparent that these simulated distributions are virtually identical with those computed for the isodesmic association ($K = 2 \times 10^3$ M^{-1}); slight differences between the results could not be shown on the present graphs.

Discussion

In relation to the results obtained with N-methylacetamide, the major point emerges that the sedimentation equilibrium distributions are not necessarily at variance with the interpretation given to spectrophotometric results.[14,15] The computed distributions in Figures 1 and 2 clearly show that the present experimental results, which agree basically with those found earlier,[10] cannot be interpreted uniquely on the basis of an isodesmic indefinite self-association with $K = 2 \times 10^3$ M^{-1}. Indeed the weight of evidence, taking cognizance of both sedimentation equilibrium and spectrophotometric results, favors a model described by two equilibrium constants. Two points merit comment in this connection.

First, the simulations based on the latter model assumed that ΔV, χ_1, and χ_2 were zero. It is therefore relevant to comment briefly on the effects on computed simulations of pressure and density variations with radial distance. This may be done more easily in relation to the theory pertaining to the isodesmic model. A distribution was simulated employing the parameters relevant to Figure 2 but with $\Delta V = -7$ ml mol^{-1}, the maximum value expected for a system involving linear hydrogen bonding.[24] It was found with a value of $\bar{v}_A$ estimated from eq 21 and χ_1 and χ_2 as before, that K varied by only 7% down the solution column and that the entire distribution was almost indistinguishable from that shown by the solid line in Figure 2. The corresponding variations in ρ_0 and $\bar{v}_A$ were also small, 3 and 1%, respectively. These findings illustrate that computed distributions would be little affected by neglecting terms involving ΔV, χ_1, and χ_2, provided these quantities are of small magnitude as in the present study. On the other hand, the variation in ρ was 12%, showing that the variation of solution density with radial distance, arising as a result of solute redistribution rather than compressibility effects, is the major second order effect. This effect has been accounted for by the use of eq 19 and 20 in the computation of distributions pertaining to the model involving two equilibrium constants, only the less significant second-order effects being neglected by assuming that ΔV, χ_1, and χ_2 equal zero.

Secondly, the closeness of fit of the two models involving $K = 2 \times 10^3$ M^{-1} and $\{K_1 = 1, K_2 = 50\}$ might suggest at first sight that analysis of sedimentation equilibrium results in terms of indefinite self-associations is insensitive to values of equilibrium constants selected. That this is not the case for a particular model is illustrated by the broken line in Figure 1 computed with $K_1 = 1$ M^{-1} and $K_2 = 38$ M^{-1}, which is clearly distinguishable from the solid line and deviates more from the experimental points. On the other hand, it is not claimed that the set $\{1,50\}$ uniquely describes the system; indeed, it may be shown using eq 3b, 3c, 18a, and 18b that when monomer concentration is negligible with respect to $\bar{c}$, the variation with $\bar{c}$ of $\Sigma M_{A_i} c_{A_i}$ (and hence of ψ) in the two equilibrium constant model is the same as that in the isodesmic case, provided only that the equilibrium constants are related by $K = K_2^2/K_1$. Thus, although further refinement of the values of the equilibrium constants may be possible using very low concentrations, it is felt that the agreement between the set $\{1,50\}$ and previously reported values[14,15] $\{1\text{–}1.5, 24\text{–}38\}$ is quite reasonable, particularly in view of the experimental errors encountered in the different types of study. It thus appears that the basic mechanism of the indefinite self-association of N-methylacetamide is cooperative[25] in the sense that the equilibrium constant for dimer formation is less than that governing the addition of monomer to higher polymers.

Final attention is given to the general applicability of the theory developed herein to the interpretation of sedimentation equilibrium results. The present approach is based on a numerical integration procedure which permits account to be taken of density variations due to solute redistribution and compressibility effects and which therefore may be extended to density gradient sedimentation equilibrium studies. In this sense, it offers advantage over the differential method[2] employed to interpret indefinite self-associations, which proceeds by determining the concentration dependence of apparent weight-average molecular weights assuming that the solvent and solution densities are independent of radial distance. The present approach also permits simulation of distributions pertaining to a wide range of solute concentrations which may have to be studied to distinguish between possible models. Moreover, it is possible using such distributions to estimate the molar volume change, which for certain protein

polymerizations may be sufficiently large to lead to more pronounced effects than were estimated for the *N*-methylacetamide system; a marked variation of equilibrium constant(s) with pressure and hence radial distance is difficult to interpret when results are presented in differential form.[6] Finally, the present theory may readily be modified for systems governed by more than two equilibrium constants and simplified in cases where $C = 0$, the situation frequently encountered in protein studies and it is hoped, therefore, that it will be of assistance in the elucidation of polymerizing systems of diverse type.

References and Notes

(1) K. E. Van Holde and G. P. Rossetti, *Biochemistry*, **6**, 2189 (1967).
(2) E. T. Adams and M. S. Lewis, *Biochemistry*, **7**, 1044 (1968).
(3) T. N. Solie and J. A. Schellman, *J. Mol. Biol.*, **33**, 61 (1968).
(4) K. E. Van Holde, G. P. Rossetti, and R. D. Dyson, *Ann. N. Y. Acad. Sci.*, **164**, 279 (1969).
(5) P. W. Chun, S. J. Kim, J. D. Williams, W. T. Cope, L. H. Tang, and E. T. Adams, *Biopolymers*, **11**, 197 (1972).
(6) G. J. Howlett, P. D. Jeffrey, and L. W. Nichol, *J. Phys. Chem.*, **76**, 777 (1972).
(7) G. J. Howlett and L. W. Nichol, *J. Biol. Chem.*, **247**, 5681 (1972).
(8) G. J. Howlett and L. W. Nichol, *J. Biol. Chem.*, in press.
(9) L. W. Nichol, A. G. Ogston, and B. N. Preston, *Biochem. J.*, **102**, 407 (1967).
(10) R. J. Albers, A. B. Swanson, and G. C. Kresheck, *J. Amer. Chem. Soc.*, **93**, 7075 (1971).
(11) I. M. Klotz and J. S. Franzen, *J. Amer. Chem. Soc.*, **84**, 3461 (1962).
(12) I. M. Klotz and S. B. Farnham, *Biochemistry*, **7**, 3879 (1968).
(13) G. C. Kresheck and I. M. Klotz, *Biochemistry*, **8**, 8 (1969).
(14) H. Lowenstein, H. Lassen, and A. Hvidt, *Acta Chem. Scand.*, **24**, 1687 (1970).
(15) L. L. Graham and C. Y. Chang, *J. Phys. Chem.*, **75**, 776 (1971).
(16) E. T. Adams and H. Fujita in "Ultracentrifugal Analysis in Theory and Experiment," J. W. Williams, Ed., Academic Press, New York, N. Y., 1963, p 119.
(17) H. Fujita in "Mathematical Theory of Sedimentation Analysis," Academic Press, New York, N. Y., 1962, p 238.
(18) J. Dayantis, *C. R. Acad. Sci., Ser. C*, **267**, 223 (1968).
(19) R. Josephs and W. F. Harrington, *Proc. Nat. Acad. Sci. U. S.*, **58**, 1587 (1967).
(20) D. D. McCracken and W. S. Dorn in "Numerical Methods and Fortran Programming," Wiley, New York, N. Y., 1964, p 330.
(21) J. Dayantis, *Makromol. Chem.*, **129**, 89 (1969).
(22) H. K. Schachman in "Methods in Enzymology," Vol. IV, S. P. Colowick and N. O. Kaplan, Ed., Academic Press, New York, N. Y., 1957, p 32.
(23) R. J. Albers, A. B. Swanson and G. C. Kresheck, *J. Amer. Chem. Soc.*, **94**, 4400 (1972).
(24) K. Suzuki and Y. Taniguchi in "The Effects of Pressure on Organisms," M. A. Sleigh and A. G. MacDonald, Ed., Cambridge University Press, New York, N. Y., 1972, p 107.
(25) D. Winklmair, *Arch. Biochem. Biophys.*, **147**, 509 (1971).

Interpretation of Migration Patterns for Interacting Mixtures of Reactants That Travel in Opposite Directions

L. W. Nichol,*[1] G. D. Smith, and D. J. Winzor

Department of Physical Biochemistry, John Curtin School of Medical Research, Australian National University, Canberra, A.C.T., 2601, Australia, and Department of Biochemistry, University of Queensland, St. Lucia, Queensland, 4067, Australia

(Received April 17, 1973)

Experimental sedimentation–flotation studies with lipoprotein–protein (or polysaccharide) mixtures, or electrophoretic studies with proteins of opposite charge, may lead to complicated migration patterns due to the reactants travelling in opposite directions and because binding yields complexes with intermediate velocities. Theory is presented to describe the migration behavior of such systems both for cases involving single complex ($A + B \rightleftarrows C$) and higher order complex ($AB_{i-1} + B \rightleftarrows AB_i$) formation. For the former situation, it is shown that by treating velocities as vector quantities the mathematical solution obtained by Gilbert and Jenkins in fact covers the range of situations encountered but their treatment is extended to illustrate the seemingly diverse patterns which may be recorded experimentally. It is shown that for a given system the constituent velocity of A or B may change sign depending on the mixing composition of A and B, and the equilibrium constant. Such a situation has been observed experimentally in the moving boundary electrophoresis of a mixture of bovine serum albumin and lysozyme, which form a 1:1 complex. The mobility of this complex was determined for the given conditions (pH 7.4, ionic strength 0.05 phosphate buffer) and an equilibrium constant determined. Finally methods are presented for using observed constituent velocities to determine the number of binding sites and the intrinsic binding constants for systems in which one of the macromolecular species binds at multiple sites on the other.

Introduction

Use of the mass migration methods of chromatography, sedimentation velocity, and electrophoresis to study rapidly equilibrating systems of macromolecular constituents has been facilitated by the theoretical treatment provided by Gilbert and Jenkins[2a] for heterogeneous associations of the type $A + B \rightleftarrows C$. Their solutions for situations where both reactants move with identical velocities or where the complex and faster moving reactant travel together have been applied directly to the interpretation of gel chromatographic results obtained with protein systems undergoing heterogeneous associations:[2b,3] in the latter instance ($v_C = v_A$) the treatment has also been extended to systems wherein multiple binding of ligand leads to a series

of complexes, all moving with the velocity of acceptor.[4,5] The behavior encountered in the migration of systems where the complex travels faster than either reactant, each moving with a different velocity, has also been illustrated,[6-8] and means established for evaluating the equilibrium constant for single complex formation.

Gilbert and Jenkins[2a] noted that the situation where the complex moves with a velocity intermediate between those of the reactants would be encountered frequently in moving boundary electrophoresis, and, indeed, behavior consistent with their theoretical predictions for this case has been observed in the electrophoresis of several interacting systems (see, *e.g.*, ref 6, 9-14); in these studies, conditions were generally selected such that all species migrated in the same direction. It is the purpose of the present work to consider in greater detail cases where the velocities of the reactants are of opposite sign. This situation may arise in practice in moving boundary electrophoresis of an interacting protein mixture at a pH value between the isoelectric points of the reactants (*e.g.*, conalbumin-lysozyme mixtures at neutral pH[14]), or in sedimentation velocity of an associating protein-lipoprotein or lipoprotein-polysaccharide system in a medium with a density between those of the two reactants. Electrophoretic patterns obtained with mixtures of lysozyme and bovine serum albumin in 0.05 ionic strength phosphate, pH 7.4, are presented to illustrate (a) some of the essential features of migration patterns which may develop, and (b) a method for analyzing the patterns in terms of interaction constants. The theory extends previous treatments by considering situations where a series of complexes is formed.

Theory

A Description of Possible Boundary Forms. Consider first the simplest type of heterogeneous association, A + B $\rightleftarrows$ C, where the velocities of the reactants are denoted by the vector quantities v_A and v_B. Discussion is restricted to the case where the velocity of the complex v_C is intermediate between v_A and v_B, which may arise even when $|v_A| = |v_B|$ if v_A and v_B are of opposite sign. The analytical solution for this case provided by Gilbert and Jenkins[2a] is applicable regardless of the signs of v_A and v_B. It describes a reaction boundary separating the original solution plateau from one of pure reactant, this being A on one conjugate side and B on the other. This is illustrated in Figure 1 drawn in terms of constituent concentrations defined on a molar basis as

$$\bar{m}_A = m_A + m_C \quad (1a)$$

$$\bar{m}_B = m_B + m_C \quad (1b)$$

The convention has been adopted that $v_A > v_B$, with electrophoretic mobilities of anionic species being classed as negative velocities, as are those of solutes that migrate centripetally in sedimentation velocity. This convention permits consideration of the conjugate side without the relabeling of reactants (see Chapter 4 of ref 15 for discussion of alternative conventions for labeling species). Consideration of the conservation of mass requirement[16] shows that the velocity of the median bisector of the A constituent gradient across which A disappears is the constituent velocity.

$$\bar{v}_A = (v_A m_A + v_C m_C)/\bar{m}_A \quad (2a)$$

Similarly, $\bar{v}_B$ obtained from the median bisector of the constituent gradient of B on the conjugate side in Figure 1 is defined by

$$\bar{v}_B = (v_B m_B + v_C m_C)/\bar{m}_B \quad (2b)$$

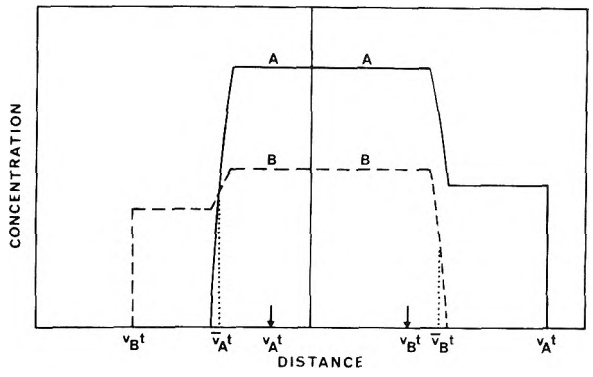

Figure 1. Schematic representation of a migration pattern for the system A + B $\rightleftarrows$ C with $v_A > v_C > v_B$, conjugate sides being illustrated. The ordinate axis refers to the constituent concentration of each reactant.

The signs of $\bar{v}_A$ and $\bar{v}_B$ determine the directions of movement of the reaction boundaries since the constituent gradients of A and B in both reaction boundaries are necessarily coextensive (*i.e.*, it is not possible to have a region where only B and C or A and C coexist). In relation to these reaction boundaries, two basic possibilities arise: the first encompasses situations where the reaction boundaries move in the same direction ($\bar{v}_A$ and $\bar{v}_B$ being of the same sign, either positive or negative), and the second involves reaction boundaries moving in opposite directions. However, each of these possibilities must be considered in relation to the migration of the boundaries of separated reactants (Figure 1), and thus for this purpose the possibilities are summarized in greater detail in Table I. The physically unreasonable situation is omitted involving the formation of a complex with a velocity of opposite sign to that of both reactants. This also excludes the case $\bar{v}_A = 0$ and $\bar{v}_B = 0$ (eq 2). However, the possibilities remain that $\bar{v}_A = 0$ and $\bar{v}_B \neq 0$ provided $v_A > 0$, $v_B < 0$, and $v_C < 0$, or that $v_A \neq 0$ and $\bar{v}_B = 0$ provided $v_A > 0$, $v_B < 0$, and $v_C > 0$: these are merely special cases of two of those now to be discussed. Utilizing Figure 1 and Table I, it is now possible to discuss the seemingly diverse patterns which may arise experimentally.

In moving boundary electrophoresis both conjugate sides may be observed, this being facilitated by shifting the initial boundaries to the central region of both limbs prior to applying current. In case 1, for which A and B are both cationic, all boundaries are seen to migrate in the positive direction. Case 2 differs from the first in that the boundary of pure reactant B moves in the opposite direction from that of the other three boundaries. A similar comparison applies to cases 3 and 4, case 3 in the electrophoretic situation being analogous to case 1 but with anionic rather than cationic reactants. Cases 5 and 6 differ from the previous ones in that the two reaction boundaries are seen to converge, while in each limb the boundary of pure reactant and the reaction boundary migrate in opposite directions; this description applies even in the special case that one reaction boundary remains stationary. Since for all cases a boundary arises between solvent and a pure reactant on both sides, there is the possibility of convective disturbance due to a density inversion in the event that either reactant is less dense than solvent. For these

unusual cases the description of the distribution given in Figure 1 will be to this extent modified and thus complicate quantitative interpretation.

In conventional sedimentation velocity, migration is usually in one direction only and the systems would thus conform with either case 1 (sedimentation) or case 3 (flotation). For case 1 a boundary of pure B sediments away from the meniscus and a reaction boundary with constituent velocity $\bar{v}_A$ moves ahead, other boundaries being obscured by pile-up at the cell base.[16] For case 3 the boundary nearest the base of the cell and moving centripetally would represent separated reactant A, the reaction boundary moving in the same direction being characterized by velocity $\bar{v}_B$, with pile-up of solute occurring at the meniscus; this type of flotation behavior may well be encountered with lipoprotein systems in a medium of suitable density. In contrast to these situations where two boundaries are observed, with cases 2 and 4 only the respective reaction boundary appears. Nevertheless, in case 2 a region of pure B exists between the meniscus (where pile-up occurs) and the reaction boundary, while in case 4 a plateau region of A separates the reaction boundary and the solute pile-up at the cell base. Systems conforming with cases 5 or 6, which differ in the sign of v_C, exhibit identical behavior that is quite distinct from that of the preceding cases; *two* reaction boundaries appear and are seen to converge, leaving pure B near the meniscus and pure A near the base of the cell. For all cases the distributions described are gravitationally stable since the sign of v_j (j = A, B, or C) is dictated by the sign of the buoyancy term $(1 - \bar{v}_j\rho)$.

Consideration of the Initial Mixing Concentrations. It should be stressed that assigning signs to the velocities v_A, v_B, and v_C is not sufficient to determine the signs of $\bar{v}_A$ and $\bar{v}_B$. For example, cases 2 and 5 of Table I define the alternative possibilities for which the sign of $\bar{v}_B$ differs even though for each case the signs of individual species velocities are identical. Indeed, cases 2 and 5 could refer to the same system studied in the same environment and yet they display seemingly quite different behavior: the question thus arises as to the condition that dictates the nature of the migration pattern. A similar situation is encountered with cases 4 and 6, because of the identity of the signs of the individual species velocities; again a given experimental system may conform with either case.

It is possible to reformulate the cases specified in Table I in terms of constituent concentrations and individual species velocities rather than in terms of constituent velocities. For example, it follows from eq 2 that cases 1 and 2 require that $v_A/v_C > -m_C/m_A$ and $v_B/v_C > -m_C/m_B$. For the former these conditions are fulfilled for all values of $\bar{m}_A$ and $\bar{m}_B$, since all species velocities are positive, but for case 2 the latter inequality must be examined further since $v_B/v_C < 0$. An equilibrium constant may be defined and rearranged using eq 1 to give

$$K = m_C/m_Am_B = (\bar{m}_A - m_A)/m_A(\bar{m}_B - \bar{m}_A + m_A) \quad (3)$$

Equation 3 is a quadratic in m_A which may be solved to yield an expression for m_A and hence for m_C/m_B (= Km_A), whereupon the condition $v_B/v_C > -m_C/m_B$ may be written as

$$2v_B + v_C\{K\bar{m}_A - K\bar{m}_B - 1 \pm [(K\bar{m}_B - K\bar{m}_A + 1)^2 + 4K\bar{m}_A]^{1/2}\} > 0 \quad (4)$$

These functions when plotted against $\bar{m}_A$ intersect at a common value of $\bar{m}_A$ on the m_A axis and assume positive values only when

$$\bar{m}_A - \{v_B(v_CK\bar{m}_B + v_C - v_B)/Kv_C(v_3 - v_C)\} > 0 \quad (5)$$

Therefore, for case 2, eq 5 requires $\bar{m}_A$ to be greater than a positive number, the magnitude of which depends on $\bar{m}_B$ for a particular system with defined species velocities and equilibrium constant. For values of $\bar{m}_B$ satisfying eq 5, the behavior attributed to case 2 pertains, but for other values of m_B that described in relation to case 5 applies. This may be shown simply by noting that the necessary and sufficient condition for case 5 is $v_B/v_C < -m_C/m_B$, which leads to eq 5 with the inequality sign reversed. Thus for a given system studied in a fixed environment (*i.e.*, with defined K and $v_A > 0$, $v_B < 0$, and $v_C > 0$) it is possible in sedimentation velocity (for example) to observe *either* a single sedimenting reaction boundary *or* two converging reaction boundaries, depending on the initial mixing concentrations. It follows that a particular set of values of $\bar{m}_A$ and $\bar{m}_B$ exists where $\bar{v}_A \neq 0$ and $\bar{v}_B = 0$; a single reaction boundary would again be observed under these circumstances.

By similar reasoning it may be shown for case 4 that the necessary and sufficient condition is given by

$$\bar{m}_B - \{v_A(v_CK\bar{m}_A + v_C - v_A)/Kv_C(v_A - v_C)\} > 0 \quad (6)$$

and that when $v_A > 0$, $v_B < 0$, and $v_C < 0$ values of $\bar{m}_B$ not satisfying eq 6 give rise to migration patterns described as case 6.

Determination of $\bar{v}_A$ *and* $\bar{v}_B$. In moving boundary electrophoresis reaction boundaries are observable in conjugate limbs for all cases listed in Table I, and thus estimates of v_A and v_B may be obtained directly, provided the electrolyte redistribution across the original boundary positions has a negligible effect on either the velocities of species or the equilibrium constant.[10,11] The exact determination of constituent velocities requires measurement of the median bisector of the gradient of that constituent within the reaction boundary across which it disappears,[8,16] and thus concentration gradients of the individual constituents should be recorded where possible by the use (for example) of absorption optics.

Similar comments apply to sedimentation velocity of systems conforming to cases 5 and 6. However, in the sedimentation of systems encompassed by cases 1–4 inclusive, only one reaction boundary is observed, which may be used to obtain the relevant constituent velocity (either $\bar{v}_A$ or $\bar{v}_B$); the other is derivable from the moving boundary equation

$$m_X{}^\beta = \bar{m}_X{}^\alpha(v' - \bar{v}_X{}^\alpha)/(v' - v_X{}^\beta) \quad (7)$$

where the subscript X denotes A or B, the superscript β the region where pure reactant exists alone, and superscript α the region containing original solution. In the situation that B separates as the β phase, for example, v′ re-

TABLE I: Possible Relative Signs of Velocities of Constituents and Individual Species for a System of the Type A + B ⇌ C with $v_A > v_B$ and $v_A > v_C > v_B$

Case	v_A	v_B	v_C	$\bar{v}_A$	$\bar{v}_B$
1	+	+	+	+	+
2	+	−	+	+	+
3	−	−	−	−	−
4	+	−	−	−	−
5	+	−	+	+	−
6	+	−	−	+	−

fers to the median bisector of the constituent gradient of B in the reaction boundary region and may thus approximate to the constituent velocity of A. For cases 1 and 3, $m_X{}^\beta$ and $\mathbf{v}_X{}^\beta$ may be measured from the observed boundary of pure reactant, while for cases 2 and 4 the use of adsorption optics would facilitate determination of $m_X{}^\beta$, the magnitude of $\mathbf{v}_X{}^\beta$ being obtainable by an integration procedure or by conducting a separate experiment with X alone.

To this point the discussion has been restricted to the mass migration of systems undergoing the simple reaction A + B $\rightleftarrows$ C. For more complicated systems of the type AB_{i-1} + B $\rightleftarrows$ AB_i (where i = 1, 2, . . . p), which still comprise two constituents, it is possible to generalize the definitions of constituent velocities given in eq 2 as follows

$$\bar{\mathbf{v}}_A = \left\{\mathbf{v}_A m_A + \sum_{i=1}^{P} \mathbf{v}_{AB_i} m_{AB_i}\right\} \Big/ \left\{m_A + \sum_{i=1}^{P} m_{AB_i}\right\} \quad (8a)$$

$$\bar{\mathbf{v}}_B = \left\{\mathbf{v}_B m_B + \sum_{i=1}^{P} i\mathbf{v}_{AB_i} m_{AB_i}\right\} \Big/ \left\{m_B + \sum_{i=1}^{P} i m_{AB_i}\right\} \quad (8b)$$

where from the definitions of the successive association constants K_i

$$m_{AB_i} = m_A m_B{}^i \prod_1^i K_i \quad (9)$$

Nichol and Ogston[17] have shown that the condition for the conservation of mass of each constituent (X = A or B) may be written as $\mathbf{u}\, d\bar{m}_X - d\bar{\mathbf{v}}_X \bar{m}_X = 0$, where $\mathbf{u}$ is the velocity of a lamina of constant composition. It follows from eq 8 that

$$(\mathbf{u} - \mathbf{v}_A)\, dm_A + \sum_{i=1}^{P} (\mathbf{u} - \mathbf{v}_{AB_i})\, dm_{AB_i} = 0 \quad (10a)$$

$$(\mathbf{u} - \mathbf{v}_B)\, dm_B + \sum_{i=1}^{P} i(\mathbf{u} - \mathbf{v}_{AB_i})\, dm_{AB_i} = 0 \quad (10b)$$

It is now desired to show for the situation $\mathbf{v}_B$ < all $\mathbf{v}_{AB_i}$ < $\mathbf{v}_A$ that the reaction boundary arises between $\mathbf{v}_A$ and $\mathbf{v}_B$ since this would extend the usefulness of Figure 1. By reason of symmetry it is only necessary to consider one side, and thus reference is made to the left-hand side of Figure 1, with distances positive in the direction solvent → solution, so that the regions $\mathbf{u} < \mathbf{v}_B$ and $\mathbf{u} > \mathbf{v}_A$ refer to solvent and solution plateaux, respectively. When $\mathbf{u} = \mathbf{v}_A$ or $\mathbf{u} = \mathbf{v}_B$, eq 10a and 10b require that all $dm_{AB_i} = 0$ and thus the reaction boundary (wherein all $dm_{AB_i} \neq 0$) must arise between $\mathbf{v}_A$ and $\mathbf{v}_B$. It follows that it is still possible to estimate $\bar{\mathbf{v}}_A$ and $\bar{\mathbf{v}}_B$ either directly or *via* eq 7 in the event that complexes of higher order than 1:1 are encountered.

Use of $\bar{\mathbf{v}}_A$ and $\bar{\mathbf{v}}_B$ in Determining Equilibrium Constants. Consider a situation where the p sites on A are equivalent and independent so that all K_i may be expressed in terms of a single intrinsic binding constant, K_A, where

$$K_i = [p - (i - 1)]K_A/i \quad (11)$$

It follows from eq 9 that

$$m_{AB_i} = m_A m_B{}^i \left(\prod_1^i [p - (i - 1)]/i\right) K_A{}^i \quad (12)$$

It also follows from the concept of equivalent and independent binding that

$$\frac{\bar{m}_B - m_B}{\bar{m}_A} = \frac{pK_A m_B}{1 + K_A m_B} \quad (13a)$$

$$K_A = \frac{m_B - \bar{m}_B}{m_B(\bar{m}_B - m_B - p\bar{m}_A)} \quad (13b)$$

Combination of eq 8b, 12, and 13b yields on rearrangement

$$m_A = (\bar{\mathbf{v}}_B \bar{m}_B - \mathbf{v}_B m_B) / \sum_{i=1}^{P} i\left(\prod_1^i [p - (i - 1)]/i\right) \mathbf{v}_{AB_i} (m_B - \bar{m}_B)^i / (\bar{m}_B - m_B - p\bar{m}_A)^i \quad (14)$$

Similarly, combination of eq 8a, 12, and 13b yields

$$m_A = \bar{\mathbf{v}}_A \bar{m}_A / \left[\mathbf{v}_A + \sum_{i=1}^{P} \left(\prod_1^i [p - (i - 1)]/i\right) \mathbf{v}_{AB_i} (m_B - \bar{m}_B)^i / (\bar{m}_B - m_B - p\bar{m}_A)^i\right] \quad (15)$$

For the case A + B $\rightleftarrows$ AB (≡C) where p = 1, m_A may be evaluated from eq 15 alone when written in the form (employing eq 1)

$$m_A = \bar{m}_A(\bar{\mathbf{v}}_A - \mathbf{v}_{AB})/(\mathbf{v}_A - \mathbf{v}_{AB}) \quad (16)$$

Alternatively, as Gilbert and Kellett[8] have noted, it is possible to determine m_A without knowledge of $\mathbf{v}_{AB}$ if both constituent velocities ($\bar{\mathbf{v}}_A$ and $\bar{\mathbf{v}}_B$) are employed. This may be seen by rearranging eq 1 and 2 to give

$$m_A = \{\bar{m}_A(\bar{\mathbf{v}}_A - \mathbf{v}_B) - \bar{m}_B(\bar{\mathbf{v}}_B - \mathbf{v}_B)\}/(\mathbf{v}_A - \mathbf{v}_B) \quad (17)$$

Once the equilibrium concentration of unbound A has been found, it is a simple matter to obtain K_A from eq 3. The difficulty arises that only one value of K_A is available from a single experiment and thus it must be regarded as apparent unless it is known that p = 1. Without this knowledge it would be necessary to perform a series of experiments with mixtures of different compositions and total concentrations, and to test the assumption that p = 1 on the basis of constancy of apparent K_A values. In the event that a larger value of p is indicated, eq 14 and 15 may be combined and solved for m_B (and K_A evaluated from eq 13b) for a range of values of p. The final selection of corresponding values of p and K_A would again be based on the observed constancy of apparent K_A values derived from separate experiments. Three points in relation to this procedure merit comment. First, it requires the joint use of both constituent velocities, which offers no great problem in moving boundary electrophoresis provided the slight discrepancy between mobilities of a solute determined from conjugate sides is disregarded. Secondly, it yields a single intrinsic binding constant and is therefore inapplicable to systems where $p > 1$ and the sites are either nonequivalent or mutually interacting. Thirdly, it is clear that when $p > 1$ the solution of eq 14 and 15 requires specification of all $\mathbf{v}_{AB_i}$, whereas only $\mathbf{v}_A$ and $\mathbf{v}_B$ are readily available. Estimates of $\mathbf{v}_{AB_i}$ could be obtained either from geometrical and hydrodynamic considerations of possible models[18,19] or by assuming a constant incremental change, q (positive or negative), in $\mathbf{v}_A$ induced by the successive addition of each molecule of B, *i.e.*, by assuming[10,20,21] that

$$\mathbf{v}_{AB_i} = \mathbf{v}_A + iq \quad (18a)$$

In the latter connection, Schachman[20,21] has suggested that an additional approximation may be reasonable in certain cases, *viz.*

$$\bar{\mathbf{v}}_A = \mathbf{v}_A + \frac{(\bar{m}_B - m_B)}{\bar{m}_A} q \quad (18b)$$

Joint use of eq 18a and 18b permits $v_{AB,i}$ to be expressed solely in terms of v_A, $\bar{m}_B$, $\bar{m}_A$, and m_B consistent with the use of eq 14 and 15 in solving for m_B.

Experimental Section

Salt-free, crystalline samples of bovine serum albumin (Armour) and lysozyme (Worthington) were used without further purification. Stock solutions of the individual proteins (~2%) were dialyzed at 5° against 4 × 500 ml of phosphate buffer, pH 7.4, ionic strength 0.05 (0.004 *M* NaH_2PO_4, 0.016 *M* Na_2HPO_4), after which they were stored in air-tight containers until required for electrophoresis. Mixtures were prepared by weight from these stock solutions, the concentrations of which were determined spectrophotometrically at 280 nm on suitably diluted aliquots: extinction coefficients ($E^{1\%}_{1\,cm}$) of 6.6 (ref 22) and 27.2 (ref 14) were used for albumin and lysozyme, respectively, the corresponding molecular weights being taken as 67,000 (ref 23) and 14,500 daltons (ref 24).

Immediately after preparation, the mixtures were used to fill the standard 15-mm cell of a Perkin-Elmer Model 238 electrophoresis apparatus in the usual manner. After allowing sufficient time for the cell and contents to equilibrate with the bath temperature (5°), the procedure of compensation to bring the initial boundaries into view was continued until they were in the centers of the two limbs, in order to permit observation of solute migration in both directions. With an applied current of 6 mA such experiments had a useful lifetime of approximately 45–55 min. Distances migrated were determined from tracings of schlieren patterns obtained with the diagonal slit assembly, median bisectors[25] of asymmetric boundaries being used to locate their positions. In calculations of mobilities, the resistances of the mixtures were assumed to be those of the buffer; since conductivities were measured at 0°, the mobilities also refer to this temperature. However, the equilibrium constants determined refer to the reaction at 5°, the temperature at which electrophoresis was performed. Boundaries corresponding to gradients of pure solute (lysozyme or albumin) were identified by distances migrated from the initial boundary positions, these being located in exposures taken prior to application of the electric field.

Results and Discussion

Electrophoretic patterns for the individual solutes albumin and lysozyme are shown in the upper and lower portions, respectively, of Figure 2. Single, fairly symmetrical boundaries were observed in each limb, although the patterns exhibited the usual degree of nonenantiography with respect to (a) boundary spreading and (b) discrepancies between apparent mobilities calculated from ascending and descending patterns. For example, apparent mobilities of -6.7 and -6.5×10^{-5} cm^2 sec^{-1} V^{-1} were obtained from the ascending and descending patterns, respectively, for bovine serum albumin; since no account was to be taken of conductivity and pH differences across the boundary anomalies,[10,11] the average of the two values was assumed to apply to both limbs. Thus values of -6.6×10^{-5} and $+3.7 \times 10^{-5}$ cm^2 sec^{-1} V^{-1} were considered to represent the electrophoretic mobilities of free albumin and free lysozyme, respectively, in mixtures undergoing heterogeneous association.

Table II summarizes the results obtained in moving boundary electrophoresis of mixtures of lysozyme and bovine serum albumin; in accordance with the adopted convention that cationic species have positive velocities, lysozyme is the faster migrating reactant and is therefore labeled A. Patterns obtained in these experiments were of two types (Figure 3): in experiments 1–5, inclusive, the electrophoretic behavior was typified by the upper patterns, in which $\bar{v}_A$ is positive and $\bar{v}_B$ negative, while in experiments 6 and 7 the alternative situation (lower patterns) with $\bar{v}_A$ and $\bar{v}_B$ both negative was observed. Columns 2 and 3 of Table II indicate the constituent concentrations of the two reactants, and columns 4 and 5 the respective constituent mobilities. These were measured from the rates of movement of the median bisectors of the reaction boundaries recorded refractometrically and hence may only approximate to the required constituent velocities. These could only be determined precisely by recording the individual constituent gradients,[8,16] a prohibitively difficult task in the present examination of reacting mixtures of two proteins which absorb in the same wavelength region. On the other hand, the median bisector of the total concentration gradient within a boundary is a defined position which at least permits consistent comparisons to be made between experiments involving mixtures of different initial composition. Column 6 tabulates the equilibrium concentration of free lysozyme, calculated from eq 17, use of which implies the formation of a 1:1 complex; the relative constancy of K (column 7) provides some justification for this hypothesis. Further support for the concept of single complex formation comes from calculation of its apparent mobility *via* the definitions of constituent velocities (eq 2a and 2b); the agreement between values of v_C calculated from the two constituent velocities measured in a single experiment (the entries recorded in columns 8 and 9 for each run) establishes the internal consistency of each experiment, while the close parallel between values of the complex mobility from different experiments implies identity of the complex species in each case. Such a result would not be expected to pertain in the event that several complex species, each characterized by a different v_C, coexisted at equilibrium, because the wide variation in the initial concentrations and mixing ratios of reactants (columns 2 and 3) would have ensured differences in the relative amounts of the various complexes from experiment to experiment. However, the absolute magnitude of the apparent equilibrium constant (K) must await verification by use of a migration technique capable of recording individual constituent gradients or the examination of the system by an equilibrium method.

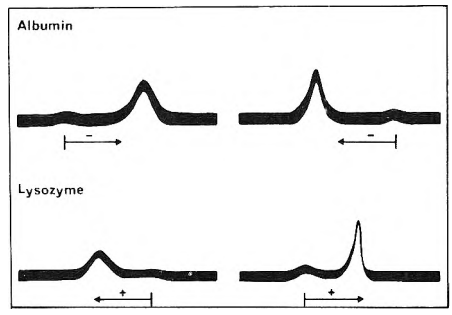

Figure 2. Electrophoresis of bovine serum albumin (upper patterns) and lysozyme (lower patterns) in phosphate buffer, pH 7.4, ionic strength 0.05, the exposures being taken 45 and 50 min, respectively, after applying a potential gradient of 14.6 V/cm. Positions of initial boundaries are indicated below the patterns, those on the right referring to ascending limbs. Migration is assigned as positive or negative on the basis that cations have positive velocities.

TABLE II: Electrophoresis of Mixtures of Lysozyme (A) and Bovine Serum Albumin (B) in Phosphate Buffer, pH 7.4, Ionic Strength 0.05, at 5°

Expt no.	Constituent concn, $M \times 10^4$		Constituent mobilities,[a] $cm^2\ sec^{-1}\ V^{-1} \times 10^5$		m_A, $M \times 10^4$	K, $M^{-1} \times 10^{-3}$	Complex mobility, $cm^2\ sec^{-1}\ V^{-1} \times 10^5$		Left-hand side of eq 5
	$\bar{m}_A$	$\bar{m}_B$	$\bar{v}_A$	$\bar{v}_B$			From $\bar{v}_A$	From $\bar{v}_B$	
1	3.00	0.86	+2.4	−4.5	2.45	7.2	−3.4	−3.3	<0
2	3.41	1.24	+2.2	−4.6	2.67	5.5	−3.2	−3.2	<0
3	2.81	1.15	+2.0	−4.7	2.13	6.8	−3.3	−3.4	<0
4	1.36	1.06	+1.6	−5.3	0.95	6.6	−3.3	−3.2	<0
5	1.70	1.87	+0.7	−5.4	0.99	6.2	−3.5	−3.5	<0
6	2.37	2.91	−0.5	−5.1	0.98	9.3	−3.5	−3.5	>0
7	1.59	3.48	−1.1	−5.8	0.58	9.4	−3.2	−3.5	>0

[a] Reactant mobilities: $v_A = 3.7 \times 10^{-5}\ cm^2\ sec^{-1}\ V^{-1}$; $v_B = -6.6 \times 10^{-5}\ cm^2\ sec^{-1}\ V^{-1}$.

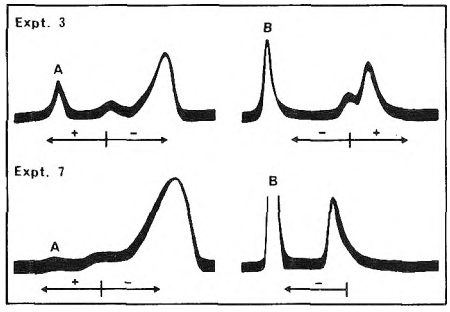

Figure 3. Electrophoresis of mixtures of lysozyme (A) and bovine serum albumin (B) at 5° in phosphate, pH 7.4, ionic strength 0.05, the exposures being taken 45 min after applying a potential gradient of 14.6 V/cm; for details of the constituent concentration of each reactant see the relevant experiment in Table II.

From the viewpoint of employing hydrodynamic models to predict complex velocities it is noted that the values of v_C derived on the basis of a 1:1 complex lead to an estimate of the net charge borne by this complex which is consistent with that predicted from titration curves for the two reactants. Under the present conditions (pH 7.4, ionic strength 0.05), bovine serum albumin bears a net charge of −14 (ref 26) and lysozyme a charge of +6 (ref 27), whereupon a valence of −8 is predicted from titration data for the 1:1 complex on the assumptions of charge conservation and absence of specific ion binding effects. The same value was obtained[18] with an average value of $-3.3 \times 10^{-5}\ cm^2\ sec^{-1}\ V^{-1}$ for v_C (Table II) and an estimated Stokes' radius ($r_C^3 = r_A^3 + r_B^3$) of $r_C = 36.9$ Å. The close agreement between the estimated valencies is somewhat fortuitous, since the method of Abramson, *et al.*,[18] as a general procedure for estimating charge is not without criticism.[28] In this connection it is noted that Waldmann-Meyer[29] has established its validity for estimating the valence of bovine serum albumin, and the present results confirm this inasmuch as our mobility value also predicts the titration value of −14 for the net charge. On the other hand, application of the same procedure to lysozyme met with far less success; a value of +3, or approximately half of the titration value, was obtained.

Finally, in connection with Table II, it is noted that the complex has a negative mobility, which now permits identification of the observed patterns with the possible classes listed in Table I; experiments 1–5, inclusive, conform with case 6, while experiments 6 and 7 typify case 4. The final column in Table II bears out the ability of eq 6 to predict the changeover between these two classes of migration patterns. By adopting the rather unlikely convention that anionic species are assigned positive velocities, experiments 1–5, inclusive, would be termed class 5, and experiments 6 and 7 class 2; again the changeover between classes would have been predicted adequately, the relevant expression in this instance being eq 5. The changeover in the nature of the migration pattern (Figure 3) has been observed before by Ehrenpreis and Warner,[14] but they made no attempt to characterize the conditions governing the type of experimental pattern obtained. Although the present experimental results are only particular examples of the migration behavior of interacting systems with reactants moving in opposite directions, they serve to stress that while a single form of theoretical solution[2a] (Figure 1) pertains for all systems of the type $v_A > v_{AB\,i} > v_B$, the experimenter may be confronted with seemingly diverse migration patterns. In discussing these in greater detail than previously attempted[2a] for both electrophoresis and sedimentation velocity, we hope that the present study may aid the detection of interactions and in favorable cases the quantitative estimation of apparent equilibrium constants from measurable constituent velocities and concentrations. The potential then exists for these estimates to be examined further by use of computer-simulated migration patterns to include the effects of diffusional spreading,[30-32] and thereby to make use of the shapes as well as positions of boundaries.

References and Notes

(1) Address correspondence to Department of Physical Biochemistry, John Curtin School of Medical Research, Australian National University, P.O. Box 334, Canberra City, A.C.T. 2601, Australia.
(2) (a) G. A. Gilbert and R. C. Ll. Jenkins, *Proc. Roy. Soc., Ser. A*, **253**, 420 (1959); (b) L. W. Nichol and D. J. Winzor, *Biochim. Biophys. Acta*, **94**, 591 (1965).
(3) L. W. Nichol and D. J. Winzor, *J. Phys. Chem.*, **68**, 2455 (1964).
(4) P. F. Cooper and G. C. Wood, *J. Pharm. Pharmacol.*, **20**, 150S (1968).
(5) L. W. Nichol, W. J. H. Jackson, and G. D. Smith, *Arch. Biochem. Biophys.*, **144**, 438 (1971).
(6) S. J. Singer, F. A. Pepe, and D. Uttern, *J. Amer. Chem. Soc.*, **81**, 3887 (1959).
(7) L. W. Nichol, A. G. Ogston, and D. J. Winzor, *Arch. Biochem. Biophys.*, **121**, 517 (1967).
(8) G. A. Gilbert and G. L. Kellett, *J. Biol. Chem.*, **246**, 6079 (1971).
(9) L. G. Longsworth and D. A. MacInnes, *J. Gen. Physiol.*, **25**, 507 (1942).
(10) R. F. Smith and D. R. Briggs, *J. Phys. Colloid Chem.*, **54**, 33 (1950).
(11) L. G. Longsworth in "Electrophoresis, Theory, Methods and Applications," M. Bier, Ed., Academic Press, New York, N. Y., 1959, p 91.
(12) F. A. Pepe and S. J. Singer, *J. Amer. Chem. Soc.*, **81**, 3878 (1959).
(13) J. R. Cann and J. A. Klapper, Jr., *J. Biol. Chem.*, **236**, 2445 (1961).
(14) S. Ehrenpreis and R. C. Warner, *Arch. Biochem. Biophys.*, **61**, 38 (1956).

(15) L. W. Nichol and D. J. Winzor, "Migration of Interacting Systems," Clarendon Press, Oxford, 1972.
(16) L. W. Nichol and A. G. Ogston, *J. Phys. Chem.*, **69**, 1754 (1965).
(17) L. W. Nichol and A. G. Ogston, *Proc. Roy. Soc., Ser. B*, **163**, 343, (1965).
(18) H. A. Abramson, L. S. Moyer, and M. H. Gorin, "Electrophoresis of Proteins," Reinhold, New York, N. Y., 1942.
(19) V. Bloomfield, W. O. Dalton, and K. E. Van Holde, *Biopolymers*, **5**, 135 (1967).
(20) H. K. Schachman, "Ultracentrifugation in Biochemistry," Academic Press, New York, N. Y., 1959.
(21) I. Z. Steinberg and H. K. Schachman, *Biochemistry*, **5**, 3728 (1966).
(22) M. J. Kronman and J. F. Foster, *Arch. Biochem. Biophys.*, **72**, 205 (1957).
(23) P. G. Squire, P. Moser, and C. T. O'Konski, *Biochemistry*, **7**, 4261 (1968).
(24) A. J. Sophianopoulos, C. K. Rhodes, D. N. Holcomb, and K. E. Van Holde, *J. Biol. Chem.*, **237**, 1107 (1962).
(25) L. G. Longsworth, *J. Amer. Chem. Soc.*, **65**, 1755 (1943).
(26) C. Tanford, S. A. Swanson, and W. S. Shore, *J. Amer. Chem. Soc.*, **77**, 6414 (1955).
(27) C. Tanford and M. L. Wagner, *J. Amer. Chem. Soc.*, **76**, 3331 (1954).
(28) L. B. Barnett and H. B. Bull, *Arch. Biochem. Biophys.*, **89**, 167 (1960).
(29) H. Waldmann-Meyer, *J. Biol. Chem.*, **235**, 3337 (1960)
(30) J. R. Cann and W. B. Goad, *J. Biol. Chem.*, **240**, 148 (1965).
(31) D. J. Cox, *Arch. Biochem. Biophys.*, **119**, 230 (1967).
(32) D. J. Cox, *Arch. Biochem. Biophys.*, **129**, 106 (1969).

Tracer Diffusion of HTO and Simple Ions in Aqueous Solutions of Sodium *p*-Ethylbenzenesulfonate. Comparisons with Polyelectrolyte Solutions and Gels[1]

Michael J. Pikal[2]

Department of Chemistry, University of Tennessee, Knoxville, Tennessee 37916

and G. E. Boyd*

Oak Ridge National Laboratory, Oak Ridge, Tennessee 37830 *(Received March 22, 1973)*

Publication costs assisted by Oak Ridge National Laboratory

The object of this research was to provide data for a detailed analysis of the analogy between tracer diffusion in polyelectrolyte solutions and gels and in aqueous solutions of a 1-1 electrolyte with the same chemical structure as the repeating unit in the polyelectrolytes. Tracer diffusion coefficients of HTO and simple inorganic cations and anions were measured at 25° in concentrated sodium *p*-ethylbenzenesulfonate (NapEBS) solutions and in the sodium form of cross-linked polystyrenesulfonate ion-exchange gels. The diffusion coefficients of all species decreased rapidly with increasing NapEBS concentration in concentrated solutions of the latter. Much of this decrease can be attributed to an obstruction effect. An analysis of the HTO diffusion data suggests that the pEBS-anion has little net effect on the structure of water. Diffusion coefficients in NapEBS solutions are compared with those for sodium polystyrenesulfonate (NaPSS) solutions and for the sodium form of cross-linked polystyrenesulfonate ion exchange gels. Although a concentrated NapEBS solution is a far better "model" for the polyelectrolyte systems than is a typical 1-1 inorganic electrolyte, the diffusion of cations is much more rapid in NapEBS than in either the NaPSS solution or in the ion exchanger. However, the diffusion coefficients for HTO and for the coion, $^{36}Cl^-$, are nearly the same in all systems. It is concluded that the analogy between polyelectrolyte solutions and gels and 1-1 type model electrolytes has validity for diffusion of *neutral species* and *coions*, but not for the diffusion of *counterions*.

I. Introduction

The analogies between equilibrium and rate processes in concentrated electrolyte solutions and in organic ion exchangers have been emphasized by a number of workers.[3-6] The hypothesis that concentrated electrolytes are useful models for organic ion exchangers at the same water content, provided the electrolyte has the same chemical structure as the repeating unit of the polymer, may be termed the "model compound concept." Several studies supporting this concept are the following.

(1) Comparisons[4,5a] of the free energies and enthalpies of ion-exchange reactions with thermodynamic data on solutions of model compounds show a close correspondence between their respective properties at high concentrations (*i.e.*, >3 *m*). The poor correspondence observed at low concentrations (*i.e.*, high water content) was attributed to the fact that the charged sites on the polymer are not separated isotropically on dilution as are the ions in an electrolyte solution.

(2) Nelson[5b] measured tracer diffusion coefficients of Br^- in samples of Dowex-1 (8% DVB), which were equilibrated with various aqueous LiCl solutions, and compared these results with diffusion in mixtures of aqueous LiCl and benzyltrimethylammonium chloride. The correspon-

dence was not quantitative, but the diffusion coefficients in the model electrolyte solution did parallel those in the anion exchanger.

(3) Recently Paterson and Gardner[3] have concluded that, when due account is taken of the tortuosity of a polystyrenesulfonate membrane, transport phenomena in the membrane become comparable to the corresponding transport properties in aqueous sodium chloride solutions.

The principal purpose of this research was to provide experimental data for a detailed analysis of the analogy between diffusion in an ion exchanger, in a linear polyelectrolyte solution, and in aqueous solutions of the model compound, sodium *p*-ethylbenzenesulfonate (NapEBS). Tracer diffusion coefficients for HTO, $^{36}Cl^-$, $^{24}Na^+$, $^{42}K^+$, $^{65}Zn^{2+}$, and $^{88}Y^{3+}$ were measured in aqueous NapEBS solutions, and for HTO, $^{36}Cl^-$, $^{24}Na^+$, and $^{65}Zn^{2+}$ in polystyrenesulfonate ion exchangers (Na form) of cross linking corresponding to nominal 1.7, 4, and 8% divinylbenzene (DVB) contents.

Tracer diffusion coefficients for Na^+ in aqueous solutions of the linear polyelectrolyte, sodium polystyrenesulfonate, are available,[7,8] hence, a comparison of Na^+ ion diffusion in three systems of the same "chemical structure" but of differing degrees of "polymerization" can be made. An examination of the model compound concept for trace diffusion of a neutral species (HTO), a coion ($^{36}Cl^-$), and counterions of single and multiple charge is made possible by our investigations.

II. Experimental Section

1. Aqueous Sodium p-Ethylbenzenesulfonate Solutions. Preparation of Materials. The synthesis and purification of NapEBS were conducted using the procedure described by Lindenbaum and Boyd.[4b] A value of 207.2 was obtained for the equivalent weight, compared with the theoretical value of 208.2. Solutions were prepared from weighed quantities of dried salt and triple-distilled water and were made slightly acid (pH 4–5) to repress hydrolysis of multivalent cationic tracer species. However, the acidity was sufficiently low for the measurements with tritium to reflect the diffusion of HTO and not T^+ ion. It may be estimated at pH 4 using the analysis described by Eisenberg and Kauzmann,[9] that an average water molecule (HTO) would undergo $\sim 5 \times 10^4$ translational "jumps" before dissociating. Thus, the diffusion mechanism involves HTO predominantly and not T^+.

The inorganic salts used were reagent grade chemicals. The potassium chloride was recrystallized once from water. Except for $^{24}Na^+$ and $^{42}K^+$, the radioactive isotopes were obtained from the Isotopes Division of the Oak Ridge National Laboratory, Oak Ridge, Tenn. The $^{24}Na^+$ and $^{42}K^+$ were prepared by thermal neutron irradiation of the appropriate reagent grade carbonate. The radiochemical purities of the γ emitting tracers were verified by checking their respective γ-ray spectra.

Diffusion Measurements. The diaphragm cell apparatus and the general procedures were the same as previously described.[10] The cells were periodically calibrated[11] by allowing 0.5 *N* KCl to diffuse into pure water. The precision of the calibration experiments was about ±0.1%.

The procedure used for measurements differed from the usual practice in that several diffusion coefficients were determined from a single experiment. For example, trace amounts of $^{24}Na^+$, $^{65}Zn^{2+}$, HTO, and $^{36}Cl^-$ were allowed to diffuse simultaneously in a diaphragm cell. The counting rate of each isotope was determined uniquely by taking advantage of the short half-life of $^{24}Na^+$ (15 hr) and the counting characteristics of the other isotopes. Standard techniques for liquid scintillation counting of doubly labeled samples (*i.e.*, HTO and $^{36}Cl^-$) were employed and the scintillation cocktail described by Bray[12] was used.

TABLE I: Tracer Diffusion Coefficients in 4.36 *m* Aqueous NaCl at 25° (Comparison with Literature Data)

Species	$10^5 D_i$ (this work)	Species	$10^5 D_i$ (lit.)
$^{24}Na^+$	0.934 [0.001][a]	$^{22}Na^+$	0.931 ± 0.005[13]
$^{36}Cl^-$	1.25_2 [0.007]	$^{36}Cl^-$	1.26_2 ± 0.006[13]
HTO	1.60_2 [0.01_3]	HTO	1.64 ± 0.06[14]
$^{65}Zn^{2+}$	0.687 [0.004]		

[a] Difference between duplicate measures with different diaphragm cells.

Diffusion coefficients, *D*, were calculated with the modified diaphragm cell equation[10]

$$D = (1/\beta t) \ln \left(\frac{1 + f C_u/C_l}{1 - C_u/C_l} \right) + (1/\beta t) \ln [(1 - \alpha_2)/(1 - \alpha_1)] \quad (1)$$

where β is the cell constant (evaluated by calibration with potassium chloride) and t is the time of diffusion. The quantity f is given by

$$f = \frac{V^u + V_D/2}{V^l + V_D/2} \quad (2)$$

where V^u and V^l are volumes of the upper and lower cell compartments, respectively, (~50 ml) and V_D is the volume of the frit. The terms C_u and C_l represent concentrations (or specific counting rates) of solutions from the upper and lower compartments, respectively. The first term on the right-hand side of eq 1 is the conventional expression[11] for the evaluation of diffusion data from the diaphragm cell measurements. The second term is a theoretical correction[10] to the conventional expression, which is significant when the product of the prediffusion time and the diffusion coefficient is small. This term reflects the lack of "filling" the frit to a linear concentration profile. The original paper[10] should be consulted for a definition of the quantities α_1 and α_2 and for the procedure to be used in evaluating this term. The contribution of the "correction" term to *D* was usually ~0.1%, except for diffusion of multivalent ions in the 3.0 and 3.25 *M* solutions. This term was largest for the diffusion of $^{88}Y^{3+}$ in 3.24 *M* NapEBS where it represented 8.5% of *D*.

Tracer diffusion coefficients of $^{24}Na^+$, $^{65}Zn^{2+}$, $^{36}Cl^-$, and HTO were determined in aqueous 4.36 *m* NaCl at 25° as a check on the apparatus and procedure. These data are compared with literature values[13,14] in Table I.

Strictly speaking, diffusion data for $^{24}Na^+$ ion may not be compared with the corresponding data for $^{22}Na^+$. However, measurements of the $D(^{22}Na^+)/D(^{24}Na^+)$ ratio in this laboratory[15] suggest that isotope effects in tracer diffusion are negligibly small.

2. Ion-Exchanger Studies. Preparation of Materials. The cross-linked sulfonated polystyrene ion exchangers were custom synthesized by A. H. Greer of the Ionac Chemical Company, Birmingham, N. J. They were of nominal 1.7, 4, and 8 wt % divinylbenzene (DVB) content, and were supplied as spheres of uniform diameter of *ca.* 1 mm. The preparations were wet screened to give narrow particle

size distribution and conditioned following Helfferich.[16] A significant percentage of defective beads (*i.e.*, cracked or broken, nonspherical) was present. These were removed by rolling the dried preparations on a flat surface to remove the defective beads. A flat metal plate, oriented at a slight angle, and subjected to a periodic vibration acted to dislodge the defective beads leaving only the spherical beads.

The sodium forms of the exchangers were equilibrated with a mixed electrolyte solution (hereafter denoted "external solution") of composition 0.200 *N* $NaNO_3$, 0.0200 *N* NaCl, and 0.0020 *N* $ZnCl_2$ (pH 5). The exchanger was placed in a column and a large excess of solution was passed through the bed. The equilibration was taken to be complete when the concentration of Zn^{2+} (determined by EDTA titration) in solution did not change on passing through the column.

Capacity, Water Content, and Size Determinations. Conventional procedures[17] for capacity determination of strong acid ion exchangers were employed. The water contents were determined as follows. A sample which had been equilibrated with the external solution was blotted dry on filter paper until microscopic examination revealed no visible surface moisture. The water content was estimated from the weight loss on drying a portion of the sample in a vacuum oven at 110°. Water contents obtained in this way are not accurate to better than 1% because of undetected surface moisture or partial drying.

The average bead diameter for a given sample of exchanger was determined by microscopic examination of a large number (50–100) of beads in contact with the external solution.

Diffusion Procedure. The limited bath technique[18] was used for the diffusion measurements. The only significant change in this research was that $^{24}Na^+$ and $^{65}Zn^{2+}$ were allowed to diffuse together, and $^{36}Cl^-$ and HTO were allowed to diffuse together.

Diffusion coefficients were evaluated from the measurements of the time dependence of the fractional attainment of equilibrium, $F(t)$, with a computer and the equation

$$F(t) = 1 - (2/3w)\sum_{1}^{\infty} e^{-\lambda_n^2\tau}/[1 + \lambda_n^2/9w(1 + w)] \quad (3)$$

where a is the average radius of the spheres and w is the ratio of the total quantity of isotope in the spheres to that in the ambient aqueous solution

$$w = \bar{C}\bar{V}/CV \quad (4)$$

In eq 4 $\bar{C}$ and C are the concentrations of the diffusing species ($^{65}Zn^{2+}$, $^{24}Na^+$, etc) in the ion exchanger of volume $\bar{V}$ and in the solution of volume V, respectively. The λ_n's in eq 3 are the roots of the transcendental equation

$$\lambda_n \cot \lambda_n = 1 + \lambda_n^2/3w \quad (5)$$

and the dimensionless variable, τ, is related to the time, t, and a and the particle diffusion coefficient, D_p, by

$$\tau = D_p t/a^2 \quad (6)$$

With HTO and $^{36}Cl^-$ diffusion, an accurate measurement of the sampling time presented a problem because of the short half-time for isotopic exchange. Accordingly, several evaluations of a diffusion coefficient were carried out to arrive at an average value. The use of eq 3 assumes particle diffusion control, and it is significant to note that the calculated diffusion coefficients showed no systematic trend with time which might suggest partial film diffusion control. Moreover, application of the usual criteria,[19] assuming plausible values for the film thickness, indicates that partial film diffusion control should not present a problem in the experiments with HTO and $^{36}Cl^-$.

TABLE II: An Illustration of the Correspondence between the Theory for Coupled Film–Particle Diffusion Control (Eq 7) and Experimental Data[a]

	Na^+ diffusion		Zn^{2+} diffusion	
Time, sec	$F(t)$ expt	$F(t)$ calcd	$F(t)$ expt	$F(t)$ calcd
30	0.35_3	0.354	0.15_7	0.148
60	0.49_6	0.495	0.25_8	0.256
90	0.59_5	0.589	0.33_5	0.342
130	0.66_9	0.678	0.43_4	0.434
500	0.96_1	0.956	0.80_3	0.801

[a] 8% ion exchanger, a = 0.0513 cm. For Na^+ diffusion, $\alpha = 5.3$, $\xi = 33.5 \pm 9.0$, $10^6 D_p = 1.32 \pm 0.08$. For Zn^{2+} diffusion, $\alpha = 0.44$, $\xi = 5.70 \pm 0.80$, $10^6 D_p = 0.31_3 \pm 0.030$. Uncertainties given are standard deviations of the coefficients.

The experiments with $^{65}Zn^{2+}$, and, to a lesser extent, those with $^{24}Na^+$ clearly involved partial film diffusion control. Partial film diffusion control might have been expected[19] because the ratio $C/\bar{C}$ was small. Moreover, assuming complete particle diffusion control resulted in diffusion coefficients that systematically increased with time. Thus, it was necessary to use a model which includes both film and particle diffusion mechanisms.

It has been shown[20] for porous spheres in a limited bath that when both film diffusion and particle diffusion mechanisms are operative, the fractional attainment of equilibrium, $F(t)$, is given by

$$F(t) = 1 - \sum_{n=1}^{\infty} \frac{6\xi^2(1 + \alpha)e^{-g_n^2\tau}}{(9/\alpha + \alpha g_n^2 + 9)\xi^2 - (6 + \alpha)g_n^2\xi + \alpha g_n^4} \quad (7)$$

where g_n are the nonzero roots of

$$\frac{\tan g_n}{g_n} = \frac{3\xi - \alpha g_n^2}{(\xi - 1)\alpha g_n^2 + 3\xi} \quad (8)$$

with $\alpha = w^{-1}$ and $\xi = (a/\delta)(D_f/D_p)(C/\bar{C})$, where δ is the film thickness in cm and D_f is the diffusion coefficient in the film. It is easily shown that eq 7 and 8 reduce to eq 3 and 5 for pure particle diffusion (*i.e.*, $\xi \to \infty$). Further, for the case $\alpha \to \infty$, eq 7–8 will reduce to the equations of Grossman and Adamson[21] for partial film–partial particle controlled diffusion in spherical particles in an *infinite bath*.

The $F(t)$ *vs.* t curve for a given experiment is a function of but two parameters, D_p and ξ, because $\alpha = w^{-1}$ is known from experiment. A fit of the $F(t)$ data to eq 7 using a non-linear "least-squares" procedure will therefore give D_p and ξ.[22] A representative example of the ability of eq 7 to reproduce the experimental $F(t)$ data is afforded by Table II. Note that the data are fitted to well within the experimental error. Assuming the plausible[23] values of 1.2×10^{-5} and 0.70×10^{-5} for the liquid film diffusion coefficients, D_f, of $^{24}Na^+$ and $^{65}Zn^{2+}$, respectively, the film thickness, δ, is found to be *ca.* 10^{-3} cm which is reasonable physically.

TABLE III: Tracer Diffusion Coefficients in Aqueous Sodium *p*-Ethylbenzenesulfonate (NapEBS) at 25°

Concn of NapEBS		$10^5 D$, cm²/sec						
m	*c*	HTO	$^{36}Cl^-$	$^{24}Na^+$	$^{42}K^+$	$^{65}Zn^{2+}$	$^{45}Ca^{2+}$	$^{88}Y^{3+}$
0	0	2.26 ± 0.08[a]	(2.032)[b]	(1.333)	(1.956)	(0.70_2)	(0.792)	(0.57_4)
0.0998	0.0982	2.19 ± 0.026[c]	1.868 ± 0.005	1.258 ± 0.003	1.853 ± 0.006	0.694 ± 0.007	0.737 ± 0.006	0.58_9 ± 0.008
0.2991	0.2868	2.06 ± 0.003	1.720 ± 0.014	1.168 ± 0.003		0.636 ± 0.008		
0.997	0.8756	1.68 ± 0.010	1.336 ± 0.000	0.920 ± 0.006	1.29 ± 0.015	0.473 ± 0.003	0.517 ± 0.000	0.385 ± 0.003
2.991	2.110	1.085 ± 0.004	0.746 ± 0.006	0.537 ± 0.003		0.234 ± 0.002		
3.236	2.227	1.03	0.72	0.50 ± 0.020		0.21_8	0.23_0	0.15_2

[a] Extrapolated by means of the least-squares equation, eq 9. The uncertainty given is the standard deviation of the coefficient of the zero-order term. [b] All values in parentheses were calculated from the limiting ionic conductances.[24] [c] The data reported with an uncertainty figure are the mean of two independent measurements. The uncertainty given is the difference between duplicate measurements.

TABLE IV: Physical Data for Ion Exchangers in Equilibrium with an Aqueous Solution of Composition 0.200 *N* $NaNO_3$, 0.020 *N* NaCl, 0.002 *N* $ZnCl_2$

Nominal cross-linking % DVB	Capacity Na form (mequiv/g dry)	Mol % Zn	Wt % H_2O (wet)	Av diameter in mm (std dev)[a]	% defective beads[b]
1.7	5.12	1.5	$73._8$	(No. 1) 1.085 (0.079)	3
				(No. 2) 1.061 (0.053)	4
4	4.73	4.0	$61._7$	0.952 (0.058)	3
8	4.82	5.1	$44._2$	1.025 (0.032)	<2

[a] Two independently sized samples were used for the 1.7% DVB resin. The number of beads measured was 50 for the 8% DVB resin and 100 for the other samples. [b] Cracked, broken, or nonspherical estimated by microscopic examination.

TABLE V: Tracer Diffusion Coefficients at 25° in Sulfonated Polystyrene Ion Exchangers in Equilibrium with Solutions of the Composition 0.200 *N* $NaNO_3$, 0.02 *N* NaCl, and 0.002 *N* $ZnCl_2$

Crosslinking % DVB	N_W, equiv/kg of H_2O	$10^5 D_p$, cm²/sec[a]			
		HTO	$^{36}Cl^-$	$^{24}Na^+$	$^{65}Zn^{2+}$
1.7	1.8	1.17 ± 0.04	0.67 ± 0.02	0.49_2 ± 0.01_3	0.13_1 ± 0.01_4
4	2.9	0.96 ± 0.04	0.70 ± 0.03	0.31_9 ± 0.01_8	0.09_5 ± 0.00_8
8	6.1	0.41_9 ± 0.005	0.26 ± 0.01	0.14_1 ± 0.00_4	0.030_1 ± 0.001_2

[a] Uncertainties given for HTO and $^{36}Cl^-$ data are the standard deviations of the mean σ_m, defined by: $\sigma_m^2 = \sum_{i=1}^{n}(D_i - \bar{D})^2/n(n-1)$, where D_i is the diffusion coefficient for the *i*th determination and $\bar{D}$ is the mean diffusion coefficient for *n* measurements. The values of *n* ranged from 15 to 29. Uncertainties given for $^{24}Na^+$ and $^{65}Zn^{2+}$ data were estimated from the standard deviations of the coefficients and the agreement between duplicate runs.

III. Results

1. Aqueous Sodium p-Ethylbenzenesulfonate. The experimental data for aqueous sodium *p*-ethylbenzenesulfonate solutions are summarized in Table III. All measurements were made at 25.00 ± 0.01°. Crude pycnometric density measurements were made to convert the experimental molalities, *m*, to molar concentrations *c*. Diffusion coefficients at infinite dilution were calculated from limiting ionic conductance data.[24]

The tracer diffusion coefficients for HTO were fit to the least-squares equation

$$10^5 D_{HTO} = 2.26 - 0.73_6 c + 0.08_3 c^2 \qquad (9)$$

with a standard deviation of ±0.006. Note that the extrapolated value of $10^5 D_{HTO}$ in pure water of 2.26 is in excellent agreement with the value of 2.25 found by Devell[14] for HDO and HTO and with the value of 2.23_6 for HTO given by Mills.[25]

2. Ion Exchangers. Physical property data for the ion exchangers are summarized in Table IV. The data refer to the exchanger in equilibrium at 25 ± 2° with the external solution used in diffusion measurements. The third column gives the mole per cent of zinc in the ion exchanger. Note that the exchangers were predominantly in the sodium form. Ionic self-diffusion does not appear to be particularly sensitive to the Zn^{2+} ion concentration in a predominantly sodium-form resin,[26] hence, the diffusion data determined in this research are essentially equivalent to data for the Na form.

Tracer diffusion coefficients for HTO, $^{36}Cl^-$, $^{24}Na^+$, and $^{65}Zn^{2+}$ in the ion exchangers are given in Table V. The error limits for the HTO and $^{36}Cl^-$ data represent the standard deviation of the mean; those for the $^{24}Na^+$ and $^{65}Zn^{2+}$ data were estimated from the standard deviations in the diffusion coefficients, as given by the computer fit of eq 7 to the data, and the reproducibility between duplicate runs. Note that $D(Cl^-)$ is essentially the same for the 1.7 and 4% DVB exchangers.

The HTO diffusion coefficients in Table V are in close agreement with the $H_2{}^{18}O$ diffusion data of Boyd and Soldano[18] in hydrogen-form polystyrenesulfonate ion exchangers. However, the Na^+ ion diffusion coefficients determined in this research are higher by about a factor of 2 than reported by Boyd and Soldano. This apparent disagreement is probably not significant since the earlier Na^+ diffusion study employed resin samples that were subject to a systematic error in DVB contents of *ca.* 33%. The $H_2{}^{18}O$ and $^{82}Br^-$ data reported by Boyd and Soldano were free of this error.

IV. Discussion

1. Diffusion in Aqueous Sodium p-Ethylbenzenesulfonate Solutions. NapEBS as a Structure Maker and HTO Diffusion. It will be noted in Table III that D_{HTO} decreases rapidly as the concentration of NapEBS increases. At 3 *m*, for example, the diminution in D_{HTO} is more than twice that observed with a typical inorganic 1–1 electrolyte such as sodium chloride. From this observation, one might be tempted to conclude that the $pEBS^-$ ion is a strong "structure maker" (*i.e.*, increases the hydrogen bonding of water). The essential observation, however, is simply that the translational freedom of the water molecule is greatly restricted. Such an effect would also be observed in a solution of large noninteracting particles in a structureless fluid. Large particles effectively block part of the area for diffusion of HTO, and therefore decrease its mobility. This is the so-called "obstruction effect," and its magnitude may be estimated from theory. The diffusion coefficient, D, of a small species in a medium containing a volume fraction, ϕ_2, of immobile obstructions has been shown by Prager[27] to be given by

$$D/D^0 = (1 - \phi_2) \times \frac{\phi_2 + (1 - \phi_2)\ln(1 - \phi_2)}{2[\phi_2 + (1 - \phi_2)\ln(1 - \phi_2)] - (1/2)(1 - \phi_2)[\ln(1 - \phi_2)]^2} \quad (10)$$

where D^0 is the diffusion coefficient of the mobile species for $\phi_2 = 0$. When $\phi_2 \ll 1$, eq 10 reduces to

$$D/D^0 = 1 - 1.333\phi_2 \quad (11)$$

Numerical calculations show that for $\phi_2 < 0.5$, the difference between eq 10 and eq 11 is quite small. A hydrodynamic analysis of the effect for spherical obstructions given by Wang[28] yields

$$D/D^0 = 1 - 1.5\phi_2 \quad (12)$$

Considering the difference in approach to the problem, the results of the Wang analysis are in surprisingly good agreement with the Prager analysis. Several other approaches[29,30] yield results which support the qualitative notion that an "obstruction" will decrease the value of D. Moreover, the treatment of Weissberg[31] for spherical obstructions yields an expression which reduces to eq 12 as $\phi_2 \rightarrow 0$, and at higher ϕ_2, Weissberg's equation is in reasonable agreement with eq 10.

Diffusion coefficients of water in aqueous NapEBS and diffusion coefficients of water in aqueous solutions of other large organic solutes are compared with eq 10 in Figure 1. The volume fraction of a large organic species may be evaluated from the molar volume of the species, V_m, in ml/mole, and the molar concentration c, using $\phi_2 = V_m c/1000$. In Figure 1, it has been assumed that the molar volume of the obstruction may be approximated by its partial molal volume at infinite dilution.[32] Except for NapEBS, the data used to construct Figure 1 were taken from the literature.[33-38] Densities for aqueous tetra-*n*-butylammonium chloride (Bu_4NCl) used to calculate molar concentrations from molalities were estimated from the apparent molal volume data for Bu_4NBr[38] assuming the difference in apparent molal volume between the chloride and bromide salts is independent of concentration. The net effect of a chloride ion on the mobility of water is very small.[33] Thus, the effect of Bu_4NCl on the mobility of water is essentially due to the Bu_4N^+ ion.

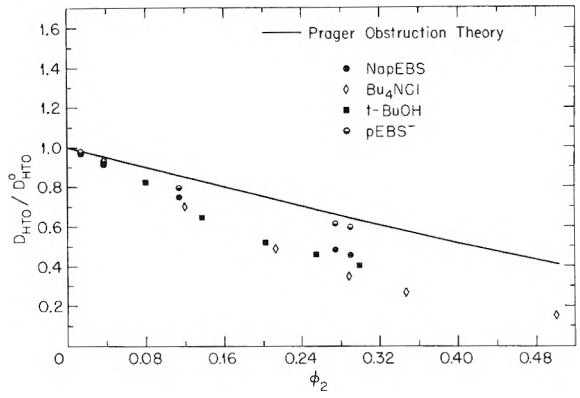

Figure 1. Comparison of the tracer diffusion coefficients of water at 25° in aqueous sodium *p*-ethylbenzenesulfonate and related systems with the obstruction theory, eq 10.

It will be noted in Figure 1 that the mobility of water is decreased more than the theory would predict. For NapEBS (the solid circles), most of the deviation is caused by the "structure making" Na^+ ion. If the effects of the Na^+ ion and the $pEBS^-$ ion on the mobility of water are separable, one may write

$$D/D^0 = 1 - (\delta_{Na^+}) - (\delta_{pEBS^-}) \quad (13)$$

where $\delta(Na^+)$ and $\delta(pEBS^-)$ represent the effects of the Na^+ ion and the $pEBS^-$ ion, respectively, on the mobility of water. Since the Cl^- ion has little effect on the mobility of water,[33] δ_{Cl^-} may be neglected and δ_{pEBS^-} may be evaluated from diffusion data on aqueous NapEBS and NaCl solutions according to the relationship

$$\left(\frac{D}{D^0}\right)_{NapEBS} - \left(\frac{D}{D^0} - 1\right)_{NaCl} = 1 - \delta_{pEBS^-} \quad (14)$$

The left-hand side of eq 14 thus represents the ratio D/D^0 in a hypothetical solution of $pEBS^-$ ions. If the $pEBS^-$ ion has little net effect on the hydrogen bonding in water, the data generated by eq 14 (*i.e.*, the half-filled circles) should be in good agreement with the obstruction theory. Within the uncertainties inherent in this analysis, Figure 1 shows there is an agreement with the theory, suggesting that the $pEBS^-$ ion has little net effect on the structure of water. Due to the approximate nature of the preceding analysis, the presence of a *small* degree of "structure making" (or "structure breaking") by $pEBS^-$ ion cannot be denied. However, the ability of $pEBS^-$ to promote "structure" in water is clearly much less than for Bu_4N^+ ion or *tert*-butyl alcohol (*t*-BuOH), and most, if not all, of the decrease in water mobility may be attributed to the obstruction effect and the "structure-making" Na^+ ion.

Ionic Diffusion. The general effect of NapEBS (Table III) is to decrease the mobility of an ionic species without changing the order of mobilities observed in pure water. A closer examination of the data reveals specific effects. For the purpose of illustrating these effects, values of the quantity $[D_i/D_i^0 - D_{HTO}/D_{HTO}^0]$ for the various ionic species are compared in Table VI at selected concentrations of NapEBS. The notation D_i^0 refers to the tracer diffusion coefficient of ionic species i in pure water. The obstruction effect, as given by either eq 10 or eq 12, will cancel when the difference $[D_i/D_i^0 - D_{HTO}/D_{HTO}^0]$ is formed. A value near zero will indicate that the interaction of ion i with the aqueous NapEBS environment is essentially the same as the corresponding interaction for HTO. A large negative value will be taken to indicate a

TABLE VI: Values of $[D_i/D_i^0 - D_{HTO}/D_{HTO}^0]$ in Aqueous NapEBS

m	$^{24}Na^+$	$^{42}K^+$	$^{36}Cl^-$	$^{65}Zn^{2+}$	$^{45}Ca^{2+}$	$^{88}Y^{3+}$
0.10	-0.025	-0.025	-0.050	$+0.020$	-0.039	$+0.057$
1.0	-0.053	-0.083	-0.069	-0.069	-0.090	-0.072
3.0	-0.078		-0.108	-0.146	-0.163	-0.180

strong interaction (compared with HTO) between the ion i and the environment.

From Table VI, it will be noted that *except for* $^{65}Zn^{2+}$ and $^{88}Y^{3+}$ at *0.10 m*, values of $[D_i/D_i^0 - D_{HTO}/D_{HTO}^0]$ are negative and increase in magnitude as the concentration of NapEBS increases. The positive values of $[D_i/D_i^0 - D_{HTO}/D_{HTO}^0]$ for $^{65}Zn^{2+}$ and $^{88}Y^{3+}$ in 0.10 *M* NapEBS are believed to be real and not an experimental artifact. Thus, it appears that at low concentrations some mechanism exists which increases the mobility of a highly hydrated ion. Partial dehydration of a highly hydrated ion by $pEBS^-$ is one possible mechanism. Tracer diffusion data in the literature[39,40] suggest that the behavior of $^{65}Zn^{2+}$ and $^{88}Y^{3+}$ in aqueous NapEBS at *ca.* 0.1 *m* is typical of the behavior of multicharged ions in systems where ion-pair formation is expected. However, the effects observed in NapEBS are much less pronounced than the effects in a strongly associated system. For example, the tracer diffusion coefficient of Zn^{2+} ion in aqueous KCl increases from 0.7×10^{-5} to 0.97×10^{-5} over the concentration range 0–3 *M*, presumably because of ion-pair formation.

The data in Table VI also indicate that the "coion," $^{36}Cl^-$, interacts more strongly with the aqueous NapEBS environment than does the "counterion" $^{24}Na^+$. Although not conclusive, this result may be taken as evidence against a high degree of ion-pair formation between Na^+ and $pEBS^-$. However, in a polystyrenesulfonate type ion exchanger the counterion interacts most strongly with the polyanion.[18] Thus, in this respect, aqueous NapEBS is not even a qualitative model for the ion exchanger. A comparison between diffusion in aqueous NapEBS solutions and diffusion in an ion exchanger will be elaborated in the next section.

2. Comparison of NapEBS Solutions with Polyelectrolyte Solutions and Cross-Linked Gels. Tracer diffusion coefficients of Na^+ ion are compared in Figure 2 in a "typical" inorganic electrolyte (NaCl), in the model compound (NapEBS) solution, in the polyelectrolyte, sodium polystyrene sulfonate (NaPSS) solution, and in cross-linked polystyrenesulfonate ion exchangers. Although NapEBS appears to be a far better model for the ion exchanger than is a concentrated NaCl solution,[41] the mobility of Na^+ in the polyelectrolyte solutions and gels is significantly lower than in NapEBS. Moreover, the NapEBS and ion-exchanger curves do not appear to be approaching one another at high concentrations. As expected, the linear polyelectrolyte (NaPSS) and cross-linked polyelectrolyte (ion-exchanger) data are in close agreement. Cross linking in polyelectrolyte systems appears to have little effect on the diffusion of a small species such as Na^+ ion.

The diffusion coefficient of Na^+ ion in aqueous NaPSS[8] is about 0.51×10^{-5} cm²/sec between 0.01 and 0.05 equiv/kg of H_2O, and as shown in Figure 2, goes through a maximum at *ca.* 0.5 *N*. Assuming an infinite line charge

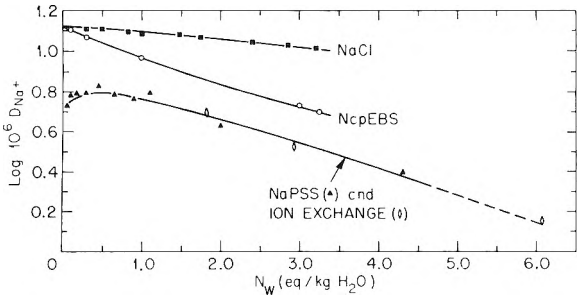

Figure 2. Comparison of log $10^6 D(Na^+)$ in selected aqueous electrolyte systems at 25°.

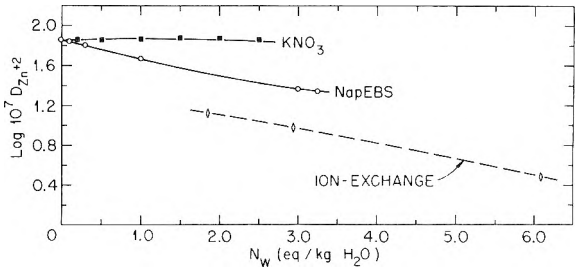

Figure 3. Comparison of log $10^7 D(Zn^{2+})$ in selected aqueous electrolyte systems at 25°.

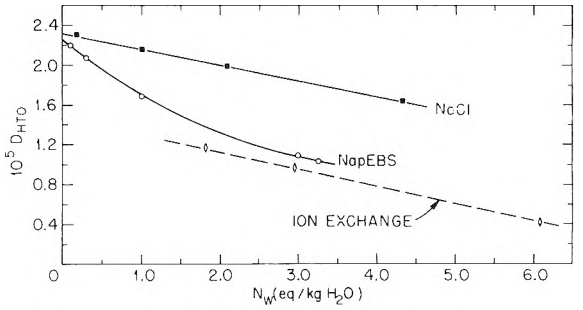

Figure 4. Comparison of $10^5 D$(HTO) in selected aqueous electrolyte systems at 25°.

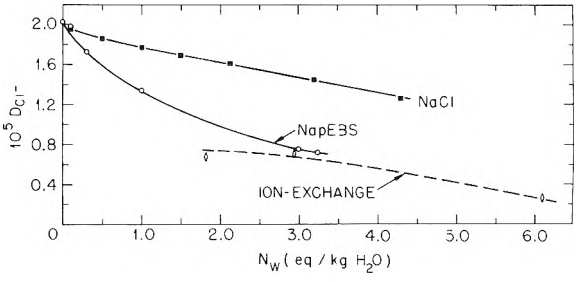

Figure 5. Comparison of $10^5 D(Cl^-)$ in selected aqueous electrolyte systems at 25°.

as an electrostatic model for a polyelectrolyte, Manning[42] has developed a theory which predicts that the diffusion coefficient for a counterion will be independent of the concentration of the polyelectrolyte. An important feature of this theory is the demonstration of partial counterion condensation when the linear charge density is high. For NaPSS, the Manning theory gives $D(Na^+) = 0.46 \times 10^{-5}$, in fair agreement with the data between 0.01 and 0.05 *N*, however, above 0.05 *N*, $D(Na^+)$ depends on the concentration.

Tracer diffusion coefficients for Zn^{2+} ion are compared in Figure 3 in a "typical" inorganic electrolyte solution,

aqueous KNO_3,[40] in aqueous NapEBS, and in cross-linked sodium polystyrenesulfonate. As with Na^+ ion, the Zn^{2+} ion mobility in a polyelectrolyte system is much less than the corresponding mobility in aqueous NapEBS solutions. Moreover, there is no evidence to suggest that better agreement would be observed at higher concentrations. The difference in counterion diffusion coefficients between the ion exchanger and the model compound solution is greater for Zn^{2+} than for Na^+ ion diffusion.

The diffusion coefficients of HTO and $^{36}Cl^-$ in aqueous NapEBS and NaCl[13,14] solutions and in cross-linked sodium polystyrenesulfonate are compared in Figures 4 and 5. As expected, concentrated NapEBS solutions are far better models for the ion exchanger than are sodium chloride solutions. Note that diffusion of water (HTO) and coion ($^{36}Cl^-$) proceeds slightly faster in concentrated NapEBS solutions than in the ion exchanger at the same concentration of sulfonate groups. However, the differences between the NapEBS and the ion-exchanger data are fairly small, particularly for Cl^- ion diffusion at *ca.* 3.0 equiv/kg of H_2O. The small, but presumably real, difference in HTO mobility between NapEBS and ion exchanger is consistent qualitatively with the expected[43,44] stronger electrostriction of the solvent in a polyelectrolyte.

On the basis of our data, it is concluded that the model compound hypothesis is valid at concentrations greater than about 3 equiv/kg of H_2O for the diffusion of *neutral species* or *coions*, but, for counterion diffusion, the hypothesis is not valid. This conclusion is consistent with Nelson's data[5] in that Nelson observed significantly lower counterion diffusion coefficients in the ion exchangers than in the corresponding model electrolyte solutions. Moreover, our conclusions agree with those of Paterson and Gardner[3] *only* with respect to *water* and *coion* diffusion.

The reduced mobility of counterions in the polyelectrolyte systems as compared with the NapEBS solutions probably is a consequence of their partial condensation on a polyelectrolyte chain. However, this interpretation does not imply necessarily that there is a significant difference between the polyelectrolyte and sodium *p*-ethylbenzenesulfonate in the specific interaction of a "counterion" with the structurally bound anion in concentrated solutions. The mobility of a cation associated with the $pEBS^-$ anion in an aqueous solution is expected to be greater than if it were associated with a large polyanion, even if the energy interaction were the same in both cases.

Acknowledgments. The assistance of H. L. Hosopple in the preparation of NapEBS, of L. D. Hulett in the ion-exchanger bead size measurements, and of R. Funderlich in the computer programming is gratefully acknowledged.

References and Notes

(1) Research sponsored, in part, by the U. S. Atomic Energy Commission under contract with the Union Carbide Corporation.
(2) Guest scientist at Oak Ridge National Laboratory. Present address, Eli Lilly and Company, Indianapolis, Ind. 46206.
(3) R. Paterson and C. R. Gardner, *J. Chem. Soc. A*, 2254 (1971). See also H. Ferguson, C. Gardner, and R. Paterson, *J. Chem. Soc., Faraday Trans. 1*, **68**, 2021 (1972); C. Gardner and R. Paterson, *ibid.*, 2030 (1972).
(4) (a) G. E. Boyd, J. W. Chase, and F. Vaslow, *J. Phys. Chem.*, **71**, 573 (1967); (b) S. Lindenbaum and G. E. Boyd, *ibid.*, **71**, 581 (1967).
(5) (a) G. E. Boyd, F. Vaslow, A. Schwarz, and J. W. Chase, *J. Phys. Chem.*, **71**, 3879 (1967); (b) F. Nelson, *J. Polym. Sci.*, **40**, 563 (1959).
(6) W. C. Bauman and J. Eichorn, *J. Amer. Chem. Soc.*, 69, 2830 (1947).
(7) E. O. Timermann, *Z. Phys. Chem. (Frankfurt am Main)*, 70, 195 (1970).
(8) R. Fernandez Prini and A. E. Lagos, *J. Polym. Sci. A*, **2**, 2917 (1964).
(9) D. Eisenberg and W. Kauzmann, "The Structure and Properties of Water," Oxford University Press, New York, N. Y., 1969, pp 220–225.
(10) M. J. Pikal, *J. Phys. Chem.*, **74**, 4165 (1970).
(11) See, for example, R. Mills and L. A. Woolf, "The Diaphragm Cell," Australian National University Press, Canberra, Australia, 1968.
(12) G. A. Bray, *Anal. Biochem.*, **1**, 279 (1960).
(13) R. Mills, *Rev. Pure Appl. Chem.*, **11**, 78 (1961).
(14) L. Devell, *Acta Chem. Scand.*, **16**, 2177 (1962).
(15) M. J. Pikal, *J. Phys. Chem.*, **76**, 3038 (1972). $[D(^{22}Na^+)/D(^{24}Na^+)$ was found to be 1.002 ± 0.001 in 0.1 *m* aqueous NaCl and 1.004 ± 0.003 in aqueous 10 *m* LiBr.
(16) F. Helfferich, "Ion Exchange," McGraw-Hill, New York, N. Y., 1962, p 230.
(17) See ref 16, p 91, second paragraph.
(18) G. E. Boyd and B. A. Soldano, *J. Amer. Chem. Soc.*, **75**, 6091, 6105 (1953).
(19) See ref 16, p 255.
(20) Ting-Chia Huang and Ku-Yen Li, *Ind. Eng. Chem., Fundam.*, **12**, 50 (1973).
(21) J. M. Grossman and A. W. Adamson, *J. Phys. Chem.*, 56, 97 (1952). It should be noted that Helfferich's quotation of these results (ref 16, eq 6-26) is incorrect. The left-hand side of Helfferich's eq 6-26 should be $1 - U(t)$.
(22) Initial "guesses" for the values of D_p and ξ must be made to initiate calculations. Values of C may be estimated from density and equivalent water content data on the exchanger. A crude value for ξ can be found assuming the density to be unity.
(23) See, for example, Table III.
(24) (a) R. A. Robinson and R. H. Stokes, "Electrolyte Solutions," 2nd ed, Academic Press, New York, N. Y., 1959; (b) F. H. Spedding and S. Jaffe, *J. Amer. Chem. Soc.*, **76**, 882 (1954).
(25) R. Mills, *J. Phys. Chem.*, **77**, 685 (1973).
(26) B. A. Soldano and G. E. Boyd, *J. Amer. Chem. Soc.*, **75**, 6107 (1953).
(27) S. Prager, *J. Chem. Phys.*, **33**, 122 (1960).
(28) J. H. Wang, *J. Amer. Chem. Soc.*, **76**, 4755 (1954).
(29) Robinson and Stokes (ref 24) argue that the coefficient of the ϕ_2 term should be 0.5. Their arguments are based upon an analogy with the effect of obstructions on the specific conductance and the dielectric constant of a fluid. This analogy may not be quantitative.
(30) The concept of "tortuosity" (see ref 16, p 302, and ref 3), although not identical with the "obstruction" concept, also predicts a decrease in D as ϕ_2 increases.
(31) H. A. Weissberg, *J. Appl. Phys.*, **34**, 2636 (1963).
(32) While this procedure is certainly not exact because of the "structural" properties of water, other procedures for estimating V_m yield similar results. For example, the molar volume of *tert*-butyl alcohol in the pure liquid is 95 ml/mol, which is not greatly different than the value of 87 ml/mol used here for its molar volume in water.
(33) D. W. McCall and D. C. Douglass, *J. Phys. Chem.*, 69, 2001 (1965).
(34) E. V. Goldammer and H. G. Hertz, *J. Phys. Chem.*, **74**, 3734 (1970).
(35) T. L. Broadwater and R. L. Kay, *J. Phys. Chem.*, **74**, 3802 (1970).
(36) H. G. Hertz, B. Lindman, and V. Siepe, *Ber. Bunsenges. Phys. Chem.*, **73**, 542 (1969).
(37) F. Millero in "Water and Aqueous Solutions," R. A. Horne, Ed., Wiley-Interscience, New York, N. Y., 1971, Chapter 15.
(38) W. Y. Wen and S. Saito, *J. Phys. Chem.*, **68**, 2639 (1964).
(39) J. H. Wang, *J. Amer. Chem. Soc.*, **75**, 1769 (1953).
(40) J. H. Wang, *J. Amer. Chem. Soc.*, **76**, 1528 (1954).
(41) It should be noted that NapEBS is a better model for an ion exchanger than is NaCl largely because the obstruction effect present in ion exchangers is well represented by NapEES but not by NaCl.
(42) G. S. Manning, *J. Chem. Phys.*, **51**, 934 (1969).
(43) B. E. Conway, J. E. Desnoyers, and A. C. Smith, *Trans. Roy. Soc. (London)*, **256**, 389 (1964).
(44) J. Lawrence and B. E. Conway, *J. Phys. Chem.*, **75**, 2353, 2362 (1971).

Interaction of a Polypeptidic Nematic Meso Phase with Acidic Molecules

Pierre Laszlo,* Agnès Paris,

Institut de Chimie, Université de Liège au Sart-Tilman, par 4000 Liège 1, Belgium

and Eve Marchal

Centre de Recherches sur les Macromolécules, C.N.R.S., Strasbourg, France *(Received June 11, 1973)*

Orientation of the synthetic PBLG polypeptide in a strong magnetic field is investigated as a function of added acid, $CH_2ClCOOH$ or CF_3COOH. The CH_2Cl_2 solvent molecules serve as probes of the local order. The chloroacetic acid molecules are found to self-associate more strongly than they bind to the polymer. Trifluoroacetic acid complexes the PBLG molecules: even at concentrations well below the helix–random coil transition, the rigidity of the macromolecules is diminished, and rapidly diffusing disordered segments are generated.

The chiral polypeptide, poly(γ-benzyl-L-glutamate) [PBLG], exists as the α helix in solvents such as methylene chloride, chloroform, trichloroethane, or dioxane.[1] While concentrated solutions are cholesteric, application of a strong magnetic field removes the cholesteric twist and produces a nematic mesophase.[2,3] At equilibrium, the long axes of the rodlike[4] PBLG molecules are lined up within ±20° of the direction of the external field.[5] This ordering phenomenon can be monitored by the dipolar splittings in the nuclear magnetic resonance spectrum of *solvent* molecules, such as methylene chloride.[2,3,5]

On the other hand, the helix–random coil transition of PBLG can be brought about by increasing the acid content of a binary solvent mixture. This rather sharp transition has been studied by a variety of methods.[6,7] It depends slightly on the concentration, molecular weight, and polydispersity of the polymer. It will occur between *ca.* 9 and 20% CF_3COOH by volume in the $CHCl_3$–CF_3COOH and CH_2Cl_2–CF_3COOH systems.[6,7] It was of interest to confront these two phenomena. This paper investigates the magnetic field ordering of PBLG molecules as a function of solvent composition in the following binary mixtures: methylene chloride–chloroacetic acid and methylene chloride–trifluoroacetic acid.

Experimental Section

The PBLG samples were prepared according to Blout and Karlson[8] with dioxane as the solvent and sodium methoxide as the initiator. The monomer concentration was kept below 3%, and the ratio of the *N*-carboxy anhydride of the amino acid to the initiator was chosen as 200:1. The molecular weight of the polymer was determined as 190,000 ± 15,000 by the viscometric method of Doty, Bradbury, and Holtzer.[1,9]

Solutions were prepared using spectral quality redistilled and dry solvents. The concentration of PBLG was kept at 18% w/v in all cases. The various solutions were homogenized by shaking and were degassed in the usual manner by a repeated freeze–thaw cycle.

The proton magnetic resonance spectra were recorded on a Varian T-60 spectrometer at a probe temperature of 30 ± 2°. The splitting of the solvent CH_2 resonance was recorded both for nonspinning and spinning samples. These two techniques are in excellent agreement; the splitting obtained with a spinning tube is one-fourth of that for a motionless tube, as theoretically predicted and as checked experimentally.[5] Better accuracy can be obtained with a spinning tube since this leads to improved homogeneity of the magnetic field. The concomitant band narrowing allows one to simply "read" the order parameter S from the doublet separation in the spectrum; it suffices to multiply it by the above factor of 4. This obviates the need for deconvolution of the strongly overlapping doublet components, which are much broader in the spectrum of a nonspinning sample.

The Methylene Chloride–Chloroacetic Acid System

The maximum doublet splitting $\langle S \rangle$ of the methylene chloride protons is plotted in Figure 1 as a function of added $CH_2ClCOOH$ for solutions containing a constant 18% w/v concentration of PBLG (this concentration is equivalent to 1.33 monomer units/l.). As the splitting of the methylene chloride resonance is progressively reduced upon acidification, the splitting of the methylene resonance of $CH_2ClCOOH$ conversely increases.

Assume as a first approximation the following model. The solvent molecules can exist in either of two environments. They can be in an ordered environment, next to the PBLG macromolecules (state A), or they can be in a completely disordered environment (state B). Only one signal is found in the pmr spectrum: exchange between state A and state B is achieved through diffusion at a rate very fast compared to the chemical shift difference of A and B. The following equations then apply

$$\langle S \rangle = p_A \cdot S_A + p_B \cdot S_B \quad (1)$$

$$1 = p_A + p_B \quad (2)$$

where p_A and p_B are the corresponding mole fractions; S_A is the splitting characteristic of, say, the CH_2Cl_2 protons in the ordered state, and S_B is equal to zero in this treatment. Molecules in state A undergo anisotropic rotational motion, so that the angular part $(3 \cos^2 \theta - 1)$ for the dipolar coupling of the methylene protons is not averaged to zero. Molecules in state B completely undergo isotropic rotation, and the dipolar coupling vanishes.

A given splitting: $\langle S \rangle_0 = p_A \cdot S_A$ (*ca.* 82 Hz) is thus measured in pure methylene chloride. If we now consider a binary solution with mole fractions x and $(1 - x)$ of chloroacetic acid and methylene chloride, respectively, the

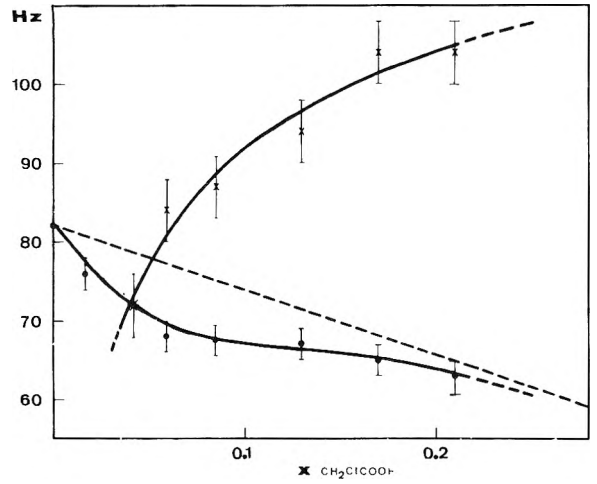

Figure 1. Splitting $\langle S \rangle$ for the methylene protons of CH_2Cl_2 (lower trace) and CH_2Cl–COOH (upper trace), at 60 MHz. The dotted line is that calculated for the methylene chloride protons if dilution by chloroacetic acid were the only phenomenon present.

splitting is reduced to $\langle S \rangle = \langle S \rangle_0 \cdot (1 - x)$ provided the acidic molecules have no preference for site A over site B. Likewise, this simplified treatment predicts that the observed splitting for the methylene protons of $CH_2ClCOOH$ should increase linearly from zero with the mole fraction x. These expectations are borne out exactly only at small acid concentrations (Figure 1). The curvatures which are present *both* for the methylene chloride and for the chloroacetic acid protons imply that the chloroacetic acid molecules have a reduced preference for the type A environment as their concentration increases. This reduced affinity for the proximity of the PBLG molecules in favor of the bulk solution is consonant with a greater degree of self-association on the part of the carboxylic acid molecules. Mainly because of the relative inaccuracy of the data, but also because distinct polymeric species may be present, no limiting $\langle S \rangle_0$ values can be derived for the monomeric and for the polymeric, possibly dimeric, $CH_2ClCOOH$ molecules.

The Methylene Chloride–Trifluoroacetic Acid System

As we shall now see, the opposite behavior is found for the trifluoroacetic acid molecules. Again using as a conceptual reference the simple statistical distribution (dotted line in Figure 2), the CF_3COOH species is seen to manifest a marked preference for the type A sites, close to the PBLG molecules. When methylene chloride is diluted with the stronger trifluoroacetic acid, the splitting $\langle S \rangle$ for the methylene protons is reduced by a significantly greater amount than would be expected on the basis of purely physical dilution. The PBLG–CF_3COOH interaction clearly competes favorably with the self-association of trifluoroacetic acid molecules. It is also noteworthy that the α-helix conformation is retained to a considerable extent up to a concentration of 15% CF_3COOH by volume. Concentrations greater than 20% are necessary for the appearance of the random coil conformation. The spectrum of the PBLG protons is then seen and the doublet observed for the methylene chloride protons in the oriented nematic phase collapses. The helix–random coil transition occurs in our experimental setup between 15 and 20% CF_3COOH by volume. We did not focus our attention on this transition, which is already very well studied.[6,7]

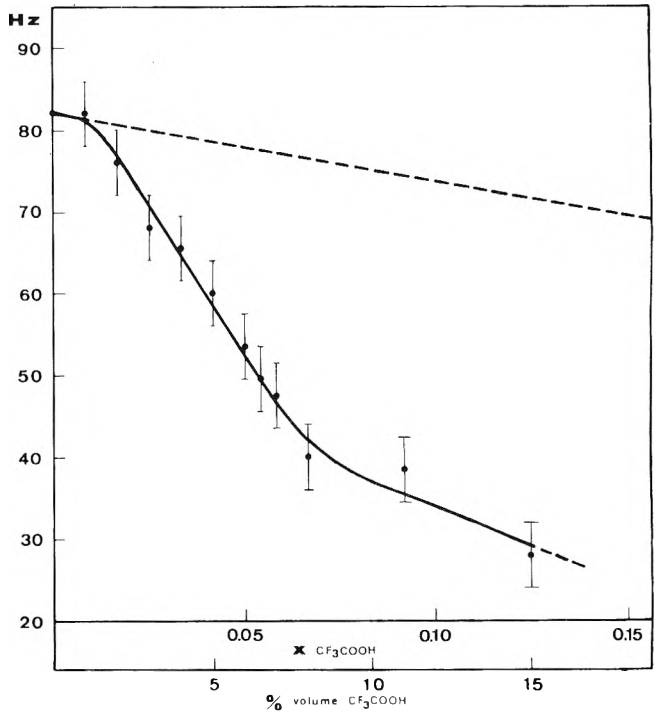

Figure 2. Splitting $\langle S \rangle$ for the methylene protons of CH_2Cl_2 in methylene chloride–trifluoroacetic acid mixtures, at 60 MHz. The dotted line is that calculated for the methylene chloride protons if dilution by trifluoroacetic acid were the only phenomenon present.

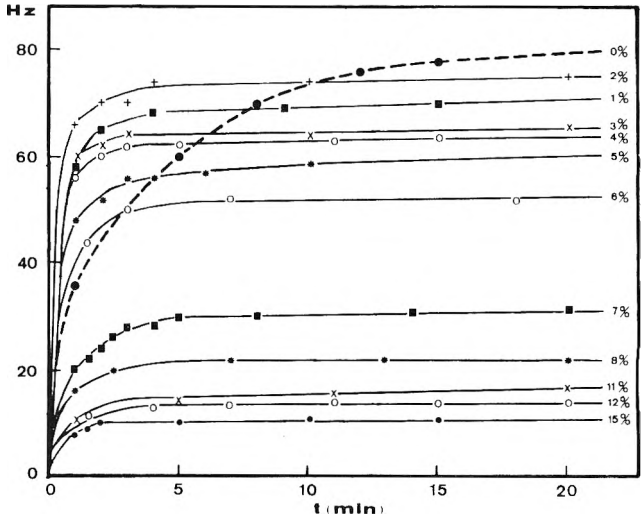

Figure 3. Rapidity of order acquisition by the PBLG samples as measured by the change with time in the apparent splitting $\langle S \rangle$ (±2 Hz) of the methylene protons for methylene chloride–trifluoroacetic acid mixtures. Note the substantia acceleration produced by even small (1–2% by volume) acid concentrations. After 12 hr, the doublet separation $\langle S \rangle$ for solution with 1% CF_3COOH has become greater than for the 2% CF_3COOH solution.

Rather, the pretransition range, 0–15% CF_3COOH by volume, deserves careful consideration.

Notice the continuous change of the $\langle S \rangle$ parameter in Figure 2. Rather than a plateau leading to an abrupt drop, it decreases progressively. Since $\langle S \rangle$ is a weighted average for the CH_2Cl_2 molecules present in the ordered sites A and in the disordered sites B, the first effect of the trifluoroacetic acid molecules could be to deplete the population at sites A in favor of the B sites, or alternatively,

the acid molecules produce a decrease in the degree of order S_A at the A sites. It is possible, we submit, to exclude the former possibility in favor of the latter.

The first possibility would correspond to a reduction in size, an erosion of the nematic domains. Yet, no spectrum of the PBLG molecules appears; it is lost in the noise below 15% CF_3COOH by volume. All of the PBLG molecules continue to be aligned; there is no evidence that the nematic domain does not encompass the whole sample. The alternative explanation, a decrease in the local order in the immediate vicinity of the PBLG molecules, is more consistent with the data. What is the origin of this reduced ordering? It should be argued that the reduction in the local order is due to charging of the PBLG rods, due to their protonation by the acidic CF_3COOH molecules. Then, electrostatic repulsion of the solute molecules would prelude their mutual approach below a given distance and thereby diminish the degree of order S_A. This explains, assuredly, the "unbundling" of the PBLG molecules. Upon addition of a little acid (1–2%) deaggregation occurs[6,10] and the rate of acquisition of order is accelerated markedly (Figure 3). However, this phenomenon appears to be constant over the 1–15% v/v range of concentrations studied. Also, formal protonation of the PBLG molecules by CF_3COOH has been excluded.[7] It could then be argued that reduction in the local order S_A simply arises from the breakdown of segments of the helical structure of the PBLG molecules; rigid rod and random coils fragments would coexist within the same macromolecule. We believe that such an interpretation, *in static terms*, can be ruled out by the experimental evidence. This would effectively amount to orientation of PBLG molecules with a molecular weight equal to a fraction of that of the original sample, *viz.* 190,000. Using similar experimental conditions, we could not achieve any measurable splitting of the methylene chloride resonance in the presence of M = 35,000 polymeric units, without any acid added.

These various incorrect interpretations, namely (a) decrease of the mean volume associated with a nematic domain, (b) repulsion between the positively charged PBLG rods due to protonation, and (c) segmentation of the PBLG macromolecules into rigid rod fragments separated by coiled portions, are thus to be rejected. An explanation of the *observed* decrease in local order as a function of added acid, must be consistent with (a) a nematic mesophase encompassing the entire sample, (b) absence of formal protonation of the PBLG molecules, and (c) increased *flexibility* of the PBLG molecules which, however, maintain the same conformation along the polymeric chain (*e.g.*, without coexistence of fixed helical and coiled structures).

The true phenomenon, we believe, has a dynamic character; locally, a few residues would be altered by the presence of the acidic molecules. There would be a number of such deviations from the ideal α helix at various points along a polymeric chain. These defects would be diffusing linearly back and forth along the chain, in the general direction of the magnetic field. This would preserve the integrity of the macromolecule as a rodlike object. It would mostly increase the flexibility of the rods, on a time average, and in a gradual fashion as more and more acid is added.

In short, in the pretransition range of 0–15% CF_3COOH by volume, the transition is prepared by a gradual loosening of the helical structure, which loses rigidity as the acid concentration is increased.

Acknowledgment. A discussion with Dr. Jean Charvolin (Orsay) is gratefully acknowledged.

References and Notes

(1) P. Doty, J. H. Bradbury, and A. M. Holtzer, *J. Amer. Chem. Soc.*, **78**, 947 (1956).
(2) S. Sobajima, *J. Phys. Soc. Jap.*, **23**, 1070 (1967).
(3) (a) M. Panar and W. D. Phillips, *J. Amer. Chem. Soc.*, **90**, 3880 (1968); (b) D. Gill, M. P. Klein, and G. Kotowycz, *ibid.*, **90**, 6870 (1968); (c) E. T. Samulski and A. V. Tobolsky, *Mol. Cryst.*, **7**, 433 (1969).
(4) A. Sanson and M. Ptak, *C. R. Acad. Sci., Ser. D*, **271**, 1319 (1970); E. L. Wee and W. G. Miller, *J. Phys. Chem.*, **77**, 182 (1973).
(5) (a) B. M. Fung, M. J. Gerace, and L. S. Gerace, *J. Phys. Chem.*, **74**, 83 (1970); (b) R. D. Orwoll and R. L. Vold, *J. Amer. Chem. Soc.*, **93**, 5335 (1971).
(6) (a) G. D. Fasman in "Poly-α-amino Acids," G. D. Fasman, Ed., Marcel Dekker, New York, N. Y., 1967, Chapter 2; (b) K. J. Liu and S. J. Lignowski, *Biopolymers*, **9**, 739 (1970); (c) E. Marchal, C. Dufour, and G. Spach, *J. Chim. Phys.*, **68**, 831 (1971); (d) L. Paolillo, T. Tancredi, P. A. Temussi, E. Trivellone, E. M. Bradbury, and C. Crane-Robinson, *J. Chem. Soc., Chem. Commun.*, 335 (1972).
(7) (a) P. Combelas and C. Garrigou-Lagrange, *C. R. Acad. Sci., Ser. C*, **272**, 1537 (1971); (b) P. Combelas, doctoral thesis, University of Bordeaux I, 1973.
(8) E. R. Blout and R. H. Karlson, *J. Amer. Chem. Soc.*, **78**, 941 (1956).
(9) J. Bandrup and E. H. Immergut, "Polymers Handbook," Interscience, New York, N. Y., 1966.
(10) F. A. Bovey, G. V. D. Tiers, and G. Filipovich, *J. Polym. Sci.*, **38**, 73 (1959).

COMMUNICATIONS TO THE EDITOR

Solubility of Helium in Water and Aqueous Sodium Chloride. A Reply

Sir: In a recent paper[1] we reported the solubility of helium in water and in aqueous sodium chloride at pressures up to 600 atm at various temperatures. The data were fitted by least squares to $\log (f_2/X_2) = a_0 + a_1P + a_2P^2$ for each solvent at each temperature (where f_2 and X_2 are fugacity and mole fraction of helium and P is the total pressure), with no weighting, and treating the pressures as errorless. On the assumption that Henry's law is valid, the parameters led to values for the limiting Henry's law constant, K^0, the limiting partial molar volume of dissolved helium, $\bar{V}_2^0$, and the compressibility of the dissolved helium, $\bar{\beta}^0 = -(1/V_2^0)\,(\partial \bar{V}_2/\partial P)_T$.

Hsieh and Eckert[2] have criticized our treatment of the results. They claim that (1) the data do not warrant the above-mentioned three-parameter treatment, but are adequately expressed by a two-parameter (linear) one, *i.e.*, $\log (f_2/X_2) = a_0' + a_1'P$, (2) a two-parameter fit gives "superior" values for K^0 and $\bar{V}_2^0$, (3) a three-parameter fit yields values of $\bar{\beta}^0$ which are incredibly large.

Table I presents the standard deviations, σ, for both the two- and three-parameter fits for all eight runs, where $\sigma = [\Sigma(\text{residuals in } \log (f_2/X_2))^2/\text{no. of degrees of freedom}]^{1/2}$ In every case σ for the three-constant fit is the smaller of the two. It is true that application of the F test at the 0.05 level of significance shows that the third constant is not warranted for runs 2, 5, 7, and 8, but it is also true that, in the two-constant fits, the signs of the residuals for the highest and lowest pressures are, in all eight runs, opposite to those for medium pressures, whereas in the three-constant fits the signs occur randomly. Since, then, three constants were indicated statistically in at least half, and probably more than half, of the runs, we treated all eight on that basis. Hsieh and Eckert claim, further, that at 100° "even a three-constant fit of the data gave standard deviations of 3–5%." This does not agree with our results in Table I. If one subjects the data to a two-parameter fit as they suggest, it is implied that there are experimental errors in $\log (f_2/X_2)$ as large as 0.01 at 50° and 0.02 at 100°, in which case the data are not of the quality credited to them by these same authors. We believe that the experimental uncertainties in $\log (f_2/X_2)$ are roughly one order of magnitude less than those just mentioned.

The *interpretation* of the parameters is a different matter. Our interpretation in terms of K^0, V_2^0, and $\bar{\beta}^0$ rests on the applicability of Henry's law to the dissolved helium at all pressures and temperatures studied. It is possible that this is not so, but the arguments presented by us seem to eliminate alternative interpretations. There is, of course, considerable uncertainty in the derived values of K^0, $\bar{V}_2^0$, and $\bar{\beta}^0$, and Table II gives these uncertainties calculated from the standard deviations in a_0, a_1, and a_2. With regard to K^0 and $\bar{V}_2^0$ it must be pointed out that no measurements of X_2 were made at pressures below 100 atm (sometimes 200 atm) so that quantities derived for the limit of zero pressure are really outside the range of measurement. The claim that the two-constant equation gives superior values for $\bar{V}_2^0$ and K^0 is not substantiated by the figures in their table. Measurements of $\bar{V}_2^0$ for helium under the conditions of the eight runs by *any* other method are nonexistent. For other gases (N_2, CH_4) two-parameter $\bar{V}_2^0$ values[3] are lower than those measured directly by dilatometry.[4] Addition of a third parameter would be expected to increase them, and so may be considered as a move in the right direction. The values of K^0, obtained with two parameters, show better agreement with the results of other workers in only two of the four comparisons made. Furthermore, Hsieh and Eckert find for helium in water at 50° that $\bar{V}_2^0$, calculated with two parameters, agrees better with that found from Wiebe's data[5] than with that found by us using three parameters. However, Wiebe's work is subject to an admitted error which seriously affects two-constant treatments of his data.

We share the surprise of Hsieh and Eckert at the size of $\bar{\beta}^0$ and can only remark that at present it is simply a result obtained as a consequence of making certain reasonable assumptions.

TABLE I: Standard Deviation of Fit for Two- and Three-Parameter Functions

Run no	Solvent and temperature, °C	Two-parameter	Three-parameter
1	1.003 *m* NaCl at 25°	0.0010	0.0003
2	4.067 *m* NaCl at 25°	0.00342	0.00336
3	Water at 50°	0.0083	0.0009
4	1.003 *m* NaCl at 50°	0.0067	0.0012
5	4.067 *m* NaCl at 50°	0.0030	0.0011
6	Water at 100°	0.0142	0.0036
7	1.003 *m* NaCl at 100°	0.0179	0.0066
8	4.067 *m* NaCl at 100°	0.0065	0.0064

TABLE II: Estimated Uncertainties in K^0, $\bar{V}_2^0$, and $\bar{\beta}^0$ from Three-Parameter Fits

Run no.	K^0, atm × 10^{-5}	$\bar{V}_2^0$, cm³/mol	$\bar{\beta}^0$, atm^{-1} × 10^3	Run no.	K^0, atm × 10^{-5}	$\bar{V}_2^0$, cm³/mol	$\bar{\beta}^0$, atm^{-1} × 10^3
1	0.002	0.2	0.03	5	0.031	1.5	0.16
2	0.096	4.1	0.50	6	0.018	3.0	0.22
3	0.005	0.7	0.08	7	0.039	5.4	0.34
4	0.009	0.8	0.04	8	0.151	9.8	0.82

We share the surprise of Hsieh and Eckert at the size of $\bar{\beta}^0$ and can only remark that at present it is simply a result obtained as a consequence of making certain reasonable assumptions.

References and Notes

(1) G. E. Gardiner and N. O. Smith, *J. Phys. Chem.* **76**, 1195 (1972).
(2) C. K. Hsieh and C. A. Eckert, *J. Phys. Chem.*, **77**, 2019 (1973).
(3) T. D. O'Sullivan and N. O. Smith, *J. Phys. Chem.*, **74**, 1460 (1970).
(4) I. Kritchevsky and A. Iliinskaya, *Acta Physicochim. URSS*, **20**, 327 (1945).
(5) R. Wiebe and V. L. Gaddy, *J. Amer. Chem. Soc.*, **57**, 847 (1935).

Environmental Maintenance Corp.
Orange, Connecticut 06477
Gregory E. Gardiner

Department of Chemistry
Fordham University
New York, New York 10458
Norman O. Smith*

Received August 6, 1973

Comment on the Bending Mode of Al_2O[1,2a]

Publication costs assisted by the Office of Naval Research

Sir: In an article entitled "Infrared Spectra of the Aluminum Family Suboxides"[2b] published in this journal, a weak absorption at 503 cm^{-1} in the spectrum of what was assumed to be matrix-isolated Al_2O was assigned to the bending mode ν_2. This was not observed in either the original investigation of Linevsky, White, and Mann[3a] nor in the subsequent studies[3b] of Snelson which focused exclusively on the missing bending fundamental ν_2. In both of these earlier studies it was suggested that this vibration should be observable below 250 cm^{-1}, a conclusion based on the assumption of ionic bonding[4] as well as what is observed in the analogous case, Li_2O.[5] This unusually high frequency of 503 cm^{-1} for the bending mode of the symmetric nonlinear molecule Al_2O was justified by Carlson, *et al.*,[2b] in terms of metal–metal bonding. This argument, although interesting, does not, however, seem plausible. We have therefore reexamined the spectrum of Al_2O with particular emphasis on impurities that on occasion give rise to bands attributable to molecular aggregates formed on matrix deposition.

In the three matrix isolation experiments discussed above,[2b,3] the molecular species Al_2O is formed by the reaction of liquid aluminum with solid Al_2O_3. The molecular beam effusing from a Knudsen cell at approximately 1300°K containing these materials consists, however, of several species. Mass spectrometric analysis of these vapors shows not only gaseous $Al_2O(g)$ but also Al(g). Thus deposition on the optically transmitting cold window produces a solid rare gas matrix containing atomic aluminum as well as Al_2O. As we have observed in our lithium experiments[6] the spectrum of such matrices, *i.e.*, matrices containing the free metallic atoms together with other impurities, can be quite complex, particularly if diffusion occurs. The reason for this, as demonstrated by Andrews,[7,8] is the formation of peroxides and superoxides on the surface of the crystallizing matrix by the reaction of the metal atoms with molecular oxygen. These are not only characteristic of the alkali metals,[8] but also metals in other groups of the periodic table.[9]

In this brief report we examine the effect of the impurity, molecular oxygen, on the spectrum of the matrix-isolated mixture of Al and Al_2O. The conditions here are identical with what has previously been reported in ref 2b and 3, namely, effusion from a Knudsen cell containing liquid aluminum in contact with Al_2O_3. The results are shown graphically in Figure 1 where we focus on two spectral regions, namely, the ν_3 region of $Al_2O(g)$ at approximately 1000 cm^{-1} and the 500-cm^{-1} region where Carlson, *et al.*,[2b] reported the bending mode ν_2. The asymmetric stretch, ν_3, of Al_2O is the most intense feature in the spectrum, when the mixture Al and Al_2O is trapped in the argon matrix at liquid helium temperatures (upper panel A of Figure 1). There is no evidence for even a very weak feature in the vicinity of 500 cm^{-1}. Introducing approximately 3% $^{16}O_2$ into the argon stream produces the spectrum in panel B. There is now a strong band at 496 cm^{-1} which is directly attributable to the oxygen impurity that codeposits with the Al and Al_2O on the cold window. In panel C the isotope $^{18}O_2$ is now introduced as the impurity. Whereas ν_3 of $Al_2O(g)$ is unaffected by the presence of $^{18}O_2$, the band at lower frequency shifts to 481 cm^{-1}. This clearly demonstrates that the absorption at 500 cm^{-1} is not due to an oxygen-containing species effusing from the Knudsen cell, but rather a molecular aggregate formed on deposition of the matrix. Finally, the lower panel D clearly illustrates that the oxygen-containing molecule formed in the matrix contains two oxygen atoms.

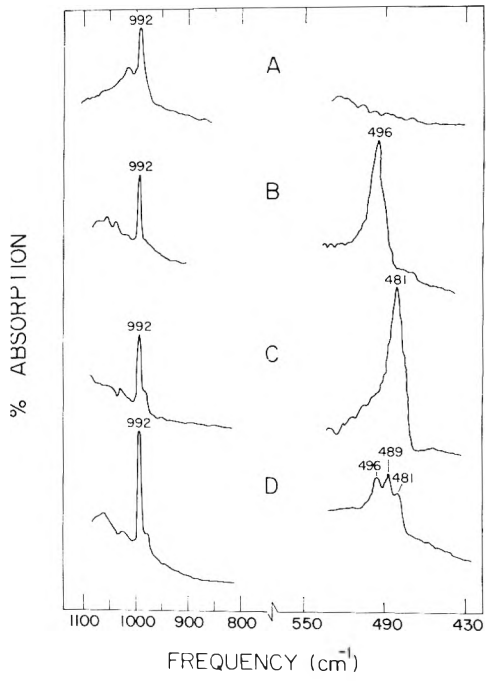

Figure 1. Composite spectra of major absorption features observed at 4°K following the deposition of Al atoms, from an Al_2O_3 Knudsen cell, with various isotopic oxygen molecules in argon in the frequency range 1100–430 cm^{-1}: (A) no oxygen; (B) 5% $^{16}O_2$ on argon; (C) 5% $^{18}O_2$ in argon; (D) 5% $^{18}O_2$, $^{18}O^{16}O$, $^{16}O_2$ in argon.

Although one cannot at this time assign the band to a particular molecule, in all probability it is due to an aluminum peroxide. From its location, intensity and ^{16}O–^{18}O shift, we are presently inclined to assign it to the B_{2u} mode of rhombic Al_2O_2. This will be discussed in greater detail elsewhere.

References and Notes

(1) This work was supported in part by the Office of Naval Research under Contract No. ONR-N000014-67-A-0216-0001.
(2) (a) Editor's Note. Professor Carlson has advised us in correspondence that on reconsidering the concentrations involved in their Al_2O experiments, he and his associates no longer accept the band at 503 cm^{-1} as being the ν_2 mode of Al_2O. They are not in a position, however, to conclude whether or not this absorption is the same as that studied by Marino and White. The energy difference amounts to 7 cm^{-1}. It is possible then that the two arise from different carriers, with the 503-cm^{-1} band perhaps being a dimer of Al_2O, similar to the so-called ν_2 modes of the heavier metal suboxides [A. J. Hinchcliffe and J. S. Ogden, *J. Phys. Chem.*, **75**, 3908 (1971)]. (b) D. M. Makowiecki, D. A. Lynch, Jr., and K. D. Carlson, *J. Phys. Chem.*, **75**, 1963 (1971).
(3) (a) M. J. Linevsky, D. White, and D. E. Mann, *J. Chem. Phys.*, **41**, 542 (1964); (b) A. Snelson, *J. Phys. Chem.*, **74**, 2574 (1970).
(4) A. Buchler, W. Klemperer, and A. G. Emslie, *J. Chem. Phys.*, **36**, 2499 (1962).
(5) D. White, K. S. Seshadri, D. F. Dever, D. E. Mann, and M. J. Linevsky, *J. Chem. Phys.*, **39**, 2463 (1963).
(6) K. S. Seshadri, D. White, and D. E. Mann, *J. Chem. Phys.*, **45**, 4697 (1966).
(7) L. Andrews, *J. Chem. Phys.*, **50**, 4288 (1969).
(8) L. Andrews, *J. Chem. Phys.*, **54**, 4935 (1971).
(9) Unpublished results, this laboratory.

Department of Chemistry
University of Pennsylvania
Philadelphia, Pennsylvania 19104

Charles P. Marino
David White*

Received August 27, 1973

On the Ammonia–Hydrogen Chloride Complex

Publication costs assisted by the Petroleum Research Fund

Sir: A recent article by Ault and Pimentel[1] offers partial experimental confirmation of the existence of an ammonia–hydrogen chloride complex first postulated by Clementi and Gayles.[2] This letter reports the results of a model calculation which supports in part the experimental findings of Ault and Pimentel.

Using a C_{3v} model of the NH_3–HCl complex, the significant vibrational motions characteristic of the complex are: (1) a modified HCl stretch (ω_1); (2) a new N–H (complex bond) stretch (ω_2); (3) a new N–H–Cl bend (ω_3); and (4) a new NH_3 bend (or rock) (ω_4).

The critical parameters for the approximate C_{3v} calculation are the N–H and H–Cl bond distances. These distances were estimated to be 1.5 and 1.7 Å, respectively. The rationale for these estimates is given in ref 2.

Using the approximate relation developed by Gordy,[3] it is possible to estimate limiting values of the necessary potential constants due to stretching. The bending potential constants must be estimated based upon their values in related compounds.[4] The other geometrical parameters are approximated by their values in the isolated or "free" compounds. The approximate stretching constants are 3.29×10^5 and 2.13×10^5 dyn/cm for the modified HCl and "new" N–H stretches (bond order ½), respectively. The bending constants were taken to be 0.03×10^5 and 0.02×10^5 dyn/cm for the N–HCl and NH_3 bends, respectively.

The GF matrix calculation of the normal mode frequencies may be carried out using conventional techniques.[5] The results are A_1, $\omega_1 = 2970\ cm^{-1}$; A_1 $\omega_2 = 617\ cm^{-1}$; E, $\omega_3 = 757\ cm^{-1}$; and E, $\omega_4 = 408\ cm^{-1}$.

These results compare well with the results of Ault and Pimentel in two cases. The 757-cm^{-1} (theoretical) value should be compared with the 705-cm^{-1} (experimental) value. Also, the 612-cm^{-1} (theoretical) value should be compared with the 630-cm^{-1} (experimental) value. The remaining experimental frequencies are 1438 and 1246 cm^{-1}. It is suggested by Ault and Pimentel that these higher experimental frequencies are overtone frequencies. Our results certainly concur with that suggestion.

The NH_3–DCl frequencies show an isotope shift that compares favorably with experiment. The experimental values for ω_2 and ω_3 are 470 and 605 cm^{-1}. The model predicts 435 and 537 cm^{-1}. The isotope ratios are 1.40 in each of the theoretical frequencies and 1.40 and 1.34 in the experimental frequencies.

The above results show an impressive confirmation of the experiments of Ault and Pimentel. It is clear, however, that two additional vibrational spectral features remain to be observed. Intensity variations in previous spectra on related substances[4] suggest that it is likely that these additional features will be found under conditions of greater experimental sensitivity.

Acknowledgment. Acknowledgment is made to the donors of the Petroleum Research Fund, administered by the American Chemical Society, for the support of this research.

References and Notes

(1) B. S. Ault and G. C. Pimentel, *J. Phys. Chem.*, **77**, 1649 (1973).
(2) E. Clementi and J. N. Gayles, *J. Chem. Phys.*, **47**, 3837 (1967).
(3) W. Gordy, *J. Chem. Phys.*, **14**, 305 (1946).
(4) J. N. Gayles, *J. Chem. Phys.*, **49**, 1840 (1968).
(5) E. B. Wilson, J. C. Decius, and P. C. Cross, "Molecular Vibrations," McGraw-Hill, New York, N. Y., 1955.

Department of Chemistry
Morehouse College
Atlanta, Georgia 30314

J. N. Gayles

Received August 27, 1973

Journal of Chemical and Engineering Data

OCTOBER 1973, Vol. 18, No. 4

TABLE OF CONTENTS

■ Supplementary material for this paper is available separately, in photocopy or microfiche form. Ordering information is given in the paper.

The leading American journal devoted to general organic chemistry:

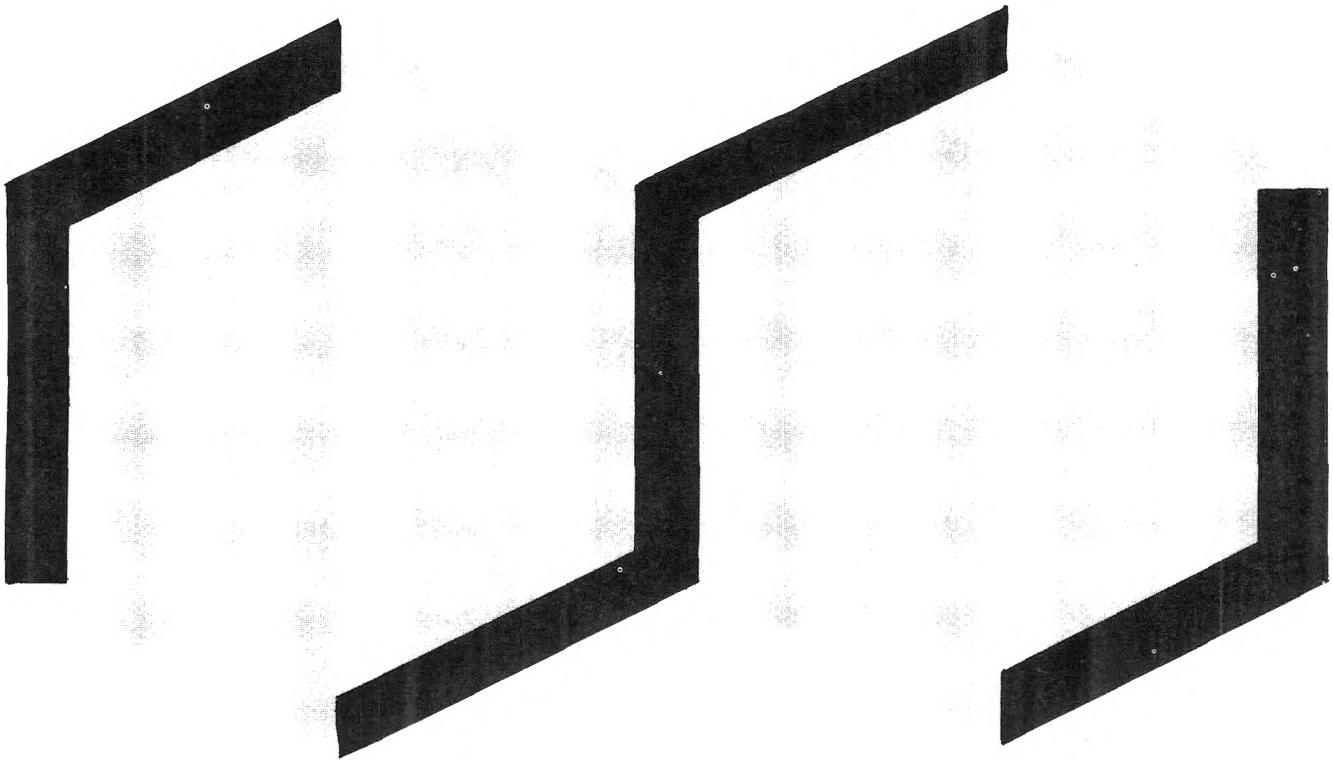

The Journal of Organic Chemistry

The career wise way to keep up with current thinking in the field. You get the *total picture* presented through forty some papers per biweekly issue Areas of emphasis include:

- Organic reactions
- Natural products
- Studies of mechanism
- Theoretical organic chemistry
- Various aspects of spectroscopy related to organic chemistry

You get all of this, in the 1100 articles and NOTES (brief, concise accounts of studies of smaller scope) and over 4000 pages a year from your big informative issues of THE JOURNAL.

You owe it to your career to find out for yourself why The Journal of Organic Chemistry is the leader in its field.

Send your order today

. . . *another ACS service*

The Journal of Organic Chemistry
American Chemical Society
1155 Sixteenth Street, N.W.
Washington, D.C. 20036

Yes, I would like to receive THE JOURNAL OF ORGANIC CHEMISTRY at the one-year rate checked below:

	U.S.	*Canada*	*Latin America*	*Other Nations*
ACS Member Personal-Use One-Year Rate	☐ $20.00	☐ $25.00	☐ $25.00	☐ $26.00
Nonmember	☐ $60.00	☐ $65.00	☐ $65.00	☐ $66.00

Bill me ☐ Bill company ☐ Payment enclosed ☐

Name _____

Street _____ Home ☐ Business ☐

City _____ State _____ Zip _____

G-73

Molecular Sieve Zeolites

ADVANCES IN CHEMISTRY SERIES No. 101 and 102

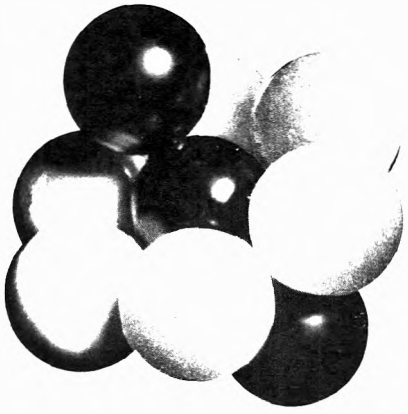

Seventy-seven papers from a symposium co-sponsored by the Divisions of Colloid and Surface Chemistry, Petroleum Chemistry, and Physical Chemistry of the American Chemical Society and Worcester Polytechnic Institute, Edith M. Flanigen and Leonard B. Sand, co-chairmen.

Do you need a group of substances that can remove radioactive isotopes from nuclear wastes, remove ammonia from secondary sewage effluents, remove sulfur dioxide from waste gases, foster formation of actinides, or disrupt bacterial cells? These and many other possibilities are available through research on molecular sieve zeolites. For example, they are used for separating hydrogen isotopes . . . solubilizing enzymes . . . carrying active catalysts in curing of plastics . . . transporting soil nutrients in fertilizers . . . filtering tars from cigarette smoke.

"Molecular Sieve Zeolites" reports recent advances in this rapidly developing field. Volume I offers 41 papers devoted to the synthesis, structure, mineralogy, and modification of sieve zeolites. These are followed in Volume II by 36 papers discussing sorption and catalysts.

Volume I: 526 pages with index	Cloth	(1971)	$16.00
Volume II: 459 pages with index	Cloth	(1971)	$16.00
No. 101 and 102 ordered together			$30.00

Postpaid in U.S. and Canada; plus 40 cents elsewhere.
Set of L.C. cards with library orders upon request.

Other books in the ADVANCES IN CHEMISTRY series on colloid chemistry include:

No. 95 Cellulases and Their Applications
Twenty-five papers stress the practical application of cellulolytic systems in biochemistry, animal nutrition, textiles, forest product utilization. Topics include new mechanisms for cellulose degradation, the cellulase complex, structure and morphology of cellulase, a commercial enzyme process and wood-derived products as nutritional sources.
470 pages with index Cloth (1969) $14.50

No. 87 Interaction of Liquids at Solid Substrates
Twelve papers survey recent research on solid/liquid interaction, including work on "coupling agents," adhesion of polymers, organic/inorganic interfaces, ultrasonic impedometry. Four more papers are concerned with heparinized surfaces at the blood/material interface.
212 pages with index Cloth (1968) $9.50

No. 84 Molecular Association in Biological and Related Systems
Nineteen articles survey and report new work on molecular association in fat digestion, in soap systems, in membrane constituents, and in mixed monolayers. Other topics include bile salt micelles, lipid monolayers and membranes, and a definitive review of biological membrane structure.
308 pages with index Cloth (1968) $10.50

No. 79 Adsorption from Aqueous Solution
Fifteen papers discuss thermodynamic and kinetic aspects of adsorption phenomena and the results of studies on a variety of adsorbate-adsorbent systems.
212 pages with index Cloth (1968) $10.00

No. 63 Ordered Fluids and Liquid Crystals
Twenty-two studies on characterization, properties, and occurrence of these phenomena in many substances such as tristearin, *p*-azoxyanisole, mono- and di-hydric alcohols, phospholipids, and polypeptides.
332 pages with index Cloth (1967) $11.50

No. 43 Contact Angle, Wettability, and Adhesion
Surface chemistry studies. Relation of equilibrium contact angle to liquid and solid constitution, contact angle as a thermodynamic property, surface energy estimation from contact angle. Contact angle hysteresis, relationship between wetting and adhesion.
389 pages with index Cloth (1964) $10.50

No. 33 Solid Surfaces and the Gas-Solid Interface
Thirty-seven papers from the Kendall Award Symposium honoring Stephen Brunauer. Theory and techniques for studying surface phenomena.
381 pages with index Cloth (1961) $12.00

Order from: **Special Issues Sales**
American Chemical Society, 1155 16th Street, N.W., Washington, D.C. 20036